School of Science
Department of Imaging and Applied Physics

A Nanostructural Investigation of Mechanochemically Synthesised Hydrogen Storage Materials

Mark Paskevicius

This thesis is presented for the Degree of
Doctor of Philosophy
of
Curtin University of Technology

December 2009

Declaration

To the best of my knowledge and belief this thesis contains no material previously published by any other person except where due acknowledgement has been made.

This thesis contains no material which has been accepted for the award of any other degree or diploma in any university.

Signature: .....

Date: .....

Dedicated to my darling wife Alicia and our beautiful son Wesley

Acknowledgements

Firstly I would like to thank my Ph.D. supervisor Prof. Craig Buckley for his tireless work in providing a first class research environment and always having time to point me in the right direction.

A special thankyou is given to the Australian Government for awarding me with an Australian Postgraduate Award (APA) and the Australian Institute of Nuclear Science and Engineering (AINSE) for providing me with a Postgraduate Research Award (PGRA). I would also like to individually thank Dennis Mather and Rhiannon Still for their support.

I would also like to acknowledge the facilities, scientific and technical assistance of the Australian Synchrotron and the Australian Microscopy & Microanalysis Research Facility at the Centre for Microscopy, Characterisation & Analysis, The University of Western Australia, a facility funded by The University, State and Commonwealth Governments. The MgH_2 work was carried out with the support of the CSIRO Energy Transformed Flagship National Hydrogen Materials Alliance (NHMA), Australia and an Australian Research Council Discovery grant DP0877155.

I would also like to thank:

My wife Alicia for all her support. Drew Sheppard for all his help in the lab and for our extensive afternoon discussions. Glen Lawson for providing valuable assistance in all things lab-based. Evan Gray, Jim Webb, Tomasz Blach, and Mark Pitt at Griffith University for their support with high pressure hydrogen measurements. Rob Hart for his assistance with TEM investigations. Ross Williams for his help with XRD analysis. William Rickard for his help with SEM investigations. Bipina Dhal for his assistance with Al synthesis. Leith Rankine and Daniel Marrable for their help in building the automated hydrogen sorption apparatus.

Thanks to everyone else who has provided help and support during my Ph.D.

Abstract

Aluminium, aluminium hydride (alane), and magnesium hydride nanoparticles have been mechanochemically synthesised in order to study their hydrogen sorption properties in contrast to the bulk. Nanoparticle formation was facilitated by the addition of a salt phase to ball milled chemical reagents that matched the reaction by-product phase. The presence of a salt buffer during ball milling prevents agglomeration and thus restricts particle growth.

Aluminium nanoparticles were mechanochemically synthesised with particle sizes from 40 – 55 nm. The LiCl salt by-product phase was removed by washing with a nitromethane/$AlCl_3$ solution resulting in 55 nm Al particles (single crystals) that did not display any crystalline oxide phases. High pressure hydrogen absorption experiments were undertaken up to 2 kbar at temperatures from 77 – 473 K to examine if there were any major thermodynamic changes to the Al. No hydrogen absorption could be detected proving that either smaller Al is required to form AlH_3 under these conditions or higher pressures are needed. Ni-coated and Ti-doped Al nanoparticles were also synthesised in order to verify if catalytic metals could enhance hydriding kinetics and allow hydrogenation to occur at lower pressures. However the doped samples did not display any hydrogen absorption up to 108 bar.

Alane nanoparticles were synthesised using both room temperature and cryogenic mechanochemical synthesis with particle sizes < 100 nm. The evolution of alane production was investigated as a function of milling time under a variety of milling conditions. Cryogenic milling was verified to form higher yields of AlH_3 than room temperature milling and four different alane phases (α, α', β, γ) were identified by XRD structural investigations. The LiCl reaction by-product phase was removed by washing with a nitromethane/$AlCl_3$ solution, which adversely reacted with the AlH_3 nanoparticles. The hydrogen desorption kinetics in washed samples were hindered, and the maximum H_2 wt.% was halved although no crystalline oxide or hydroxide phases were found using XRD. Unwashed mechanochemically synthesised AlH_3 was found to desorb at room temperature over months and significantly at 50°C in a 24 hr

period. Quantitative Rietveld results coupled with hydrogen desorption measurements suggested the presence of an amorphous AlH_3 phase in the mechanochemically synthesised samples.

The mechanochemical synthesis of MgH_2 was undertaken with varying LiCl buffer quantities. Increasing the buffer resulted in MgH_2 crystallite sizes down to 6.7 nm, measured by XRD, whilst TEM investigations showed that increasing the buffer resulted in smaller, more highly dispersed MgH_2 nanoparticles. The size of these MgH_2 particles approached theoretical predictions for thermodynamic changes, where the MgH_2 is only physically bound by the LiCl. Hydrogen equilibrium pressure measurements were used to determine the decomposition enthalpy and entropy for MgH_2 nanoparticles that were mechanochemically synthesised. A reduction in both the decomposition enthalpy (ΔH decrease of 2.84 kJ/mol H_2) and entropy (ΔS decrease of 3.8 J/mol H_2/K) was found for ~7 nm MgH_2 nanoparticles in relation to bulk MgH_2. The consequence of this thermodynamic destabilization is a drop in the 1 bar hydrogen equilibrium pressure of ~6°C. The temperature drop is not as large as theoretical predictions due to the decrease in reaction entropy which partially counteracts the effect from the decrease in reaction enthalpy.

Table of Contents

List of Figures

List of Tables

Chapter 1

Introduction

"The science of today is the technology of tomorrow" – Edward Teller

1.1 OVERVIEW

This thesis is directed towards investigating the hydrogen storage properties of both aluminium and magnesium nanoparticles. Materials that are widely available have been chosen to be investigated because the Earth's mineral resources are running low and many minerals and metals are set to run out within the next 10 - 50 years given current demand [1]. If a metal-based hydrogen storage system is to be made commercially viable, and available for installation into most of the cars on the planet, then a material with a very high abundance in the Earth's crust must be selected as a major component (see Figure 1-1). Both aluminium and magnesium comprise major fractions of the Earth's crust making them ideal for mass implementation as a hydrogen fuel tank from an economic standpoint. Furthermore, the high worldwide production of aluminium metal (33.9 million tonnes in 2006 [2]) means that aluminium-based hydrogen fuel tanks could be built very quickly without increasing production. Whereas magnesium metal has a relatively low worldwide production (708,000 tonnes in 2006 [2]) indicating that an increase in production would need to be undertaken before mass implementation of magnesium-based hydrogen fuel tanks.

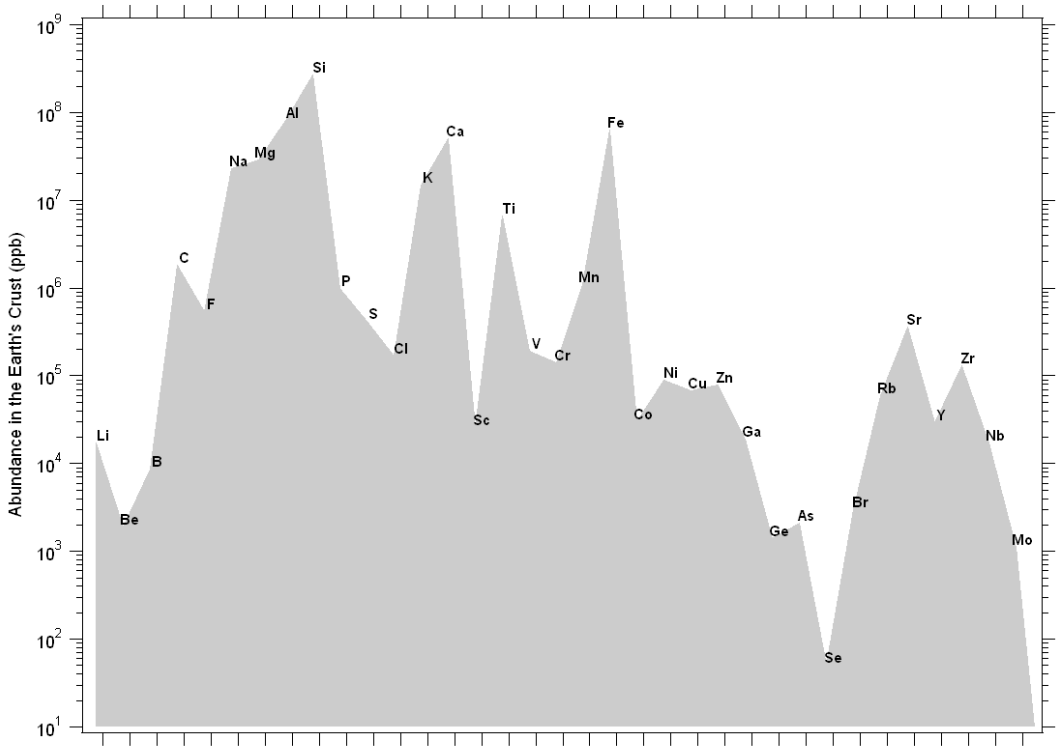

Figure 1-1: Abundance of relevant, light elements in the Earth's crust [3]. Abundances are given in parts per billion (ppb) by weight and are scaled logarithmically.

Aluminium and magnesium form chemical hydrides (AlH_3 and MgH_2 respectively) when hydrogen gas pressure is applied under favourable conditions. The metal hydrides decompose to their respective metals and hydrogen gas when samples are heated. Both aluminium and magnesium have many favourable hydrogen storage properties, however both metals also have major problems that prevent them from being immediately implemented for vehicular applications. Aluminium metal requires extreme hydrogen pressure (~ 2.5 GPa [4-5]) in order to form its respective hydride (AlH_3). Magnesium can form MgH_2 at low hydrogen pressure but requires high temperatures (~ 300 ºC) for hydrogen equilibrium pressures greater than 1 bar [6].

The intention of this thesis is to investigate how hydrogen interacts with nanoparticle Al/AlH_3 and Mg/MgH_2 systems in comparison to their bulk systems. Many materials have different inherent characteristics when particle size is sufficiently reduced [7], a property that may influence the interaction of hydrogen with these nanoparticle systems. Aluminium, aluminium hydride, and magnesium hydride nanoparticle samples are synthesised, characterised, and their interactions with hydrogen are analysed using samples with different particle sizes in order to understand their behaviour with hydrogen in contrast to the bulk.

1.2 SIGNIFICANCE

The body of literature concerning hydrogen storage materials is immense, which is an indication of the difficulties that researchers around the world are encountering in storing hydrogen to commercially relevant specifications for use in automotive vehicles. It is also an indication of the necessity to solve the problem of on-board hydrogen storage before fossil fuel production begins to dwindle due to the lack of oil reserves. Early predictions expected oil production to peak in 2005 however more recent studies predict a peak in production in the next 10 - 40 years [8]. These predictions are based on the amount of oil that the Earth still holds and given expected demand. Limited oil reserves with an expiry date in the foreseeable future are the main driving force behind the large amount of research undertaken around the globe in the hydrogen storage field.

Another important reason to find an alternative to oil-based fuels for vehicles is related to the fact that these fuels are responsible for over half of all greenhouse gas emissions [9] and thus have a major impact on global warming. Hydrogen has been recognised as the ideal future fuel [10], because it has an extremely high energy density (141 kJ/g compared to 47.6 kJ/g for petrol [11]) and is the cleanest fuel with its only reaction by-product being pure water, H_2O. Hydrogen is only an energy carrier however and it must be generated using an energy source. Most of the hydrogen currently generated relies upon energy from fossil fuels that can also generate carbon dioxide by-products. Therefore to make hydrogen cleanly in bulk it must be generated by the electrolysis of water using renewable energy sources [12]. The mass production of hydrogen for use as an alternate energy carrier has been studied in detail in the literature with socioeconomic considerations (i.e. by Ogden [9]), however there are major hurdles that have to be overcome, and a gradual transition to an alternate energy carrier is inevitable. It has been reported [13] that it may take several decades to make the transition to a 'hydrogen economy', suggesting that hydrogen-based research must be undertaken without delay.

The U.S. Department of Energy (DOE) has outlined a set of targets that would allow a hydrogen based storage system to be implemented in a commercially viable sense. These DOE FreedomCAR goals are outlined in Table 1-1 and it is stressed that these targets are based almost purely on commercial requirements and as the demand for

alternative fuels grow (when oil production begins to peak) these targets will change and hydrogen storage systems that do not currently meet these targets will become commercially viable. The challenging nature of these targets has also been expressed in the literature [14] suggesting that they are far beyond the current state-of-the-art for all known reversible metal hydrides.

Table 1-1: U.S. Department of Energy (DOE) FreedomCAR goals for 5 kg on-board hydrogen storage systems [15].

	2010	**2015**
Gravimetric System	7.2 MJ/kg	10.8 MJ/kg
Gravimetric Capacity	~ 6 wt.% H_2	~ 9 wt.% H_2
Specific Energy	0.060 kg · H_2/kg_{system}	0.090 kg · H_2/kg_{system}
Total Weight	83 kg	55.6 kg
Volumetric System	5.4 MJ/L	9.7 MJ/L
Volumetric Capacity	0.045 kg · H_2/L	0.081 kg · H_2/L
System Cost	~$133USD/kg · H_2	~$67USD/kg · H_2
Total Cost	$665USD	$335USD
Refuelling Rate	1.5 kg · H_2/min	2.0 kg · H_2/min
Total Refuelling Time	3.3 min	2.5 min

1.3 HYDROGEN STORAGE

The storage of hydrogen is one of the most important issues that needs to be solved before the mass implementation of hydrogen as an energy carrier begins commercially [13]. There are a number of factors that must be considered in the construction/synthesis of a hydrogen storage system including weight density, volume density, cost, flow rates, speed of response, and life cycles [7]. There are also other considerations that may be applicable for some storage systems such as: absorption and desorption temperatures, plateau pressures, hysteresis, ease of activation, reversibility and the ability to withstand poisoning or deactivation with impure gas streams.

1.3.1 Hydrogen Storage Methods

There are four reversible hydrogen storage methods that are of primary interest [16]:

1. Compressed hydrogen gas
2. Liquid hydrogen
3. The physisorption of hydrogen
4. The chemisorption of hydrogen

A future storage system for hydrogen must meet the requirements of being compact, lightweight, low cost, rugged, easily and rapidly refillable, safe, and with a high hydrogen storage capacity [9]. These requirements have been outlined by the DOE with specific targets for 2010 and 2015. None of the aforementioned storage methods currently meet all of these criteria but research is underway around the world to achieve these targets.

1.3.1.1 *Compressed Hydrogen Gas*

Compressed hydrogen gas can be stored in composite tanks at pressures up to 700 bar allowing 4 – 6 kg of hydrogen to provide a 400 – 500 km range for vehicles. 5 kg of hydrogen occupies 61 m^3 (at room temperature and atmospheric pressure) which can be improved to 0.13 m^3 (internal tank volume) under 700 bar. However high pressures raise certain safety concerns and current composite tanks have high failure

risks at sub-zero operational temperatures [17]. The major concern with using compressed hydrogen gas is the low volumetric density (less than 40 kgm^{-3} in new tanks capable of withstanding 800 bar [16]), significantly less than most metal hydrides (80 – 160 kgm^{-3}). However, compressed hydrogen tanks are relatively simple to implement as they are based on existing technology, and they have already been used in a range of hydrogen powered vehicles such as the 2006 Ford Explorer [18].

1.3.1.2 *Liquid Hydrogen*

Liquid hydrogen must be cooled to 21 K, requiring a considerable initial energy input, which is made worse by gradual heat transfer during storage resulting in further energy loss [17]. However liquefied hydrogen storage tanks are attractive due to their relatively high volumetric storage density of 70.8 kg/m^3. Despite the drawbacks, car companies have built production cars (such as BMW's "Hydrogen 7" [19]) that use liquefied hydrogen fuel tanks.

1.3.1.3 *The Physisorption of Hydrogen*

The physisorption process is essentially a van der Waals interaction between hydrogen molecules and a materials surface as illustrated in Figure 1-2. Physisorption is only significant at low temperatures (< 273 K) [16] due to the weak bonding forces involved, thus limiting its usefulness in vehicular applications. The majority of research on hydrogen physisorption is directed towards low-mass, high surface area materials such as carbon aerogels [20], activated carbons [21], and carbon nanotubes [21]. Further research is directed towards high surface area materials that have additional bonding forces (to trap the hydrogen at higher temperatures) in structures such as metal organic frameworks (MOF's) [22]. Although hydrogen physisorption materials have so far met limited success at room temperature they are still promising given their low-cost and low operating pressures [16].

1.3.1.4 *The Chemisorption of Hydrogen*

The work presented in this thesis is based on the principle of chemisorption as this is the process by which both Al and Mg absorb hydrogen. The chemisorption process firstly involves the collision of a H_2 molecule with the metal surface which is followed by trapping and sticking [23]. The dissociation of the hydrogen molecule requires an energy of 4.476 eV [24]. When the hydrogen molecule is close to the metal

surface it must overcome an activation barrier before the hydrogen molecule will dissociate, as illustrated in Figure 1-2. Once dissociated the hydrogen atoms contribute their electron to the band structure of the metal and generally exothermically absorb [16]. As such, the energy of chemisorption can be defined as [23]:

$$E_{ad} = 2E_{M-H} - E_{diss} \tag{1.1}$$

where E_{M-H} is the metal hydride binding energy and E_{diss} is the H-H bond energy.

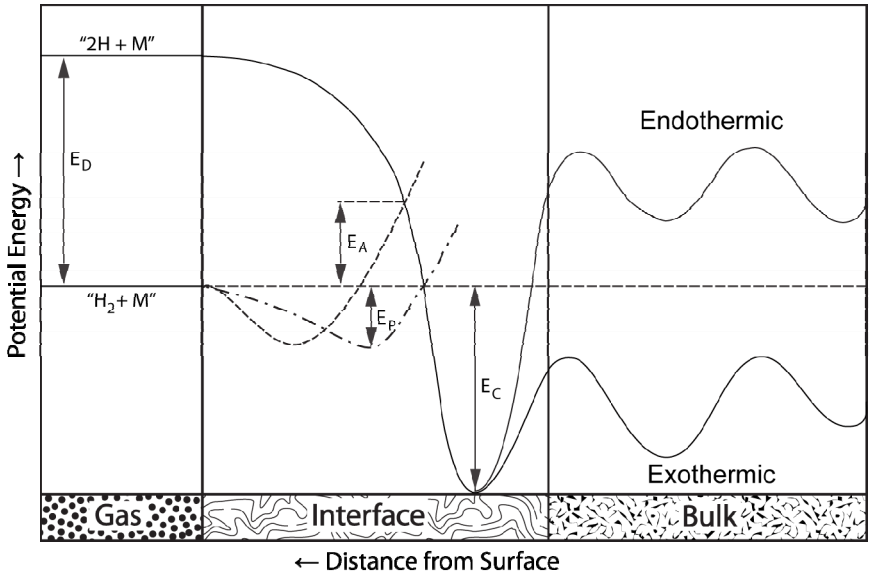

Figure 1-2: Illustration of the interaction of molecular hydrogen with a metal surface. The physisorption potential energy well is given by the dot-dashed line. Dissociative chemisorption of hydrogen is given by the dashed line. The dissociation energy E_D, chemisorption activation energy E_A, chemisorption energy well E_c, and the physisorption energy well E_P are shown. Adapted from [25].

Most metal hydrides are formed from the absorption of hydrogen which then occupies interstitial atomic sites within the metal crystal lattice. However both Mg and Al differ from the norm similarly, whereby hydrogen solubility is reported to be very low, and high hydrogen concentrations are associated with stoichiometric compositions (MgH_2 and AlH_3 respectively) that are more readily produced chemically than by combining their constituents under pressure [26].

There are such a variety of parameters that are required for a hydrogen storage system to be viable it can be difficult to display how each system compares to one another. A common comparison diagram is given in Figure 1-3 that provides an

overview of the hydrogen weight percent and volumetric hydrogen density for a variety of different metal hydride compounds. Similarly, Figure 1-4 displays reported desorption temperatures as a function of the hydrogen weight percent.

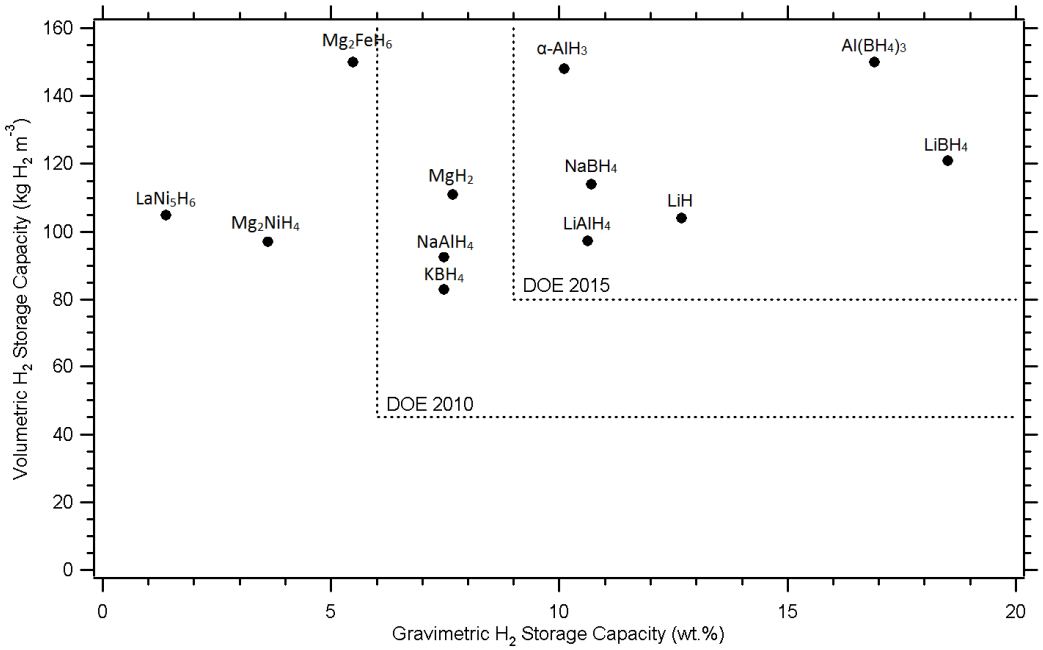

Figure 1-3: The volumetric hydrogen storage capacity of a variety of metal hydride systems in comparison to their gravimetric storage capacities as calculated from crystallographic data. United States Department of Energy (DOE) 2010 and 2015 target guidelines are shown.

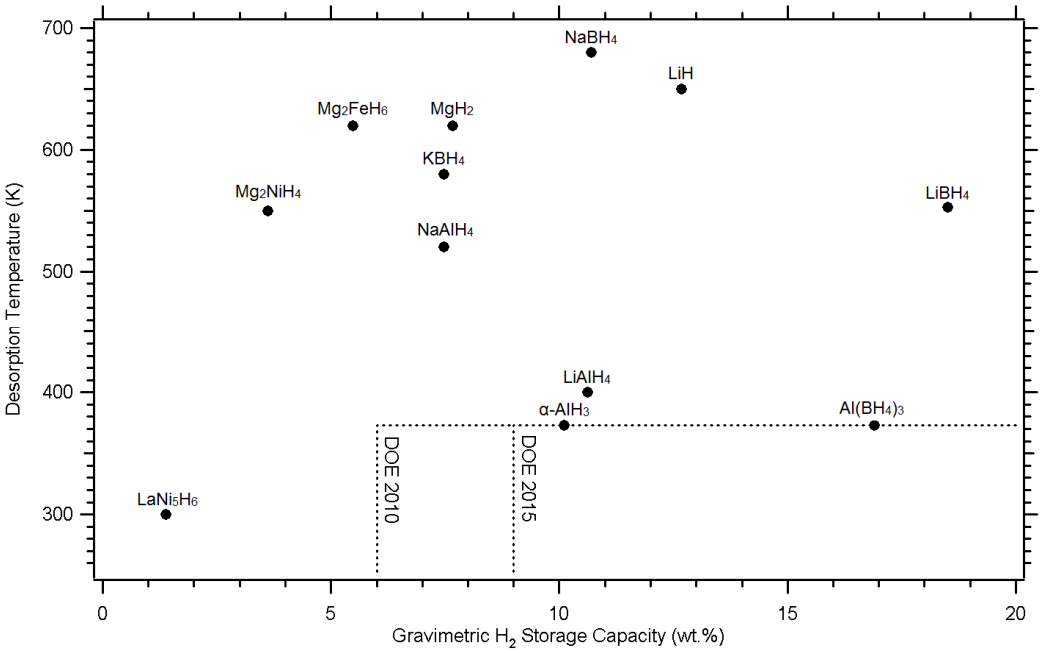

Figure 1-4: The typical desorption temperatures of a variety of metal hydride systems in comparison to their gravimetric storage capacities. United States Department of Energy (DOE) 2010 and 2015 target guidelines are shown.

Figures 1-3 & 1-4 illustrate the fact that many metal hydrides meet the DOE volumetric and gravimetric targets, but most metal hydrides have desorption temperatures that are much too high (such as MgH_2) due to their relatively large enthalpies of desorption. It should be noted that although AlH_3 meets all of the above criteria it is faced with reversibility problems under standard conditions and does not meet all of the other DOE targets.

1.3.2 Thermodynamics

Thermodynamic parameters control the properties exhibited by different hydrogen storage materials. The thermodynamics of a particular material can be used to describe and calculate its interactions with hydrogen at different temperatures and pressures. It should be made apparent that the thermodynamics of a material have no impact on the kinetics of its reaction with hydrogen. These kinetics can be critical in understanding the temperatures and pressures required for a reaction to occur on a finite timescale. There are three primary quantities that are essential in defining the thermodynamics of hydrogen storage compounds:

1. Enthalpy change (ΔH): The enthalpy (H) is related to the internal energy of the system (U) at a particular pressure (p) and volume (V) via: $H = U + pV$. Therefore the change in enthalpy (ΔH) is related to the change in energy of the system which can be explained as a change in heat [27]. ΔH can be experimentally determined using a bomb calorimeter by measuring the internal energy change of the system that has a constant volume [28]. Enthalpy values are standardised by assigning an enthalpy of 0 kJ mol^{-1} to the most stable phase of pure elements at 298.15 K and 1 bar [29].

2. Entropy change (ΔS): Entropy (S) is a measure of the molecular disorder of a system [28]. The entropy can be determined by calorimetry by measuring a material's heat capacity down to as low a temperature as possible [28]. Entropy values are standardised on an absolute entropy scale by assigning an entropy of 0 J mol^{-1} K^{-1} at 0 K and 1 bar [29] where S = 130.7 J mol^{-1} K^{-1} at 298.15 K for H_2 gas.

3. Change in Gibbs free energy (ΔG): The change in Gibbs free energy dictates whether a chemical reaction will progress because "*at a constant temperature*

and pressure, chemical reactions are spontaneous in the direction of decreasing Gibbs energy" [28]. Therefore reactions that have negative ΔG will progress, given adequate kinetics, whilst reactions with more negative ΔG will be more reactive at the given temperature.

The values of ΔH and ΔS are relatively constant as a function of temperature for most hydrogen storage materials as shown in Figures 1-5 and 1-6 which include both experimental (—) and extrapolated (····) data from the HSC Chemistry software package [29]. Strong deviations do exist however, which means the assumption that these values are constant over all temperatures cannot be made. It should also be noted that Gibbs free energies for all reactions provided in this thesis are also sourced from the HSC Chemistry database [29] unless stated otherwise.

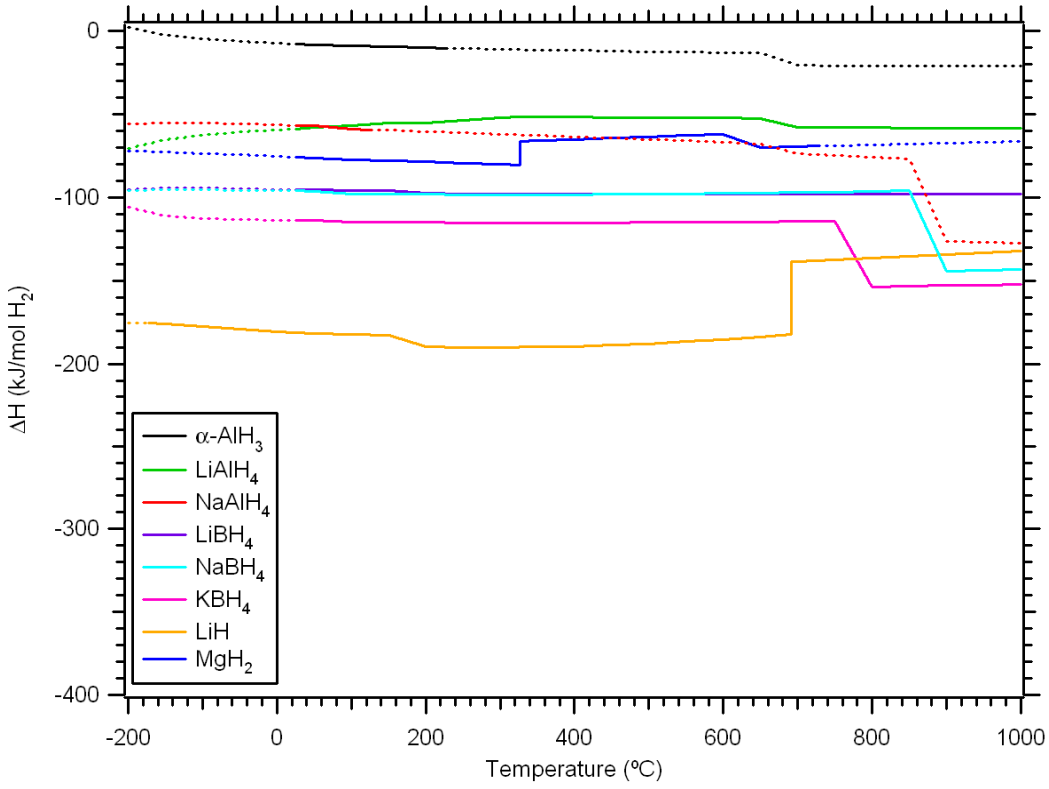

Figure 1-5: The change in reaction enthalpy for a range of hydrogen storage compounds calculated from known data [29]. ΔH is calculated per mole of H_2 from the enthalpy difference between the reactants and products in the hydride formation reaction. Dashed lines represent extrapolated data. Data was calculated assuming single-step decompositions.

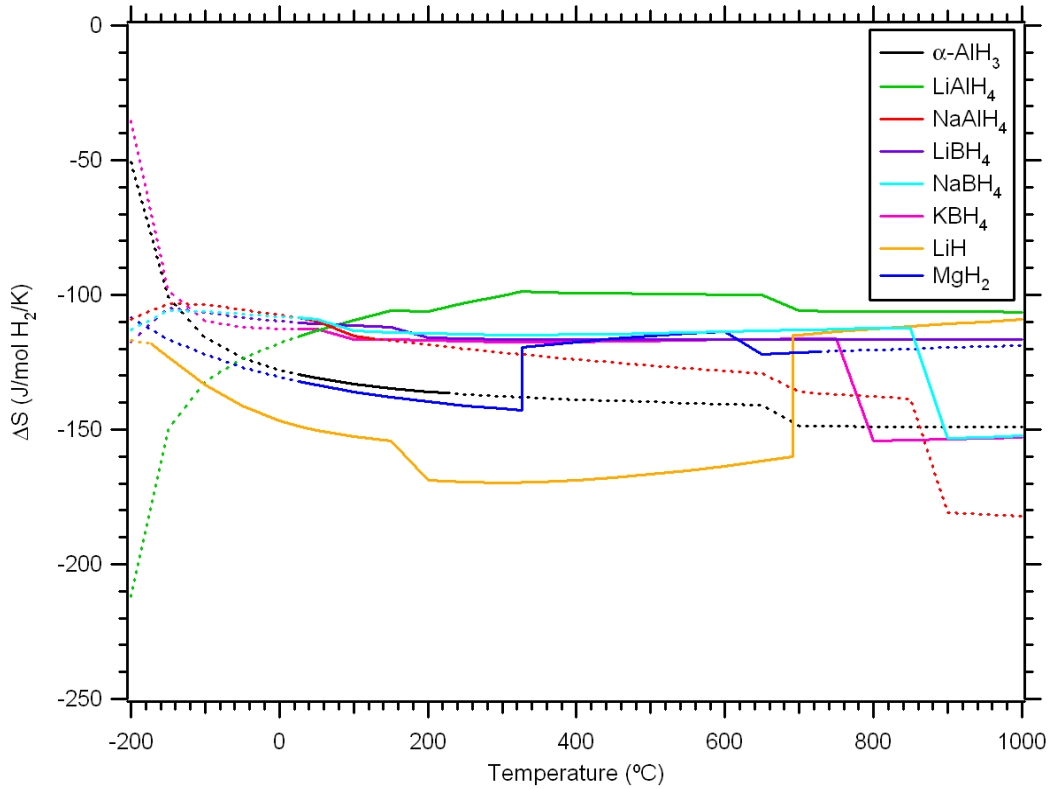

Figure 1-6: The change in reaction entropy for a range of hydrogen storage compounds calculated from known data [29]. ΔS is calculated per mole of H_2 from the entropy difference between the reactants and products in the hydride formation reaction. Dashed lines represent extrapolated data. Data was calculated assuming single-step decompositions.

The change in Gibbs free energy can be expressed by a function of the change in enthalpy and the change in entropy as follows [30]:

$$\Delta G = \Delta H - T\Delta S \qquad (1.2)$$

Figure 1-7 depicts ΔG as a function of temperature for each of the hydrogen storage materials given in Figures 1-5 and 1-6 as calculated from Equation 1.2. The change in Gibbs free energy is the most informative thermodynamic parameter in regards to hydrogen storage materials because when $\Delta G = 0$ at a given temperature a material will have a hydrogen equilibrium pressure of 1 bar. Thus the material will absorb hydrogen at higher hydrogen pressures and desorb hydrogen at lower hydrogen pressures, given kinetic limitations are overcome at the given temperature.

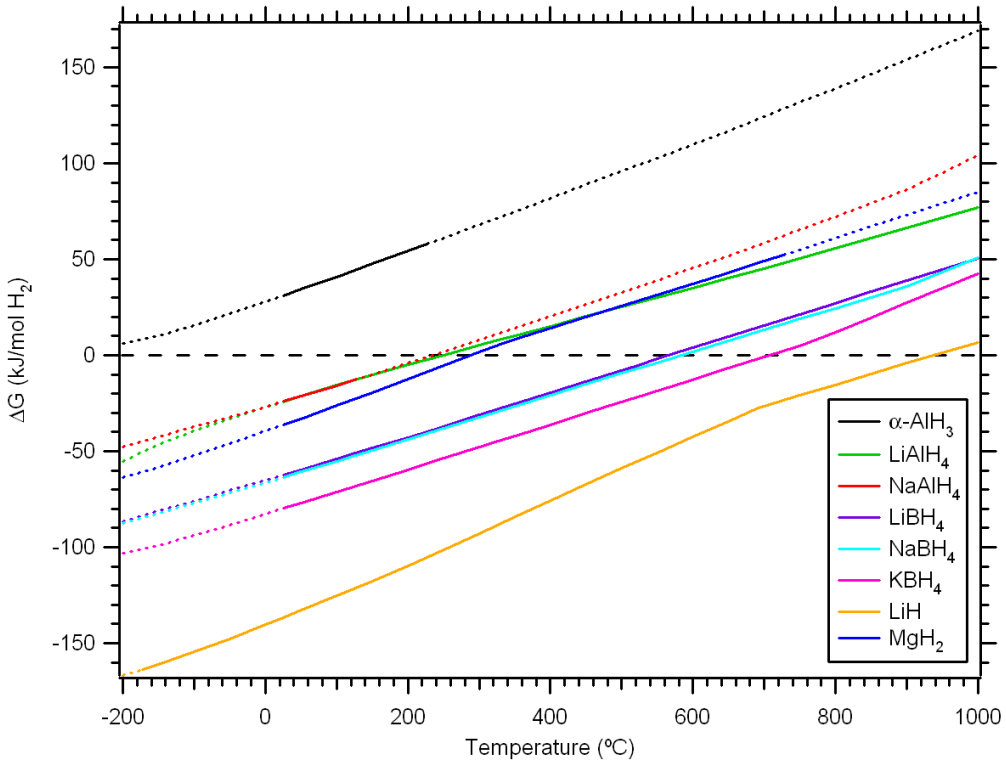

Figure 1-7: The change in the Gibbs free energy for a range of hydrogen storage compounds calculated from known data [29]. Δ*G* is calculated per mole of H_2 from Equation 1.2. Dashed lines represent extrapolated data. The zero line indicates a hydrogen equilibrium pressure of 1 bar. Data was calculated assuming single-step decompositions.

The equilibrium pressure of hydrogen gas (p_{eq}) can be determined from the relationship between fugacity and temperature as expressed by the van't Hoff equation [16,31]:

$$\ln\left(\frac{f_{eq}}{f_0}\right) = \frac{\Delta H}{RT} - \frac{\Delta S}{R} \qquad (1.3)$$

where f_{eq} is the equilibrium fugacity of hydrogen gas (bar), f_0 is a reference fugacity constant of 1 bar, ΔH is the change in enthalpy between the hydride phase and non-hydride and hydrogen phases (J/mol H_2), ΔS is the change in entropy between the hydride phase and non-hydride and hydrogen phases (J/mol H_2/K), R = 8.314472 J/mol/K is the gas constant, and T is the temperature (K). It should be noted that the van't Hoff equation is often provided in the literature with a pressure term replacing the fugacity term in Equation 1.3, which is not strictly correct and only valid at very low pressure where the ideal gas law can be assumed valid [32].

The fugacity (f) is the activity of the real gas which provides a better representation of the chemical potential of the system then pressure (p) itself, however the two terms can be related when the compressibility of the gas (hydrogen) is taken into account by [33]:

$$\ln\left(\frac{f}{p}\right) = \int_0^p \left(\frac{V_m}{RT} - \frac{1}{p}\right) \mathrm{d}p \qquad (1.4)$$

where V_m is the molar volume of H_2 that is calculated from an equation of state (EOS) for hydrogen such as those given in Section 2.6.1.

Both the change in enthalpy (ΔH) and change in entropy (ΔS) in a reaction between gaseous hydrogen and a metal hydride are crucial in controlling the hydrogen equilibrium pressure at a given temperature as seen from Equations 1.3 & 1.4. It is often assumed that the typical ΔS is -130 J/mol H_2/K in the literature [16] however the change in entropy can vary significantly from this average value in a typical range from -100 to -130 J/mol H_2/K [34], which can also be seen in Figure 1-6. Even though it is often overlooked, the variability of ΔS between different hydrogen storage materials can have a great impact on their hydrogen equilibrium pressures. Order of magnitude variations in the hydrogen equilibrium pressure occur with ± 10 kJ/mol uncertainties in ΔG [35], which is strongly dependent on ΔS. Alapati [34] states that in order for a hydrogen storage compound (within the ΔS range above) to have a decomposition temperature within the 300 - 600 K range it must also have ΔH ranging from -30 to -78 kJ/mol H_2. Reactions with significantly more negative ΔH will have unacceptably low hydrogen pressures (at modest temperatures) and reactions with significantly less negative ΔH will not be easily reversible. Figure 1-5 displays ΔH values for a range of hydrogen storage materials, and it should be noted that the above guideline holds true where: LiH which has a highly negative $\Delta H \approx$ -180 kJ/mol H_2 requires extremely high temperature to reach an adequate hydrogen equilibrium pressure, and AlH_3 which has a less negative $\Delta H \approx$ -11.4 kJ/mol H_2 is not easily reversible.

Equations 1.3 & 1.4 can be utilised to calculate hydrogen equilibrium pressures at given temperatures from the thermodynamic parameters ΔH and ΔS as shown in Figure 1-8. The hydrogen equilibrium pressure was calculated from Equation 1.4 by

solving the equation using numerical methods in the Maple software package (Maplesoft, Ontario, Canada). The molar volume of H_2 must also be solved numerically when using the Hemmes equation of state (as described in Section 2.6.1). The numerical solving program code is provided in Appendix B, which determines pressure from fugacity for 1 bar to 1 Mbar from 100 K to 1000 K and for 1 bar to 5 kbar at 77 K. It can be seen that almost all of the hydrogen storage materials have a hydrogen equilibrium pressure of 1 bar at modest to high temperatures, except AlH_3. Thermodynamically AlH_3 has extreme equilibrium pressures that are still unacceptable, albeit lower, at -200 °C. In order to make AlH_3 reversible at modest pressure its thermodynamic properties must be altered. Thermodynamic properties must also be altered in order to reduce the temperatures at which many of the other hydrogen storage materials have acceptable equilibrium pressures. The work herein is directed towards the goal of thermodynamic alteration by particle size reduction.

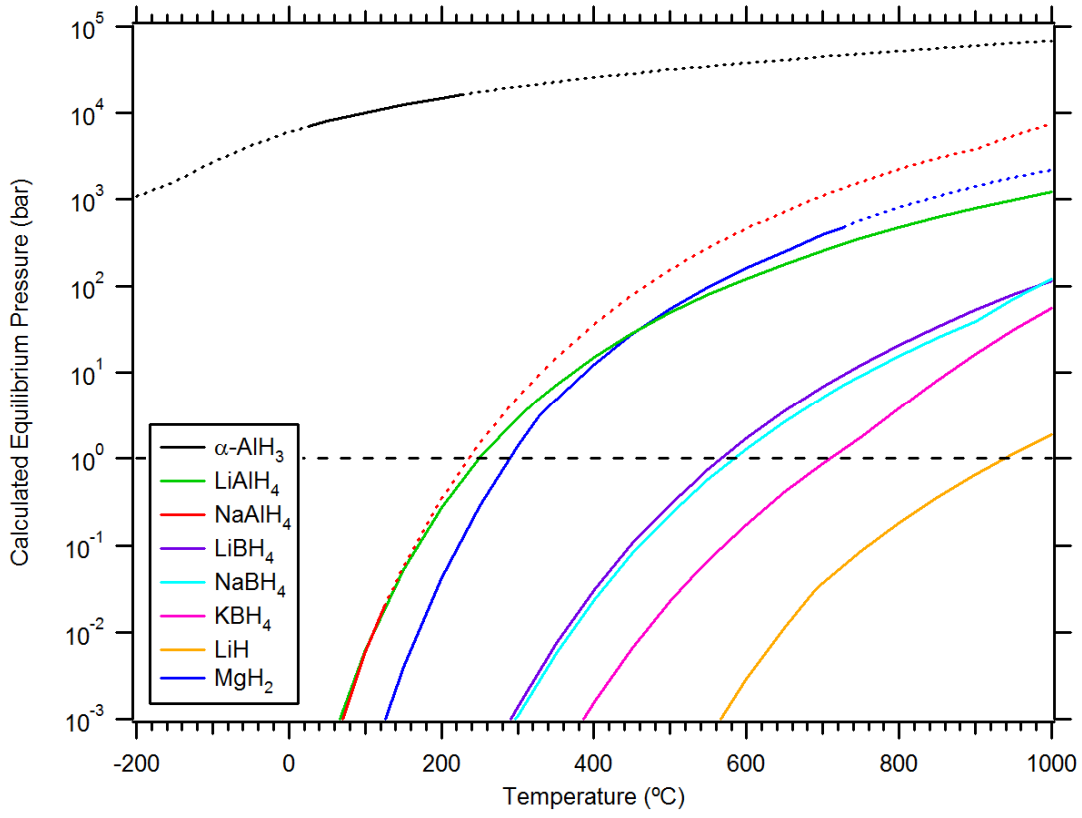

Figure 1-8: Calculated equilibrium pressures calculated using Equation 1.3 & 1.4 from Δ*H* and Δ*S* values given in Figures 1-5 & 1-6. Dashed lines represent extrapolated data. A 1 bar dashed baseline is also shown. Data was calculated assuming single-step decompositions.

Thermodynamic properties (ΔH and ΔS) can be experimentally determined from hydrogen sorption measurements. If the hydrogen equilibrium pressure is measured for a given material at various temperatures then ΔH and ΔS can be determined using Equations 1.3 and 1.4. This calculation is undertaken by means of a van't Hoff plot as shown in Figure 1-9. Four different hydrogen sorption isotherms are given in the pressure-composition (P-C) plot (left in Figure 1-9) that represent hydrogen sorption equilibrium pressures as a function of the hydrogen to metal ratio (H/M) under different temperatures (T). The H/M increases as the α-phase (hydrogen poor) transitions into the β-phase (hydrogen rich). For temperatures below the critical temperature (T_c) an equilibrium plateau is observed that can be matched to a data point on the van't Hoff plot (right in Figure 1-9), allowing the changes in enthalpy and entropy to be determined by Equations 1.3 and 1.4.

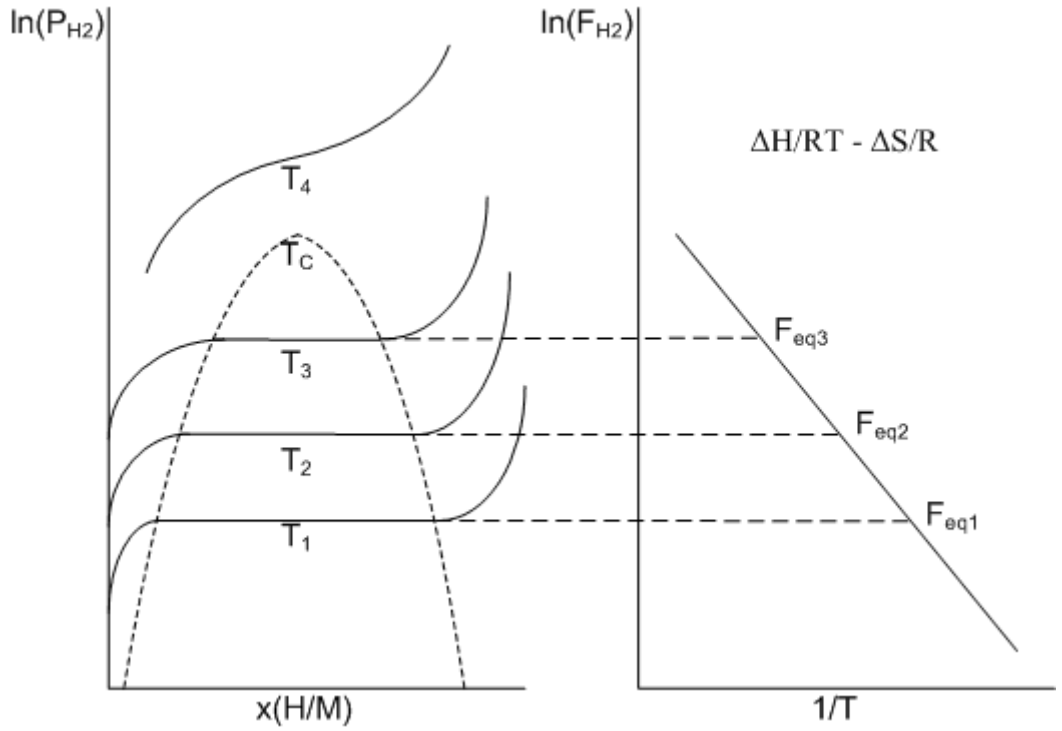

Figure 1-9: The relationship between pressure-composition (P-C) isotherms (left) and the van't Hoff plot (right) in which thermodynamic data is determined. Fugacity values (F_{eq}) correspond to equilibrium plateau pressures measured at constant temperature T. T_c is the critical temperature above which no equilibrium plateaus are observed. Adapted from [36].

1.4 NANOPARTICLES

Nanoparticles have been found to have quite different mechanical, chemical, electrical, thermodynamic, and other properties than their parent (precursor) materials [7]. One example is given by the chemical reactivity of magnesium which is proportional to the reciprocal of its particle size, meaning that nanoparticular magnesium can undergo reactions that are considered unreactive with bulk magnesium [37].

The changes observed in nanoparticle systems are related to the proportion of atoms that are in contact with a free surface [38]. This is expressed by the specific surface area (SSA) (see Figure 1-10), which is equal to $4\pi r^2/(4/3\pi r^3\rho)=3/r\rho$ for isolated spherical particles (or approximately half this value if the particles are in contact with one another) where r is the particle radius and ρ is its density [38]. The surface area directly alters the proportion of atoms at or near the free surface (i.e. ~30 - 50% of the atoms in a 5 nm particle are influenced by its surface compared to a few percent for a 100 nm particle), which gives rise to differences in bonding and electronic structure of these surface atoms [38].

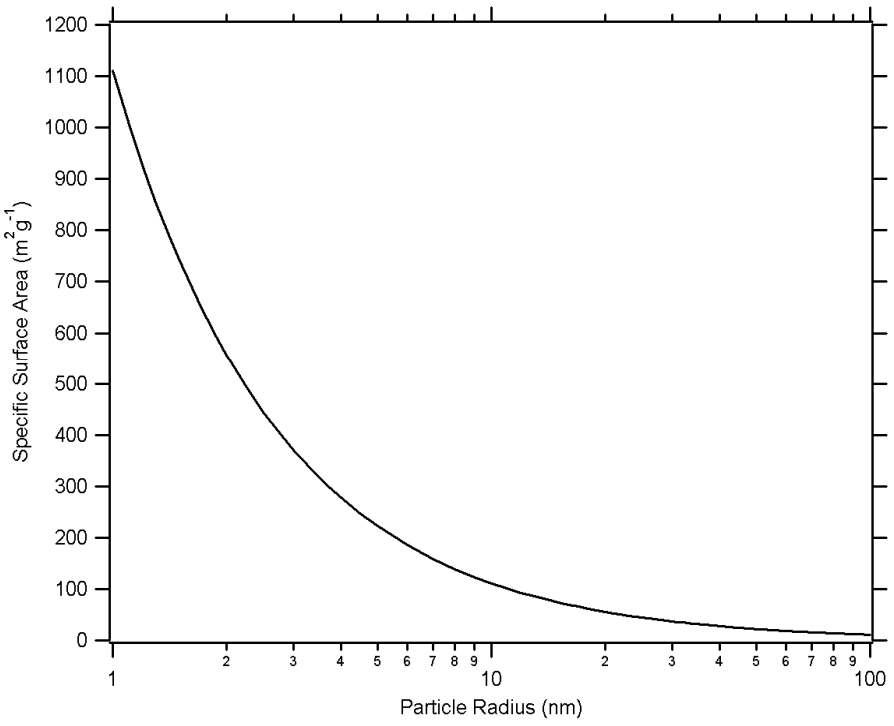

Figure 1-10: The theoretically calculated surface area of different sized spherical aluminium nanoparticles, assuming that they are smooth and not in contact with one another.

1.4.1 Bulk Nanocrystalline Materials

Nanoparticle powders differ from nanocrystalline materials. A nanocrystalline material is one that consists of a sum of grains each of which is nanoscale in size. This nanocrystalline material can however be a much larger bulk structure that is not on the nanoscale [7]. Snow & Brumlik [7] state that "many materials with some nanoscale feature (e.g., crystals or grains) are often confusingly called nanoparticles". The crystallites inside the nanocrystalline material integrally form a part of the bulk and they are not separable like nanoparticles [7].

1.4.1.1 *Traditional Ball Milling*

Ball milling is a technique used to produce materials with target particle and/or grain sizes, alloys, or compositions. The procedure is undertaken by confining the sample to be milled (powder) with a grinding medium (hardened steel balls) in a chamber that is agitated to initiate collisions between the grinding medium, the powder and the chamber walls [39]. Particle sizes are only usually reduced to the micrometer level but reaction kinetics are enhanced because crystallite sizes within the particles are reduced to the nanometre level [7,40].

The sample chamber is often loaded with high purity elemental powder inside a glove box with an inert argon atmosphere [41]. Therefore the sample is of high purity with minimal oxidation and contamination before ball milling is undertaken. The sample can also be ball milled in a reactive atmosphere (i.e. N_2, H_2) or with other chemical compounds. Additives (i.e. methanol) are often added to prevent sticking of the powder to the milling tools [42]. A minimum crystallite size is reached after a given period of time depending on the sample and ball milling conditions (i.e. 20 nm after 10 h for high energy [43] or 100/200 h for low energy ball milled aluminium [41-42]).

1.4.2 Thermodynamic Changes with Particle Size

The formation reaction for a simple metal hydride system (where M is a metal and MH is its respective hydride) can be expressed as follows:

$$M + \frac{1}{2}H_2 \longrightarrow MH \qquad (1.5)$$

The thermodynamics of the reaction between a metal and hydrogen are characterised by the energy difference between the reactants and product phases in Equation 1.5. Thermodynamic changes can occur from particle size reduction due to changes in the internal energy of both M and MH materials in going from bulk materials to nanoparticles [44]. The M and MH phases are destabilised to differing degrees upon particle size reduction (i.e. Mg compared with MgH_2 [45]) causing changes in the thermodynamic properties ΔH, ΔS, and ΔG, which affect hydrogen sorption conditions. Entropy is especially important in reactions between nanoscale solids that are "*characterised by a higher degree of disorder due to the significantly larger contribution of phase boundaries to the overall volume*" [46].

Thermodynamic changes in nanosized hydrogen storage materials have primarily been examined by use of theoretical investigations due to the difficulty in synthesising materials experimentally. Kim *et al.* [44] provides a theoretical examination of thermodynamic changes in a number of simple metal hydride systems as a function of particle size including AlH_3 and MgH_2. The effect of particle size reduction is found to be beneficial for both hydrides with a reduction in size resulting in a stabilisation of AlH_3 and destabilisation of MgH_2. However the magnitudes of the thermodynamic changes are low, resulting in desorption temperature alterations of +13 K and -33 K predicted for 2 nm AlH_3 and MgH_2 particles respectively.

Changes in the desorption temperature of hydrogen storage materials have been reported in the literature that do not in fact relate to the thermodynamics. Baldé *et al.* [47] reported a reduction in the desorption temperature of $NaAlH_4$ with a reduction in particle size. However the lowered desorption temperature is a result of changes in the activation energy of the decomposition reaction and not related to a thermodynamic destabilisation due to particle size. A lower activation energy results in faster kinetics that allow hydrogen to evolve quicker at lower temperatures.

Nanoparticles that are 1 – 3 nm in size are expected to have strongly size-dependent properties, possibly exhibiting changes in geometric and electronic structure, binding energy, and thermodynamic properties such as melting points [48]. Larger particles > 10 nm are thought to approach the bulk properties of a material [48]. As particles approach small cluster sizes of only a few atoms, significant changes in the structural stability of the material can occur. There have been a large number of experimental

and theoretical studies performed on small aluminium clusters that are stabilised with hydrogen [49-58]. Certain Al-H cluster configurations present high stabilities exhibited by their large HOMO-LUMO (highest occupied and lowest unoccupied molecular orbital respectively) gaps. For example, $Al_{13}H$, or Al_nH_{n+2} ($4 \leq n \leq 8$) were found to have high structural stabilities along with Al_2H_6, which is a di-borane analogue [59].

It is apparent that nanosized aluminium and magnesium particles exhibit different interactions with hydrogen than in bulk systems. To date there have been no comprehensive hydrogen sorption studies performed on either aluminium or magnesium nanoparticles < 10 nm.

1.4.3 Synthesis of Nanoparticles

Metal nanoparticles can be formed by a variety of techniques such as [7,60-63]: chemical and physical vapour deposition, physical vapour synthesis, reactive sputtering, digestive ripening, electrodeposition, laser pyrolysis, laser ablation, laser/microwave plasma-induced breakdown and pyrolysis of organometallic compounds, hydrogen decrepitation, aerosol through plasma (ATP) method, spray conversion, mechanical alloying, inverse micelle techniques, sol gel techniques, and evaporation-condensation methods. The mechanochemical synthesis method is utilised in the current study.

1.4.3.1 *Mechanochemical Synthesis*

Mechanochemical techniques have been employed to synthesise a range of nanoparticles in the past including metals and metal hydrides. Many metal nanoparticles have been synthesised mechanochemically including Ag, Cd, Co, Cr, Cu, Er, Fe, Gd, Mn, Mo, Nb, Ni, Pb, Si, Sm, Ta, Ti, V, W, Zn, Zr [64-65] and even alloys of these metals [65-66]. Metal hydrides such as AlH_3 [67], $LiAlH_4$ [68], $Ca(AlH_4)_2$ [69], $Mg(AlH_4)_2$ [70-72], and $LiMg(AlH_4)_3$ [73] have also been synthesised mechanochemically, although nanoparticle hydrides have not been explored in detail.

A standard ball milling process results in the formation of nanosized grains within microsized particles [74], however a mechanochemical method involves the initiation of a solid-state displacement reaction during a ball milling process [74]. The chemical reaction involves the reduction of a compound (often an oxide, chloride, or sulphide

[65]) with an appropriate reducing agent. Tsuzuki & McCormick [64] state that a wide range of nanoparticles can be synthesised by appropriate selection of chemical reaction paths, stoichiometry of starting materials, milling conditions, and washing solvents. For example the reduction of iron chloride by sodium metal proceeds as follows [64]:

$$FeCl_3 + 3Na \longrightarrow Fe + 3NaCl \qquad \Delta_r G_{298K} = -820 \text{ kJ/mol} \qquad (1.6)$$

The large negative Gibbs free energy change ($\Delta_r G_{298K}$) is indicative of this reaction being feasible at room temperature [65]. The time required for the reaction to reach completion is therefore only limited by kinetic considerations involving the contact between the reactant phases [65]. Mechanically milling the reactant and product phases leads to microstructural refinement that allows the reaction to proceed without the need for the reactant phases to slowly diffuse through the product phases [65].

Once the mechanochemical reaction is complete small particles of the metal and by-product phase remain. The ball milled powder can then be washed with a solvent to remove the by-product phase in order to obtain pure nanoparticles that can be < 10 nm in size [75]. The washing procedure may also remove residual reactant phases from the product material [66].

The role of the mechanical milling process in the mechanochemical synthesis of nanoparticles is [66]:

1. To blend the reactants in order to form nanoscale mixtures.

2. To cause a chemical reaction between the reactants enabling the product phase to form.

3. Increasing the chemical reactivity and/or reaction kinetics which normally would occur on heating but can instead occur at lower temperature than those which lead to grain growth or particle coarsening.

Particle size control (e.g. 10 nm to 10 μm) can be gained by adjusting such factors as: the volume fraction of the by-product phase formed during milling, milling time, milling collision energy (ball to powder mass ratio and ball size) [66], milling temperature, and the use of process control agents [65].

The use of a buffer material can be used to increase the volume fraction of the by-product phase during milling which acts to separate the reactants resulting in smaller particle sizes [76]. The buffer also reduces the reaction rate and reduces the energy transferred to the reactants causing a reduced temperature during milling [77]. The buffer material present after milling also acts as a separating agent so that particle growth is restricted. i.e. during high temperature annealing [77]. The particle and grain size of the precursor reagents used in mechanochemical synthesis can also have a significant effect on the resulting product phase particle size [76]. Therefore ultrafine (~5 nm) particles are preferentially synthesised by using large reaction buffers along with pre-milled reagents.

Chapter 2

Experimental

“The most exciting phrase to hear in science, the one that heralds new discoveries, is not 'Eureka!' but 'That's funny...'” - Isaac Asimov

2.1 SAMPLE PREPARATION

All sample handling was undertaken in an argon filled Unilab glovebox (mBraun, Germany) at Curtin University in order to minimise oxygen (O_2 < 5 ppm) and moisture (H_2O < 1 ppm) contamination of samples. The glovebox has live oxygen and moisture monitoring, argon purifiers that constantly remove oxygen and moisture, and two antechambers that can be evacuated for removal and insertion of samples and/or apparatus.

2.1.1 Ball Milling

Ball milling was performed with a custom made ball milling canister (650 cm^3 internal volume) (see Figure 2-1) attached to a Glen Mills Turbula T2C shaker mixer. The ball milling canister was made from stainless steel (316) and was sealed with an o-ring on both ends. The balls were made from the same material as the canister to minimise sample contamination due to the degradation of both the canister and balls. The milling equipment was made from 316 stainless steel because this grade of steel has a good corrosion resistance and also resistance to pitting.

The milling canister was cleaned between runs by the following procedure:

1. washing with water and then ethanol in a fume hood
2. milling with ethanol and NaCl for at least 30 minutes
3. washing with water and then ethanol
4. milling with ethanol for at least 30 minutes (repeated if not clean)
5. washing with water and then ethanol
6. drying with compressed air

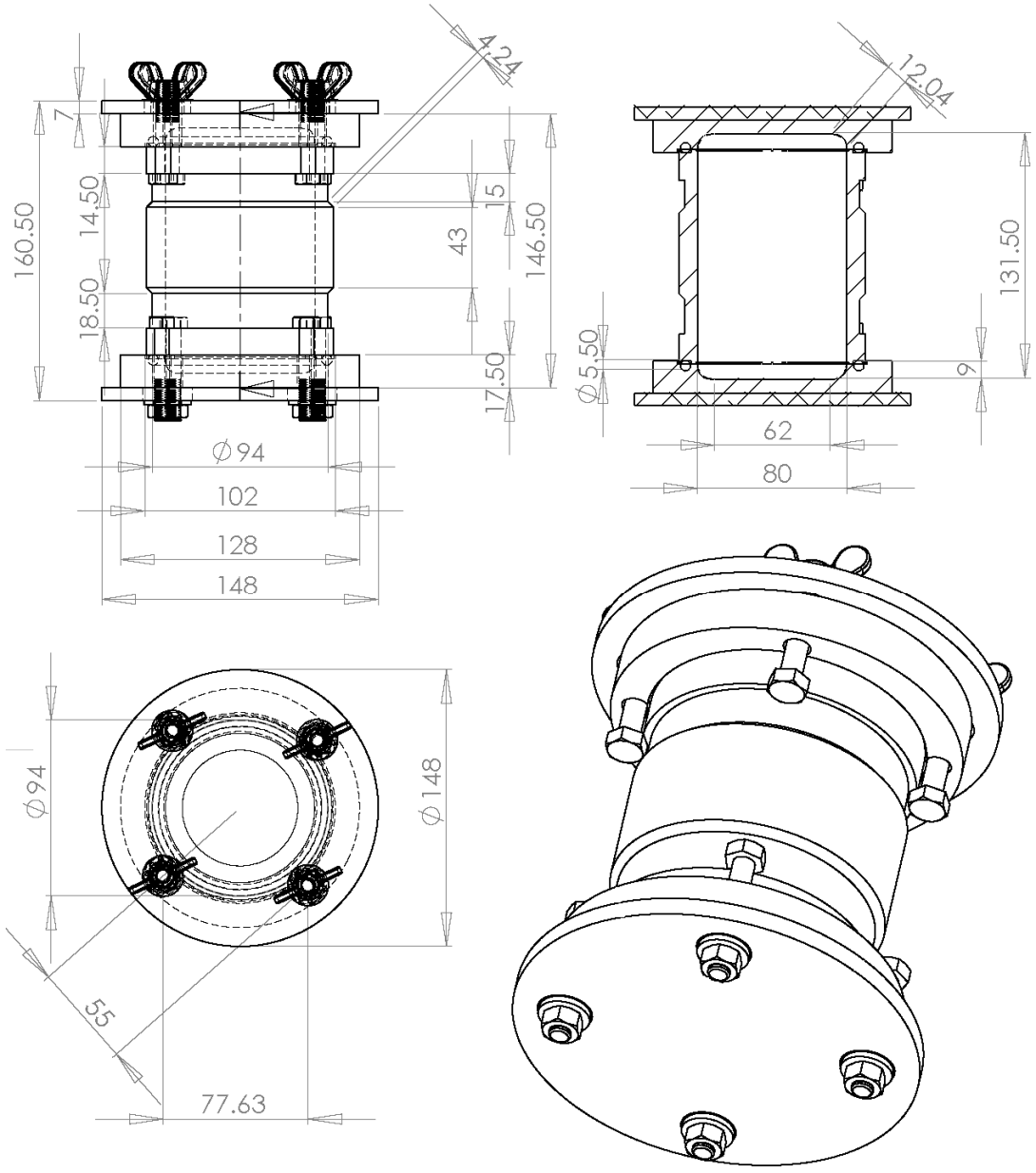

Figure 2-1: Custom-made ball milling canister used at Curtin University on a Glen Mills Turbula T2C Shaker-Mixer. Top & bottom plates are aluminium, the o-rings are rubber, and all other components (including milling media) are 316 grade stainless steel. All measurements are given in mm. The internal chamber volume is 650 cm^3.

2.1.2 Cryogenic Milling

Cryogenic milling was performed using a Spex 6850 freezer mill. Two different canister types were utilised: A supplied 190 cm^3 canister and a custom made 14.3 cm^3 canister. The 14.3 cm^3 milling canister was custom made (obtained from

E.MacA. Gray & M.P. Pitt at Griffith University) from 440c stainless steel in order to minimise sample contamination and provide a vacuum tight seal achieved using Teflon taped screw fittings that are made from steel and silver. The milling canister is held within two electromagnets in a chamber that is filled with liquid nitrogen. The large milling rod (145.5 g) and the small milling rod (32 g) are magnetically displaced 20 times per second within the canister between the end caps to provide a milling action at 77 K.

2.1.3 Centrifugal Separation

A Wifug X-1 centrifuge (3000 rpm providing an average relative centrifugal force of 1200 g's) and a Kokusan H-103N refrigerated centrifuge (3500 rpm providing an average relative centrifugal force of 2050 g's) were used for centrifugal separation of solid-liquid samples. Samples were sealed (using o-ring lids) within 50 ml polypropylene copolymer (PP) or fluorinated ethylene propylene (FEP) centrifuge tubes depending on solvent reactivity. Centrifugation was undertaken until liquid-solid particle separation was complete. The liquid phase was then decanted by using a syringe or pipette within a glovebox. Complete solvent removal (after successive washing steps) was undertaken by exposing the sample to vacuum, or an evaporation process was performed within an argon atmosphere.

2.1.4 Synthesis Overview

Mechanochemical synthesis was undertaken to form aluminium, aluminium hydride (alane), and magnesium hydride nanoparticles. Mechanochemical synthesis was the chosen nanoparticle synthesis method because of its simplicity and versatility, enabling particle size control via a ball milling process, allowing air-sensitive materials to be synthesised. The mechanochemical reaction can be adapted to many synthesis reactions and only the product metal (i.e. Al, Mg) must remain in the chemical equation. For example the reductant in the mechanochemical reaction can be any alkali metal such as lithium (Li) or potassium (K) and the reacting metal compound can be any halide such as a chloride or iodide (i.e. $AlCl_3$ or AlI_3). This can be advantageous as the solubility of certain salts (such as LiCl) can be more soluble in a variety of non-aqueous liquids.

2.1.5 Washing Overview

Mechanochemically synthesised metal (or metal hydride) nanoparticles are formed with an unwanted by-product phase (usually a salt). There are some kinetic benefits for hydrogen storage within ball milled metal-salt systems mentioned in the literature [78]. However the kinetics of these systems are most likely improved due to the cleavage of heavy oxide layers coating the metal powders and from a reduction in particle size enhanced by a salt buffer phase. The salt phases can be involved in the reaction between a metal and hydrogen, but only if there is some chemical interaction between the salt and metal during milling.

A solvent must be selected to dissolve the salt by-product phase, which will be unreactive towards the nanoparticle product phase. The extraction of the solvent with the dissolved salt by-product is achieved through centrifugation and decantation. This step requires the use of a low viscosity solvent in order to centrifugally separate the nanoparticles from the salt laden solvent. The time required to separate particles from solution is a function of the viscosity of the solvent [79] and the size of the particles so the viscosity should be kept as low as possible, especially when separating nanosized particles from solution.

Washing is performed on the nanoparticles embedded within salt as a three stage process in order to entirely remove the salt by-product:

1. The washing procedure is undertaken within an argon glovebox until centrifuge tubes are sealed and removed for stirring and/or centrifuging. 30 ml of solvent is added to a centrifuge tube containing a magnetic stir bar, then any other salts required to increase the solubility are added (i.e. $AlCl_3$ in nitromethane). The sample (i.e. Al in LiCl) is then added to the solvent slowly (over 2-3 minutes) in order to prevent excess heating of the solution. This process is undertaken slowly as the dissolution of salt can be quite exothermic, in fact if the solvent is instead added to a portion of dry sample a large volume of smoke and fumes can be produced due to extreme sample heating causing solvent-particle reactions. The centrifuge tube is then placed on a magnetic stirrer for at least 3 hours before being placed into the centrifuge until the nanopowder is separated from the salt-laden solvent.

2. The clear solvent is then decanted by pipette or syringe. 30 ml of solvent is again added to the centrifuge tube as well as any other salts required for solubility (i.e. $AlCl_3$). The centrifuge tube is then placed on a magnetic stirrer for at least 3 hours before being placed in the centrifuge once again until the powder is separated from the salt-laden solvent. The washing process is performed twice in order to remove as much salt buffer as possible because the solvent becomes ineffective during the first wash once it is in a saturated state.

3. The clear solvent is then decanted by pipette or syringe. A final 30 ml of solvent is added to the centrifuge tube to perform a rinse of the sample, so no other salts (i.e. those used for solubility) are present. The centrifuge tube is then placed on a magnetic stirrer for at least 3 hours before being placed in the centrifuge once again until the powder is separated from the salt-laden solvent. The clear solvent is then decanted by pipette or syringe and the damp powder is placed under vacuum (or let sit in argon) for at least 3 hours to remove any traces of solvent from the powder. Only pure nanoparticles remain.

2.1.5.1 *Solvents*

Solvent choice is made difficult (especially when dealing with hydride nanoparticles) due to solvent-nanoparticle reactions and solubilities. It is advantageous to tune the mechanochemical reaction in order to form an easily dissolvable by-product phase that is soluble in a large range of solvents.

Lithium chloride (LiCl) was chosen as the preferred salt by-product because it is a low cost, abundant salt that is highly soluble in a wide range of solvents. However most of these LiCl solvents are highly reactive with the nanoparticle product phases or unsuitable for use in a centrifugal separation process. The solubility parameters, physical properties, and reactivities of a variety of solvents capable of dissolving LiCl are shown in Table 2-1.

Many of the solvents in Table 2-1 were tested for reactivity and/or solubility in the present work (see Table 2-2). Adverse reactions varied from minor reactions causing slight bubbling from the solvent (i.e. MgH_2 and ethanol) to violent reactions causing

large quantities of smoke and heat in an argon environment (i.e. MgH_2 and nitromethane) and even fire when reacted in an air environment (i.e. AlH_3 and water).

Table 2-1: Solubility information for the LiCl phase formed during mechanochemical synthesis. A solvent rating is given in the final column - A: Good for AlH_3, B: Good for MgH_2, C: Further testing required, D: Possible for Al or Mg, E: Bad.

Solvent	***LiCl Solubility***		***Ref.***	***M.P. (°C)*** ***B.P. (°C)***[80]	***Viscosity (m Pa s) (25 °C)***[80]	***Reactivity/Notes***	
	wt.%	***temp. (°C)***					
Acetone C_3H_6O	1.70 1.17 0.83	0 20 25	[81] [81] [82]	-94.7 56.05	0.306	Reaction with MgH_2 [83] and AlH_3	E
Acetonitrile CH_3CN	0.14	25	[82]	-45 82	0.345	Low solubility	E
Ammonia NH_3	0.535 1.39	-33.9 0	[81]	-77.73 -33.33	-	Dangerous and low temperature difficulties	E
1-Butanol $C_4H_{10}O$	11.49	25	[81]	-88.6 117.73	2.544	Alcohols can react	E
1,2-Dichloroethane $C_2H_4Cl_2$	soluble	-10	see note	-35 83.5-84	0.779	Soluble with ultrasonic treatment [84] or with $AlCl_3$ in solution [85]	C
Dichloromethane CH_2Cl_2	soluble	-	[86]	-96.7 39.8	0.413	Similar to dichloroethane	C
Diethyl Ether $C_2H_5OC_2H_5$	0.0006 soluble	25 25	[87] see note	-116.3 34.6	0.224	Dangerous. Soluble with $AlCl_3$ in solution [88]. Dissolves AlH_3 to form alane-ether complex. MgH_2 is insoluble [83]	C/D
1,2-Dimethoxyethane $C_4H_{10}O_2$	2.15 0.5	25 75	[87]	-69.2 84.5	-	Similar to diethyl ether	C
Dimethyl Formamide C_3H_7NO	11 or 28	25	[82]	-60.48 153	0.794	Ketones can react	D
1,3-Dioxolane $C_3H_6O_2$	2.35	25	[87]	-97.22 78	-	Similar to tetrahydrofuran	C
Ethanol C_2H_6O	12.61 19.57 20.22	0 20 40	[81]	-114.14 78.29	1.074	Reaction with MgH_2 [83] and AlH_3	E
Ethylene Glycol $C_2H_4(OH)_2$	soluble	-	[86]	-12.9 197.3	16.1	Too viscous	E
Formamide CH_3NO	28.2	25	[82]	2.49 220	3.343	Reaction with AlH_3	E
Glycerol $C_3H_8O_3$	10.0	15	[81]	18.1 290	934	Too viscous	E
Hydrazine N_2H_4	160	20	[81]	1.4 113.55	0.876	Very dangerous	E
4-Hydroxy-4-Methyl-2-Pentanone $C_6H_{12}O_2$	6.14 9.93	20 65	[81]	-44 167.9	2.798	Ketones can react	D
Isopropylamine C_3H_9N	8.67	25	[87]	-95.13 31.76	0.325	Possible reaction with AlH_3 as with other amines [89]	D

Solvent	*LiCl Solubility* *wt.%*	*temp. (°C)*	*Ref.*	*M.P. (°C)* *B.P. (°C)*[80]	*Viscosity (m Pa s) (25 °C)*[80]	*Reactivity/Notes*	
Methanol CH_4O	31.1 29.75	0 25	[81]	-97.53 64.6	0.544	Alcohols can react	E
N-Methyl-Formamide C_2H_5NO	23.0	25	[82]	-3.8 199.51	1.678	Ketones can react	D
N-Methyl-2-Pyrrolidone C_5H_9NO	soluble	-	[90]	-24 202	-	Ketones can react	D
Nitrobenzene $C_6H_5NO_2$	soluble	-	[91]	5.85 210.9	1.863	Possible hydrazine formation if reduced [89]	C
Nitromethane CH_3NO_2	soluble soluble soluble soluble	>2.2 - - -	[86] [92] [93] [94]	-29 100-103	0.61	No noticeable reaction with AlH_3 or Al, except in cryomilled AlH_3. Soluble with other salts such as $AlBr_3$ [93] or $TiCl_4$ [94] in solution. Reaction with MgH_2	A/D
1-Pentanol $C_5H_{12}O$	6.71 8.28	20 25	[81]	-77.6 137.98	3.619	Alcohols can react	E
1-Propanol C_3H_8O	13.68 13.95	20 25	[81]	-124.39 97.2	1.945	Alcohols can react	E
Pyridine C_5H_5N	11.31 11.87 18.35	8 28 97	[81]	-41.70 115.23	0.879	Reaction with AlH_3	C/D
Quinoline C_9H_7N	0.3537 1.2218	25 67	[81]	-14.78 237.16	3.337	Possible reaction as in pyridine case	C/D
Tetrahydrofuran C_4H_8O	>4.77 2.91 soluble 6.14	0 25 - 15-35	[87] [87] [91] [95]	-108.4 66	0.48	AlH_3 soluble, possible reactivity at temperature or over days [89]. MgH_2 virtually insoluble [83]. Reaction with MgH_2 powder	D
Toluene C_7H_8	soluble	25	see note	-93 110.6	0.560	Soluble with $AlCl_3$ in solution [88]. MgH_2 soluble	A/D
Water H_2O	55	25	[82]	0 100	0.890	Reaction with MgH_2 [83] and AlH_3	E

Certain solvents require the addition of salts in solution before LiCl solubility is possible (i.e. $AlCl_3$ in nitromethane). These solvents can become much more viscous as they become highly salt-laden. Increased viscosity is detrimental to centrifugal separation of nanoparticles as much longer centrifugal separation times are required. On a similar note, ionic liquids can also be used as solvents for salts as an alternative to regular solvents which are often more toxic and dangerous in nature [96], however they are viscous [97] making them unsuitable for standard centrifugal separation.

Table 2-2: Solvent reactivity towards as-synthesised nanoparticles. All testing was undertaken in a glovebox except testing with water. RT: milled at room temperature, cryo: milled at 77 K, degassed: freeze-pump-thaw method to remove dissolved oxygen from solution.

Solvent	Material	Reaction
Acetone	Al	gas evolution
	AlH_3	smoke
1,2-Dichloroethane	AlH_3	no visible reaction
Ethanol	Al	gas evolution
	AlH_3	smoke
	MgH_2	smoke
Ethylene Glycol	Al	gas evolution
Formamide	AlH_3	smoke
Glycerol	Al	gas evolution
Nitromethane & $AlCl_3$	Al	no visible reaction
	AlH_3 (RT)	no visible reaction
	AlH_3 (cryo)	gas evolution
	MgH_2	gas evolution
2-Propanol	AlH_3	smoke
2-Propanol (degassed)	AlH_3	smoke
Pyridine	AlH_3	smoke
Tetrahydrofuran	MgH_2	gas evolution
Toluene	Al	no visible reaction
	AlH_3	no visible reaction
	MgH_2	no visible reaction
Water (in air)	Al	gas evolution
	AlH_3	fire
	MgH_2	fire

2.2 X-RAY DIFFRACTION (XRD)

Laboratory based x-ray diffraction (XRD) was performed using two different diffractometers. Initially a Siemens D500 diffractometer at Curtin University was utilised with a 2θ range of 10 - 80º using 0.02º steps with 2 s of count time per step. The instrument was operated with the instrument configuration given in Table 2-3 and was configured according to Figure 2-2. Samples were loaded into XRD sample holders in an argon glovebox and sealed under either 2.5 μm or 4 μm mylar film to prevent oxygen/moisture contamination during data collection.

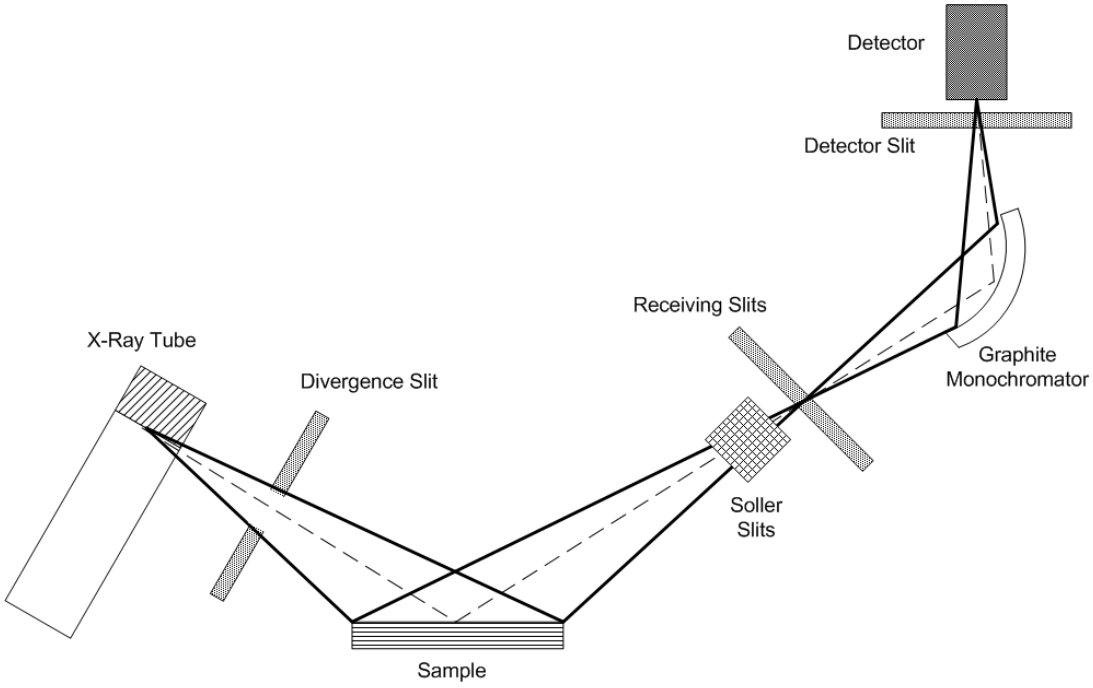

Figure 2-2: D500 X-ray diffractometer (XRD) optics. Graphic derived from [98].

Table 2-3: X-Ray Diffraction (XRD) instrumental parameters

Parameter	D500	D8
Radiation (wavelength)	Cu (1.5418 Å)	Cu (1.5418 Å)
Operating voltage	40 kV	40 kV
Operating current	30 mA	40 mA
Detector	Scintillator	Linear PSD (3º 2θ)
Monochromator	Graphite	- (Ni filter)
Lorentz-Polarisation factor	26.4	0
Goniometer radii	200.5 mm	250 mm
Source length	12 mm	12 mm
Sample length	15 mm	25 mm
Receiving slit length	12 mm	17 mm
Receiving slit width	0.5 mm	-
Fixed divergence slit angle	1º	0.3º
Primary Soller slit angle	-	2.5º
Secondary Soller slit angle	2º	2.5º

XRD was also undertaken on a Bruker D8 Advance diffractometer at Curtin University with a 2θ range of 10 - 100º using 0.02º steps with 0.8 s of count time per step. The instrument configuration is given in Table 2-3. The D8 optics were similar to those displayed in Figure 2-2 except a primary set of Soller slits were used (pre-sample) and no receiving slits or monochromator were used post-sample, instead a nickel filter and a linear position sensitive detector (PSD) were implemented. Samples were loaded into XRD sample holders in an argon glovebox and sealed using a Bruker poly(methylmethacrylate) (PMMA) bubble holder which is sealable with a rubber o-ring to prevent oxygen/moisture contamination during data collection.

2.2.1 Basic Theory

X-ray diffraction operates under the principle of interactions between x-ray radiation and regions of high electron density that occur within the crystallographic planes of a solid material. Constructive interference occurs when the difference in path lengths of two scattered rays is equal to a whole number of wavelengths as expressed by Bragg's Law [99]:

$$n\lambda = 2d\sin\theta \qquad (2.1)$$

where n is an integer, λ is the x-ray wavelength, d is the inter-planar spacing, and 2θ is the scattering angle. Diffraction at a fixed wavelength thus allows for the determination of d-spacing based on the angular detection of scattered x-rays, and phase identification is made possible by powder diffraction databases.

XRD peak broadening is a function of both instrumental and sample contributions which can be convoluted together to provide a model for x-ray diffraction. The measured pattern is a convolution of the geometric instrument profile, x-ray wavelength profile, and specimen broadening function [98]. The geometric aberrations have a dominating influence on the shape of the measured pattern at low 2θ angles (< 50º) whereas the wavelength distribution have a dominating influence at high 2θ angles (> 100°) [98]. Specimen contributions to broadening can arise from small crystallite size or any lattice imperfection in the sample such as dislocations, vacancies, interstitials, and substitutional defects which lead to lattice strain [100].

2.2.2 Air-Sensitive Samples

A range of different techniques were utilised in order to perform XRD on air-sensitive samples in instruments that usually operate in air. To begin with, capillary sealed samples were tested using a Gandolfi camera to determine if data quality was sufficient for quantitative XRD analysis, which was not the case. Samples were also tested using a Kapton film seal using the D500 XRD which proved to unacceptably attenuate the sample's diffraction pattern. Mylar film was utilised successfully using the D500 XRD to collect diffraction patterns on air-sensitive samples with little to no air contamination. A factory built air-tight dome sample holder was utilised using the D8 XRD which proved very successful in maintaining an air-free environment for samples during data collection.

2.2.2.1 *Capillary XRD*

Initially air-sensitive samples were sealed within 0.5 mm glass capillaries in order to be analysed using XRD. A Gandolfi camera was available at The Australian Resources Research Centre (ARRC) at Technology Park (Kensington, WA, Australia) under the supervision of Michael Verrall. The Gandolfi camera utilises x-ray sensitive film encased within a circular camera in which the sample is centred. Two apertures are present enabling the primary x-ray beam to intercept the sample and produce a diffraction pattern which is collected by the now-cylindrical film centred about the sample (see Figure 2-3).

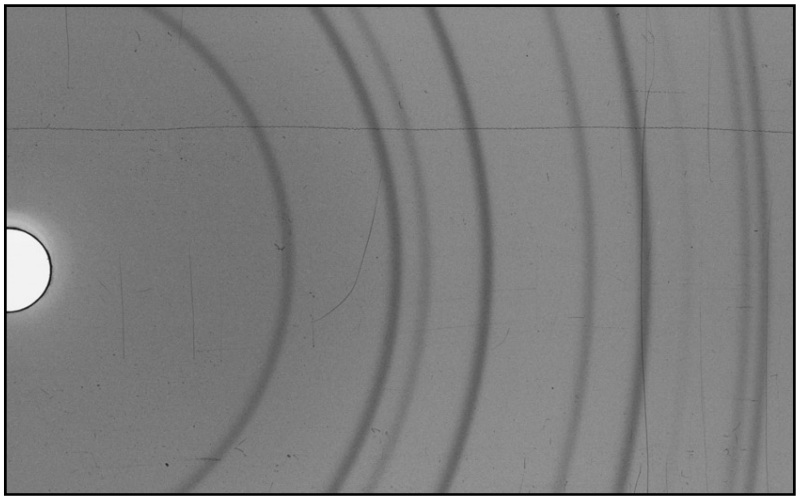

Figure 2-3: X-Ray Diffraction (XRD) pattern collected on film from alumina (Al_2O_3) captured using a Gandolfi camera with a glass capillary sample holder.

The diffraction peaks (as shown in Figure 2-3) present as dark elliptical lines on a 2-dimensional film strip can either be assigned angular 2θ diffraction angle values by eye using a known conversion factor between millimetres and degrees or the film can be scanned into a computer and digitally analysed. The film diffraction pattern (Figure 2-3) was digitally scanned and an intensity profile was calculated using a line profile through the centre of the film pattern (see Figure 2-4A). Once the XRD pattern is displayed digitally it becomes apparent that the collected data is not of high enough quality for in-depth analysis.

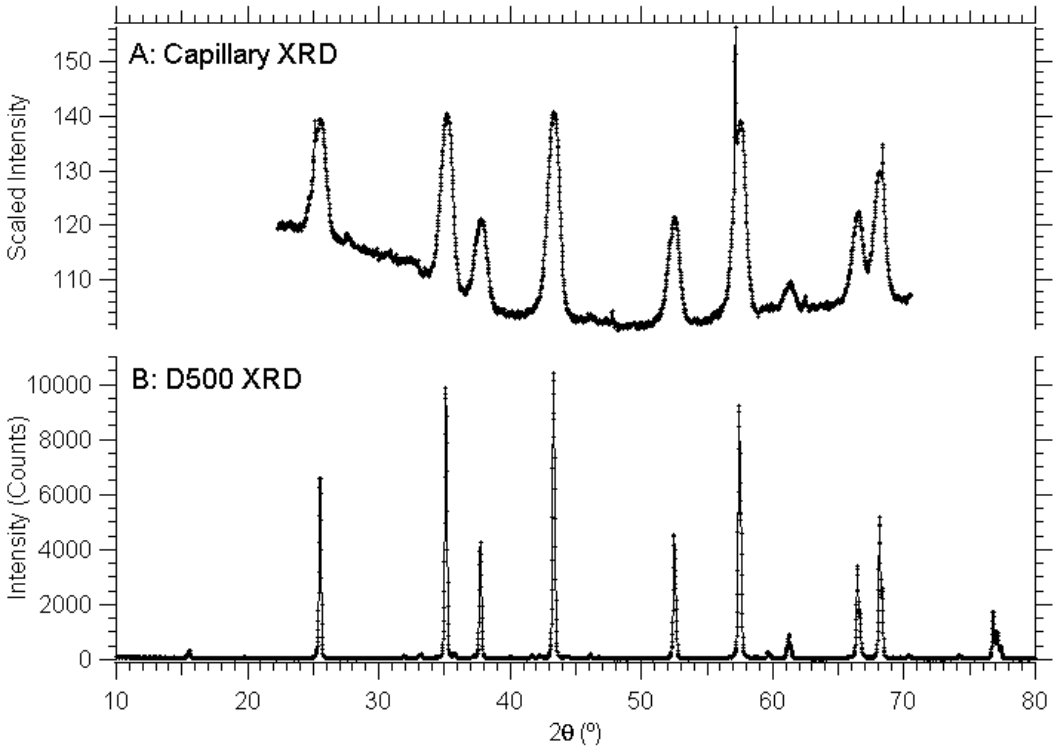

Figure 2-4: X-Ray Diffraction (XRD) patterns of alumina (Al_2O_3) which have been collected using A: Capillary XRD using a Gandolfi camera and B: a standard XRD pattern collected on the D500. Intensity spikes in Pattern A are due to scratches on the x-ray film.

Firstly there is a high inconsistent scattering background present, which can be removed but makes quantitative data analysis more difficult. Secondly, and more importantly, instrumental peak broadening is a major problem, resulting in peaks that are incredibly broad making any crystallite size and strain measurements near impossible. The instrumental broadening is most likely due to the thickness of the capillary sample as opposed to the more usual single crystal sample which acts like a point-source when analysed using a Gandolfi camera. These problems meant that

local capillary XRD was not acceptable for good quality data analysis, and due to the hazardous nature of the samples to be analysed, non-local capillary XRD was impractical.

2.2.2.2 *Kapton Film (D500)*

In an attempt to provide XRD data for air sensitive samples (using the D500 XRD instrument) Kapton film was affixed over the XRD sample holder containing the sample to be measured. This was undertaken in an argon glovebox to prevent sample air exposure. The coated XRD sample holder was then removed from the glovebox and placed within the XRD instrument for measurement. The Kapton film prevented sample air exposure but it generated a large amorphous hump in the XRD data set (from 10 - 35º 2θ) as shown in Figure 2-5. An amorphous hump can be modelled successfully when performing Rietveld analysis on XRD data and its contribution to the scattering can be accounted for. However the Kapton film also produced a large degree of angle-dependent attenuation of the sample diffraction pattern over the range of the amorphous hump.

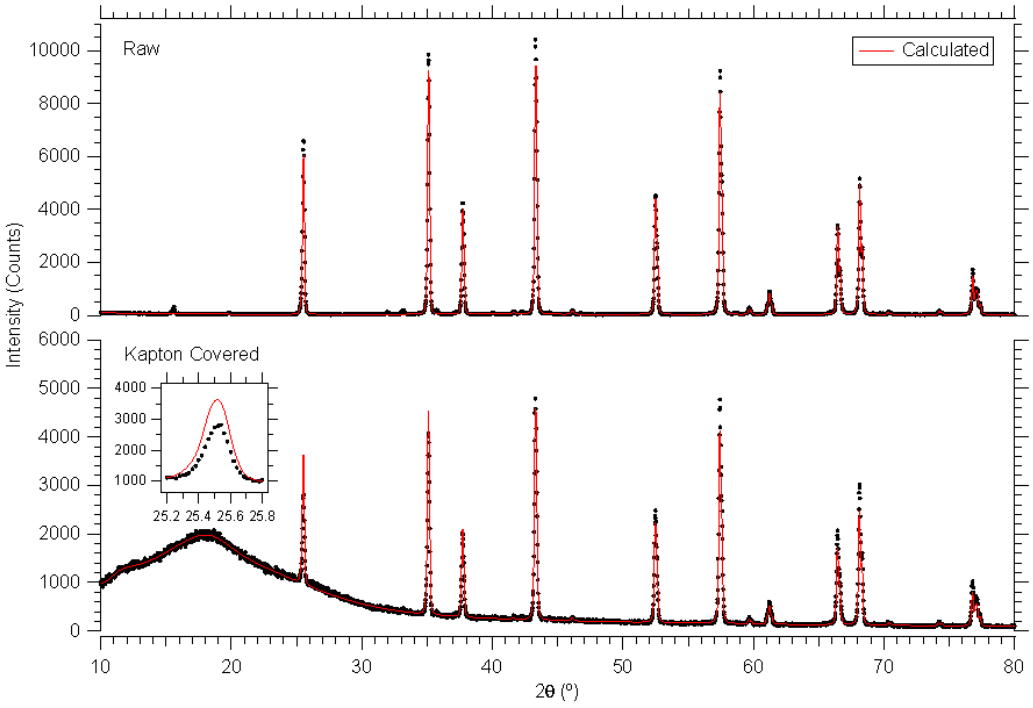

Figure 2-5: X-Ray Diffraction (XRD) patterns (D500) of alumina (Al_2O_3) which have been collected with and without a Kapton film coating. The inset displays the peak intensity attenuation which is present when a sample is coated with Kapton film.

The attenuation is demonstrated by the inset in Figure 2-5 which displays a large discrepancy in the Al_2O_3 diffraction peak intensity at 25.5º in contrast to high-angle peaks. Minor peaks at low angles given in the raw Al_2O_3 XRD pattern in Figure 2-5 are totally attenuated by the Kapton film and are not present in the coated XRD pattern. It is obvious that the Kapton film is not ideal for coating air-sensitive materials, however it was used for a small quantity of samples before mylar film became available. In these cases all Rietveld analysis performed excluded XRD data below 31º, in an attempt to eliminate any biasing of the Rietveld fit due to low angle attenuation.

2.2.2.3 *Mylar Film (D500)*

Mylar film (2.5 μm or 4 μm) was affixed over the XRD sample holder containing the sample to be measured. This was undertaken in an argon glovebox to prevent sample air exposure. The coated XRD sample holder was then removed from the glovebox and placed within the XRD instrument for measurement. The mylar film prevented sample air exposure but it generated two broad peaks in the XRD data set (from 20 - 30º 2θ) as shown in Figure 2-6.

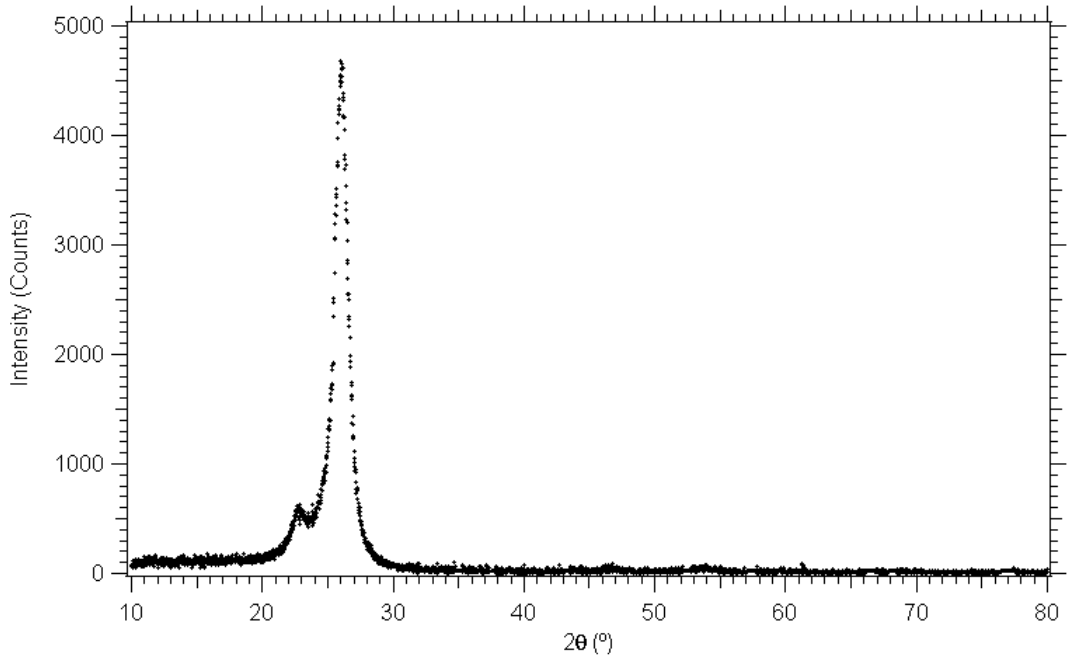

Figure 2-6: X-Ray Diffraction (XRD) pattern (D500) of an aluminium XRD sample holder that has been covered with a mylar film. Both peaks present are due to the mylar. Al_2O_3 peaks have been subtracted from the data set in order to better display the pure mylar pattern.

The mylar film was superior to Kapton because it did not attenuate the diffracted x-rays from samples, allowing quantitative phase analysis to be undertaken. The lack of attenuation can be seen in Figure 2-7 from the good fit to a diffraction data set even when diffraction peaks overlap the mylar amorphous humps.

It is possible to eliminate the two mylar peaks from 20 - 30º 2θ in a collected XRD pattern by physically bubbling the mylar into a dome shape over the sample. This can result in no mylar peaks being present in a collected pattern or sometimes results in a smaller hump present at low angles < 20º 2θ. However this method can be inconsistent between samples and in the majority of XRD patterns collected with a mylar coating the mylar was placed flat onto the sample holder resulting in two amorphous humps in the collected pattern.

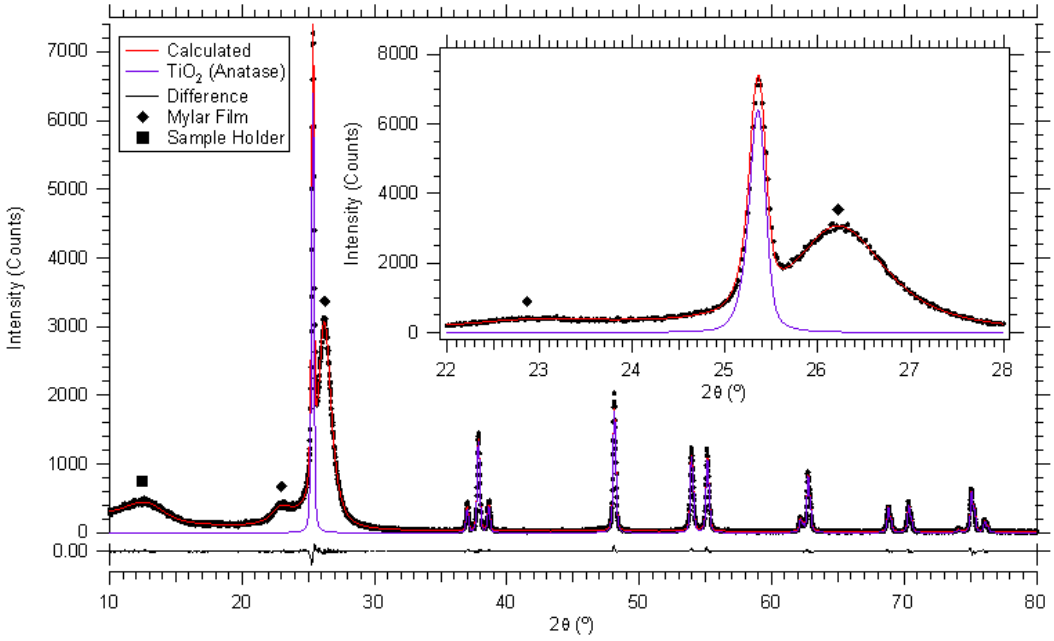

Figure 2-7: X-Ray Diffraction (XRD) pattern (D500) of a plastic XRD sample holder containing anatase (TiO_2) that has been covered with a mylar film. There is no peak attenuation due to the mylar film as seen in the inset.

The mylar film was affixed to the XRD sample holder using Vaseline (paraffin) in order to provide an air-tight seal during measurement. If the Vaseline is present on parts of the sample holder that are in contact with the x-ray beam then an amorphous hump and two crystalline peaks will also be present in the dataset (see Figure 2-8). Hence the Vaseline was kept clear from the measuring area of the XRD sample holder to prevent any peaks from being introduced into the data sets.

The mylar film was not consistently 100% air-tight resulting in some collected patterns containing slight air contamination. Only LiCl displayed obvious air contamination in samples analysed with XRD using an insufficiently sealed mylar film, leading to a minor $LiCl.H_2O$ phase being present in some cases. The mylar seal can be partially broken by either an incomplete Vaseline seal or micro-tears in the mylar film due to its extreme thinness. The slight air contamination does not appear to have any major impact on the samples other than the addition of another phase in the collected pattern that can be accounted for quantitatively. Additionally, the reaction between LiCl and H_2O is only mildly exothermic as follows:

$$\mathrm{LiCl} + \mathrm{H_2O}(l) \longrightarrow \mathrm{LiCl} \bullet \mathrm{H_2O} \qquad \Delta_r H_{298K} = -19 \text{ kJ/mol} \qquad (2.2)$$

and thus will not cause any major sample heating effects that could affect hydrogen content.

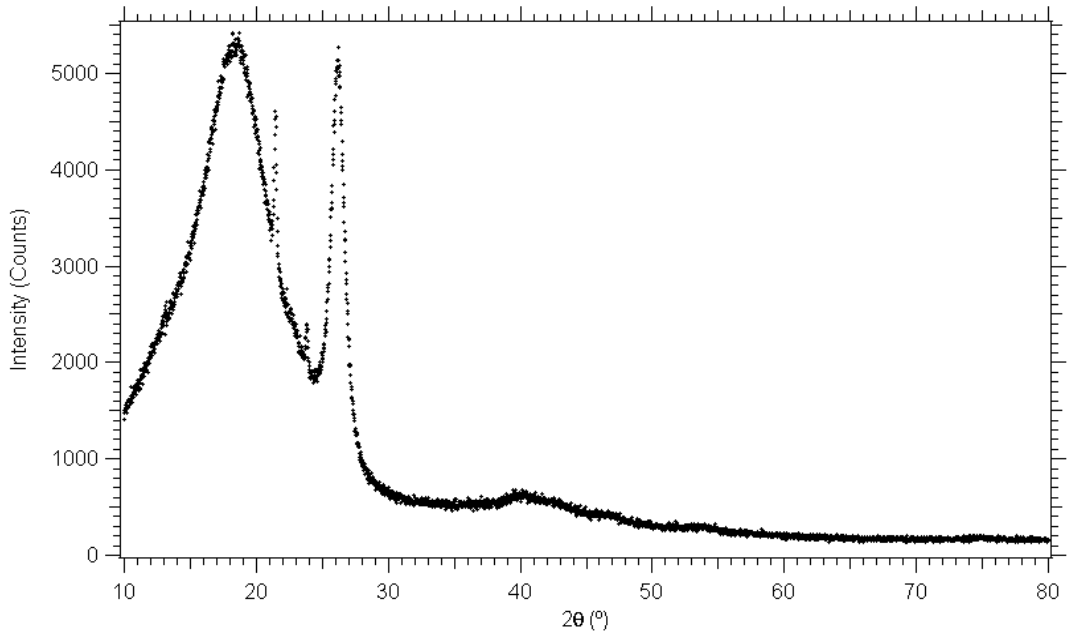

Figure 2-8: X-Ray Diffraction (XRD) pattern (D500) of an aluminium XRD sample holder that has been coated with Vaseline and covered with a mylar film. The large amorphous hump at ~ 18 º and the two crystalline peaks at 21.5 º and 23.8 º are due to the Vaseline (paraffin).

2.2.2.4 *Air-Tight Dome Holder (D8)*

XRD data collected on the D8 diffractometer utilised specialised dome-type sample holders for air-sensitive materials. The holders (base & dome) were constructed from poly(methylmethacrylate) (PMMA) plastic that provides an air-free environment via

an enclosed sample cell sealed with a rubber o-ring. The PMMA does provide an air-tight seal but significantly but uniformly attenuates the x-ray beam (by a factor of 3), especially when it is filled with argon gas (from sample loading within a glovebox) as shown by Figure 2-9.

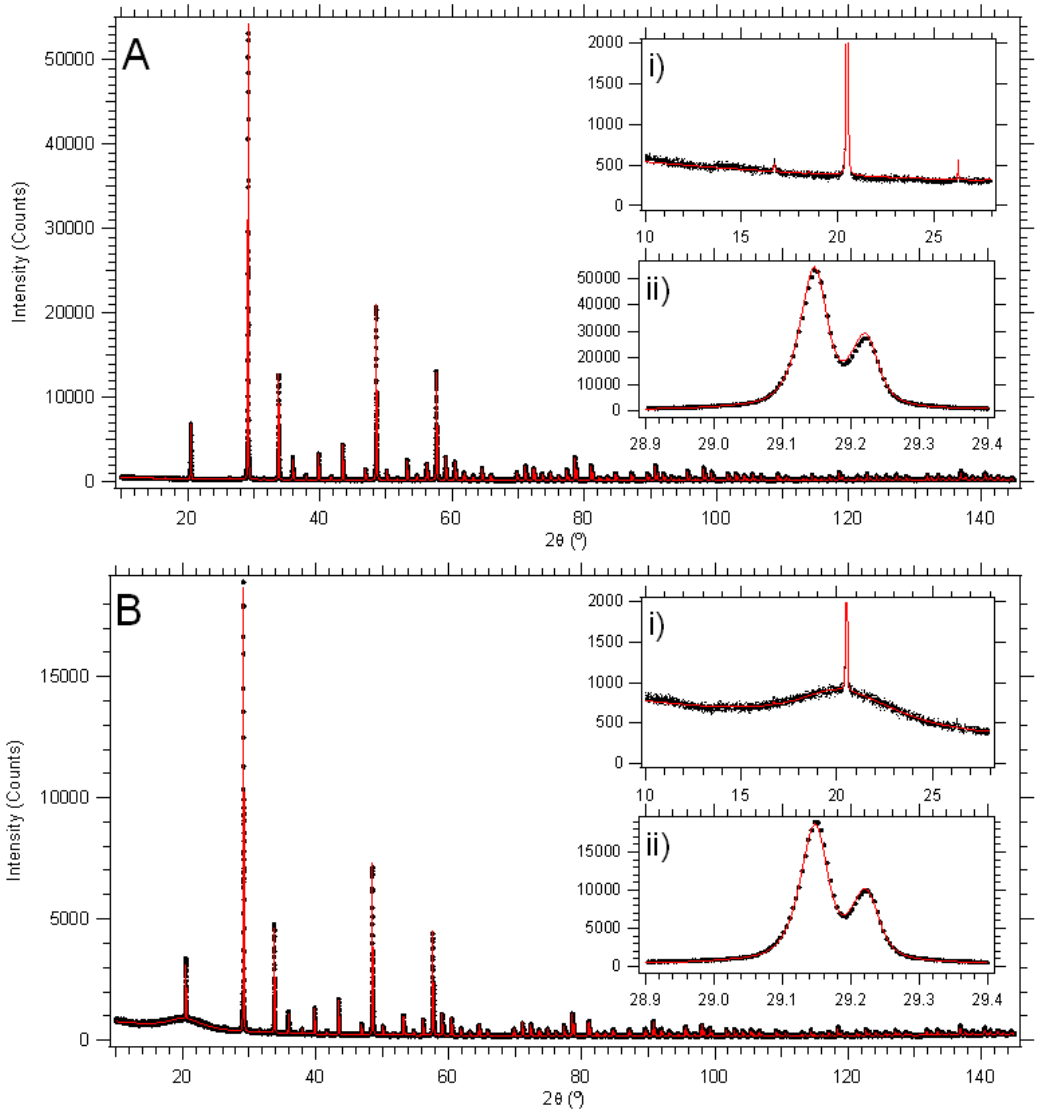

Figure 2-9: X-Ray Diffraction (XRD) patterns (D8) of annealed Y_2O_3 [101] measured in a sample holder without (A) and with (B) a protective poly(methyl methacrylate) (PMMA) plastic dome. Insets are provided demonstrating i) the background due to the protective dome and ii) the most intense peak. The pattern collected without the dome (A) has 2.8 times the number of counts as the pattern collected with the argon filled dome (B).

The PMMA plastic dome introduces another issue (other than attenuation) in relation to the scattering background. Two amorphous humps are present in the diffraction data set due to the PMMA dome at ~ 10° & 20° 2θ as shown in Figure 2-9. The

amorphous background does not significantly contribute to the diffraction pattern of a highly crystalline sample (i.e. Figure 2-9) but produces significant contribution to patterns which do not exhibit high numbers of counts as shown in Figure 2-10. However even large amorphous backgrounds can be accounted for during Rietveld analysis, shown by the close fit given in Figure 2-10, indicating that the air-tight sample holder provides adequate data to be collected for quantitative analysis.

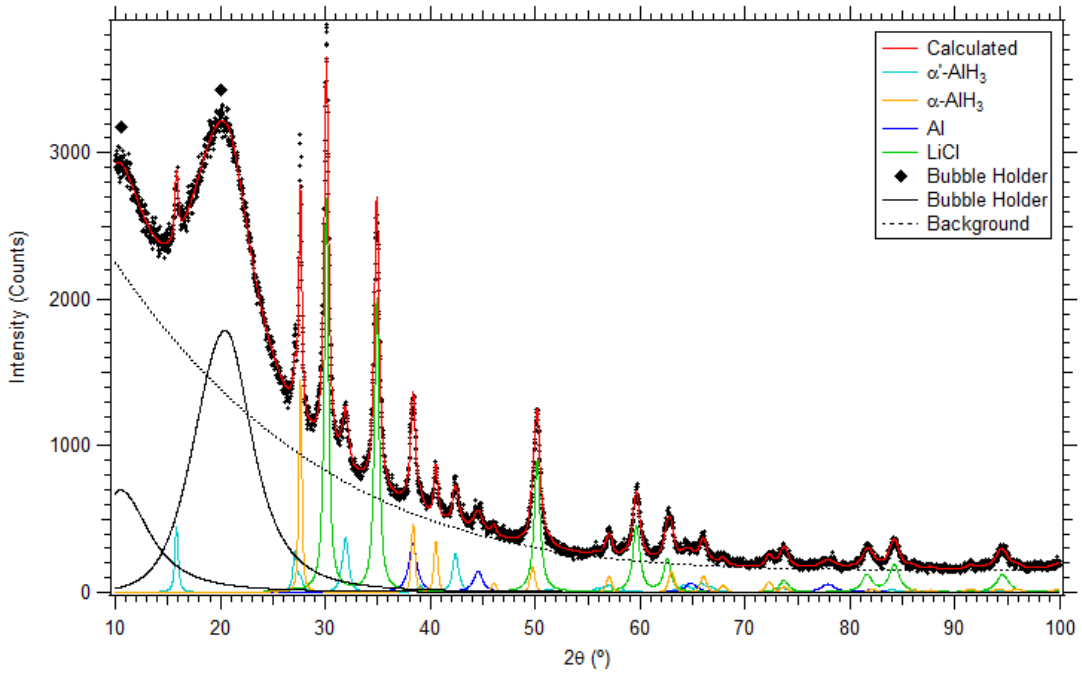

Figure 2-10: X-Ray Diffraction (XRD) pattern (D8) which demonstrates a significant scattering background due to the protective poly(methyl methacrylate) (PMMA) plastic dome when used on a sample which does not strongly diffract.

2.2.3 Synchrotron Powder Diffraction

Powder diffraction (PD) was undertaken at the PD beamline at the Australian Synchrotron in Melbourne in order to provide high resolution data with better detection limits than lab based XRD. A wavelength of ~1 Å (12.3985 keV) was selected as a compromise between resolution and *d* range whilst avoiding wavelengths close to any sample specific x-ray absorption edges. Samples were sealed within rotating 0.5 mm glass capillaries (Charles Supper Company, MA, USA) that were aligned within the x-ray beam using a 5-axis goniometer. Capillaries were loaded within a glovebox at Curtin University, temporarily sealed, removed into air, and then sealed with a flame. The capillaries add an amorphous background

to the collected XRD patterns that can be accounted for during data analysis by peak fitting the amorphous hump.

The PD detector consists of 16 discrete MYTHEN (microstrip system for time resolved experiments) detector modules that each cover 4.8° 2θ with a 0.2° 2θ gap between modules, resulting in a total 2θ range of ~80°. In order to provide total angular coverage two separate data collection runs were undertaken (under the same conditions) for each sample at a 0.5° 2θ offset with one another. Both data sets were merged to provide an ~85° 2θ collection range for each sample analysed. Data resolution (Δd) under these experimental conditions ranges from 8.555×10^{-3} Å to 2.658×10^{-5} Å in d-space (or $\Delta d/d$ ranging from 7.485×10^{-4} to 3.585×10^{-5}).

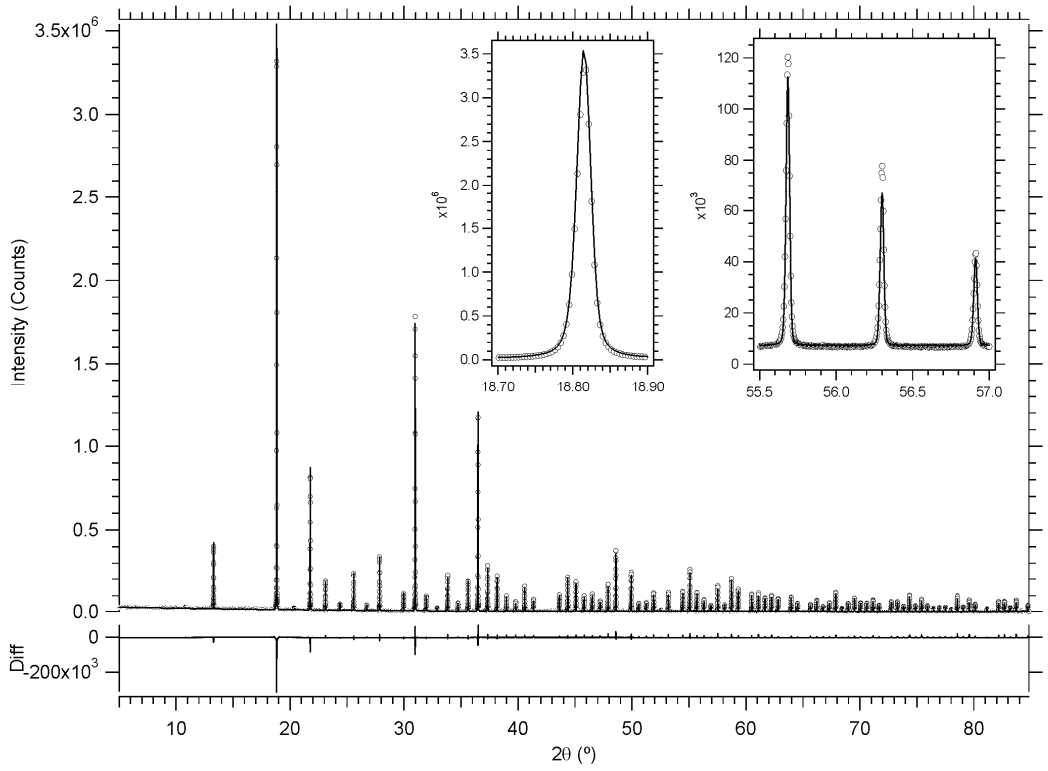

Figure 2-11: X-Ray Diffraction (XRD) pattern (Australian Synchrotron) for Y_2O_3 displaying the fit to the data in which the instrumental function was derived. Insets are provided which better display the goodness of fit.

Data was collected from a number of standards in order to determine beamline instrument parameters that allow for Rietveld analysis to be undertaken on sample data allowing for quantitative phase analysis and crystallite size determination. The operating wavelength was obtained exactly by using a NIST 660a LaB_6 standard as

1.00007 Å. An instrument function was generated in the Topas software (Bruker, Germany) from a Y_2O_3 sample [101] with known crystallite size as shown in Figure 2-11.

2.2.4 Neutron Powder Diffraction

Neutron powder diffraction (ND) was undertaken on the Wombat beamline at the Australian Nuclear Science and Technology Organisation (ANSTO) in Sydney. Samples were sealed within 6 mm vanadium cans. The cans were loaded within a He glovebox at ANSTO, sealed using an indium o-ring, and then removed into air. A Ge(115) monochromator reflection with a 90° take-off angle was selected to produce a wavelength of ~1.54 Å and provide a compromise between resolution, *d*-spacing range, and neutron flux. Data resolution (Δd) under these experimental conditions ranges from 2.163×10^{-2} Å to 3.073×10^{-4} Å in *d*-space (or $\Delta d/d$ ranging from 5.470×10^{-3} to 3.775×10^{-4}). A 10 minute data collection time was used for a calibration standard, whilst 120 minute collection times were used for samples in order to provide high signal to noise patterns so that minor peaks could be adequately resolved.

The ND detector consisted of a continuous 2-D detector bank that spanned 120°. The 2-D data files were processed using the Large Array Manipulation Program (LAMP) software package [102]. The data was first converted onto a 2θ scale and was then calibrated against a flood field image to account for a detector response function. The 2-D data file was then linearised to correct for radial line profiles, and was finally vertically integrated to generate a 1-D data file.

Data was collected from a NIST 676 Al_2O_3 standard reference material (SRM) in order to determine beamline instrument parameters allowing Rietveld analysis to be undertaken on sample data. The operating wavelength was obtained exactly by performing a refinement of the NIST 676 standard as 1.53826 Å. An instrument function was generated in the Topas software (Bruker, Germany) using the known crystallite size of the standard [103] as shown in Figure 2-12.

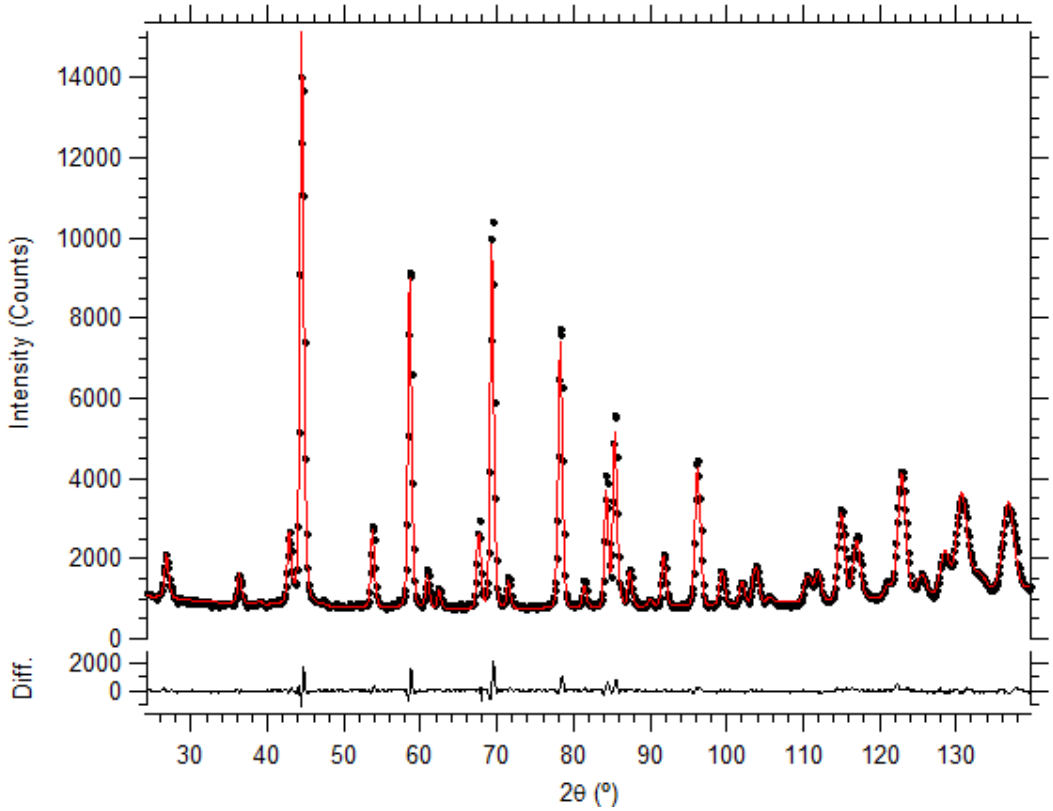

Figure 2-12: Neutron Diffraction (ND) pattern (ANSTO: Wombat) for NIST SRM 676 (Al_2O_3) displaying the fit to the data in which the instrumental function was derived. A difference plot is also displayed.

2.2.5 Computer Modelling: Rietveld Analysis

A fundamental parameters approach to XRD Rietveld analysis was undertaken using the Topas v.4.1 (Bruker, Germany) software package. "The fundamental parameters approach to line profile fitting uses physically based models to generate the line profile shapes" [98] involving the convolution of an array of geometric instrumental profiles with wavelength distributions and specimen broadening to provide a realistic diffraction model. All uncertainties are quoted to 2 standard deviations (95% confidence interval).

Copper emission profiles were utilised in Rietveld analysis, in line with the instrumental radiation. A 5-point Cu-K_α wavelength spectrum was used for D500 XRD patterns and a 10-point Cu-K_α & -K_β wavelength pattern was used for D8 XRD patterns. Cu-K_β radiation was utilised for D8 data because minor -K_β contributions present themselves despite the fact that a Ni filter was used when using a linear

position sensitive detector (PSD). The instrumental parameters used for both the D500 and D8 are provided in Table 2-3.

The crystallite sizes were determined from an LVol-IB method (volume averaged column height calculated from the integral breadth) [104] which provides a good measure of the volume-weighted average crystallite size. The crystallite sizes from XRD and particle sizes from TEM cannot be directly compared because the XRD crystallite size is a volume weighted mean whereas the TEM particle size is a number weighted mean (see Figure 2-13). The volume weighted mean is crystallite shape dependent and if the shape is known then a conversion between volume weighted and number weighted means can be performed.

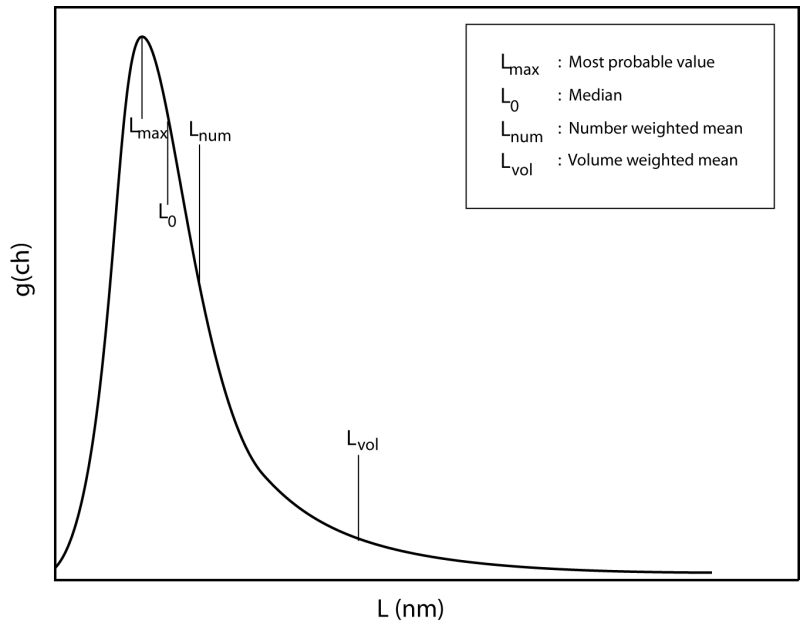

Figure 2-13: Crystallite column height distribution displaying values determined from alternate methods as described in the text. *g*(*ch*) is a crystallite column height distribution, whereas *L* is the column height size. Adapted from Coelho [104].

The integral breadth (β) can be calculated from the integrated intensity of the diffraction line profile above the background divided by the peak height, I_p, as follows [105]:

$$\beta = \frac{\int I(2\theta)\, d(2\theta)}{I_p} \tag{2.3}$$

where a double-Voigt approach to line profile shape is implemented.

2.3 SMALL ANGLE X-RAY SCATTERING (SAXS)

Small angle x-ray scattering (SAXS) patterns were collected with a Bruker NanoSTAR SAXS instrument at Curtin University. Samples were loaded and sealed within glass capillaries in an argon glovebox to prevent oxygen/moisture contamination prior to data collection. Data was recorded at a sample-detector distance of 65.0 cm using a wavelength, λ, of 1.5418 Å (CuK_α) and scattered photons were counted with a 2D multiwire detector for 3 hours per sample. The raw data was radially averaged, background subtracted and placed on an absolute scale. Resulting intensities, after discarding low q data points affected by the beam stop, spanned a q-range of 0.0114 to 0.327 $Å^{-1}$.

2.3.1 Basic Theory

Small angle x-ray scattering (SAXS) is a method that is used in order to provide information about the distribution and structure of matter on the nanoscale, from a few Å to a few thousand Å [106]. The small angle scattering optics are displayed in Figure 2-14. X-rays are generated, collimated by the Göbel mirrors and a pinhole and then interact with the sample. X-rays are scattered from the sample and are projected upon a 2-dimensional detector whilst the primary beam is halted by a beamstop.

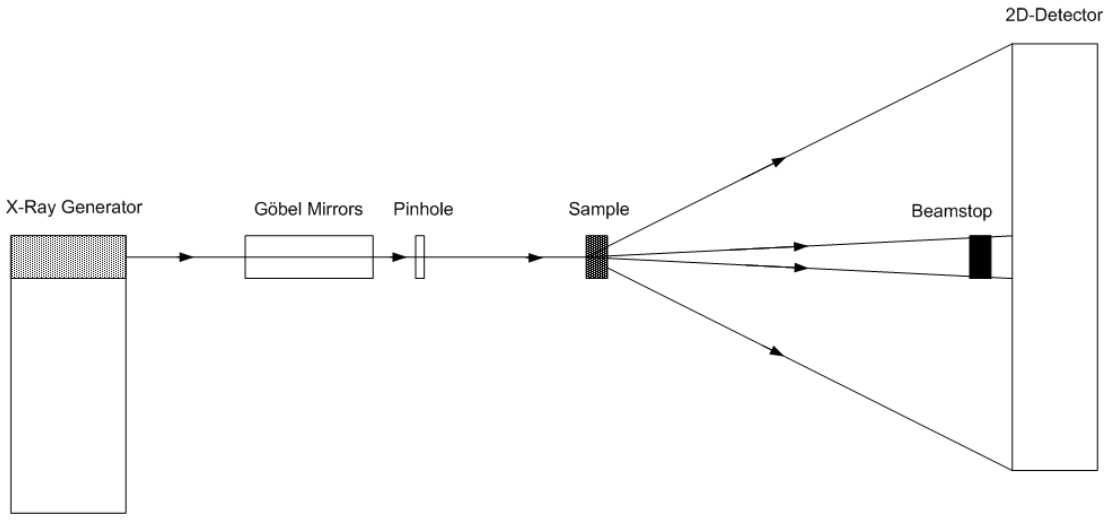

Figure 2-14: Small angle x-ray scattering (SAXS) simplified optics schematic.

X-ray scattering from a sample is the result of an electromagnetic interaction between the incident x-ray wave and the electrons within the sample. This is

explained by Schmidt [107] where "the oscillating electric field of the incident plane-wave x-ray exerts an electric force on the electrons in an atom". This creates an oscillating electric moment in the atom which produces an oscillating electromagnetic field, which is known as the scattered field. The scattered intensity is measured as a function of the scattering angle. However it is more useful to analyse the scattered intensity as a function of the scattering vector [108]:

$$q = \frac{4\pi \sin 2\theta}{\lambda} \tag{2.4}$$

Where θ is the scattering angle and λ is the wavelength (CuK_α = 1.5418 Å).

2.3.2 Absolute Intensity Data Conversion

When performing an analysis on scattering data obtained from SAXS it is important to be working with absolute (or scaled) intensity $I_{abs}(q)$ that has units of cm^{-1}. When the data has been converted to absolute intensity relevant parameters such as the specific surface area or volume fractions can be determined [109]. Absolute intensity data was generated by the NanoSTAR SAXS instrument at Curtin University using the following procedure.

Five long SAXS runs and four short SAXS runs are performed (see Table 2-4) for one sample to be analysed and converted to absolute intensity. Multiple samples can be run simultaneously reducing the need for excessive background and standard runs.

Table 2-4: SAXS Runs Required for Absolute Intensity Calculation.

Run	Intensity	Description of Sample	Run time
Short	I_{mGC}	The sample to be analysed in a sample holder with the glassy carbon sample also inserted.	t_{mQ} = 100 s
Short	I_{bGC}	An exact replica of the above sample holder minus the sample with the glassy carbon sample also inserted.	t_{mQ} = 100 s
Short *Optional*	I_{stmGC}	The standard (i.e. S-2907 from Oak Ridge National Laboratories) with the glassy carbon sample also inserted.	t_{mQ} = 100 s
Short *Optional*	I_{stbGC}	The background for the standard (i.e. air) with the glassy carbon sample also inserted.	t_{mQ} = 100 s
Long	I_m	The sample to be analysed in a sample holder.	t_s = 10800 s
Long	I_b	An exact replica of the above sample holder minus the sample.	t_s = 10800 s
Long	I_{stm}	The standard (i.e. S-2907 from Oak Ridge National Laboratories).	t_{st} = 10800 s
Long	I_{stb}	The background for the standard (i.e. air).	t_{st} = 10800 s
Long	I_{noise}	No sample and x-ray generator off	t_{st} = 10800 s

The glassy carbon sample is used because it has a known transmission $\tau_{GC} = 0.13$ that allows for the calculation of sample transmission scale from:

$$\tau_s = \frac{I_{mGC} - \tau_{GC} I_m}{I_{bGC} - \tau_{GC} I_b} \tag{2.5}$$

The transmission calculation can be performed quickly by the accompanying Bruker NanoSTAR SAXS software. The transmission of the standard S-2907 is known to be τ_{st} = 0.539 or its transmission can be worked out from the optional runs with the standard's measured parameters using Equation 2.5.

The measured intensity must be corrected for sample transmission and background effects in order to obtain I_c a corrected intensity which is equal to:

$$I_c = I_m - \tau_s I_b - (1 - \tau_s) I_{noise} \tag{2.6}$$

The correction calculation (Equation 2.6) removes any scattering produced by the system that is not related to the sample (i.e. from the sample holder or from any air present in the vacuum chamber). A proportion of the background scattering pattern is removed from the measured scattering pattern that is related to the transmission of x-rays through the sample (i.e. equal to the amount of background scattering present in the measured scattering pattern). The measured scattering pattern and the background scattering pattern both contain noise from the detector which has to be totally removed from the measured scattering pattern. The remaining portion of the detector noise pattern is removed using the non-transmitted x-ray fraction.

Certain other parameters must also be known to determine the absolute intensity:

- The differential scattering cross section per unit volume of the standard $I_{abs,st}$ at q = 0.0227 Å $^{-1}$ must be known for S-2907. This was measured to be 41.2 cm^{-1} at Oak Ridge National Laboratory (ORNL).

- The number of photons detected I_{st} for the S-2907 standard in time t_{st} at q = 0.0227 Å^{-1}. This is found graphically from the measured S-2907 intensity plot.

- The measured thickness of the standard d_{st} that is known to be 0.1715 cm.

- The measured thickness of the sample d_{sp} must also be known.

The thickness of the sample is often difficult to obtain especially when dealing with powder samples [109]. This thickness can however be determined from the following relation [109]:

$$d_{sp} = -\frac{\ln \tau_s}{\mu} \tag{2.7}$$

where μ is the linear attenuation coefficient of the solid phase which is given by:

$$\mu = \rho_m \mu_m = \rho_m \sum_{i=1}^{n} w_i \mu_{m_i} \tag{2.8}$$

where ρ_m is the sample's atomic true density (g cm^{-3}), μ_m is the x-ray mass absorption coefficient for the x-ray energy under which it was measured: $E = (hc)/(\lambda e) = \left(6.63\times10^{-34}\times3\times10^{8}\right)/\left(1.5418\times10^{-10}\times1.602\times10^{-19}\right) = 8.05\times10^{-3}$ MeV for the Nanostar SAXS, n is the number of elements in the powder, w_i is the weight % of each element and μ_{mi} is the x-ray mass absorption coefficient for each element.

An example of the sample thickness calculation can be performed for silica aerogel that is made up from SiO_2. Aerogel has two different elements, silicon and oxygen, so n = 2. The relative atomic mass of silicon is 28.09 and for oxygen it is 16.00 therefore the weight percentages are respectively w_1 = 28.09/60.09 and w_2 = 32.00/60.09. The x-ray mass absorption coefficients for an energy of 8 keV are μ_{m1} = 64.68 cm^{2}g^{-1}, μ_{m2} = 11.63 cm^{2}g^{-1}.

The atomic (or true) density is given as the mass of a particle divided by its volume, excluding open pores and closed pores [110]. For aerogel this is the density of silicon dioxide (vitreous silica), which has a density of ρ_m = 2.2 g cm^{-3} [111-112]. Therefore for a silica aerogel sample (with τ_s = 0.841) the sample thickness d_{sp} is given by:

$$
\begin{aligned}
d_{sp} &= \frac{-\ln \tau_s}{\rho_m \sum_{i=1}^{n} w_i \mu_{m_i}} \\
&= \frac{-\ln 0.841}{2.2\left(\frac{28.09}{60.09}64.68 + \frac{32.00}{60.09}11.63\right)} \\
&= 2.16 \times 10^{-3}\,\text{cm}
\end{aligned}
\tag{2.9}
$$

The absolute intensity $I_{abs}(q)$ is then given by the following:

$$
I_{abs}(q) = I_{abs,st} \frac{I_c(q)}{I_{st}} \frac{t_{st}}{t_s} \frac{d_{st}}{d_{sp}} \frac{\tau_{st}}{\tau_s} \ (\text{cm}^{-1}) \tag{2.10}
$$

2.3.3 The Unified Model

There are a multitude of different equations that can be used to model the scattering from various systems analysed by small angle scattering. These equations are usually valid in modelling only small regions of a small angle scattering plot, often not being able to model large sections of data that are explained by different mathematical models. Beaucage [111,113-114] describes a unified Guinier/power-law approach to modelling small angle scattering data which can be used with a wide range of physical systems to provide complete fitting of the small angle scattering curve.

This unified approach can model complex systems that contain multiple levels of structural features, where each structural level is described by both a Guinier and an associated power-law regime. Beaucage [113] notes that both low-*q* and high-*q* limits to power-law scattering regimes are taken into account and that this unified approach can distinguish Guinier regimes which lie between two power-law regimes.

The structural limits that are observed in power-law regimes are "*manifested as regimes of exponential decay in scattering*" [113] which follow Guinier's law. Beaucage [113] states that "*this behaviour has been interpreted as reflecting interfacial or mass-fractal scattering from a large scale structure in the low-q power-law regime composed of small-scale substructures whose mass fractal or surface fractal scaling is observed in the high-q power-law regime*".

A visual representation of the relationship between a physical system and its small angle scattering data is shown in Figure 2-15. It is useful to see the scattering plot

related to a multi-level structured material in this way. It can be seen that this material consists of aggregate structures composed of primary particles which have rough surfaces and that these primary particles are formed from atomic lattice bonding. Scattering is observed from the aggregate structure at *A* which is modelled as a mass fractal regime, the scattering shown by the hump at *B* is a function of the size of the primary particles which is modelled by a Guinier regime, the linear scattering region at *C* occurs because of scattering from the surface of the primary particles and is modelled by a surface fractal regime, and the peak at *D* is the result of diffraction from the atomic lattice which is not modelled by the unified equation.

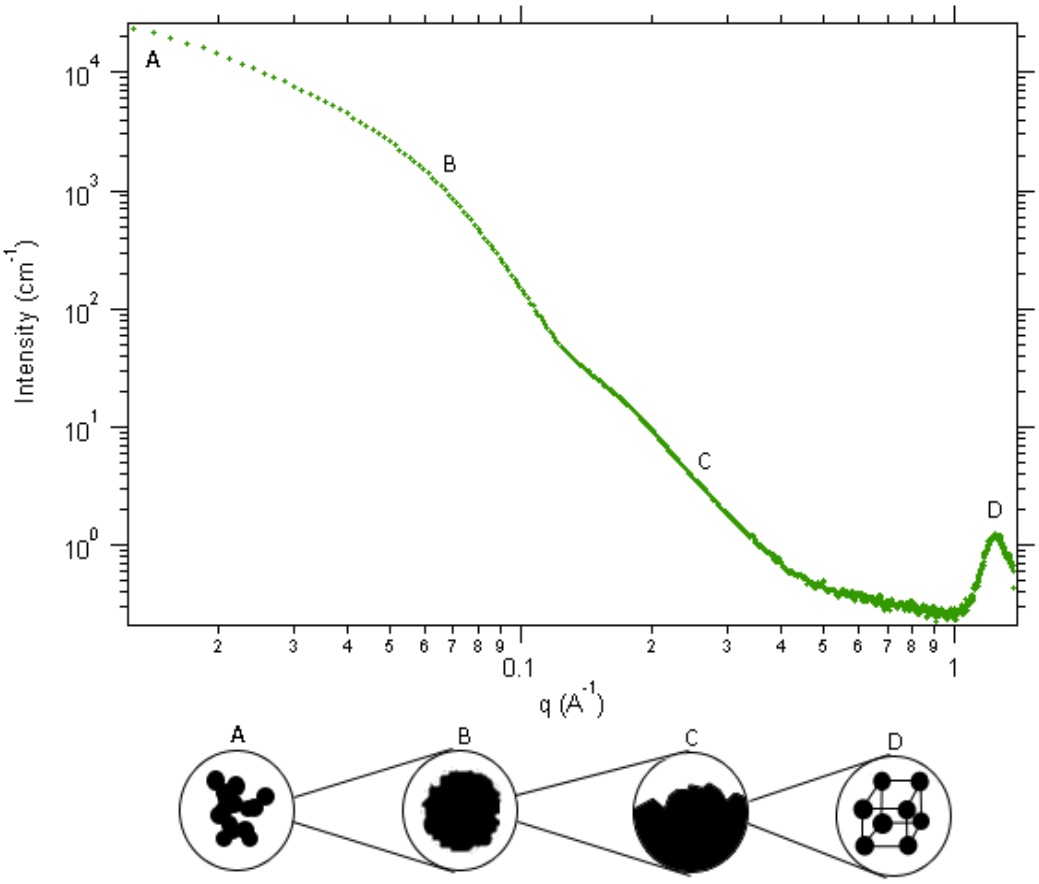

Figure 2-15: The relationship between physical material properties (aggregate, primary particles and atomic structure) and a synthesised small angle scattering plot. The scattering data was collected from a silica aerogel sample (Marketech International Inc., USA).

It should be noted that the average size of the primary particles can be determined from the Guinier regime formulae and the fractal dimensions can be determined from the power law regimes. These power law regimes describe the mass- or surface-

fractal scaling [111] that is inherent to fractal systems and provides information about how disordered the aggregate or surface structure is respectively.

Beaucage [113] notes that there are several advantages to using a unified approach to fitting scattering data rather than applying multiple, individual power-law and exponential fits. The use of the unified approach results in more accurate fits which include a larger number of data points than individual fits. When individual fits are used some Guinier regimes may be incapable of being fit because of an overlap of neighbouring power-law regimes. Beaucage [113] states that "*the unified approach clarifies the limits to power-law and Guinier-exponential scattering, thereby removing uncertainty as to the appropriate fit range for these functional forms*" which leads to the fact that the unified approach is more suitable for use as a fitting function than other functions which only fit individual regimes.

The unified equation for two structural levels is represented by the following equation [111]:

$$\begin{aligned} I(q) \cong\ & G\exp\left(-q^2R_g^2/3\right) + B\exp\left(-q^2R_{sub}^2/3\right)\left\{\left[\mathrm{erf}\left(qkR_g/\sqrt{6}\right)\right]^3/q\right\}^P \\ & + G_s\exp\left(-q^2R_s^2/3\right) + B_s\left\{\left[\mathrm{erf}\left(qk_sR_s/\sqrt{6}\right)\right]^3/q\right\}^{P_s} \end{aligned} \tag{2.11}$$

where G is the exponential prefactor and takes the form $G = n^2N_PI_e$ where n is the number of electrons in a particle, N_p is the number of particles in the scattering volume and I_e is the scattering factor for a single electron. R_g is the radius of gyration of the particle, R_{sub} defines the high-q structural level cut-off limit for the low-q level, R_s is the radius of gyration of the high-q structural level, B is a constant prefactor specific to the type of power-law scattering observed as determined by the regime in which P falls (see Table 2-5), P is the scattering exponent which defines the scattering regime, and 'erf' is the error function given by [115]:

$$\mathrm{erf}(x) = \frac{2}{\sqrt{\pi}}\int_0^x e^{-t^2}\,\mathrm{d}t \tag{2.12}$$

In Table 2-5: ρ_e is the electron density difference which is equivalent to n^2/V_p^2, n is the number of electrons in a particle, V_p is the volume of a particle, I_e is the intensity

scattered from one electron, N_p is the number of particles in the scattering volume, S_p is the particulate surface area, R_g is the radius of gyration for the same structural level and d_m & d_s are the mass and surface fractal dimensions respectively, d_{min} is the minimum dimension which refers to branching, and Γ is the Gamma function given by [115]:

$$\Gamma(x) = \int_0^\infty t^{x-1} e^{-t} \mathrm{d}t \tag{2.13}$$

Table 2-5: Prefactors *B* for Scattering Exponents *P* in the unified model.

Regime	*P*	*B*	units
Rod of Height 2H [113]	$P = 1$	$B = \pi G/(2H)$	$cm^{-1}Å^{-1}$
Lamellar Disc of Radius R [113]	$P = 2$	$B = 2G/R^2$	$cm^{-1}Å^{-2}$
Gaussian Polymer [111]	$P = 2$	$B = 2G/R_g^2$	$cm^{-1}Å^{-2}$
Polymeric Mass Fractal (Linear) [111]	$1 < P < 3$	$B = \left(d_m G/R_g^{d_m}\right)\Gamma(d_m/2)$	$cm^{-1}Å^{-dm}$
Polymeric Mass Fractal (Branched) [116]	$1 < P < 3$	$B = \left(d_{\min} G/R_g^{d_m}\right)\Gamma(d_m/2)$	$cm^{-1}Å^{-dm}$
Surface Fractal [113-114]	$3 < P < 4$	$B = 4\pi^2 G V_p^{-2} R_g^{d_s}\Gamma(5-d_s)\sin\left(\pi(3-d_s)/2\right)/(3-d_s)$	$cm^{-1}Å^{ds-6}$
Porod (Smooth Surface) [113]	$P = 4$	$B = 2\pi N_P \rho_e^2 S_P I_e$	$cm^{-1}Å^{-4}$

The unified equation given by Equation 2.11 is best explained in steps. The first term $G\exp\left(-q^2R_g^2/3\right)$ describes the large scale structure of size R_g which is composed of smaller substructure of size R_s which is described by the third term $G_s\exp\left(-q^2R_s^2/3\right)$.

The second term $B\exp\left(-q^2R_{sub}^2/3\right)\left\{\left[\mathrm{erf}\left(qkR_g/\sqrt{6}\right)\right]^3/q\right\}^P$ describes the power law scattering regime for the large scale structure which includes two structural limits. The low-q limit is at R_g and is described by the error function [111]. The high-q limit is at R_{sub} and is described by the exponential prefactor [111].

The third and fourth terms $G_s\exp\left(-q^2R_s^2/3\right) + B_s\left\{\left[\mathrm{erf}\left(qk_sR_s/\sqrt{6}\right)\right]^3/q\right\}^{P_s}$ describe the "*smaller substructure, R_s, with the high-q cut-off for the substructural power law outside of the observed size range*" [113]. Therefore there is no exponential prefactor to power law scattering in the fourth term.

2.3.3.1 *Computer Modelling: The Unified Equation*

The unified model can be applied to small angle scattering data sets using the Irena package [117] for Igor Pro (Wavemetrics, Oregon). Irena provides a fitting package that enables the user to obtain the relevant parameters from the unified model. The small angle scattering data set must be converted to an absolute scale first in order to obtain accurate values for the power-law prefactor constant B and the Guinier exponential prefactor G. Irena also provides a global normalised mathematical fitting uncertainty and mathematical fitting uncertainties for each of the refined variables in the unified model.

2.3.4 Surface Area Determination

If a material is found to have primary particles that are found to be surface fractal then their surface area can be determined from the surface fractal scaling regime by using the unified model. Beaucage [111] notes that the surface area for a surface fractal at a particular size of measurement, r, is given by the following:

$$S(r) = Sr^{2-d_s} \tag{2.14}$$

where the surface fractal dimension, d_s, is given by:

$$d_s = 6 - P_s \tag{2.15}$$

where P_s is the surface fractal scattering exponent obtained from a unified fit to the SAXS data set, and S is given as:

$$S = \frac{2\pi\varphi(1-\varphi)B_s}{Q\rho_{sample}F(d_s)} \quad (\text{units of } \mathrm{m}^{ds}\mathrm{g}^{-1}) \tag{2.16}$$

where B_s is the surface fractal power law prefactor, Q is the high-q invariant, ρ_{sample} is the bulk density (for non-particulates) or the effective particle density which is "*defined as the particle mass divided by the particle volume, including the volume of all pores*" [118], $F(d_s)$, φ, and Q are given by the following [111]:

$$F(d_s) = \frac{\Gamma(5-d_s)\sin[\pi(3-d_s)/2]}{(3-d_s)} \tag{2.17}$$

$$\varphi = \frac{\rho_{sample}}{\rho_{base}} \tag{2.18}$$

$$Q = \int_0^\infty I(q) q^2 \mathrm{d}q = \frac{2\pi^2 G_s}{V_{base}} \quad (\text{units of } \mathrm{cm^{-1}\AA^{-3}}) \tag{2.19}$$

where ρ_{base} is the primary particle density (true or atomic density), G_s is the Guinier prefactor for the primary particle substructure, V_{base} is the volume of the primary particles and $I(q)$ is expressed as follows (from the unified equation):

$$I(q) = G_s \exp\left(\frac{-q^2 R_s^2}{3}\right) + B_s \left(\frac{\left[\mathrm{erf}\left(q k_s R_s / \sqrt{6}\right)\right]^3}{q}\right)^{P_s} \quad (\text{units of } \mathrm{cm^{-1}}) \tag{2.20}$$

where k_s is a constant that "*accounts for an approximation involved in the description of the low-q power limit*" [111] which is given a value of 1 for steep power-law decays where the scattering exponent, P_s, is greater than 3.

Care must be taken in converting all units appropriately so that the value for S can be determined. B_s has units of $\mathrm{cm^{-1}\AA^{ds-6}}$ and therefore must be multiplied by $10^{(2+10*(-(ds-6)))}$ to convert to $\mathrm{m^{-5}}$. Q has units of $\mathrm{cm^{-1}\AA^{-3}}$ and therefore must be multiplied by 10^{32} to convert to $\mathrm{m^{-4}}$. ρ_{sample} has units of g $\mathrm{cm^{-3}}$ and therefore must be multiplied by 10^6 to convert to g $\mathrm{m^{-3}}$. Therefore S can be determined in terms of $\mathrm{m^{ds}g^{-1}}$.

The formula for surface area given by Equation 2.14 requires a size (or measuring stick) of measurement to be used to indicate at which part of the surface fractal scaling regime the surface area should be determined. Beaucage [111] uses the size of a nitrogen molecule (r = 4 Å) akin to nitrogen adsorption in order to find a comparable value (once it has been converted to meters).

2.4 TRANSMISSION ELECTRON MICROSCOPY (TEM)

Transmission electron microscopy (TEM) was conducted on a JEOL JEM2011 instrument operating at 200 kV at Curtin University and a JEOL 3000F FEGTEM instrument operating at 300 kV at The Centre for Microscopy, Characterisation and Analysis (CMCA) at The University of Western Australia. Both microscopes were coupled with an Oxford Instruments energy dispersive x-ray spectrometer (EDS) for elemental analysis. Both instruments also had electron diffraction capabilities.

Samples were loaded onto 200 mesh copper grids with holey carbon support films drop-wise via suspension in either nitromethane or toluene. The TEM grids contained minor traces of silicon resulting from the manufacturing process. Samples must be exposed to air before being loaded into the TEM column; however air-exposure time was kept as short as possible (up to a few minutes).

2.4.1 Difficulties

Samples were generally unstable within the electron beam and portions of the samples often altered over time. The decomposition of a sample under the beam is evident in Figure 2-16 where parts of the sample have disappeared or altered over time. Sample decomposition made sample morphology investigations more difficult, especially when very small nanoparticles were present.

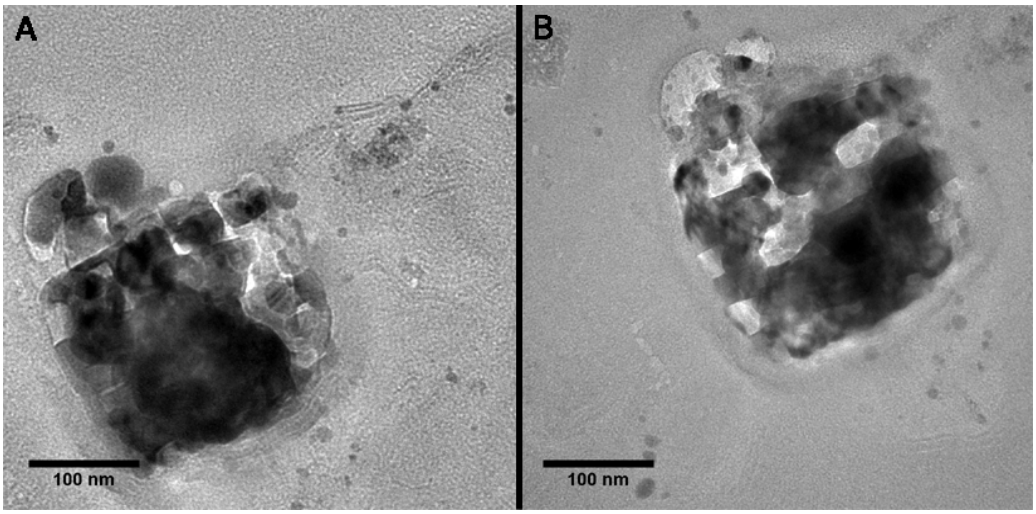

Figure 2-16: Transmission Electron Microscopy (TEM) micrographs of a sample (MgH_2 + LiCl) that has undergone decomposition under the electron beam over time. Micrograph B was taken 10 minutes after micrograph A.

2.4.2 Energy Dispersive X-Ray Spectroscopy (EDS)

EDS provides elemental analysis of selected sample regions during TEM investigations. The interaction between charged electrons and different elemental constituents of the sample cause characteristic x-rays to be emitted which can be detected by a detector with a range of energy channels. Each element emits x-rays with different energies allowing elemental determination. The electron beam can be directed toward specific parts of a sample during imaging allowing EDS to be performed on minor sample features of interest.

2.4.3 Electron Diffraction

Electron diffraction (ED) can be undertaken within a TEM during imaging investigations. The EM optics can be altered in order to display reciprocal space information for the sample features illuminated by the electron beam [119]. Electron diffraction is a consequence of the de Broglie wave-particle duality which allows detection of structural periodicity within a sample akin to x-ray diffraction. Due to the 2-D detector within the TEM, spot and ring patterns can be detected allowing single and polycrystalline sample to be analysed and distinguished.

ED patterns can be indexed once the real distances in the diffraction image (R) are converted to d-spacing (d_{hkl}) using:

$$d_{hkl} = \frac{L\lambda}{R} \tag{2.21}$$

where L is the camera length and λ is the electron wavelength calculated from:

$$\lambda = \frac{h}{\sqrt{2meV\left(1+\frac{eV}{2mc^2}\right)}} \tag{2.22}$$

where h is Plank's constant, m and e are the electron mass and charge respectively, V is the accelerating voltage, and c is the speed of light in a vacuum.

A polycrystalline Al calibration standard was used to correctly calculate detected ED patterns at Curtin University.

2.5 SCANNING ELECTRON MICROSCOPY (SEM)

Scanning electron microscopy (SEM) was conducted on a Philips XL-30 at Curtin University of Technology using secondary as well as backscattered electron detectors. The microscope was coupled with an Oxford Instruments energy dispersive x-ray spectrometer (EDS) for elemental analysis. Samples were briefly (< 1 – 2 min) exposed to air and then coated with gold prior to imaging in the SEM.

2.6 SIEVERTS APPARATUS

A Sieverts de/hydriding apparatus allows for the study of absorption and desorption kinetics as well as the determination of pressure composition (P-C) isotherms of hydrogen storage materials depending on the technique used. There are three types of hydrogen sorption apparatus that are routinely used to experimentally determine the quantity of absorbed or desorbed hydrogen from a sample [120-121]:

1. Thermogravimetric techniques, where the sample mass change is measured using a microbalance.

2. Manometric techniques, where the hydrogen pressure variation in the reaction chamber of known volume is measured.

3. Temperature programmed desorption techniques, where the quantity of hydrogen is determined by desorption measurements with a thermal ramp.

The manometric technique has been reported to be more accurate due to the measurement of large pressure variations rather than small mass variations [120] however different techniques can be more appropriate depending on the type of sample being analysed [121].

Hydrogen absorption and desorption measurements were undertaken using a custom made manometric (Sieverts) apparatus as shown in Figure 2-17. A Sieverts apparatus operates by inputting hydrogen into a known reference volume and measuring the pressure and temperature of the gas to determine the number of moles of hydrogen in the system. The hydrogen is then allowed to enter the known sample side volume (which also contains the sample of interest) by opening a valve. By monitoring pressure and temperature, a change in the number of moles of hydrogen in the system can be calculated and hence the amount of hydrogen in the sample can be determined.

The Sieverts apparatus in Figure 2-17 is constructed from 316 stainless steel components (Swagelok, Australia) with the exception of the calibration volume which is 304L stainless steel. All components consist of VCR face sealing fixtures (except for the calibration volume that is sealed using NPT fittings) that are sealed by

compression against silver coated stainless steel washers. VCR components have very low leak rates, which is essential for a manometric apparatus, they also allow for only a very minor internal volume change if parts are removed and reassembled. Diaphragm valves are used that also have very low internal leak rates. A 0.5 μm stainless steel filter is used at the top of the sample cell to prevent sample contamination of the main apparatus.

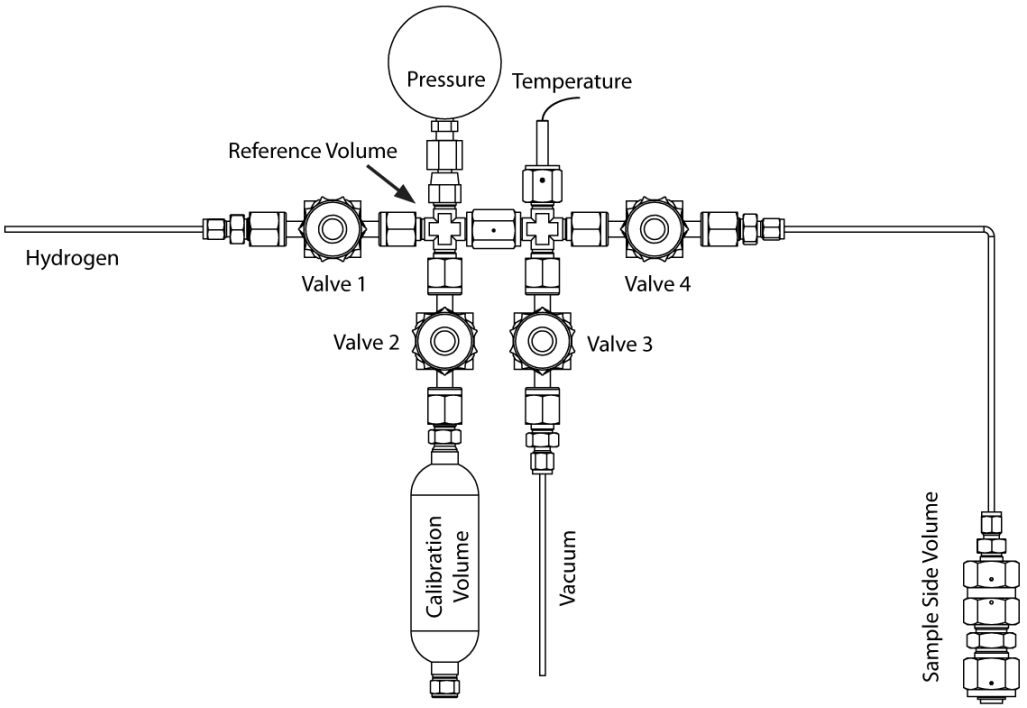

Figure 2-17: Custom made manual Sieverts apparatus at Curtin University.

The pressure gauge used (model 3051S_T Ultra (Rosemount, Emerson Process Management, Australia)) has extremely high precision over its calibrated range (0.01% of the pressure range) with an accuracy of 0.02% of the pressure range. The pressure gauge used operates using "gauge pressure", which is relative to atmospheric pressure so an atmospheric pressure reading is also recorded using a Baromec M1975 barometer (Mechanism Ltd., England).

Temperature is measured with a K-type thermocouple (Hinco Instruments, Australia) that penetrates deep within the reference volume in order to determine the ambient gas temperature. High sample temperatures were achieved by using a Labec tube furnace (Laboratory Equipment P/L, Australia) that is rated to 1200 ºC and was

temperature calibrated using a K-type thermocouple at a set sample depth. Cryogenic temperature (77 K) is achieved by submerging the sample cell into a bath of liquid nitrogen at a set depth during measurements.

2.6.1 Compressibility

The compressibility of hydrogen is a very important parameter when the number of moles of hydrogen is calculated from pressure and temperature measurements. The number of moles of hydrogen is calculated from:

$$n = \frac{PV}{ZRT} \tag{2.23}$$

where P is the pressure of hydrogen gas, T is the temperature, V is the volume that the hydrogen occupies, R = 83.14472 bar cm^3 K^{-1} mol^{-1} (R = 8.314472 J K^{-1} mol^{-1} in S.I. units) is the gas constant, and Z is given by:

$$Z = \frac{V_m}{V_i} \tag{2.24}$$

where V_i is the molar volume of H_2 calculated from the ideal gas law as follows:

$$V_i = \frac{RT}{P} \tag{2.25}$$

and where V_m is the molar volume of H_2 which for temperatures > 100 K is calculated from an equation of state (EOS) for hydrogen developed by Hemmes, Driessen & Griessen [122] and given by McLennan & Gray [123] as:

$$\left(p + \frac{a(p)}{V_m^{\alpha(T)}} \right)\left(V_m - b(p)\right) = RT \tag{2.26}$$

where

$$a(p) = \exp\left[a_1 + a_2 \ln(p) - \exp\left(a_3 + a_4 \ln(p)\right)\right] \tag{2.27}$$

$$b(p) = \begin{cases} \sum_{i=0}^{8} b_i \ln(p)^i & (p \geq 100\,\text{bar}) \\ b(100\,\text{bar}) & (p < 100\,\text{bar}) \end{cases} \tag{2.28}$$

$$\alpha(T) = \begin{cases} \alpha_0 + \alpha_1 T + \alpha_2 T^2 & (T \le 300\,\mathrm{K}) \\ \alpha(300\,\mathrm{K}) & (T > 300\,\mathrm{K}) \end{cases} \tag{2.29}$$

where $p > 1$ bar (1 bar = 0.1 MPa), T is the temperature, and the coefficients are given in Table 2-6.

Table 2-6: Coefficients for equations (2.26) - (2.29) for pressure in bar, molar volume in cm^3 mol^{-1} and temperature in Kelvin.

α_0	2.9315	b_5	-0.12385414
α_1	-1.531×10^{-3}	b_6	9.8570583×10^{-3}
α_2	4.154×10^{-6}	b_7	$-4.1153723 \times 10^{-4}$
b_0	20.285	b_8	7.02499×10^{-6}
b_1	-7.44171	a_1	19.599
b_2	7.318565	a_2	-0.8946
b_3	-3.463717	a_3	-18.608
b_4	0.87372903	a_4	2.6013

The EOS given by Equation 2.26 must be solved numerically to determine the molar volume of hydrogen (see Appendix A). A comparison between the molar volumes given by the EOS and ideal gas law can be seen in Figure 2-18 at 298.15 K and in Figure 2-19 as a function of temperature.

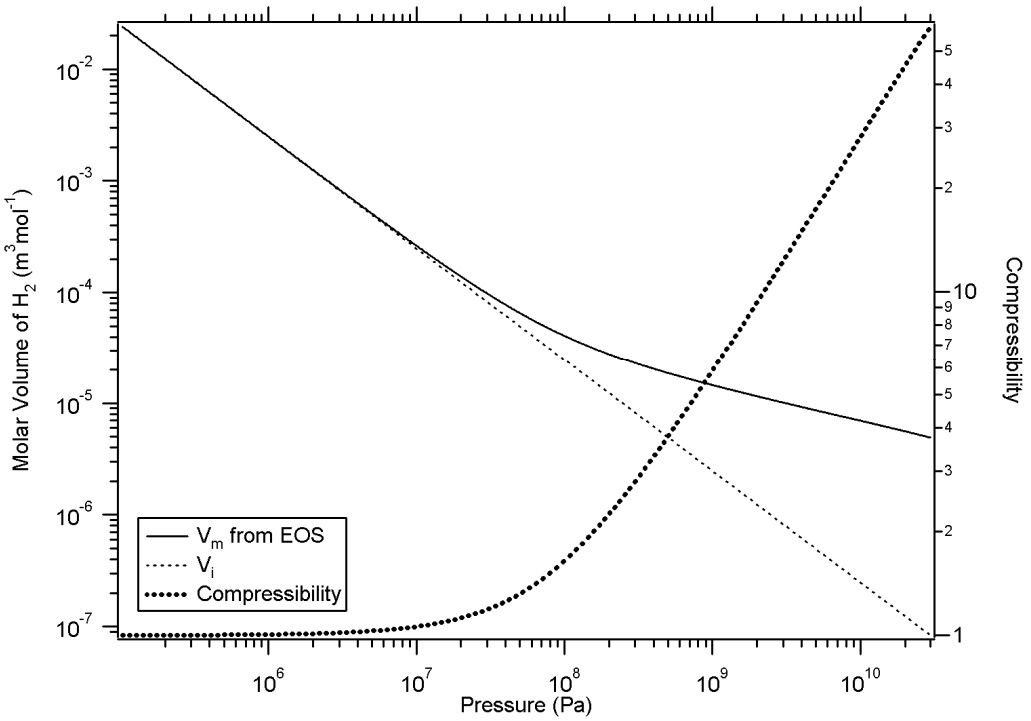

Figure 2-18: The molar volume of hydrogen at 298.15 K over a variety of pressures. The molar volume has been calculated according to the equation of state (EOS) (V_m) as given by Hemmes, Driessen & Griessen [122] and according to the ideal gas law (V_i). The compressibility is also shown which is the volume ratio $Z = V_m/V_i$.

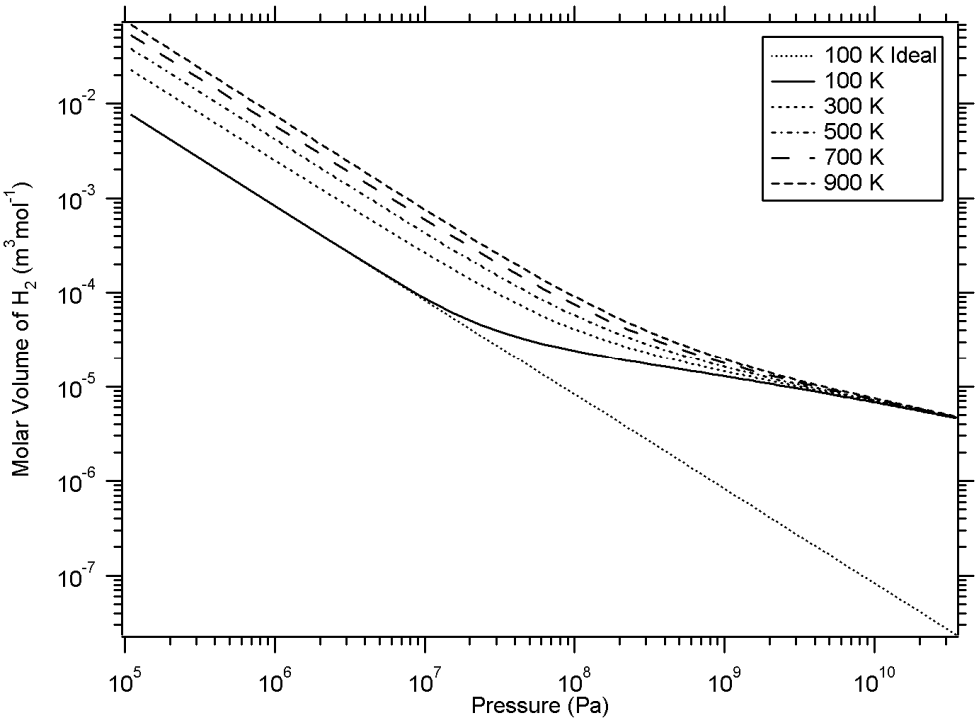

Figure 2-19: The molar volume of hydrogen at typical temperatures, numerically calculated from the equation of state (EOS) given by Hemmes, Driessen & Griessen [122]. The molar volume as calculated from the ideal gas law at 100 K is also shown for comparison.

A different equation of state (EOS) for hydrogen must be used for hydrogen measurements taken below 100 K that more accurately models the compressibility of hydrogen at these low temperatures. A comparison of the compressibility for different EOS is shown in Figure 2-20. The Hemmes EOS [122] is not valid at 77 K, but is shown for comparison as is the ideal gas law which has no compressibility. The two models that are valid at 77 K are the McCarty EOS [124] and the EOS from NIST Standard Reference Database Number 69 [125]. The NIST EOS is preferred because it has been updated recently and provides accurate compressibilities which can be verified by doing pressure measurements at 77 K with known volumes.

The NIST EOS data [125] at 77 K can be fit by a polynomial that relates the pressure to the compressibility as follows:

For P = 1 to 140 bar

$$\begin{aligned} Z = {} & 1 - 0.0017359P + 1.4459\times10^{-5}P^2 - 6.8988\times10^{-8}P^3 \\ & + 5.5334\times10^{-9}P^4 - 1.1555\times10^{-10}P^5 + 1.3545\times10^{-12}P^6 \\ & - 9.7473\times10^{-15}P^7 + 3.9175\times10^{-17}P^8 - 6.6383\times10^{-20}P^9 \end{aligned} \qquad (2.30)$$

For P = 140 to 5000 bar

$$Z = 0.68302 + 0.0028112P + 9.6708\times10^{-7}P^2 - 2.0147\times10^{-9}P^3 + 1.6679\times10^{-12}P^4 - 7.9345\times10^{-16}P^5 + 2.2979\times10^{-19}P^6 - 3.9964\times10^{-23}P^7 + 3.8367\times10^{-27}P^8 - 1.5627\times10^{-31}P^9 \quad (2.31)$$

where Z is the compressibility of hydrogen gas at 77 K and P is the hydrogen pressure in bar.

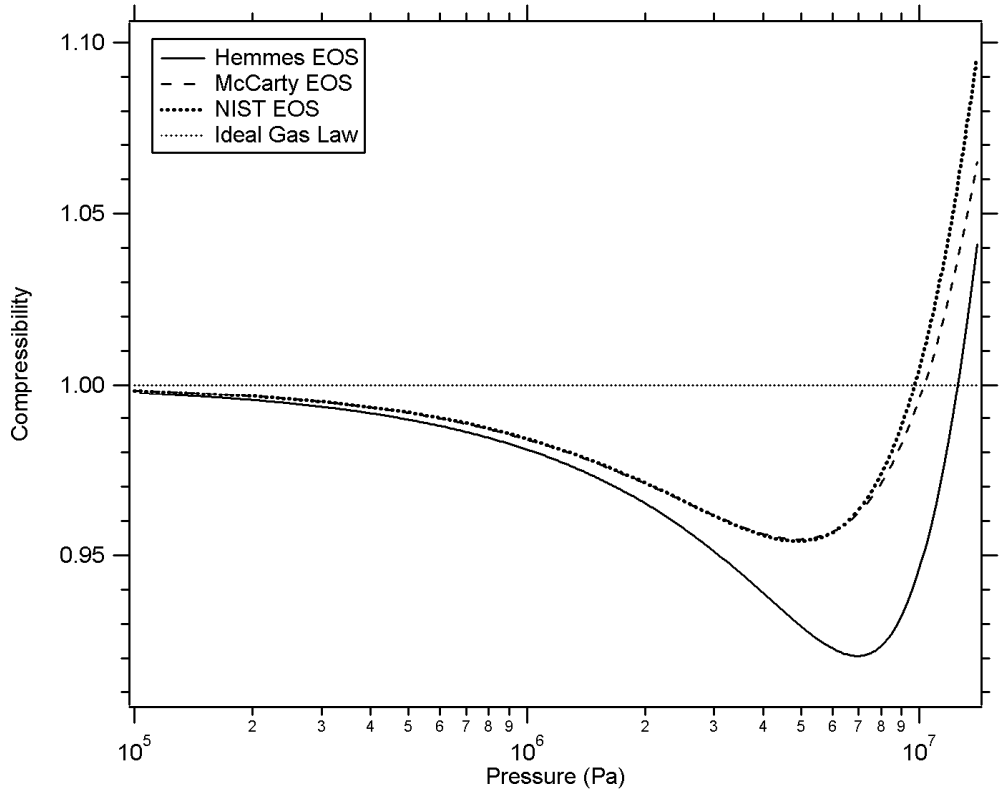

Figure 2-20: Comparison of equation of state (EOS) models for hydrogen at 77 K. The EOS shown include the Hemmes EOS [122-123] (which is not experimentally determined for 77 K), the McCarty EOS [124], the EOS from the NIST database [125] and the zero compressibility of the ideal gas law is shown for comparison.

2.6.2 Volume Calibrations

Volume calibrations were undertaken by allowing hydrogen gas to enter two separate volumes within the manometric apparatus where one of these volumes is known. Pressure and temperature readings are taken which allow the unknown volume to be calculated. A calibration volume (see Figure 2-17) was used for an initial known volume. The calibration volume was calibrated ex-situ by filling liquid ethanol up to

Valve 2 which was then closed. The calibration volume is then determined by measuring the mass of ethanol within the volume and given the density of ethanol [80,126] at the measured temperature the volume that the ethanol displaces can be calculated.

All volume calibration formulae are determined from a first principles approach by assuming that the number of moles of hydrogen is constant within the system, and when a valve is opened it is only the change in the volume of the system that causes a change in the pressure of the gas. The volume calibrations are undertaken at least 5 times in order to obtain statistically significant numbers.

2.6.2.1 *Reference Volume Calibration*

The reference volume is calibrated from the known calibration volume using the following procedure (with reference to Figure 2-17):

1. The system is evacuated by opening Valves 2 & 3 for about 15 minutes.
2. Valves 2 & 3 are closed and Valve 1 is opened then closed to bring the reference volume (V_r) to a known pressure (P_r) and temperature (T_r).
3. Valve 2 is opened and then closed after waiting for a long period (~1 hr) for adiabatic effects to settle to bring the whole system, V_r and the calibration volume (V_c), to a known pressure (P_e) and temperature (T_e).
4. The reference volume is calculated by:

$$V_r = V_c \frac{\dfrac{P_e}{Z_e T_e}}{\dfrac{P_r}{Z_r T_r} - \dfrac{P_e}{Z_e T_e}} \tag{2.32}$$

where V_r is the unknown reference volume, V_c is the known calibration volume, P_r is the initial reference pressure, T_r is the initial reference temperature, Z_r is the compressibility associated with the initial reference measurements, P_e is the final equilibrium pressure, T_e is the final equilibrium temperature, and Z_e is the compressibility associated with the final equilibrium measurements.

2.6.2.2 *Ambient Sample Side Volume Calibration*

The ambient sample side volume is calibrated from the known reference volume using the following procedure (with reference to Figure 2-17):

1. The system is evacuated by opening Valves 3 & 4 for about 15 minutes.

2. Valves 3 & 4 are closed and Valve 1 is opened then closed to bring the reference volume (V_r) to a known pressure (P_r) and temperature (T_r).

3. Valve 4 is opened and then closed after waiting for a long period (~30 min) for adiabatic effects to settle to bring the whole system, V_r and the sample side volume (V_s), to a known pressure (P_e) and temperature (T_e).

4. The ambient sample side volume is calculated by:

$$V_s = V_r \frac{\frac{P_r}{Z_r T_r} - \frac{P_e}{Z_e T_e}}{\frac{P_e}{Z_e T_e}} \tag{2.33}$$

where V_s is the unknown ambient sample side volume, V_r is the known reference volume, P_r is the initial reference pressure, T_r is the initial reference temperature, Z_r is the compressibility associated with the initial reference measurements, P_e is the final equilibrium pressure, T_e is the final equilibrium temperature, and Z_e is the compressibility associated with the final equilibrium measurements.

2.6.2.3 *Non-Ambient Sample Side Volume Calibration*

A non-ambient sample side volume accounts for a proportion of the sample side volume being at a different temperature than the rest of the sample side volume, i.e. when the sample cell is in a furnace or liquid nitrogen. The non-ambient sample side volume is calibrated from the known reference volume and the known sample side volume using the following procedure (with reference to Figure 2-17):

1. The non-ambient sample cell volume is brought up to temperature and let to reach equilibrium for at least 30 minutes.

2. The system is evacuated by opening Valves 3 & 4 for about 15 minutes.

3. Valves 3 & 4 are closed and Valve 1 is opened then closed to bring the reference volume (V_r) to a known pressure (P_r) and temperature (T_r).

4. Valve 4 is opened and then closed after waiting for a long period (~30 min) for adiabatic effects to settle to bring the whole system, V_r and the sample side volume (V_s) containing the non-ambient sample side volume (V_{na}), to a known pressure (P_e), ambient temperature (T_e), and non-ambient temperature (T_{ena}).

5. The non-ambient sample side volume is calculated by:

$$V_{na} = \frac{V_r\left(\frac{P_r}{Z_r T_r} - \frac{P_e}{Z_e T_e}\right) - V_s\left(\frac{P_e}{Z_e T_e}\right)}{\frac{P_e}{Z_{ena} T_{ena}} - \frac{P_e}{Z_e T_e}} \tag{2.34}$$

where V_{na} is the unknown non-ambient sample side volume, V_s is the known ambient sample side volume, V_r is the known reference volume, P_r is the initial reference pressure, T_r is the initial reference temperature, Z_r is the compressibility associated with the initial reference measurements, P_e is the final equilibrium pressure, T_e is the final equilibrium ambient temperature, Z_e is the compressibility associated with the final ambient equilibrium measurements, T_{ena} is the final equilibrium non-ambient temperature, and Z_{ena} is the compressibility associated with the final non-ambient equilibrium measurements.

2.6.3 Hydrogen Sorption Measurements

Hydrogen sorption measurements are made by firstly sealing a sample (of known mass and density) within the sample side of the apparatus within an argon glovebox. The sample side is then reattached to the manometric apparatus and the following procedures are performed.

Hydrogen absorption is performed using the following procedure:

1. The system is evacuated by opening Valves 3 & 4 for about 1 hour. This can be performed at temperature to allow any adsorbed gases to escape. Valves 3 & 4 are then closed.

2. Valve 1 is slowly opened and then closed to bring the reference volume (V_r) to the desired pressure (P_r) at a given temperature (T_r) which is recorded after adiabatic effects have dissipated.

3. Valve 4 is then slowly opened to minimise adiabatic effects and once equilibrium has been reached between the hydrogen gas and the sample (i.e. no change in pressure) Valve 4 is slowly closed and the final pressure (P_e) and final temperature (T_e) are recorded.

4. Steps 2 & 3 are then repeated until no absorption takes place and the sample has reached its maximum hydrogen content for a given pressure and temperature. The values of P_e and T_e become the initial sample side pressure (P_s) and initial sample side temperature (T_s) respectively.

Hydrogen desorption is performed using the following procedure:

1. The system is evacuated by opening Valves 3 & 4 for a given time depending on the sample so as not to desorb the sample significantly. This process removes any other gases present in the system. Valves 3 & 4 are then closed.

2. The reference volume is evacuated by opening Valve 3 and then closing it after about 15 minutes. The initial pressure (P_r) in the reference volume (V_r) is zero and is recorded.

3. Valve 4 is then opened and once equilibrium has been reached between the sample and the hydrogen gas (i.e. no change in pressure) Valve 4 is slowly closed and the final pressure (P_e) and final temperature (T_e) are recorded.

4. Steps 2 & 3 are then repeated until no desorption takes place and the sample has released its maximum hydrogen content. The values of P_e and T_e become the initial sample side pressure (P_s) and initial sample side temperature (T_s) respectively.

2.6.3.1 *Ambient Sorption*

The change in the number of moles of hydrogen within the manometric apparatus due to a sample during hydrogen sorption measurements at ambient temperature can be calculated by the following:

$$n_{ads} = n_r + n_s - n_e \tag{2.35}$$

where n_r is the number of moles of hydrogen in the reference volume initially, n_s is the number of moles of hydrogen in the sample side volume initially, and n_e is the final number of moles of hydrogen in the total system after equilibrium. The numbers of moles of hydrogen are given by the following equations:

$$n_r = \frac{P_r V_r}{Z_r R T_r} \tag{2.36}$$

where V_r is the reference volume, P_r is the initial reference pressure, T_r is the initial reference temperature, Z_r is the compressibility associated with the initial reference measurements, and R is the gas constant (8.314472 J K^{-1} mol^{-1}).

$$n_s = \frac{P_s\left(V_s - V_{sample}\right)}{Z_s R T_s} \tag{2.37}$$

where V_s is the sample side volume, P_s is the initial sample side pressure, T_s is the initial sample side temperature, Z_s is the compressibility associated with the initial sample side measurements, and V_{sample} is the volume that the sample displaces within the sample side volume which can be calculated from its mass and density.

$$n_e = \frac{P_e\left(V_r + V_s - V_{sample}\right)}{Z_e R T_e} \tag{2.38}$$

where P_e is the final equilibrium pressure, T_e is the final equilibrium temperature, and Z_e is the compressibility associated with the final equilibrium measurements.

2.6.3.2 *Non-Ambient Sorption*

The change in the number of moles of hydrogen within the manometric apparatus due to a sample during hydrogen sorption measurements at non-ambient temperature can be calculated by the following:

$$n_{ads} = n_r + n_s - n_e \tag{2.39}$$

where n_r is the number of moles of hydrogen in the reference volume initially, n_s is the number of moles of hydrogen in the sample side volume initially, and n_e is the

final number of moles of hydrogen in the total system after equilibrium. The numbers of moles of hydrogen are given by the following equations:

$$n_r = \frac{P_r V_r}{Z_r R T_r} \tag{2.40}$$

where V_r is the reference volume, P_r is the initial reference pressure, T_r is the initial reference temperature, Z_r is the compressibility associated with the initial reference measurements, and R is the gas constant (8.314472 J K^{-1} mol^{-1}).

$$n_s = \frac{P_s\left(V_s - V_{na}\right)}{Z_s R T_s} + \frac{P_s\left(V_{na} - V_{sample}\right)}{Z_{na} R T_{na}} \tag{2.41}$$

where V_s is the sample side volume, P_s is the initial sample side pressure, T_s is the initial sample side ambient temperature, Z_s is the compressibility associated with the initial sample side ambient measurements, V_{sample} is the volume that the sample displaces within the sample side volume which can be calculated from its mass and density, V_{na} is the non-ambient sample side volume, T_{na} is the non-ambient sample side temperature, and Z_{na} is the compressibility associated with the initial sample side non-ambient measurements.

$$n_e = \frac{P_e V_r}{Z_e R T_e} + \frac{P_e\left(V_s - V_{na}\right)}{Z_e R T_e} + \frac{P_e\left(V_{na} - V_{sample}\right)}{Z_{ena} R T_{na}} \tag{2.42}$$

where P_e is the final equilibrium pressure, T_e is the final equilibrium ambient temperature, Z_e is the compressibility associated with the final equilibrium ambient measurements, and Z_{ena} is the compressibility associated with the final equilibrium non-ambient measurements.

2.6.4 Uncertainty

A number of system parameters determine the accuracy of a Sieverts hydrogen sorption apparatus and insufficient consideration of these parameters can lead to significant sources of measurement error [121]: Calibration, temperature monitoring, sample thermal effects, the approach to equilibrium, sample size, gas purity, system volume to sample size ratio, sample degassing, sample history, pressure

measurement, the compressibility of hydrogen, thermal transpiration effects, accumulative errors, and leaks.

The uncertainty in the number of moles measured in a carefully selected Sieverts system is less than 1 % and a detailed analysis is provided by Sheppard [127]. The sensitivity of the Sieverts apparatus can be calculated [128] which is a function of the volumes in the apparatus and the sample itself. Large errors in measurement are especially likely at low temperatures (i.e. 77 K) due to the high density of hydrogen at these temperatures which can seriously affect molar hydrogen calculations if the sample density is not known with high accuracy.

2.6.5 Automated Sieverts Apparatus

A computer controlled volumetric hydrogen apparatus was constructed for the purpose of providing a user-configurable system for automatically operating the apparatus and providing large quantities of data and live measurements. Similar automatic Sieverts apparatus have been built before [120] which are also able to measure both kinetics and pressure-composition data.

2.6.5.1 *Hardware*

The automated Sieverts apparatus was built using the same principles and components as a manual apparatus, but with computer controlled pneumatic valves and computer inputs for pressure and temperature as shown in Figure 2-21. Computer control was made possible through use of a USB-6009 data acquisition device (National Instruments, Austin, USA) that interfaces with a PC via USB and provides analogue and digital inputs/outputs.

Pneumatic valves (Swagelok, Australia) are a normally-closed type and were connected to a 7 bar nitrogen line to provide valve opening pressure that was controlled by four electrically operated pneumatic actuators (Norgren, Australia). The USB-6009 data acquisition device was used to operate the pneumatic actuators via four 5 V digital outputs that were passed through a custom built current amplifier and used to activate four 24 V relays which opened and closed the actuators providing opening pressure to the valves.

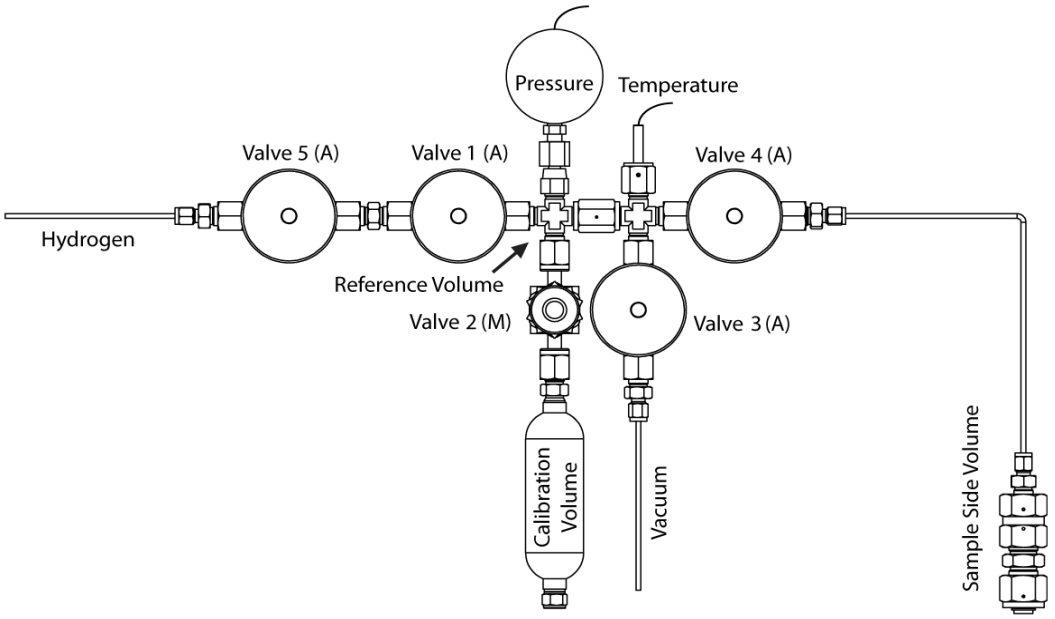

Figure 2-21: Custom made automated Sieverts apparatus at Curtin University.

A fifth valve was used in the automated apparatus (Valve 5 in Figure 2-21) that was used to moderate the input hydrogen pressure into the reference volume. Control over the hydrogen pressure in the reference volume on a manual apparatus is made possible with precise manual control of the hydrogen input valve (Valve 1 in Figure 2-17). The pneumatic valves on the automated apparatus are either fully open or fully closed and so the small volume between Valve 5 and Valve 1 in Figure 2-21 allows for some control over the hydrogen input pressure into the reference volume, which is related to the pressure differential between valve-separated volumes.

The pressure gauge (model 3051S_T Ultra, Rosemount, Emerson Process Management, Australia) provided absolute pressure readings that were digitally displayed on the gauge face. The pressure gauge has a high precision linear relationship between the absolute pressure measurements and the gauge's 4 – 20 mA current draw. The pressure gauge power cable was interfaced to an analogue input on the USB-6009 data acquisition device with a high stability resistor with a very low temperature coefficient (< ± 5 ppm/ºC). The resistor provided a voltage range that was linearly correlated with the gauge's pressure range. The voltage was calibrated over the entire pressure range (0 – 140 bar) by recording multiple voltage-pressure readings.

Ambient temperature measurements were undertaken with a custom built four-wire platinum resistance temperature detector (RTD) (Hinco Instruments, Australia) that was interfaced with a USC701-2001 universal signal conditioner (Analog Process Control Services A.P.C.S, Australia) that outputs a voltage signal to an analogue input on the USB-6009 data acquisition device. A linear voltage-temperature relationship existed that was calibrated against multiple data points from 0 – 100 ºC.

2.6.5.2 *Software*

The software was programmed using Labview 8.2.1 (National Instruments, USA) which provides a graphical programming environment. The programming environment does not allow lines of code but instead allows the user to construct blocks of code that are wired together to form a program. Unfortunately this type of program is almost impossible to print on paper due to the complexity of the code display. Therefore code schematics are provided in Appendix C that detail the inner workings of the software program that was designed to automate hydrogen measurements.

The software has been designed to provide live pressure and temperature readouts and allow for user defined computer-operated control of all pneumatic valves. Automated volume calibrations and hydrogen sorption runs are also possible with user-defined run conditions provided in the user interface or in a configuration file given in Appendix C.

The software automates reference volume calibrations (with manual prompts), ambient sample volume calibrations and non-ambient sample volume calibrations. Volume calibrations are undertaken five or more times under different pressure conditions in order to provide statistically significant volume measurements. Data is recorded to an output file which provides all of the necessary details of the calibration cycles including the average volume and its standard deviation.

The software was also designed to allow for customised hydrogen absorption and desorption runs, which are able to provide both kinetic and pressure-composition measurements. This is made possible by providing the user with a list of options regarding the type of sorption run they wish to perform.

Data is recorded to an output file that provides the initial run condition parameters used: date, time, absorption or desorption, sample notes, reference volume, ambient sample volume, non-ambient sample volume, internal valve volume, whether the conditions were non-ambient, non-ambient sample temperature, sample mass, and sample density. Data is output at user-defined intervals at which time the following data is recorded to the output file: Pressure, temperature, and compressibility measurements for the sample-side, reference and final (total rig) volumes. Data is also recorded at the user-defined intervals for the number of moles of hydrogen absorbed, the weight % of hydrogen in the sample, and the time interval from the run start time. Live outputs are also displayed on-screen for the current weight % absorbed at each user-defined output time, and a live pressure-composition (P-C) plot is also displayed.

Chapter 3

Aluminium Nanoparticles

"Research is the process of going up alleys to see if they are blind" - Marston Bates

3.1 BACKGROUND

Aluminium (Al) is the most abundant metal in the Earth's crust and the third most abundant element, but it is not found in its pure form in nature because of its extreme affinity for oxygen [129]. Pure Al only has one structural phase, face centred cubic (FCC), despite some confusion in the literature that is likely related to different phases being identified due to sample impurities [130]. Aluminium can be used as a hydrogen storage compound in the form of alane (AlH_3). Alane is a promising hydrogen storage compound due to its very high hydrogen storage capacity (10.1 weight %), low hydrogen desorption temperature, fast desorption kinetics, and the widespread availability of aluminium. The major problem related to using aluminium as a hydrogen storage material is the extremely high (~2.5 GPa) pressure required for the absorption of H_2 into bulk aluminium metal [4-5], a consequence of its unstable formation enthalpy of -11.4 kJ/mol [131]. Alane is discussed in detail in Chapter 4.

The hydrogen absorption properties of Al nanoparticles are not well known, and the mechanochemical synthesis of Al nanoparticles is promising in order to analyse the behaviour of hydrogen at moderate pressures with unoxidised aluminium nanoparticles. It is expected that the small particle size and clean nanoparticle surface would allow hydrogen to absorb into aluminium under more reasonable hydrogen pressures, compared to the very large ~150 μm Al powder used in previous studies [4], that was most likely oxidised. Small nanoparticles are expected to alter both the thermodynamics and kinetics of the aluminium-hydrogen system. Significant thermodynamic changes are theoretically predicted for aluminium nanoparticles smaller than 5 nm in comparison to the bulk [44] however these thermodynamic changes have not yet been experimentally demonstrated and it is not yet known with certainty if these changes extend to larger aluminium nanoparticles.

Aluminium nanoparticles are also of interest to a variety of fields including pyrotechnic, propellant and explosive industries. Aluminium powder has been added to a variety of these compositions in order to increase their performance through raising reaction energies, flame temperatures and increasing blast rates [132-133]. Nanoparticles of aluminium are more favourable because of their high enthalpy of combustion [134] and rapid kinetics [132] that increase these reaction properties even further.

3.1.1 Synthesis

In the 1880's aluminium was a semi-precious metal that was commercially synthesised on a small scale by the reduction of aluminium chloride ($AlCl_3$) with sodium metal [135]. Today aluminium is generally produced by a process that begins with the mining of bauxite ore which is then refined into alumina (Al_2O_3) using the Bayer process [136]. Alumina is then electrolytically reduced to aluminium metal using the Hall-Heroult process which proceeds as follows [136]:

$$2Al_2O_3 + 3C \longleftrightarrow 4Al + 3CO_2 \qquad \Delta_r G_{298K} = +991 \text{ kJ/mol} \qquad (3.1)$$

Unfortunately the process generates significant volumes of CO_2 that has a detrimental environmental impact. In addition, a large quantity of electricity is required to reduce Al_2O_3 due to the very high positive ΔG. However, aluminium is produced in great amounts around the world (33.9 million tonnes in 2006 [2]) and it is utilised in numerous industries due to its low cost, high abundance, and useful properties.

3.1.1.1 *Nanoparticles*

A number of methods have been utilised in the literature to synthesise aluminium nanoparticles as outlined in Section 1.4.3. A mechanochemical synthesis method was chosen for Al nanoparticle synthesis due to the method's versatility and simplicity. The use of different synthesis conditions allows particle size to be controlled, allowing hydrogen sorption studies to be undertaken on Al with a variety of particle sizes. The aluminium nanoparticles are also synthesised in a pure form (embedded in a salt by-product phase) without any oxide contamination that would restrict hydrogen absorption.

3.1.2 Oxide Layers

The presence of an oxide layer (Al_2O_3) on aluminium nanoparticles is a significant problem if it is used as a hydrogen storage material. It has been suggested [137] that aluminium oxide (alumina) can be used as a coating for hydrogen tanks in order to reduce the permeation of hydrogen through the tank walls because the permeation rate in alumina is much less than in metals. Aluminium oxide surface layers can be detrimental to molecular [138] and even atomic [139] hydrogen permeation. Low oxide

content is also beneficial for the pyrotechnic, propellant and explosive industries where aluminium nanoparticles with thinner oxide layers are associated with higher reactivities [133]. Significant oxidation has been evidenced [140] when aluminium nanoparticles are heated above their melting point (940 K) in air, causing combustion to occur.

The reaction between elemental aluminium and oxygen is extremely exothermic:

$$2\mathrm{Al} + \frac{3}{2}\mathrm{O_2} \longrightarrow \alpha\text{-}\mathrm{Al_2O_3} \qquad \Delta_r G_{298K} = -1582 \text{ kJ/mol} \qquad (3.2)$$

The reaction with water (that is also present in air) is less reactive but still significant:

$$2\mathrm{Al} + 3\mathrm{H_2O(g)} \longrightarrow \alpha\text{-}\mathrm{Al_2O_3} + \mathrm{H_2(g)} \qquad \Delta_r G_{298K} = -897 \text{ kJ/mol} \qquad (3.3)$$

Different phases of aluminium oxide can be formed during oxidation however it has been shown theoretically [141] and experimentally [142] that it is thermodynamically favourable for an amorphous aluminium oxide layer to be formed.

3.1.2.1 *Surface Passivation*

One solution to eliminating the formation of an oxide coating is coating the nanoparticles with some other material that may be more permeable to hydrogen but not oxygen. Aluminium particles have been coated by a number of materials in order to prevent oxidation during storage or handling. The coatings have been applied by: carbon deposition [143], stearic acid aluminium diboride deposition [144], polyvinylidene fluoride deposition by supercritical fluid carbon dioxide [145], polystyrene polymerisation [146], and high density polyethylene using a modified Ziegler-Natta process [147]. Chemical synthesis techniques have also been used [148] in the construction of aluminium nanorods (diameter ~ 20 - 300 nm) that have a hydrocarbon coating that repels oxygen and moisture. The hydrocarbon coating is removed upon heating the material to ~150 °C [148].

3.1.3 Hydrogen Interactions

Molecular hydrogen has a very low sticking probability on aluminium [25] and there is also a large barrier for hydrogen dissociation in the order of 1 eV [149]. These

properties in addition to the poor hydrogen permeation through aluminium oxide layers result in extremely detrimental conditions for hydrogen absorption into aluminium. However aluminium clusters have been identified in experimental [50] and theoretical studies [58] to allow dissociative hydrogen chemisorption with low activation energies. The activation barriers can be overcome with a modest supply of thermal energy or possibly through use of a catalyst.

The solubility of hydrogen in solid aluminium metal is very low whereby just below its melting point 6.04×10^{-5} at.% H and 0.03 at.% H dissolves at 1 bar and 1 kbar respectively [150]. It has also been shown by Paskevicius and Buckley [151] that there is a negligible change in the lattice parameter for Al ($\delta a/a_0 = 3.7 \times 10^{-7}$) upon plasma charging aluminium with hydrogen [152]. Three distinct hydrogen trapping states have been identified [153] that are associated with interstitial lattice sites, dislocations, and vacancies. The types of trapping states present have an impact on the diffusivity of hydrogen in Al [153] however hydrogen diffusion is very low even in very pure aluminium with limited trapping sites.

The formation of alane (AlH_3) is discussed in detail in Chapter 4.

3.2 MECHANOCHEMICAL SYNTHESIS

A reaction between aluminium chloride and sodium metal has been used historically to synthesise bulk aluminium powder [135]. The historical reaction chemistry has been adapted where aluminium nanoparticles were synthesised mechanochemically using two reaction pathways as follows:

$$AlCl_3 + 3Na \longrightarrow Al + 3NaCl \qquad \Delta_r G_{298K} = -522 \text{ kJ/mol} \qquad (3.4)$$

$$AlCl_3 + 3Li \longrightarrow Al + 3LiCl \qquad \Delta_r G_{298K} = -522 \text{ kJ/mol} \qquad (3.5)$$

The reaction products are aluminium metal particles that are embedded within larger salt (LiCl or NaCl) clusters. The addition of a buffer material (i.e. LiCl) with the reactants allows for a medium that promotes nanoparticle formation and restricts the growth of large agglomerates of the desired aluminium phase by tempering combustion. Reactions 3.4 and 3.5 were both undertaken at room temperature to determine their viability. Reaction 3.4 was initiated with a B:P of 55:1 for 280 min using a NaCl reaction buffer (14.6:1 NaCl:Al volume ratio). Reaction 3.5 was initiated by milling with a ball to powder ratio (B:P) of 35:1 for 180 min using a LiCl buffer (9.7:1 LiCl:Al volume ratio). Both reactions proceeded to completion as verified by XRD shown in Figure 3-1.

There is a minor peak in the LiCl pathway XRD pattern (Pattern B in Figure 3-1) at 2θ = 32.9° that has been attributed to lithium chloride hydrate ($LiCl.H_2O$) which is present due to an improper seal with the mylar film during XRD as LiCl is hygroscopic. Rietveld fitting results are provided in Table 3-1 that outline phase wt.% and crystallite sizes. The aluminium synthesised using the sodium pathway has almost twice the crystallite size of that synthesised using the lithium pathway even though a higher volume ratio was used in the sodium pathway. The hardness of both lithium (0.6) and sodium (0.5) on the Mohs scale are very similar as are LiCl (1.5-2) and NaCl (2.5), so it is unlikely that the Al crystallite size difference is a result of reagent hardness. Larger aluminium crystallites are likely a result of the size of the initial reagents. The sodium metal used as an initial reagent was much larger than the lithium metal used. However both metal reagents used were bulk materials (> 1 mm pieces) which likely resulted in relatively large Al crystallites.

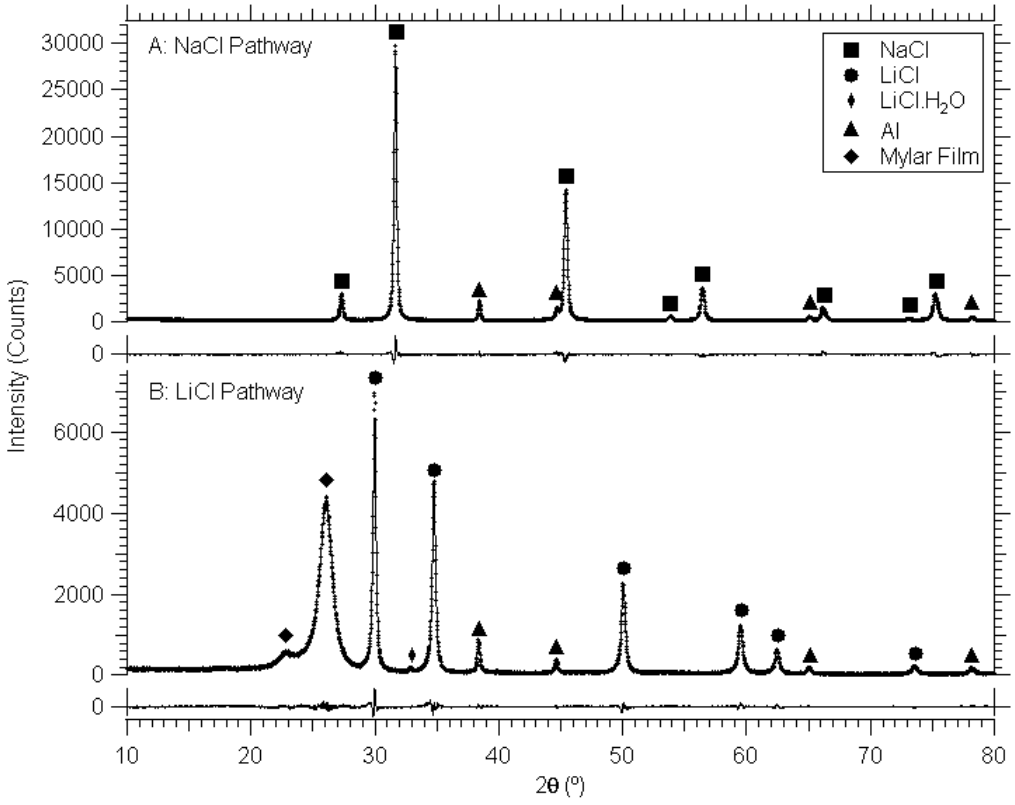

Figure 3-1: X-Ray Diffraction (XRD) patterns (D500) for mechanochemically synthesised samples that were initiated by Reactions A: 3.4 & B: 3.5. The patterns were collected after ball milling was complete and show that the reactions ran to completion. The XRD sample for Reaction A: 3.4 (NaCl) was not sealed under a mylar film as it was air stable. Rietveld fitting results and calculated difference plots are also shown.

Table 3-1: Rietveld fitting results for XRD patterns from mechanochemically synthesised Al as given in Figure 3-1. Mathematical fitting uncertainties are provided (2 standard deviations).

	Phase	Wt. %	Crystallite Size (nm)
NaCl Pathway	Al	6.0 ± 0.2	70 ± 4
	NaCl	94.0 ± 0.2	130 ± 10
LiCl Pathway	Al	8.6 ± 0.2	38 ± 4
	LiCl	90.8 ± 0.2	110 ± 20
	LiCl.H2O	0.6 ± 0.2	70 ± 60

TEM investigations were undertaken in order to provide a visual representation of the as-synthesised samples. Aluminium nanoparticles embedded within larger NaCl salt clusters are shown in the TEM micrographs in Figure 3-2. Energy dispersive spectroscopy (EDS) mapping was used to identify the small particles as aluminium which were embedded within larger chlorine rich (NaCl) clusters. The aluminium particle size (while still embedded in NaCl) was determined from direct TEM

imaging as ~ 40 - 50 nm. Much larger aggregate structures of salt and aluminium were found to dominate the sample in TEM investigations as shown in Figure 3-3.

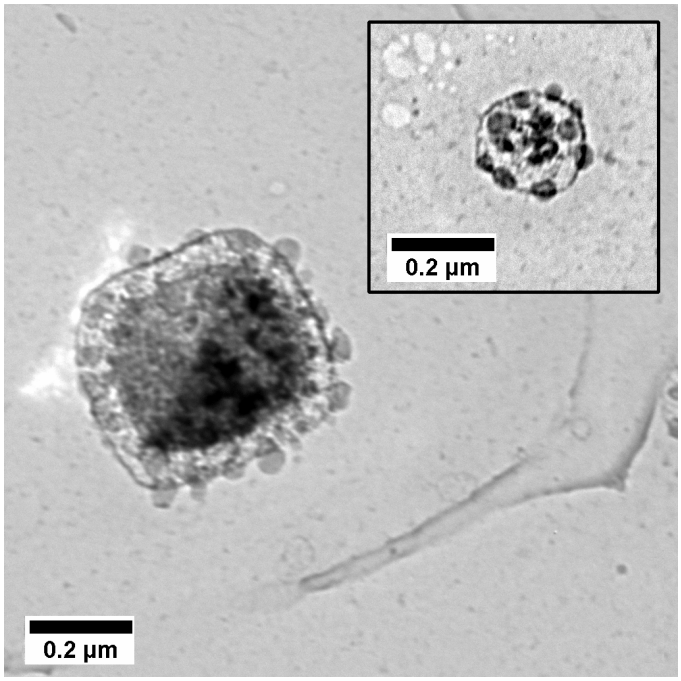

Figure 3-2: Transmission Electron Microscope (TEM) micrographs of aluminium nanoparticles (40 - 50 nm) embedded within larger (200 - 500 nm) NaCl salt clusters. Elemental mapping was used to identify the smaller particles as aluminium and the larger matrix as salt.

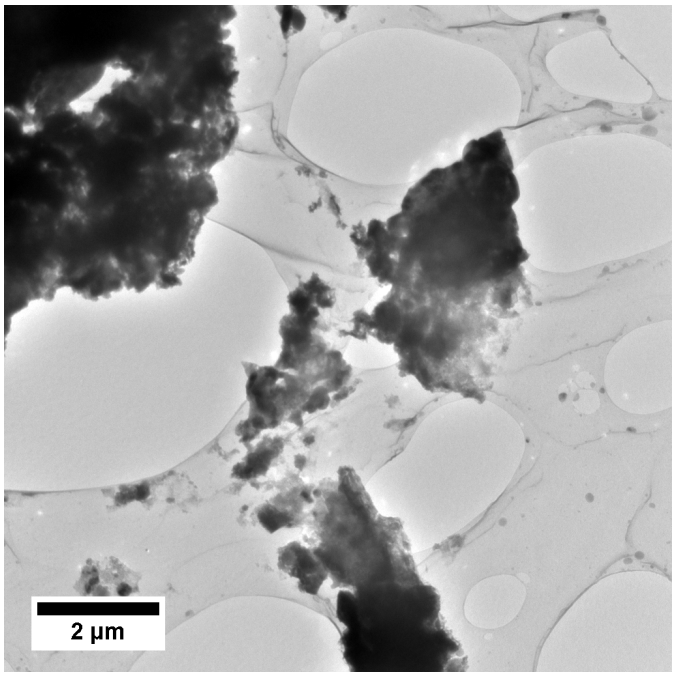

Figure 3-3: Transmission Electron Microscope (TEM) micrograph of large aggregate clusters of Al and NaCl that were prevalent within ball milled samples. A holey carbon support film is present.

3.2.1 Milling Conditions

Nanoparticle size can be tuned by altering the milling conditions during mechanochemical synthesis [66,76]. In order to understand the relationship between certain milling parameters and the as-synthesised Al crystallite size a range of samples were synthesised using room temperature ball milling under a variety of milling conditions, as outlined in Table 3-2. All samples were milled using equal numbers of 7.938 mm and 12.7 mm balls with a 1 g Al yield.

Table 3-2: Aluminium Sample Synthesis Details

Sample Name	Ball to Powder Ratio	Milling Time (hr)	LiCl Buffer (g)	Product Volume Ratio (LiCl:Al)
Al_35to1_3hr_6.8	35:1	3	0	6.8:1
Al_35to1_3hr_9.7	35:1	3	2	9.7:1
Al_35to1_3hr_12.5	35:1	3	4	12.5:1
Al_35to1_6hr_9.7	35:1	6	2	9.7:1
Al_35to1_12hr_9.7	35:1	12	2	9.7:1
Al_35to1_24hr_9.7	35:1	24	2	9.7:1
Al_70to1_3hr_9.7	70:1	3	2	9.7:1

XRD was performed on all samples (see Figure 3-4) so that the aluminium crystallite size could be determined. Unfortunately the mylar film used to seal the XRD samples from air (O_2 & H_2O) during measurement was not adequately air-tight during data collection. This resulted in a large quantity of $LiCl.H_2O$ formation from the reaction between LiCl and the moisture in the air. Fortunately the aluminium nanoparticle phase did not appear to be adversely affected by this LiCl moisture contamination, allowing crystallite sizes to be determined from Rietveld analysis of XRD data. There is noticeable Al peak offset in 2θ which is due to sample displacement variations during XRD sample packing. Although crystallite size is not equivalent to particle size, in high buffer samples the crystallite size does approach the particle size.

Rietveld analysis revealed trends in aluminium crystallite size under altered milling conditions as shown in Figure 3-5. The most significant factor controlling Al crystallite size appears to be the amount of reaction buffer (LiCl) that is used (A in Figure 3-5). A large decrease in Al crystallite size is observed for samples with larger buffers, which were all milled for the same time (3 hr).

The variation of aluminium crystallite size with milling time (B in Figure 3-5) decreases rapidly between milling times of 3 hours and 6 hours and then appears to reach an equilibrium crystallite size of ~22 nm that is maintained for milling times of 6, 12, and 24 hours. The crystallite size behaviour with increased milling time is remarkably similar to that observed for traditional ball milling of aluminium metal [41] where 40 nm Al crystallite sizes are observed for short milling times and a ~ 25 nm crystallite size plateau is observed for longer milling times. Mechanochemically synthesised aluminium however consists of discretely separated Al particles that are often single crystals due to the reaction buffer preventing particle agglomeration during milling. However it is likely that long milling times would allow previously separated Al crystallites to come into contact and agglomerate into larger particles with little change in crystallite size.

A minor decrease in Al crystallite size is also observed for a sample that was milled with a 70:1 ball to powder ratio in contrast to 35:1 (C in Figure 3-5). It is apparent from Figure 3-5 that large buffers are necessary for significant Al crystallite reduction, however increased reaction buffers result in samples that have much more salt to remove (using washing) in order to produce pure Al nanoparticles.

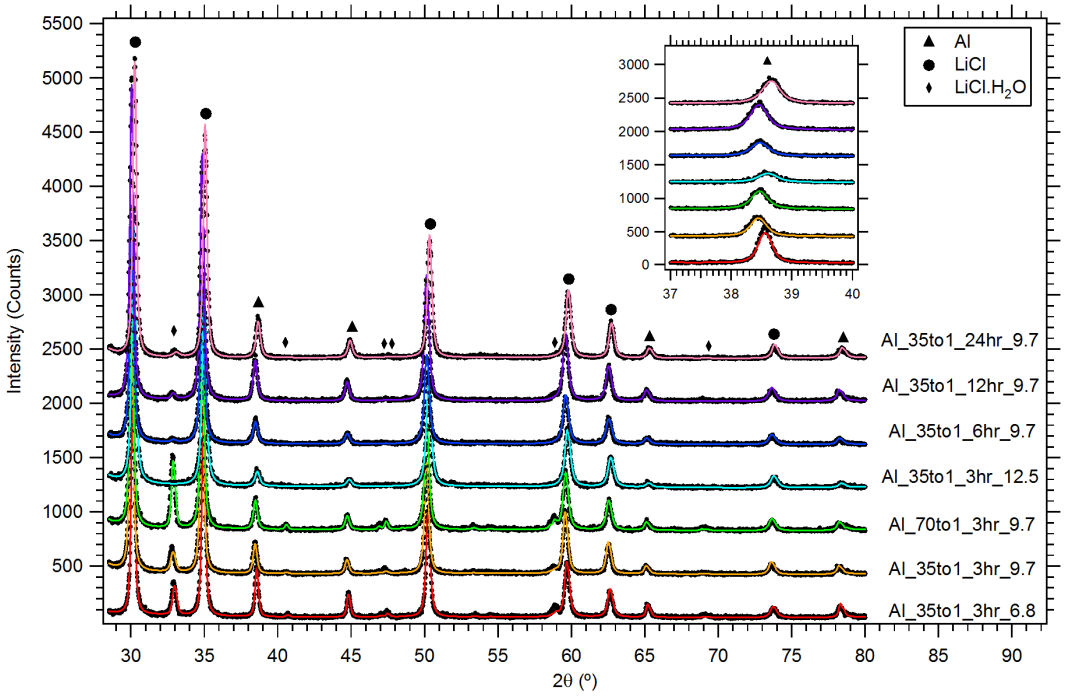

Figure 3-4: X-Ray Diffraction (XRD) patterns (D500) for mechanochemically synthesised aluminium using Reaction 3.5 with varied milling times, LiCl buffer amounts, and ball to powder (B:P) ratios. Ball milling was performed at room temperature with equal numbers of

12.7 and 7.938 mm balls. $LiCl.H_2O$ is present due to improper sealing of the mylar film which protects samples from the atmosphere during XRD measurement. Patterns are vertically offset for clarity and an inset is given of the strongest peak for aluminium for comparison. Rietveld fitting results are given by the solid lines.

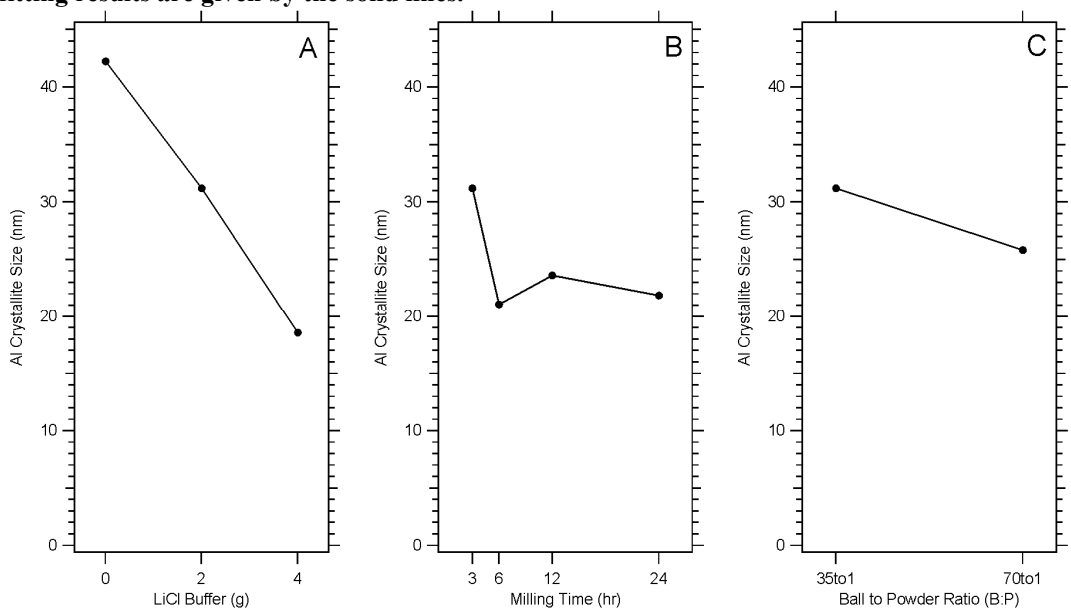

Figure 3-5: Variation of aluminium (Al) crystallite size with milling parameters: A – LiCl buffer (3 hr, 35:1 B:P), B – milling time (35:1 B:P, 9.7:1 buffer), and C – ball to powder ratio (3 hr, 9.7:1 buffer). Crystallite size was calculated by XRD Rietveld fitting results.

3.2.2 Washing

The mechanochemically synthesised samples can be washed with a solvent capable of removing the salt by-product phase in order to produce a pure Al nanoparticle product. The washing process is made difficult for Reactions 3.4 & 3.5 because aluminium nanopowders are highly reactive to water [154] and many other solvents in which salts are soluble result in the formation of surface layers such as aluminium oxide, hydroxide or oxy-hydroxide [155]. The removal of the by-product phase can also be achieved by heating in some cases [66] however this is also impractical due to the possibility of particle growth at high temperatures.

Samples synthesised using Reaction 3.5 that have a LiCl by-product were assumed to be more easily washed because of the preferred solubility of LiCl in a wider range of solvents. A range of solvents were tested for reactivity with aluminium and in regards to their LiCl solubility. Testing was required as, in general, reactivity and solubility information is often very difficult to obtain from the literature. The list of solvents considered is provided in Table 2-1, although not all were tested due to

some of the solvents presenting obvious incompatibilities. More information on the solvents tested is provided in Section 2.1.5.1. Three solvents were identified as being appropriate for washing LiCl from Al nanoparticles: pure tetrahydrofuran (THF), and nitromethane or toluene when $AlCl_3$ is pre-dissolved in solution.

Nitromethane was used as the LiCl solvent because it was found to be relatively inert towards the aluminium nanoparticles, and had a low viscosity that made particle separation possible. However, in order to promote LiCl solubility in nitromethane, aluminium chloride was added in a 3:1 ratio of $AlCl_3$:LiCl because the presence of certain other salts in solution have been found to promote the solubility of LiCl in nitromethane [93]. It was also found that NaCl dissolves within the nitromethane-$AlCl_3$ solution.

XRD data is provided in Figure 3-6 which details the effect of washing Al/LiCl samples with nitromethane/$AlCl_3$. It is obvious that the washing procedure is successful in removing the LiCl salt whilst not adversely affecting the aluminium nanoparticles (i.e. no crystalline oxide phases present). Rietveld analysis was undertaken on each of the XRD patterns in Figure 3-6 to provide quantitative phase information as given in Table 3-3. After one wash the LiCl content is reduced significantly and the average LiCl crystallite size increases slightly which can be attributed to smaller LiCl crystallites dissolving more quickly in solution during washing. After three washes all traces of LiCl are removed, and only pure Al nanoparticles remain, however it is likely that trace LiCl is still present in undetectable quantities (< 1 wt.%). Any amorphous content that could be attributed to an oxide phase is not detectable with XRD and therefore is unknown.

The Rietveld analysis in Table 3-3 also reveals considerable aluminium crystallite size growth (~40%) after successive washing procedures. The elimination of LiCl buffer material from the washing procedure results in Al-Al crystallite interactions (after removal of the physical phase separation barrier) that may lead to crystallite agglomeration increasing the average Al crystallite size. Al crystallite growth upon washing is of significance if ultra-small Al nanoparticles are to be produced, as they would be lost to agglomeration. It is likely that a physical barrier to agglomeration will be required (such as a nanoparticle coating) in order to maintain small Al nanoparticles. It is also possible that there could be a minor loss of very small Al

particles during the centrifugation step in the washing process. This would result from insufficient centrifugation times and would lead to a bias of larger particles being separated and continuing onto subsequent washing stages.

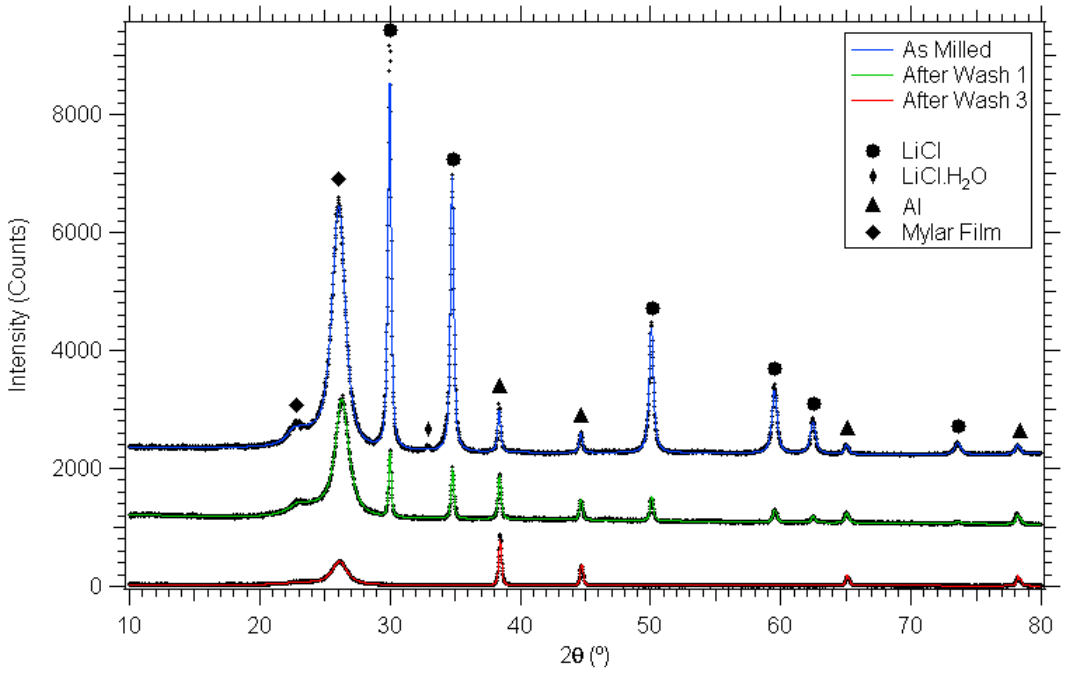

Figure 3-6: X-Ray Diffraction (XRD) patterns (D500) for mechanochemically synthesised aluminium nanoparticles in lithium chloride (Al_35to1_3hr_9.7). An as milled sample (—), a sample washed once with nitromethane and $AlCl_3$ (—), and a sample washed three times (twice with nitromethane & $AlCl_3$ and once with just nitromethane) (—) are shown. Patterns are offset for clarity and scaled to a constant aluminium peak intensity to provide a comparison of relative salt content.

Table 3-3: Rietveld results for XRD patterns in Figure 3-6 for Al_35to1_3hr_9.7 samples which have undergone washing with nitromethane/$AlCl_3$. Mathematical fitting uncertainties are provided (2 standard deviations).

	Phase	Wt. %	Crystallite size (nm)
As Milled	Al	8.6 ± 0.2	38.3 ± 2.4
	LiCl	91.4 ± 0.2	115 ± 21
After Wash 1	Al	41.0 ± 0.6	42.3 ± 2.2
	LiCl	59.0 ± 0.6	127 ± 48
After Wash 3	Al	100	54.4 ± 1.6

Figure 3-7 displays XRD patterns for both mechanochemically synthesised (washed) Al nanoparticles and commercially available Al nanoparticles (American Elements, Los Angeles, USA, 99%+). It is immediately obvious that the purchased Al nanoparticles are heavily oxide contaminated despite the suggested high purity,

whereas no crystalline oxide phases are present in the mechanochemically synthesised Al.

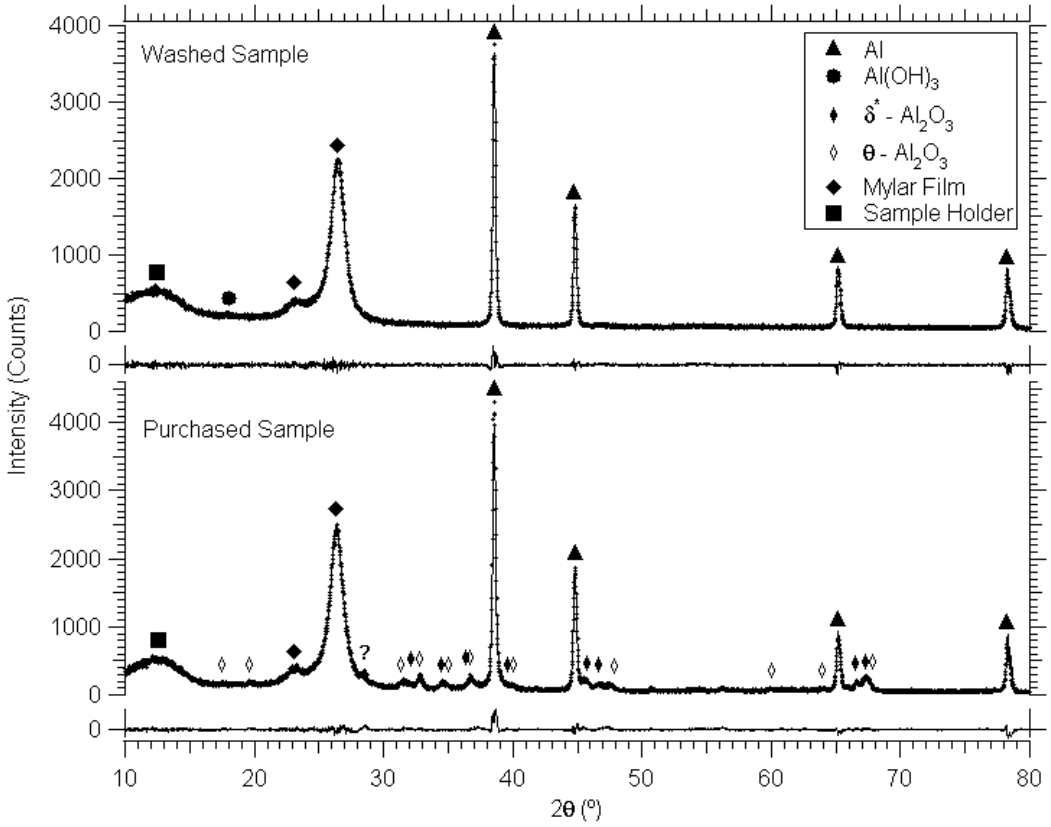

Figure 3-7: X-Ray Diffraction (XRD) patterns (D500) for a mechanochemically synthesised sample once ball milling is complete (Al_35to1_3hr_9.7), and for purchased aluminium nanoparticles. The XRD pattern for the washed sample shows that the lithium chloride salt is completely removed after washing and only aluminium nanoparticles remain. The purchased aluminium nanoparticles show high quantities of aluminium oxide and there is also one unknown peak (?). Rietveld fitting results and calculated difference plots are also shown.

There is a very minor peak in the washed mechanochemically synthesised sample pattern at 17.95 degrees that has been attributed to trace aluminium hydroxide $Al(OH)_3$, although the peak position is offset by 0.36 degrees in 2θ (d-spacing difference (Δd) = 0.097 Å) suggesting that this may not be a positive match (which is made difficult due to the very low peak intensity). It is also possible that the peak at 17.95 degrees is due to an amorphous hump present at ~18 degrees from minor amounts of soft paraffin used to seal the mylar film during XRD analysis (see Figure 2-8). There are no aluminium oxide (Al_2O_3) peaks present in the washed XRD pattern (but possibly a trace $Al(OH)_3$ phase) which suggests there was no significant reaction between the solvent and the aluminium nanoparticles. The aluminium

nanoparticles are therefore pure and any oxide content is either amorphous or below the XRD resolution limit suggesting the nanoparticles possess relatively oxide-free clean surfaces. Although no crystalline oxides were detected it has been shown [141-142] that the formation of amorphous aluminium oxide is thermodynamically favourable. A low aluminium oxide content is beneficial for hydrogen storage where aluminium oxide surface layers can be detrimental to molecular [138] and even atomic [139] hydrogen permeation.

The purchased sample contains a large quantity of crystalline Al_2O_3 despite advertising a high purity. Two Al_2O_3 phases were identified as δ^* [156] and θ because these phases provide the best match to the collected data as shown by the Rietveld fit in Figure 3-7. However a single peak in the purchased sample pattern at 28.5 degrees could not be indexed to any known aluminium oxide, hydroxide, or oxy-hydroxide phase and is an unknown sample component. The extent of oxidation is apparent by means of the quantitative Rietveld analysis shown in Table 3-4. In the mechanochemically synthesised sample there is only trace aluminium hydroxide, however the purchased sample is almost 50% Al_2O_3 by weight. Both samples have comparable Al crystallite sizes however the purchased sample's particle size would be significantly larger due to the extent of its oxide layer.

Table 3-4: Rietveld results for XRD patterns in Figure 3-7 for a washed Al_35to1_3hr_9.7 sample and a purchased (American Elements) sample.

	Phase	Wt. %	Crystallite size (nm)
Mechanochemical	Al	96.9 ± 1.9	56.8 ± 1.3
	$Al(OH)_3$	3.1 ± 1.9	13.8 ± 13.4
Purchased	Al	52.3 ± 1.3	46.7 ± 1.4
	δ^*-Al_2O_3	29.4 ± 1.3	11.5 ± 1.2
	θ-Al_2O_3	18.2 ± 1.4	17.0 ± 2.6

Transmission electron microscopy (TEM) investigations were undertaken in order to understand the extent of aggregation, agglomeration and polydispersity within the washed, mechanochemically synthesised aluminium nanoparticle sample (Al_35to1_3hr_9.7). The TEM micrographs in Figure 3-8 show a range of aluminium particles from ~25 nm to ~100 nm in size that exist in aggregate structures. The particles were identified as aluminium by energy dispersive spectroscopy (EDS) as shown in Figure 3-9. EDS also showed the existence of O which was most likely due to Al_2O_3, a result of TEM sample air exposure. TEM

investigations revealed polydispersity of the aluminium particles that is most likely due to their formation during the mechanical milling procedure under varied conditions. The crystallite sizes from XRD and particle sizes from TEM cannot be directly compared because the XRD crystallite size is a volume weighted mean whereas the TEM particle size is a number weighted mean. However the aluminium crystallite size from XRD is of the same order of magnitude as the particle size from TEM measurements suggesting that each nanoparticle consists of few individual crystallites.

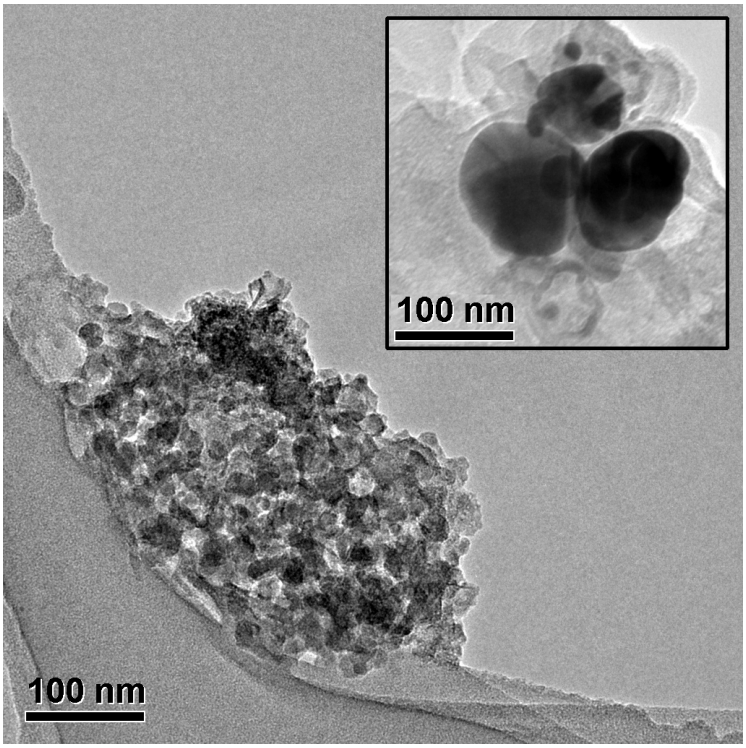

Figure 3-8: Transmission electron microscope (TEM) micrographs of mechanochemically synthesised aluminium nanoparticles (Al_35to1_3hr_9.7) that have been washed with nitromethane to remove the LiCl salt by-product. An aggregate of ~25 - 40 nm aluminium particles is shown and larger ~100 nm aluminium particles are shown in the insert. Both scale bars are 100 nm.

SAXS data was collected for the washed nanoparticles as shown in Figure 3-10 in order to provide more statistically significant structural information. A power law relationship between scattered intensity and the scattering vector q dominates the data set and there is a hump in the data set at low-q has been attributed to a Guinier region generated by the average aluminium nanoparticle size. The data was modelled using the unified equation [114] with the Irena package [157] for Igor Pro (Wavemetrics,

Oregon, USA). A unified fit was applied to the data resulting in a Guinier region at low-q with a radius of gyration R_g = 21.2 nm and a power-law region with a slope of -3.55. It is reasonable to assume that the particles are roughly spherical from TEM investigations so that the radius of gyration can be related to the aluminium particle size by $R_g = \sqrt{3/5}\, r$ where r is the particle radius, resulting in an overall average particle size (diameter) of 55 nm. This is in agreement with the average particle size obtained from TEM investigations. The slope of the power law region (-3.55) at high-q is indicative of rough particle surfaces [107] which is expected from a sample that is synthesised by ball milling. Rough particle surfaces are also evidenced with the TEM results in Figure 3-8.

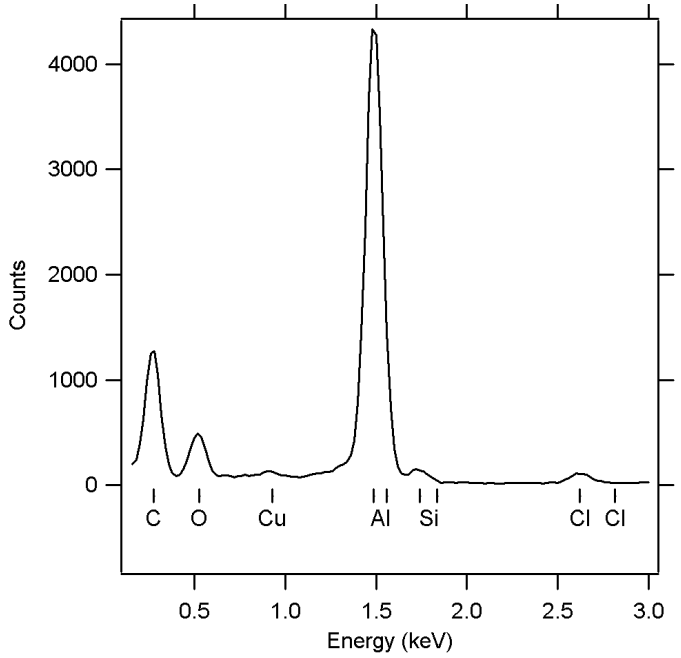

Figure 3-9: A typical energy dispersive x-ray spectroscopy (EDS) spectra from TEM investigations of washed nanoparticles (Al_35to1_3hr_9.7) as given in Figure 3-8 showing a high Al content, minor traces of Cl from residual LiCl, O from aluminium oxide due to sample air-exposure, and TEM grid components Cu, C, and Si.

The surface area (including open and closed porosity) can be calculated for particles with rough surfaces by using the method outlined in Section 2.3.4 according to Beaucage [111]. The unified fit to the SAXS data results in determination of parameters relating to the aluminium nanoparticles: the Guinier prefactor (G_s = 31000 cm^{-1}), the radius of gyration (R_s = 21.2 nm), the power-law prefactor (B_s = 0.000294 cm^{-1}Å^{ds-6}), and the power-law exponent (P_s = 3.55). The Porod invariant can be calculated as Q

= 0.0129 $cm^{-1}Å^{-3}$ by integrating according to Equation 2.19 by using the Maple software package (Maplesoft, Ontario, Canada).

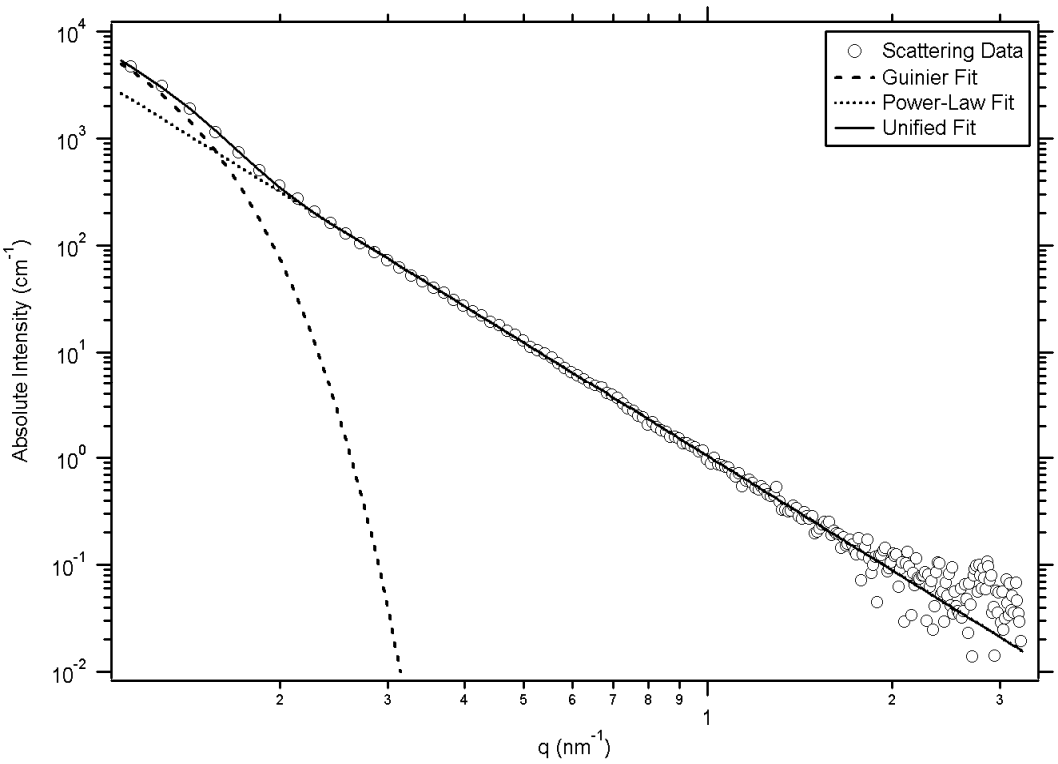

Figure 3-10: Small angle x-ray scattering (SAXS) data from washed (LiCl removed) aluminium nanoparticles (Al_35to1_3hr_9.7) which are shown in TEM micrographs in Figure 3-8. The result of a unified fit to the data is also displayed.

Transmission measurements during SAXS can provide a measure of the bulk density of the Al nanoparticle sample. Equation 2.7 relates the effective thickness of the sample (solid portion thickness) to the measured x-ray transmission (τ_s = 0.241). If the true density of aluminium (ρ_{base} = 2.7 g cm^{-3}) is used in conjunction with its x-ray mass attenuation coefficient (μ_{8keV} = 50.33 cm^2g^{-1}) then the effective thickness can be calculated as d_{sp} = 0.01047 cm. The total sample thickness is known (d_{tot} = 0.1 cm) due to the fact that it was packed within a capillary which means that the bulk density can be calculated as follows (see Appendix D for equation formulation):

$$\rho_{bulk} = \frac{\rho_{base} d_{sp}^{\ 3}}{d_{tot}^{\ 3}} \tag{3.6}$$

The bulk density is calculated as ρ_{bulk} = 0.0031 g cm^{-3}. The surface area can then be calculated using Equation 2.14 with φ = 0.00115, d_s = 2.45, $F(d_s)$ = 1.905, S =

0.00877 $m^{ds}g^{-1}$, r = 4 Å (for N_2) providing a surface area of 149 m^2g^{-1}. The calculated surface area is much higher than those theoretically predicted (~ 22 m^2g^{-1}) assuming smooth non-contacting nanoparticles (see Section 1.4). The discrepancy is most likely due to the rough surface structure of the nanoparticles that dramatically increases the surface area. A high surface area is a beneficial characteristic for a hydrogen storage material as it increases the reaction area for hydrogen, increasing kinetics [158].

The Porod invariant (Q) also allows for the determination of the nanoparticle volume (V_{base}) as 47,400 nm^3 by a manipulation of Equation 2.19. If the particles are assumed to be spherical then the average particle size can be calculated as $d = 2\sqrt[3]{3V_{base}/4\pi}$ = 45 nm. There is a discrepancy between the average particle size calculated from the Porod invariant (45 nm) and that which was extracted from the Guinier regime (55 nm). The discrepancy is most likely due to the spherical assumption used and because the particle sizes are calculated by different means (volume and radius of gyration respectively) a difference is noted indicating that the particles may have a slightly non-spherical shape. It is likely that the particles are irregularly shaped due to aggregation that is seen in TEM investigations. However both particle sizes are in line with those observed during TEM.

SAXS data was also collected for aluminium nanoparticles embedded in salt but the data only contained surface scattering information (a single power-law over measured q-space) most likely due to the abundance of surface scattering from salt particles that masked the scattering information from the aluminium nanoparticles.

3.2.3 Buffer Variations

A LiCl buffer was utilised in the synthesis of Al because it is already a reaction by-product in Equation 3.5. The LiCl by-product was found to be advantageous because it can be removed with a solvent that does not adversely react with the Al nanoparticle product. However in order to dissolve the LiCl by-product $AlCl_3$ is required to promote LiCl solubility in nitromethane. In an attempt to amalgamate the synthesis with the washing procedure it was devised that an $AlCl_3$ buffer would be advantageous in the reaction as it is already required for washing the LiCl by-

product. Unfortunately the reaction between Li and $AlCl_3$ with excess $AlCl_3$ buffer undergoes a secondary reaction and proceeds as follows:

$$3Li + 4AlCl_3 \longrightarrow Al + 3LiAlCl_4 \qquad \Delta_r G_{298K} = -633 \text{ kJ/mol} \qquad (3.7)$$

Reaction 3.7 was undertaken with a 3:4 Li:$AlCl_3$ molar ratio by room temperature ball milling for 8 hours with a 15:1 ball to powder ratio (equal mass of 12.7 mm and 7.938 mm balls) in order to generate a 1 g Al yield. The reaction products were analysed using XRD as shown in Figure 3-11. It can be seen that the reaction progressed according to Reaction 3.7 forming a $LiAlCl_4$ reaction by-product. Some LiCl is also present that is most likely an intermediate reaction product. $AlCl_3$ is not present in the XRD pattern as it often undergoes significant crystalline deformation during milling.

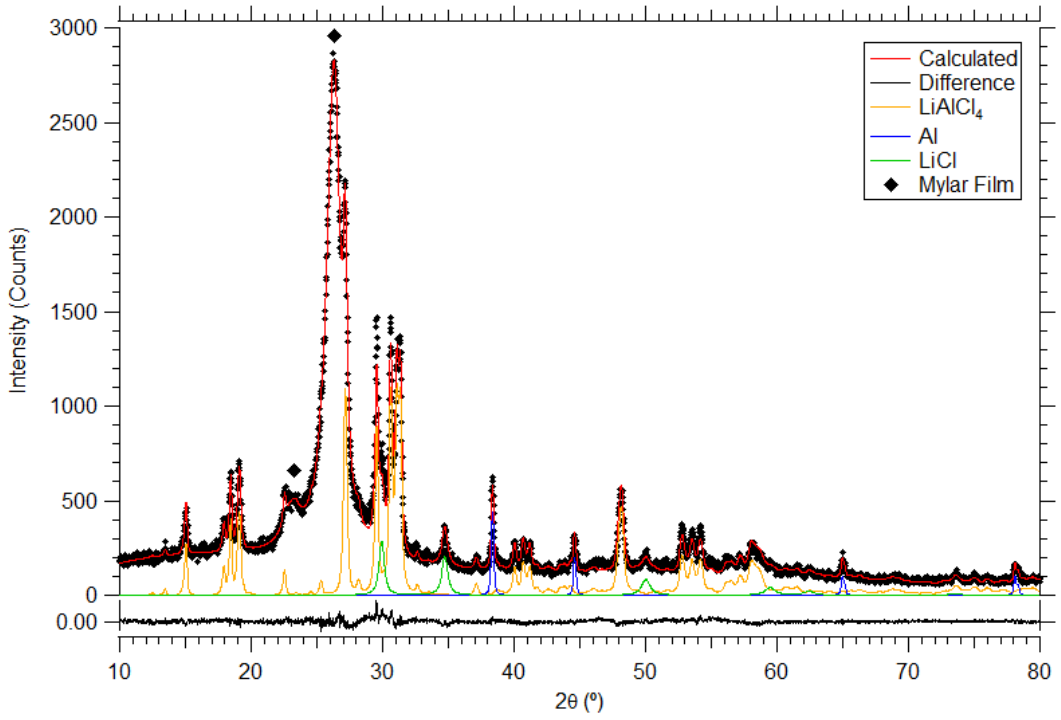

Figure 3-11: X-Ray Diffraction (XRD) pattern (D500) for a mechanochemically synthesised sample using an $AlCl_3$ buffer. Milling conditions are as described in the text.

In order to investigate the progress of Reaction 3.7 the reaction between LiCl (the reaction by-product of Li and $AlCl_3$) and $AlCl_3$ (which is in excess) was undertaken as follows:

$$AlCl_3 + LiCl \longrightarrow LiAlCl_4 \qquad \Delta_r G_{298K} = -37 \text{ kJ/mol} \qquad (3.8)$$

A comparison between the Gibbs free energy change in reactions 3.5 and 3.8 (-522 kJ/mol and -37 kJ/mol respectively) reveals that in a reaction between Li and excess $AlCl_3$ the initial reaction product will be Al and LiCl (given the high Gibbs free energy change). However over time Reaction 3.8 will also proceed (even though it has a very low Gibbs energy change) reacting the synthesised LiCl with the excess $AlCl_3$ forming $LiAlCl_4$.

XRD was used to analyse the reaction products of Reaction 3.8 undertaken by room temperature ball milling for 8 hours with a 30:1 ball to powder ratio (equal mass of 12.7 mm and 7.938 mm balls) to synthesise a 5 g $LiAlCl_4$ yield as shown in Figure 3-12. A significant fraction of $LiAlCl_4$ has been synthesised after milling is complete, and some initial reagents remain.

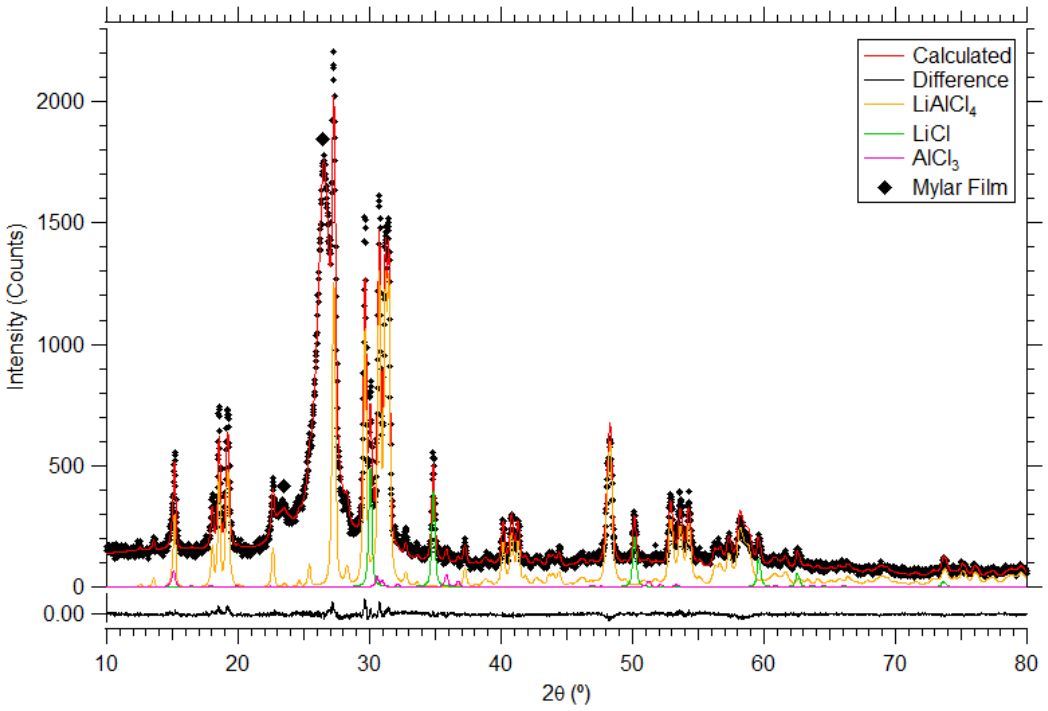

Figure 3-12: X-Ray Diffraction (XRD) pattern (D500) for mechanochemically synthesised $LiAlCl_4$ synthesised according to Reaction 3.8. Milling conditions are as described in the text.

$LiAlCl_4$ production during aluminium mechanochemical synthesis is unwanted because it has been found to dissolve inconsistently in solution [88]. It has also been shown to crystallise out of solution when LiCl and $AlCl_3$ are dissolved in toluene

with a high LiCl content [88]. If an alternate solvent was found that dissolved high quantities of $LiAlCl_4$ then the reaction pathway given by Reaction 3.7 could be utilised in Al nanoparticle synthesis.

3.2.4 Titanium-Doped Aluminium

The chemisorption of hydrogen into aluminium is only possible at extreme pressures (< 2.5 GPa [4-5]) and moderate temperatures. However extrapolations from experimental data reveal that at 77 K much lower hydrogen equilibrium pressures are expected (50 bar [159] or 1 kbar [29]). Theoretical calculations have shown that Al surfaces do not dissociatively chemisorb molecular hydrogen under normal conditions [160] because Al has a low affinity for hydrogen due to a relatively large activation barrier [149]. In addition, the kinetics of hydrogen absorption are very slow at low temperatures due to the low probability of atomic collisions. Al-Ti complexes have been studied in relation to catalytic hydrogen absorption into $NaAlH_4$ showing that certain Al-Ti configurations allow for barrierless H_2 dissociation [161] making them promising for low temperature hydrogen absorption.

The formation of an Al_3Ti phase is supported by Al-Ti phase diagrams [162] however many intermediate intermetallics are also possible including titanium rich Al-Ti compounds that absorb hydrogen at modest pressures (50 bar) at room temperature [163]. Although Al_3Ti has been reported not to absorb hydrogen under normal conditions [164] it has been suggested that a Al_3Ti phase (or a localised surface Al-Ti phase) could be extremely important in synthesising AlH_3 due to Ti driving chemisorption of H_2, resulting in significant bonding interactions with Al [160]. The absorption of hydrogen into pure Al_3Ti was attempted by Semenenko *et al.* [165] at pressures up to 1800 atm and temperatures to 500°C with no success. Although no hydrogen absorption was detected it is difficult to determine if this was due to poor sample composition or even oxide contamination because no sample details were provided therein.

Aluminium nanoparticles were synthesised mechanochemically with titanium doping according to the following reaction:

$$\begin{aligned} AlCl_3 + 0.05TiCl_3 + 3.15Li \longrightarrow 0.85Al + 0.05Al_3Ti + 3.15LiCl \\ \Delta_r G_{298K} = -553 \text{ kJ/mol} \end{aligned} \quad (3.9)$$

Reaction 3.9 was undertaken in two steps. Firstly $AlCl_3$ and 5 mol % $TiCl_3$ were pre-milled at room temperature for 3 hours with a 35:1 ball to powder ratio (B:P) (equal number of 12.7 mm & 7.938 mm balls) in order to achieve a homogeneous $AlCl_3/TiCl_3$ mixture. A uniform mixture is important so that when Reaction 3.9 is undertaken to completion the synthesised aluminium nanoparticles will contain similar proportions of the Al_3Ti phase that may act as a catalyst for hydrogen absorption. The reaction product was a bright pink colour resulting from the violet colour of pure $TiCl_3$. Secondly the $AlCl_3/TiCl_3$ mixture was milled with Li metal at room temperature for 12 hours with a 35:1 B:P (equal number of 12.7 mm & 7.938 mm balls) to complete the mechanochemical reaction forming alloyed (Al + Al_3Ti) nanoparticles embedded within a LiCl salt matrix. A LiCl buffer was also added to the initial reagents (9.02:1 LiCl:metal product volume ratio) in order to promote nanoparticle formation. The reaction products can be verified from the XRD pattern given in Figure 3-13.

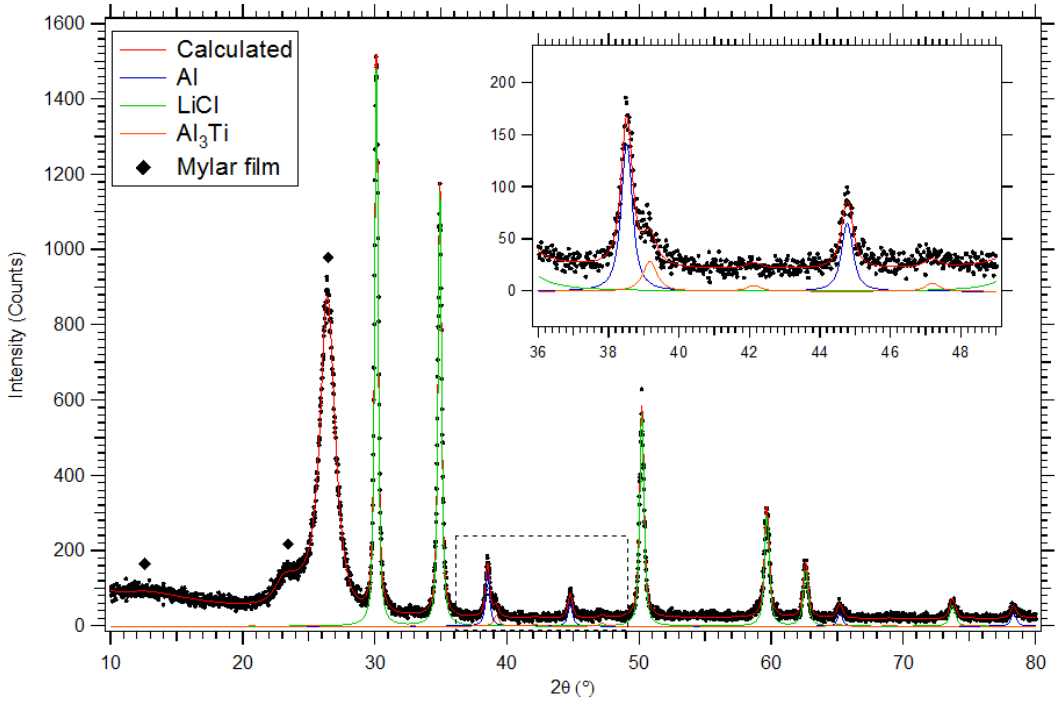

Figure 3-13: X-ray diffraction (XRD) pattern (D500) of the product of Reaction 3.9 that was mechanochemically synthesised at room temperature as described in the text. Pattern fitting was achieved using the Rietveld method in the Topas software package by using a fundamental parameters approach. Mylar peaks are present due to the film used to prevent O_2 & H_2O exposure during data collection.

3.2.5 Nickel-Coated Aluminium

Nickel-coated aluminium nanoparticles were synthesised as they could provide a pathway for hydrogen dissociation ($H_2 \rightarrow 2H^{ions}$). This is because hydrogen is known to dissociate rapidly on nickel due to the very high sticking probability and barrierless dissociation for hydrogen [25], whereas dissociation on aluminium is negligible at 300 K [166]. Nickel doped magnesium has been hydrogenated in the past [167] demonstrating a reduction in the energy barrier for hydrogen dissociation as well as good catalytic properties allowing hydrogen diffusion into magnesium (whereas titanium doped samples did not have good catalytic properties).

Aluminium nanoparticles have been chemically synthesised previously [168] and then coated with transition metals (Pd, Ag, Au, or Ni) in order to reduce the formation of aluminium oxide. However these transition metals do not have any significant impact on the growth of aluminium oxide in air [168]. Nickel-coated aluminium has even been suggested as a promising solid propulsion source for use on Mars due to its combustion properties in a range of gas environments including O_2 & CO_2 [169].

The coating technique [168] involves suspending the aluminium nanoparticles in solution (i.e. dimethoxyethane) and mixing them with a solution of a non-aqueous soluble compound of the transition metal in question (i.e. nickel (II) acetylacetonate). The mixture is stirred and is then washed of any excess material, providing transition metal coated aluminium nanoparticles.

Aluminium nanoparticles were prepared with the mechanochemical synthesis method given by Reaction 3.5. Mechanochemical synthesis was undertaken at room temperature akin to sample Al_35to1_3hr_9.7 in Section 3.2.1. In order to nickel coat 0.5 g of pure aluminium nanoparticles 3.86 g of milled sample (13 % Al, 87 % LiCl) was first washed three times to remove any LiCl (twice using nitromethane & $AlCl_3$ and finally using only nitromethane). The aluminium was not dried however (which is the case in a standard washing procedure) in order to reduce the likelihood of grain/particle growth. Instead the nitromethane was decanted and the aluminium nanoparticles were mixed into a slurry with 20 ml of toluene.

0.099 g of nickel (II) acetylacetonate was added to 20 ml of toluene and magnetically stirred for 1 hour for total dissolution, resulting in a light green solution. The nickel

(II) acetylacetonate solution was then added to the aluminium nanoparticle slurry and magnetically stirred for 19.5 hours to ensure that nickel coating was complete. The solution was then centrifuged for 4 hours resulting in a separated nanoparticle product and a clear toluene solution, indicating that the nickel (II) acetylacetonate was totally reacted. The toluene was then decanted and 30 ml of fresh toluene was mixed with the nanoparticle product for a second wash to remove any excess reagents. The mixture was then magnetically stirred for 68 hours and centrifuged for 2 hours at which point the mixture was separated. The toluene was then decanted and the wet coated nanoparticles were placed under vacuum for 19 hours to remove any final traces of toluene. This procedure resulted in nickel-coated aluminium nanoparticles.

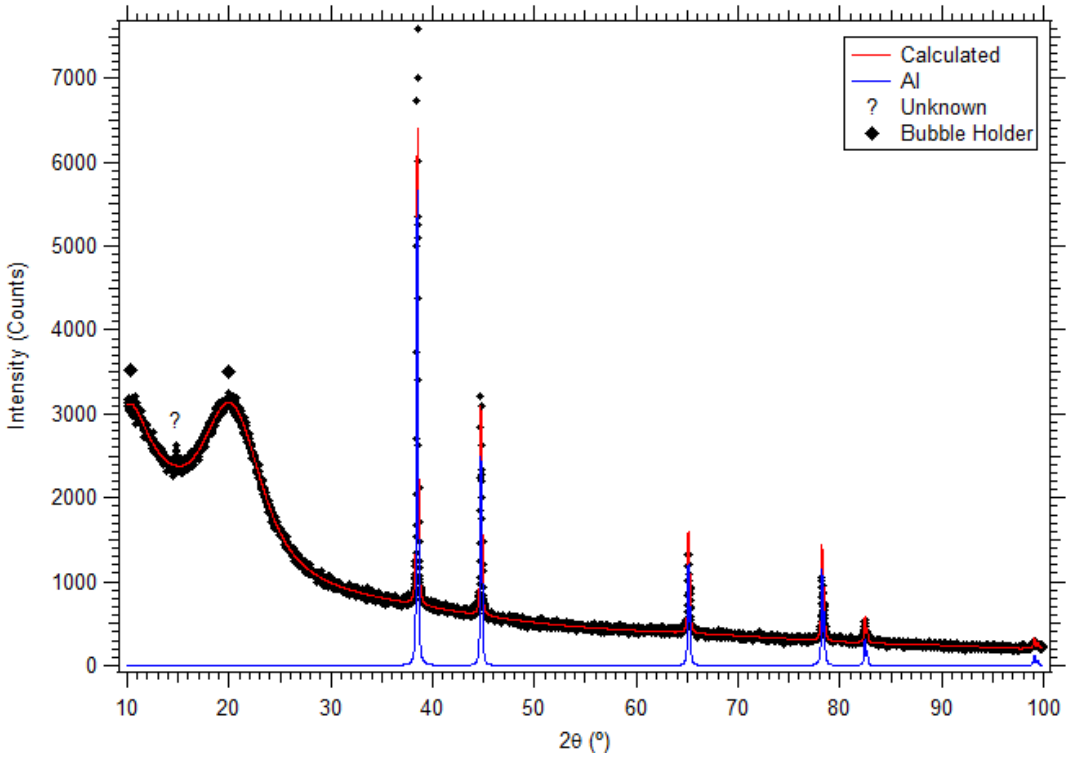

Figure 3-14: X-ray diffraction (XRD) pattern (D8) of the resultant Ni-coated Al as described in the text. Pattern fitting was achieved using the Rietveld method in the Topas software package by using a fundamental parameters approach. Peaks are present due to the bubble holder used to prevent O_2 & H_2O exposure during data collection.

XRD was performed on the as-synthesised Ni-coated Al product as shown in Figure 3-14. A small quantity of the Al-Ni powder was suspended in nitromethane and dropped onto a silicon wafer using a pipette that was sealed using an XRD bubble holder. Rietveld analysis resulted in a poor fit to the data set due to problems with the

sample interaction volume on the low background holder. The Al phase is predominant and no Ni phase could be identified akin to the XRD undertaken by Foley *et al.* [168] where only an Al phase could be identified. The unknown XRD peak in Figure 3-14 could not be indexed to any known Al-Ni phase or any Ni-organic structure, however it may be slight $AlCl_3$ contamination from the LiCl washing procedure. The absence of a Ni phase in XRD suggests that the Ni phase is in fact non-crystalline.

3.3 HYDROGEN SORPTION

3.3.1 Pure Al

Hydrogen absorption experiments were performed on mechanochemically synthesised Al nanoparticle samples up to 100 bar at temperatures from 77 K - 623 K with no measurable absorption over long periods of time (150 hrs). As a result of the null result absorption, high pressure (up to 2 kbar) measurements were undertaken as described below.

High pressure deuterium absorption measurements were attempted at Griffith University (with the assistance of Jim Webb, Tomasz Blach, and Evan Gray) on two different samples: Al nanoparticles embedded in NaCl (as described in Section 3.2), and Al nanoparticles (Al_35to1_3hr_9.7 washed from LiCl). An overview of the absorption conditions is provided in Table 3-5. Al in NaCl underwent pressures of 1560 bar at room temperature and at 473 K with no measurable deuterium absorption. Al (washed) underwent pressures of 1917 bar at room temperature, 1958 bar at 423 K and up to 1875 bar at 77 K with no measurable deuterium absorption. Purchased Al nanoparticles (10 – 22 nm) were also tested in Paskevicius *et al.* [170] up to 1900 bar at 298 K with no measurable absorption. However these pressures are still considered low compared to the 28 kbar at 573 K required for hydrogen absorption into bulk aluminium [4-5].

Table 3-5: Overview of deuterium absorption conditions for the three samples tested as described in the text. No measurable absorption was observed for any samples at the conditions indicated.

Sample	Average particle size (nm)	Deuterium absorption conditions	
		Pressure (bar)	Temperature (K)
Al in NaCl	40 – 50	1560	298
		1560	473
Al (washed)	55	1875	77
		1917	298
		1958	423
Al (purchased) [170]	10 – 22	1900	298

As the attempts to hydride Al nanoparticles below 2 kbar were unsuccessful, it is clear that no significant change in the thermodynamic properties compared to the

bulk occurs, for 40 – 55 nm Al, assuming that other factors are favourable for hydrogen absorption at the temperatures studied. Both the absorption kinetics and hydrogen dissociation ability will be hindered at low temperatures, especially 77 K, which could mean that low temperature hydrogen absorption into pure aluminium is extremely slow and near undetectable under normal conditions. Recent theoretical investigations indicate that hydrogen absorption into bulk aluminium may be thermodynamically favourable at low temperatures where low equilibrium pressures are predicted (7 kbar at 300 K [171] and 50 bar at 77 K [159]). It should be noted that the predicted 50 bar equilibrium pressure [159] assumes that ΔH and ΔS are temperature independent which is a dubious assumption over a temperature range of 77 – 1000 K. If we assume that the predicted pressure of 50 bar is correct and compare it to the experimental hydrogen absorption attempt in the current work (1875 bar at 77 K) then an extreme kinetic barrier must be present given the significant overpressure produced experimentally.

3.3.2 Doped Al

Low pressure hydrogen absorption measurements were performed on both a 2 g titanium doped Al sample (synthesised according to Section 3.2.4) and a 0.3 g nickel-coated Al sample (synthesised according to Section 3.2.5). The samples were first evacuated for 24 hrs at room temperature in order to remove any adsorbed argon. The samples were then kept under a hydrogen pressure of 108 bar at both room temperature (RT) and at 77 K for 24 hours each. No measurable drop in hydrogen pressure was detectable at either temperature and XRD results showed no change in the crystal structure of the Al after hydrogenation was attempted, as shown in Figures 3-15 and 3-16. The null result suggests that the hydrogen equilibrium pressure of the Al nanoparticles is above 108 bar at 77 K and at RT. It may also be possible that the equilibrium pressure is actual below 108 bar at 77 K but the nickel and Al_3Ti is not able to efficiently dissociate the hydrogen at these temperatures and/or the reaction is hindered by very slow kinetics. However, given the similar null result in hydriding pure Al at even higher pressures (in Section 3.3.1) it is likely that the equilibrium pressure for the Al nanoparticles is much greater than 108 bar.

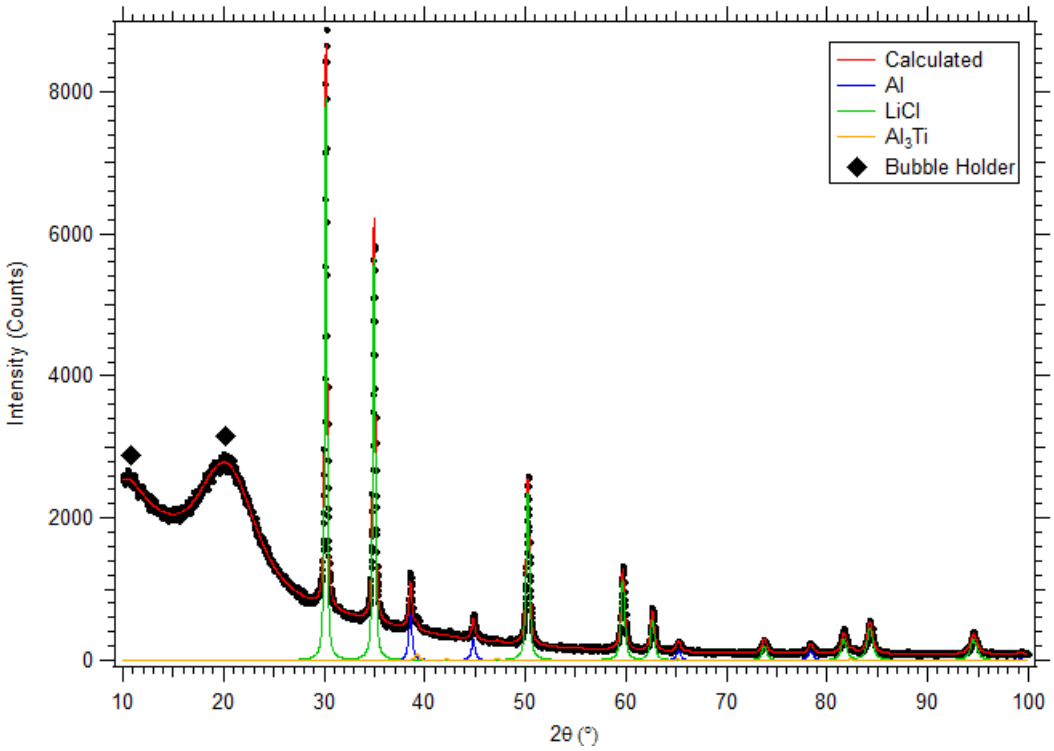

Figure 3-15: X-ray diffraction (XRD) pattern (D8) of Ti-doped Al after hydrogenation at 77 K. Pattern fitting was achieved using the Rietveld method in the Topas software package by using a fundamental parameters approach.

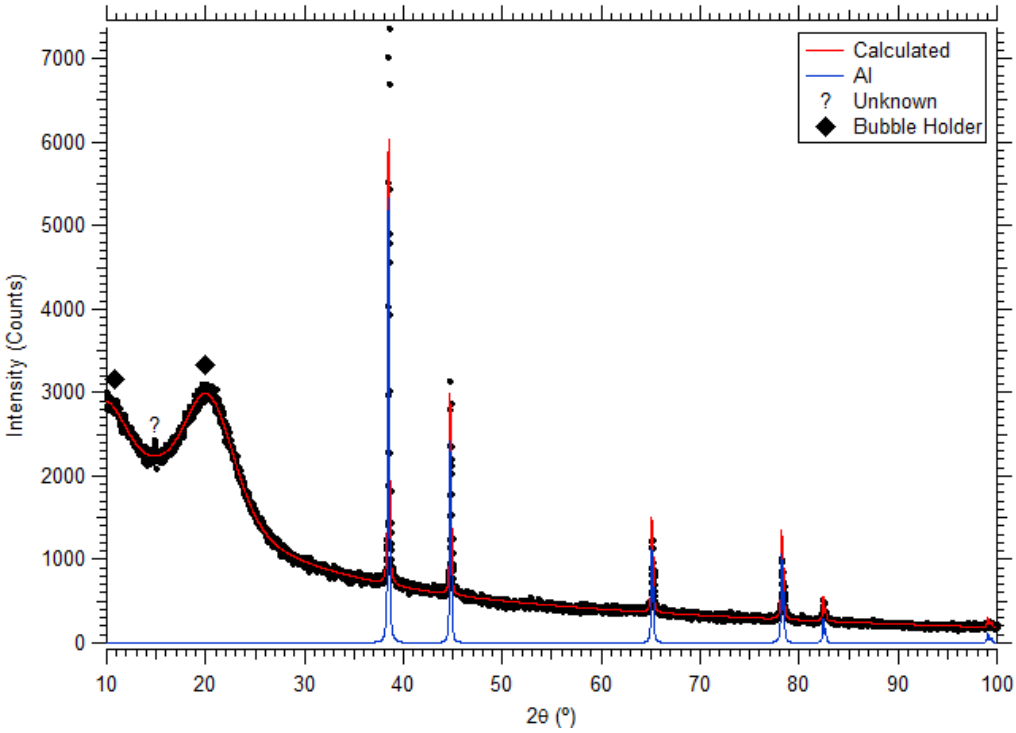

Figure 3-16: X-ray diffraction (XRD) pattern (D8) of Ni-coated Al after hydrogenation at 77 K. Pattern fitting was achieved using the Rietveld method in the Topas software package by using a fundamental parameters approach.

3.4 CONCLUSIONS

Aluminium nanoparticles were mechanochemically synthesised by a number of different reaction pathways. Sodium or lithium metal were reacted with aluminium chloride during milling with different quantities of salt buffer to examine the resultant aluminium particles. Aluminium with particle sizes 40 – 55 nm (and crystallite sizes > 18 nm) were synthesised. The relatively large sizes are likely due to the large particle size of the initial starting reagents (Na or Li). The salt by-product phase was removed using a washing process with a nitromethane/$AlCl_3$ solution resulting in 55 nm Al particles (single crystals) that did not display any crystalline oxide phases.

High pressure hydrogen absorption experiments were undertaken up to 2 kbar at temperatures from 77 – 473 K to examine if there were any major thermodynamic changes to the Al. No hydrogen absorption could be detected and either higher pressure or smaller Al is required to form AlH_3 under these conditions.

Ni-coated and Ti-doped Al nanoparticles were also synthesised in order to verify if catalytic metals could enhance hydriding kinetics. Kinetics are vital in low temperature hydrogen sorption where hydrogen equilibrium pressures have been predicted to be much lower (50 bar – 1 kbar). However no hydrogen absorption was detected in these doped samples at room temperature or at 77 K under hydrogen pressures up to 108 bar.

3.5 DIRECTIONS FOR FUTURE WORK

- Pure Al nanoparticles must be synthesised < 10 nm in order to cause significant thermodynamic destabilisation of Al, reducing the hydrogen equilibrium pressure to modest levels. Al nanoparticles < 10 nm could be formed mechanochemically by using very large quantities of reaction buffer.

- In order to absorb hydrogen into aluminium at modest pressures, low temperatures (~77 K) must be considered in detail. The thermodynamics for alane formation dictate that lower pressures are required at lower temperatures. Kinetics are hindered at low temperatures but they may be overcome by implementing dopants/catalysts.

- A method must be utilised to investigate any amorphous aluminium oxide layers that may form during washing with nitromethane. Many methods may be able to detect amorphous aluminium oxide layers without sample air exposure such as reflectometry, Fourier transform infrared (FTIR), Inelastic neutron scattering (INS), or x-ray photoelectron spectroscopy (XPS). Internal standards during XRD analysis could also be used to determine an amorphous content albeit without identifying the amorphous phase. Another solvent must be used for washing (such as THF) if amorphous oxides are found to be formed.

- Ti-doped and Ni-coated Al nanoparticles should be investigated under high hydrogen pressure (~2 kbar) at a range of temperatures (including 77 K) to determine the effectiveness of their catalytic properties. Other dopants may also be investigated such as Pd or Pt which could allow for hydrogen dissociation at low temperatures.

Chapter 4

Aluminium Hydride Nanoparticles

"A physicist is an atom's way of knowing about atoms" - George Wald

4.1 BACKGROUND

Aluminium hydride is a metal hydride also known as alane or AlH_3 that has seven known crystalline structural phases (α, α', β, γ, δ, ε, ζ). It was first discovered by O. Stecher and E. Wiberg in 1939 [129] and has been described [172] as a covalently bonded, metastable solid at room temperature. AlH_3 has a high 10.1 wt.% gravimetric H capacity and α-alane has a volumetric capacity of 0.148 kg H_2/L [173]. Despite its usefulness in a number of industries, alane has not become widely available primarily due to difficulties in large-scale wet chemical synthesis [174]. Alane has potential applications in the fields of hydrogen storage, chemical catalysis, explosives, propellants and pyrotechnics.

4.1.1 Synthesis

Alane has been synthesised by a range of different methods that range in experimental difficulty which are outlined in the following sections. Aluminium does not readily absorb hydrogen to form AlH_3, only under extreme hydrogen pressure. Hydrogen also has a low solubility in aluminium metal which is a function of the interstitial lattice sites, dislocations and vacancies present [153]. Alane synthesis is most often synthesised chemically in the literature.

4.1.1.1 *Elemental Synthesis*

Alane (AlH_3) readily decomposes to the elements upon heating and it has been shown that the synthesis of α-alane from the elements is also possible under high pressures (> 20 kbar) between 150 – 300°C as follows [4-5,175]:

$$Al + \frac{3}{2}H_2 \longleftrightarrow \alpha\text{-}AlH_3 \qquad \Delta_r G_{298K} = +46.517 \text{ kJ/mol} \tag{4.1}$$

The discrepancy between the formation temperatures reported in the literature [4-5,175] is likely a result of oxide coated Al/AlH_3 particles causing a shift from the actual equilibrium conditions. It has been suggested [176] that for the synthesis of alane to be possible an oxide free surface and the presence of some nuclei of the hexagonal aluminium hydride phase may also be required. Hydrogen absorption below 20 kbar has not been achieved [175] despite theoretical predictions that lower equilibrium

pressures exist below 150°C. It is likely that kinetic barriers restrict absorption within reasonable time periods.

It has been noted [4] that the hydrogen equilibrium pressure can be determined from the AlH_3 decomposition process. The plateau pressure is a function of the free energy of formation of aluminium hydride and it indicates the minimum pressure of gaseous hydrogen required for its synthesis [4]. It is also noted [4] that the formation pressure could be higher than the decomposition pressure due to the well known hysteresis in metal hydrides. A volume increase of 90% occurs when α-AlH_3 is synthesised from Al supporting the possibility of a substantial hysteresis effect. However calculating the equilibrium conditions from the decomposition plateau can be risky due to the very slow kinetics that can exist causing misleading plateau pressures at any given temperature.

It has been suggested [177] that the synthesis of alane is possible under much milder conditions (34.2 MPa at 65°C) given that the aluminium is in the form of nanoparticles (~100 nm). However these results have not been published in peer-reviewed literature to date and the low hydriding pressure and temperature have not been experimentally duplicated herein or elsewhere. Low hydrogenation pressures are reported from certain theoretical calculations (i.e. ~50 bar at 77 K) in the literature in relation to bulk aluminium [159], however these calculations were undertaken assuming the enthalpy and entropy of AlH_3 formation do not change over a significant temperature range, which is a dubious assumption.

Recent theoretical predictions given in Section 1.4.2 by Kim *et al.* [44] suggest a moderate increase in the enthalpy of Reaction 4.1 for alane nanoparticles < 10 nm. The enthalpy change would result in stabilisation of AlH_3 which would reduce hydrogen equilibrium pressures at any given temperature. The relationship between AlH_3 particle size and the hydrogen equilibrium pressure has not been investigated to date in the literature.

4.1.1.2 *Hydrogen Ion Bombardment Synthesis*

Aluminium hydride has been produced by bombarding an ultrapure aluminium target specimen with 12.5 MeV deuterons [178]. This radiation is much more intense than the 1 keV hydrogen ions that have been used to form hydrogen bubbles in aluminium [152].

By applying high energy ions, hydrogen (deuterium) to aluminium ratios were computed to be 4.6 at.% instead of several parts per million in the case of lower energy bombardment. X-ray diffraction was performed on the irradiated aluminium [178] and a diffraction pattern similar to that obtained by chemical means [179] was reproduced. The XRD patterns appear to show multiple alane phases present (possibly α, β and γ) when compared to more recent patterns [180]. However the patterns are roughly assigned to the γ-AlH_3 phase by Turley & Rinn despite the poor quality of the data [181]. Alane (most probably γ-AlH_3) has also been identified in the plasma hydrogenation of thin aluminium films [182].

4.1.1.3 *Atomic Hydrogen Reaction Synthesis*

Atomic hydrogen can undergo a reaction between aluminium when it is evaporated or present as a film [183]. The reaction can form an aluminium hydride phase which has H/Al ratios of 0.1 to 1.02. The ratio suggests a product of aluminium atoms and a hydride AlH_x which had an x value greater than unity (probably 3) [183].

4.1.1.4 *Wet Chemical Synthesis*

All seven of alane's structural phases (α, α', β, γ, δ, ε, ζ) as well as AlH_3 etherate can be synthesised chemically [180]. The most stable phase is reported as α-AlH_3 which can be prepared from other solid metastable phases or by crystallising directly from solution [180]. The alane synthesis reaction was first provided in 1947 [184] but is more accurately given as [185]:

$$AlCl_3 + 3LiAlH_4 + n\left[(C_2H_5)_2O\right] \longrightarrow 4AlH_3 \bullet 1.2\left[(C_2H_5)_2O\right] + 3LiCl \qquad (4.2)$$

This ethereal reaction is the basis for synthesising all of the structural phases of alane. The reaction between sodium alanate ($NaAlH_4$) with aluminium chloride ($AlCl_3$) to form AlH_3 and sodium chloride (NaCl) has also been undertaken in the past [186]. The ether could not originally be removed [184] because the diethyl etherate $AlH_3 \bullet 0.3[(C_2H_5)_2O]$ crystallises out of solution shortly after preparation. However it was found [180] that in the presence of excess $LiAlH_4$ (and optionally $LiBH_4$) the ether can be removed. Borohydride salts ($LiBH_4$) are expensive, their by-products require special disposal, and they are not recovered in the reaction. Because of this, a method was provided [187] in order to synthesise α-AlH_3 without the use of borohydride salts.

Different alane phases can be synthesised under various temperature, pressure and reaction conditions during the ether removal [180]. The synthesis has been described [185] to be extremely sensitive to the given desolvating conditions.

The resultant alane that forms directly from the reaction solution has a particle size from 10 - 50 microns or larger [188]. The morphology of α-alane is cubic or rhombohedral, while α'-alane forms needle-like crystals and γ-alane forms a bundle of fused needles [187]. It should be noted that the chemical synthesis of alane must be performed under an inert atmosphere to avoid contamination from the oxygen [189] and moisture [187] content of the air. It has been noted [185] that freshly prepared, non-passivated AlH_3 is pyrophoric and reacts violently in water and as such must be treated with caution.

Wet chemical synthesis of ~200 nm (size not directly measured) particles of α-AlH_3 has also been performed by Graetz & Reilly [185] using a refined procedure. Graetz & Reilly state that the β-phase can instead be obtained if the final heating time given above is only 45 min instead of 3 h. The γ-phase can also be obtained using a similar method as given above but with different molar ratios [185].

An alternative wet chemical AlH_3 synthesis technique has been suggested involving ionic liquids [190] which act as aluminium and hydrogen donors allowing alane to form in ionic liquid reactions.

4.1.1.5 *Mechanochemical Synthesis*

The mechanochemical synthesis procedure has been applied in the synthesis of deuterated alane (AlD_3) nanoparticles recently [67]. By using the mechanochemical synthesis process, particle refinement and a reduction in diffusion distances act to increase reaction kinetics and reduce the required reaction temperature significantly [65]. This allows for the alane synthesis reaction given by Reaction 4.2 to occur without the presence of diethyl ether as follows [67]:

$$AlCl_3 + 3LiAlH_4 \longrightarrow 4AlH_3 + 3LiCl \qquad \Delta_r G_{298K} = -191\ \text{kJ/mol} \qquad (4.3)$$

The reaction progresses both at room temperature and at 77 K due to the relatively high change in Gibbs free energies. Brinks et al. [67] surmised that room temperature

synthesis was inefficient at synthesising AlH_3 due to the low alane yields and high Al content. Aluminium forms due to the high milling energy at room temperature which allows for AlH_3 to decompose to Al and H_2 as follows:

$$AlH_3 \longrightarrow Al + \frac{3}{2}H_2 \qquad \Delta_r G_{298K} = -46.5 \text{ kJ/mol} \tag{4.4}$$

The cryogenic mechanochemical method results in high AlH_3 yields with a LiCl salt by-product. As a result, cryogenic milling is the preferred synthesis method in synthesising AlH_3 because low temperatures restrict alane decomposition.

Knott developed [191] a wet mechanochemical method of synthesising AlH_3 in solution (1,4-dioxane) as follows:

$$2AlCl_3 + 3MgH_2 \longrightarrow 2AlH_3 + 3MgCl_2 \qquad \Delta_r G_{298K} = -161 \text{ kJ/mol} \tag{4.5}$$

The AlH_3 reaction product after milling is in a dissolved form in 1,4-dioxane and is separated from the $MgCl_2$ by-product by filtration or centrifugation. If the solution is milled for too long AlH_3 is noted to decompose according to Reaction 4.4.

Recently Sartori *et al.* [192] performed mechanochemical synthesis of alane by a number of other chemical pathways. The following reactions all resulted in α and α'-alane formation in different ratios [192]:

$$3LiAlD_4 + AlCl_3 + nFeF_3 \tag{4.6}$$

where small quantities of FeF_3 was used to promote α'-alane formation,

$$3NaAlH_4 + AlCl_3 \tag{4.7}$$

which is the sodium analogue of Reaction 4.3, and

$$3LiAlD_4 + AlBr_3 \tag{4.8}$$

Additional reactions were also attempted [192] with no crystalline alane detected: $Na_3AlH_6 + AlCl_3$, $3LiAlD_4 + TiCl_3$, and $3LiH + AlCl_3$.

4.1.1.6 *Supercritical Synthesis*

Supercritical fluids have been used in the past to enable hydrogenation of depleted metal hydride compounds at lowered pressure and temperature conditions [193]. A preliminary study [194] revealed that 0.5 wt.% H_2 introduction into aluminium metal was possible through supercritical CO_2 techniques, forming a partial AlH_3 phase. However it has been noted [195] that supercritical CO_2 is not a particularly good solvent as many other fluids have higher solubility properties. These alternative supercritical fluids allow for improved AlH_3 yields [196].

4.1.1.7 *Electrochemical Synthesis*

Alane has been reported to be synthesised using an electrochemical charging technique [197] that is undertaken in a non-aqueous medium (i.e. in tetrahydrofuran or diethyl ether). A hollow Pd/Ag electrode is filled with dehydrided AlH_3 (i.e. Al) that acts as an anode forming part of an electrochemical cell using a solution containing either dissolved $LiAlH_4$, $NaAlH_4$, $KAlH_4$, or $AlCl_3$ [197]. The synthesis method is reported to be very slow at present, requiring 450 hr to form 1 g of AlH_3 [197].

4.1.1.8 *Synthesis of Solvates or Complexes*

Aluminium has been hydrided using H_2 gas pressure when titanium doped Al is present in a tetrahydrofuran (THF) or diethyl ether solution, which acts as an electron donor, stabilising AlH_3 with an organic adduct [198]. Hence the AlH_3 is not synthesised in its pure form but is stabilised by an adduct, however in some cases this adduct can then be removed with heating resulting in pure AlH_3 [198]. A range of alane complexes, or adducts, are reported to form under much milder synthesis conditions including $AlH_3.C_6H_{12}N_2$, $AlH_3.Et_2O$, AlH_3.TEDA, $AlH_3.N(C_2H_5)_3$, $AlH_3.n$THF [159].

4.1.2 Properties

Alane can be synthesised by a number of means resulting in samples that behave differently during decomposition. Alane powder which was chemically synthesised [180] by the Dow Chemical Company is reported [199] to consist of 50 – 100 μm cuboids that are light grey in colour. It should be noted that the Dow synthesised material used by an array of journal authors [4,131,173,199-203] consisted of large micrometer sized

particles and it was allowed to be handled extensively in open air leading to oxygen contamination by the creation of a heavy aluminium oxide layer (Al_2O_3).

4.1.2.1 *Phases*

Alane has been described to exist with both ionic and covalent characteristics [204]. It has sometimes been explained by its polymeric characteristics as $(AlH_3)_n$, where a single alane molecule has the symmetry given by the point group D_{3h} [204]. There are seven (α, α', β, γ, δ, ε, ζ) known structural phases of alane [180]. Diffraction patterns for all of the phases have been obtained although indexing of the patterns has only been performed on some of the phases (α, α', β, γ) [67,181,205-206]. As such, the crystal structures of three alane phases are not yet known. No structural phase changes have been evidenced in α-alane even when it has been loaded under very high compressive forces up to 35 GPa [189]. However it was found that γ-AlH_3 irreversibly transitions to α-AlH_3 at ~ 12 GPa [207].

The crystallisation of the alane phases has been observed by polarising-light microscopy [180], which has led to a description of the crystal shapes. Brower *et al.* [180] determined that during bulk synthesis the α-phase forms crystals with hexagonal or cubic silhouettes, the γ-phase appears as bundles of fused needles, the α'-phase appears as small multiple needles growing from single points to form fuzzy balls, and the etherated phase precipitates as translucent spheres.

Crystal structure information is provided in Table 4-1 which illustrates the significant volume expansion required upon aluminium hydrogenation. The densities of the known AlH_3 phases are much lower than for aluminium, especially in the case of β-AlH_3. Consequently the crystalline volume expansion required to form AlH_3 from Al and H_2 is very large (> 79.9%). The large crystalline volume expansion is likely a main factor in the necessity for the extreme hydrogen pressures required to form AlH_3. As such, only the highest density α-AlH_3 phase has been formed in the past by applying hydrogen pressure (as described in Section 4.1.1.1).

Table 4-1: Alane phase information from solved crystal structures [67,181,205-206]. The volume expansion in comparison to Al is provided.

	Al	α-AlH_3	α'-AlH_3	β-AlH_3	γ-AlH_3
Crystal Structure	Cubic Fm-3m	Trigonal R-3c	Orthorhombic Cmcm	Cubic Fd3m	Orthorhombic Pnnm
Density (g/cm^3)	2.70	1.49	1.27	0.71	1.31
Volume expansion	-	79.9%	111.0%	277.5%	104.6%

4.1.2.2 *Thermodynamics*

The thermodynamics of formation for AlH_3 from the elements (see Reaction 4.1) has been studied theoretically and experimentally in the literature. Thermodynamic data is presented in Table 4-2 illustrating that some variability in the enthalpy data exists. However, all of the data suggests that the formation enthalpy of AlH_3 is weakly negative leading to a strongly positive change in Gibbs free energy.

Table 4-2: Alane thermodynamic formation data summary.

Phase	ΔH_{298K} (kJ/mol AlH_3)	Technique	Reference	ΔG_{298K} (kJ/mol H_2)
α-AlH_3	-11.4 ± 0.8	Calorimetry	Sinke *et al.* [131]	46.5
α-AlH_3	-	Eq. Pressure	Baranowski & Tkacz [4]	30.2
α-AlH_3	-6.95	Theoretical	Wolverton *et al.* [208]	49.8
α-AlH_3	-12.35	Theoretical	Ke *et al.* [209]	44.8
α-AlH_3	-9.9 ± 0.6	DSC	Graetz & Reilly [172]	48.5
β-AlH_3	-8.0 ± 1.0	DSC	Graetz & Reilly [172]	50.5
γ-AlH_3	-7.1 ± 1.0	DSC	Graetz & Reilly [172]	51.4

Calorimetry was performed during the decomposition of alane (AlH_3) in order to determine the alane formation enthalpy. In order to do this it was assumed that the magnitude of the decomposition enthalpy is equivalent to the formation enthalpy with the only difference being a sign change [172]. The differential scanning calorimetry (DSC) results [172] are especially interesting for the α, β and γ-phases of alane because ex-situ XRD was performed at significant intervals during alane decomposition. The XRD demonstrated a phase change for both β-AlH_3 and γ-AlH_3 into α-AlH_3 occurred before decomposition to the elements (see Section 4.1.3.2 for more information).

The thermodynamic data in Table 4-2 indicates that aluminium hydride is unstable with respect to the formation of its elements under normal conditions of temperature and pressure [4]. This means that alane should naturally decompose to yield aluminium and hydrogen gas [210]. It is however kinetically stabilised, primarily by oxide layers, which prevent hydrogen release. The thermodynamic properties for bulk alane are presented in Section 1.3.2, which are an extrapolation from experimental data. The thermodynamic properties allow for hydrogen equilibrium pressures to be calculated as presented in Figure 1-8.

It is possible to alter the thermodynamic properties to some degree by forming nanoparticles of alane and/or aluminium as discussed in Section 1.4.2. Slight variations in the thermodynamic properties of AlH_3 formation may have a significant impact on the hydrogen equilibrium pressure. This is due to the low magnitude of the formation reaction enthalpy (see Table 4-2) that could be altered by a significant percentage.

4.1.2.3 *Pressure Relationships*

The availability of experimental data regarding hydrogen equilibrium pressures for AlH_3 is limited due to the experimental difficulty of these high pressure measurements. The equilibrium pressure for alane has been experimentally shown [4] to be 7 - 10 kbar at 140 - 150°C for AlH_3 desorption and 28 kbar at 300°C for absorption. Other results in the literature are in line with these measurements where equilibrium pressures of 25 kbar at 120°C [5] and 20 kbar at 150°C [175] have been determined. Despite the very high equilibrium pressures, bulk AlH_3 is stable at room temperature because of surface oxide layers which acts as a kinetic barriers to decomposition [185]. More information is provided in Section 4.1.1.1.

Hydrogen equilibrium pressures for AlH_3 can be calculated from published thermodynamic data. However it is of vital importance to use fugacity to represent the chemical potential of the system rather than pressure as discussed in Section 1.3.2. Mistakes have been made in the literature where a hydrogen pressure of 500 kbar has been calculated for AlH_3 at 25°C [172,211] which is in fact the fugacity, not the pressure. The same mistake has also been made by Claudy *et al.* [212] where a pressure of 100 kbar is reported, which is actually the fugacity.

4.1.2.4 *Safety Concerns*

Concerns have been made [173] over the need for detailed safety studies on alane before its use as a hydrogen storage medium in commercial vehicles. The concerns are justified, especially due to the fact that alane is used as an additive to solid rocket fuel [173], where its ignition temperature has been determined as 1450 K [213]. Pyrophoricity is a major concern, especially when dealing with doped alane, even though undoped ~300 nm alane particles were not pyrophoric before or after decomposition [173]. Graetz & Reilly [185] do however note that freshly prepared, non-

passivated alane (~150 - 200 nm) is pyrophoric and reacts violently with water and as such must be treated with caution. Concerns have also been raised over the sensitivity of AlH_3 to friction [213].

The combustion of AlH_3 has been investigated at 1500 K [213] where a two-step reaction is proposed to occur as follows:

$$\begin{aligned} AlH_3 &\longrightarrow Al + \frac{3}{2}H_2(g) \qquad \Delta_r G_{298K} = -46.5 \text{ kJ/mol} \\ Al + \frac{3}{4}O_2 &\longrightarrow \frac{1}{2}Al_2O_3 \qquad \Delta_r G_{298K} = -791 \text{ kJ/mol} \end{aligned} \tag{4.9}$$

The dehydrogenation reaction was found to take place on a time scale of 100 μs at 1500 K which is faster than the ignition and combustion of the AlH_3 particles. However at milder temperatures it is possible that other, more exothermic reaction pathways could proceed as follows:

$$2AlH_3 + 3O_2(g) \longrightarrow Al_2O_3 + 3H_2O(g) \qquad \Delta_r G_{298K} = -2361 \text{ kJ/mol} \tag{4.10}$$

$$2AlH_3 + 3H_2O(g) \longrightarrow Al_2O_3 + 6H_2(g) \qquad \Delta_r G_{298K} = -990 \text{ kJ/mol} \tag{4.11}$$

Care must be taken when handling AlH_3 especially when it is in the form of a fine powder. Further safety studies must be undertaken prior to implementation of AlH_3 (or any other fine metal hydride) as a fuel tank for vehicles. Engineering solutions may be able to significantly minimise the risks in storing hydrogen in this manner.

4.1.3 Decomposition

Early studies [180] identified seven non-solvated AlH_3 polymorphs but until recently subsequent studies [4,131,173,199-203] were all based upon α-alane samples obtained from the Dow Chemical Company. The Dow alane samples consisted of large cuboids (50 – 100 μm) that had a thick oxide coating creating a high activation barrier and slow desorption kinetics. These problems are not observed in freshly synthesised α-alane [185]. The aluminium oxide (Al_2O_3) surface barrier can be disrupted by adding dopants during ball milling thereby enhancing the desorption kinetics [203]. Similarly the desorption kinetics can be improved by particle size reduction e.g. by ball milling [173]. Exposure to UV light has also been found [199] to induce the decomposition of alane. It

has been found [211] that it is not necessary to ball mill freshly prepared alane or add dopants/catalysts in order to obtain adequate desorption rates at low temperatures (< 100°C) due to their lack of a significant oxide layer.

Results in the literature are contradictory in relation to changes in particle structure upon AlH_3 decomposition. It was found by Sandrock *et al.* [173] that there was no significant decrepitation from the decomposition of AlH_3 to Al and H_2 contrary to findings by Herley *et al.* and also Ismail & Hawkins [199,210]. It has been noted [210] that a theoretical density increase (1.486 to 2.71 g/cm^3) occurs when α-alane completely desorbs to form aluminium cuboids. During the desorption process the crystal size and structure will change from hexagonal α-alane (lattice parameters: a = 4.449 Å and c = 11.804 Å [181]) to face centred cubic (FCC) aluminium (a = 4.0496 Å [214]); this change in density has since been verified to occur during the total decomposition of α-alane [210].

4.1.3.1 *Kinetics of Decomposition*

There are a number of different parameters that influence the kinetics of the AlH_3 decomposition reaction, such as: grain boundaries, defects, surface area, nucleation sites, and thermal conductivity [185]. The decomposition kinetics have been found to be only slightly affected by the introduction of mild back pressures (~3 bar) [203]. It has been noted [185] that generally a single mechanism will dominate the decomposition reaction as a rate-limiting step which can be determined from isothermal decomposition experiments.

4.1.3.2 *Effect of Phases*

The effect of different alane phases on the decomposition reaction has been studied using DSC [172]. The decomposition of alane (AlH_3) is represented by an exothermal trough in each DSC plot. The DSC plot for α-AlH_3 only has one exothermal trough representative of this decomposition, but the DSC plots for both the β and γ-phase contain an endothermal peak prior to decomposition. It can be seen from XRD data [172] that these endothermal peaks are representative of the deterioration of the β and γ-phases that form the more stable α-phase prior to decomposition into aluminium and hydrogen gas. The phase transformations can create confusion (i.e. Graetz & Reilly [185]) if an Arrhenius plot is generated, describing decomposition rates at various

temperatures. This is because the decomposition of β and γ-alane behaves in a non-linear fashion as the phase change and decomposition reaction are not noticeably separable.

It was found [180] that Dow synthesised α-AlH_3 decomposed between 0.5 – 2% at 60°C after 6 days. More notable was the finding that the metastable phases (β & γ) decomposed to the elements at rates 3 - 10 times faster than α-AlH_3 at 60°C [180]. The increased rates of decomposition for non-α-alane have also been verified for freshly prepared alane [211]. The kinetics for β & γ-AlH_3 are affected by the phase transition to the α-phase (especially at $T > 100$°C) which complicates their analysis, but it has been determined that some fraction of the β & γ-polymorphs decompose directly to $Al + H_2$ at low temperature [211]. This direct decomposition of the β & γ-phases is faster than the α-phase due to the total formation enthalpy being lower [211] as shown in Table 4-2.

4.1.3.3 *Effect of Particle Size Reduction*

The effect of particle size reduction on the temperature required for desorption has been studied previously [173]. This study still however concentrates on bulk AlH_3 but from this research it is clear that a reduction in particle size increases the rate of alane decomposition. There is a concern over the measures taken to minimise sample oxidation in these experiments. It appears that measures were not taken as smaller particles have a lower total percentage of hydrogen desorption indicating that they have higher levels of oxide content due to their higher surface areas. The oxide layer can be reduced by not allowing the alane to be exposed to air or moisture, and it is expected that the rate of decomposition might be faster for alane without an oxide/passivated surface layer. It should also be noted that the particle size values given by Sandrock *et. al.* [173] are very approximate as there is high polydispersity present in the samples. For these samples the isothermal desorption curve displays two segments which undergo different desorption rates. This behaviour can be explained by incomplete grinding of the AlH_3 particles [173].

Brower et al. [180] determined that thermal stability increases with increasing crystal size and perfection, which leads to the conclusion that particles of smaller sizes may decompose quicker or at lower temperatures. The effect of particle size on the

thermal stability of alane is a product of solid-phase reaction kinetics [215] which was determined by NMR measurements at 380 K for a variety of AlH_3 samples of altered particle sizes. The fact that particle size is related to the kinetics indicates that the decomposition reaction occurs at the AlH_3 grain surface [215].

4.1.3.4 *Effect of Doping*

An array of dopants have been ball milled with alane to induce alloying and to increase the decomposition reaction rate [173]. Both Ni and Ti were found to have no measurable effect on the rate of decomposition [173]. Similarly CaH_2 was used as a potential reductant of the Al_2O_3 surface layer with little or no beneficial effect [173]. However positive kinetic results were obtained with the addition of alkali-metal hydrides such as LiH, NaH, KH, [203] and $LiAlH_4$ [173]. These dopants are expected to form "*surface layers or islands of alanate that serve as 'windows' for hydrogen egress from the decomposing* AlH_3" [173]. The alkali metal hydride dopants almost entirely convert to their associated alanate after ball milling [203]. By adding Ti to LiH doped alane during ball milling significant room temperature desorption is observed [203].

4.1.3.5 *Stabilisation*

Increased thermal stability of aluminium hydride is possible by coating the surface with an organic compound containing a phenyl group or a condensed ring structure [216]. Alane has also been coated with aluminium metal which can assist in friction sensitivity problems [213]. Coating techniques have primarily been used to extend the shelf life of alane for use in rocket propellant formulations.

4.1.4 Oxide Layers

When alane is exposed to air a fine white powder forms on the AlH_3 crystal surfaces and when the alane is re-exposed to air there is no further degradation [181]. This behaviour is indicative of a surface oxide/hydroxide layer forming on the alane particles [189] which then prevents further interaction of a clean alane surface with the atmosphere, hence stabilising the particles.

Hydrogen bubbles (1-10 μm) have been found to form during the decomposition of alane (after aluminium thin films were plasma charged) which has been attributed to

an Al_2O_3 oxide layer acting as a permeation barrier [182]. Permeation of hydrogen through Al_2O_3 is very low and hence it is used as a barrier coating in hydrogen gas storage systems [137-138].

4.2 MECHANOCHEMICAL SYNTHESIS

Alane has recently been synthesised mechanochemically as a mixture of both the α-AlH_3 and α'-AlH_3 phases according to [67]:

$$AlCl_3 + 3LiAlH_4 \longrightarrow 4AlH_3 + 3LiCl \qquad \begin{matrix} \Delta_r G_{298K} = -191\,\text{kJ/mol} \\ \Delta_r G_{77K} = -158\,\text{kJ/mol} \end{matrix} \qquad (4.12)$$

The reaction progresses both at room temperature and at 77 K due to the relatively high change in Gibbs free energies. Brinks *et al.* [67] surmised that room temperature synthesis was inefficient in synthesising AlH_3 due to low alane yields and high Al content. Aluminium forms due to the high milling energy at room temperature which allows for AlH_3 to decompose to Al and H_2. As a result, cryogenic milling is the preferred synthesis method in synthesising AlH_3 because low milling temperatures restrict AlH_3 decomposition.

The mechanochemical synthesis of alane according to Reaction 4.12 was undertaken in an attempt to understand the impact of variations to milling parameters at both room temperature and 77 K. The use of a reaction buffer to promote nanoparticle formation has not been used in the past during AlH_3 mechanochemical synthesis and its effect on the hydrogen sorption properties are of interest due to the ability to control particle size when using a buffer [66].

In order to simplify discussion, sample names have been assigned to each sample synthesised under varied conditions as presented in Table 4-3. It should be noted that all room temperature synthesised samples were milled in fixed quantities to produce a 1 g yield of AlH_3. The milling time for cryogenically synthesised samples was broken into 2 min milling sessions separated by either 0.5 or 1 min rest periods for the 190 cm^3 and 14.3 cm^3 canisters respectively. The canister was allowed to rest whilst submerged in 77 K liquid nitrogen in order to cool the milled powder in an attempt to restrict hydrogen evolution during high energy milling. Cryogenic milling was undertaken with a milling rod impact rate of 20 impacts/s with 1 g total sample quantities (except in the 190 cm^3 canister where 2 g total samples were milled).

Table 4-3: Mechanochemically synthesised AlH_3 sample details. B:P and R:P are the ball to powder and rod to powder mass ratios respectively. Volume ratios refer to final reaction products.

Sample Name	Milling Temp. (K)	Time (min)	B:P / R:P	Volume Ratio ($LiCl:AlH_3$)	Ball and Canister Sizes (Notes)
AlH3_RT_7.7to1_50min_Step_7.938	298	50	7.7:1	2.2:1	7.938 mm (stepwise time)
AlH3_RT_7.7to1_60min_7.938	298	60	7.7:1	2.2:1	7.938 mm
AlH3_RT_39.3to1_60min_7.938_12.7	298	60	39.3:1	2.2:1	7.938 & 12.7 mm
AlH3_RT_39.3to1_120min_7.938_12.7	298	120	39.3:1	2.2:1	7.938 & 12.7 mm
AlH3_RT_39.3to1_180min_7.938_12.7	298	180	39.3:1	2.2:1	7.938 & 12.7 mm
AlH3_RT_13.2to1_120min_4	298	120	13.2:1	2.2:1	4 mm
AlH3_RT_13.2to1_240min_4	298	240	13.2:1	2.2:1	4 mm
AlH3_RT_13.2to1_360min_4	298	360	13.2:1	2.2:1	4 mm
AlH3_Cryo_190cc_180min_0.76vol	77	180	70.6:1	0.76:1	190 cm^3
AlH3_Cryo_14.3cc_1min_0.76vol	77	1	32:1	0.76:1	14.3 cm^3
AlH3_Cryo_14.3cc_15min_0.76vol	77	15	32:1	0.76:1	14.3 cm^3
AlH3_Cryo_14.3cc_30min_0.76vol	77	30	32:1	0.76:1	14.3 cm^3
AlH3_Cryo_14.3cc_60min_0.76vol	77	60	32:1	0.76:1	14.3 cm^3
AlH3_Cryo_14.3cc_60min_2vol	77	60	32:1	2:1	14.3 cm^3

4.2.1 Unique Washing Difficulties

The selection of an appropriate solvent is a crucial part of the synthesis process as the solvent must firstly be able to dissolve large quantities of the by-product phase (LiCl), it must be relatively unreactive to the alane nanoparticles, and it must also have a low viscosity so that it may be separated from the nanoparticles once it has dissolved the by-product phase. Solvent choice is made very difficult because alane is a powerful reducing agent that has been found to react very rapidly with a large quantity of materials [89]. The reactions are known to either evolve hydrogen gas or form solution by-products. Alane also dissolves in certain solvents which dissolve LiCl such as tetrahydrofuran (THF). However, in the literature, some solvents were found to be relatively inert or only reacted very slowly with alane that was dissolved in tetrahydrofuran such as [89]: 1-nitropropane, nitrobenzene, azobenzene, azoxybenzene, methyl p-tolyl sulfide, diphenyl sulfone, and cyclohexyl tosylate.

Information regarding the tested solvents is provided in Section 2.1.5.1. Testing revealed that two solvents (nitromethane and toluene) appeared to be suitable in washing LiCl from AlH_3 due to the fact that these solvents appeared to be relatively or completely inert to alane. The solvents were able to dissolve high quantities of lithium chloride if there were other salts present in solution such as aluminium chloride ($AlCl_3$). As such, aluminium chloride was added in a 3:1 ratio of $AlCl_3$:LiCl

in order to promote LiCl solubility in nitromethane and toluene. Centrifugation was used to separate the solvent containing the dissolved LiCl by-product phase from the alane nanoparticle product, and the saline solution was decanted. Washing was performed three times, twice with a solvent/$AlCl_3$ mix and once with the pure solvent.

Room temperature milled AlH_3 samples did not present any visible signs of reaction with the nitromethane/$AlCl_3$ solvent however noticeable gas evolution was present on addition of the cryogenically milled samples to the nitromethane solution. The gas evolution indicates an adverse reaction between the solvent and cryogenically milled sample. This is an indication that either the cryogenically milled alane is more reactive, or that a reaction between nitromethane and the $LiAlH_4$ starting reagent was observed, due to the cryogenic reaction not reaching completion. It should be noted that $LiAlH_4$ is violently reactive with nitromethane and significant quantities of heat and fumes are generated upon contact with one another, even in dilute concentrations. Given the mild reaction between the solvent and the cryogenically milled sample it is unlikely that $LiAlH_4$ is present. Despite the observed reaction in cryogenically milled samples, the as-synthesised and washed alane samples were characterised to determine their hydrogen desorption kinetics and structural properties.

Washing the alane nanoparticles with toluene/$AlCl_3$ was attempted with limited success. The final stage of the washing procedure involves the removal of remaining solvent from the washed nanoparticle product. Final solvent removal is usually undertaken under vacuum as this results in rapid drying. XRD data is presented in Figure 4-1B for an AlH_3 sample that was washed with a toluene/$AlCl_3$ solution and evacuated for 19 hrs at room temperature to dry. XRD data reveals that only Al remains in the sample after washing. It is possible that all of the AlH_3 decomposes over time under vacuum, however the kinetics for alane decomposition are not generally this quick (see Section 4.3). It is most likely that the AlH_3 dissolved within the toluene/$AlCl_3$ solution as alane is known to dissolve in certain solvents such as THF. As such, the nitromethane/$AlCl_3$ solution was utilised for all AlH_3 washing procedures.

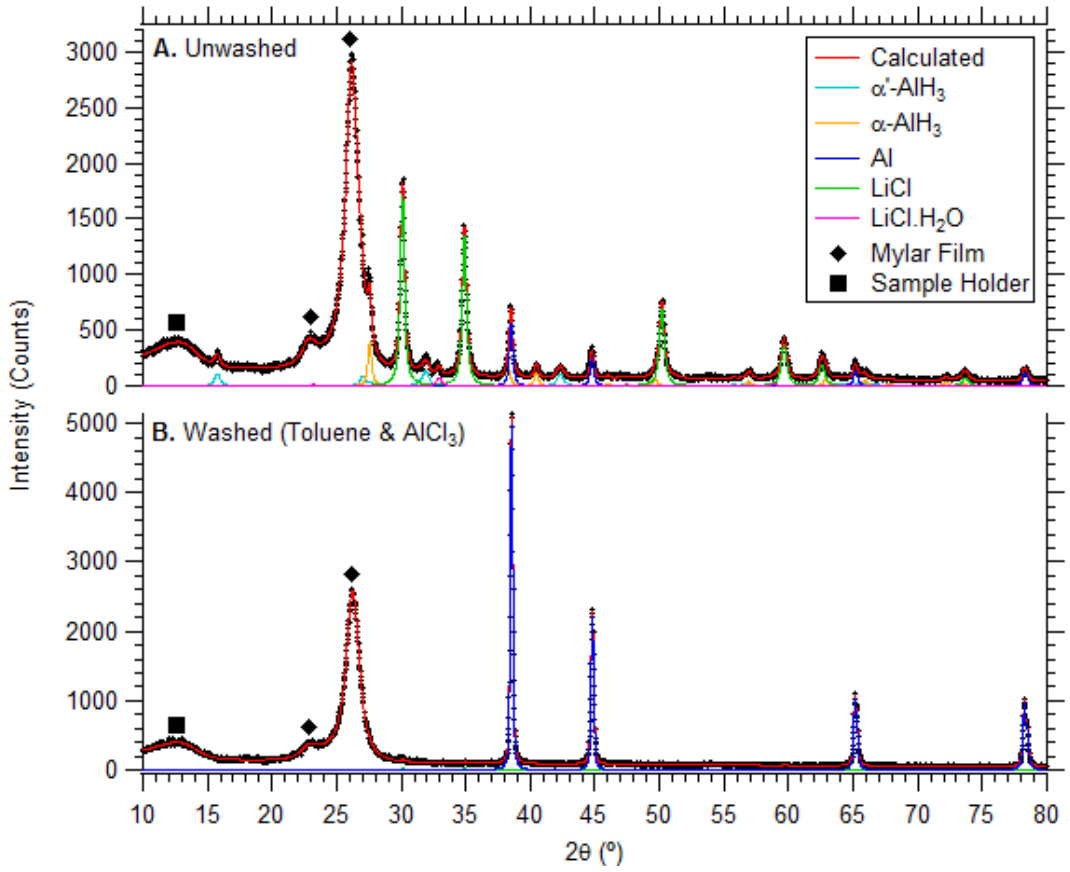

Figure 4-1: X-ray Diffraction (XRD) patterns (D500) from AlH3_Cryo_190cc_180min_0.76vol. Samples are A) as-milled and B) washed with toluene and $AlCl_3$.

4.2.2 Aging

Aluminium hydride (AlH_3) has been reported to be stable in air for decades at room temperature due to its heavy oxide coating [173], however freshly mechanochemically synthesised alane is unstable due to its clean oxide-free surface, which does not significantly kinetically restrict decomposition. Alane is prone to decomposition as a result of its thermodynamic properties because ΔG of formation is positive at temperatures greater than approximately -200°C (when extrapolated from experimental data [29] as shown in Figure 1-7). In fact, theoretical calculations [217] suggest that ΔG of formation is positive (for the AlH_3 phases investigated) at all temperatures, and as such decomposition may occur spontaneously.

Mechanochemically synthesised samples exhibit relatively rapid decomposition at room temperature (significantly over months) when stored under an argon atmosphere. The decomposition is evidenced by XRD data provided in Figure 4-2,

which displays a significant reduction in the AlH_3 content over one month, matched by an increase in the Al content of the sample when stored at ~ 25°C.

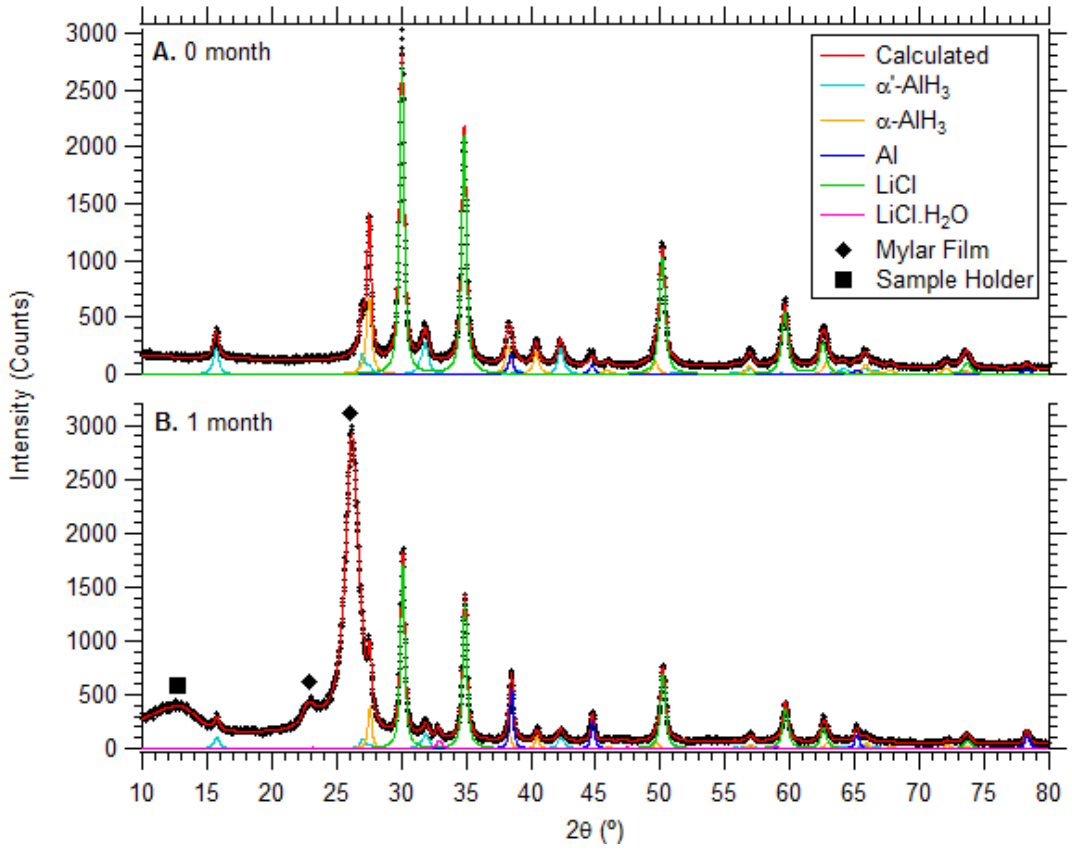

Figure 4-2: X-ray Diffraction (XRD) patterns (D500) from AlH3_Cryo_190cc_180min_0.76vol for A) as-milled powder, and B) after one month stored under argon.

Quantitative phase analysis results (see Table 4-4) outline the decomposition of the mechanochemically synthesised alane sample over time. After one month, the alane content has been reduced to 73% of its as-synthesised content, increasing the aluminium content significantly. LiCl content does not change over time, although some $LiCl.H_2O$ is present in the aged sample due to an improper seal with the mylar film during data collection. The α'-AlH_3 phase decreased by 20.3% whereas the α-AlH_3 phase decreased by 31.9 % over one month.

The disproportionate decomposition indicates that α-AlH_3 decomposes more readily at room temperature, provided that α-AlH_3 does not undergo a phase transition to α'-AlH_3 during this time. The result is curious because α-AlH_3 is reported to be the most stable alane phase [173] as both β- and γ-AlH_3 were shown to transition to α-AlH_3

before decomposition evidenced by calorimetry [172] and in-situ XRD [218-219]. The calorimetry results discount the possibility of an α-$AlH_3 \rightarrow \alpha'$-$AlH_3$ phase transition as no thermodynamic transitions were found during α-AlH_3 decomposition [172]. In fact, experimental and theoretical results [220] demonstrate that the opposite reaction can occur where α'-$AlH_3 \rightarrow \alpha$-AlH_3 if conditions are both kinetically and thermodynamically favourable. Therefore the disproportionate decomposition instead suggests a more rapid α-AlH_3 decomposition at room temperature in comparison to α'-AlH_3. α'-AlH_3 has been shown to be more stable than α-AlH_3 in other work [220] when stored at room temperature, where it was suggested that the high surface stability of α-AlH_3 may be the primary cause of the disparity. In the literature α-AlH_3 is the phase that is synthesised reversibly from the reaction of hydrogen gas with aluminium at extreme pressures [5,221]. The preferred formation may be due to α-AlH_3 having the most compact crystal structure, but the XRD results herein indicate that α'-AlH_3 is more stable over time at room temperature. In addition, theoretical results also show [209] that α'-AlH_3 is more stable than α-AlH_3 in regards to the thermodynamics of decomposition. It is not know if the α'-AlH_3 stability (seen at room temperature) is a function of either kinetic or thermodynamic factors.

Table 4-4: Quantitative results calculated from Rietveld fits to XRD data given in Figure 4-2 using Topas. Mathematical fitting uncertainties are provided (2 standard deviations).

	Phase	Crystalline wt. %	Crystallite size (nm)
0 Month	α'-AlH_3	14.8 ± 0.2	16.1 ± 0.6
	α-AlH_3	19.1 ± 0.3	15.0 ± 0.4
	Al	3.6 ± 0.1	18.0 ± 1.2
	LiCl	62.5 ± 0.3	27.5 ± 1.0
1 Month	α'-AlH_3	11.8 ± 0.3	15.6 ± 1.0
	α-AlH_3	13.0 ± 0.3	23.8 ± 1.2
	Al	13.4 ± 0.2	30.0 ± 0.9
	LiCl	59.4 ± 0.4	25.4 ± 1.0
	$LiCl.H_2O$	2.3 ± 0.2	18.8 ± 10.2

The stability over time does not seem to be related to crystallite size, as the average crystallite size of α-AlH_3 was found from Rietveld fits to be 15.0 ± 0.5 nm and 19 ± 1 nm for the 0 month and 1 month samples respectively, whilst the average crystallite size was 17.0 ± 0.6 nm and 17 ± 1 nm for α'-AlH_3 in the 0 month and 1 month samples respectively. The crystallite sizes are comparable between both phases but it is possible that particle size differences between the phases could lead to different decomposition rates. It is also possible that any phase transformations to or from

amorphous phases could bias these crystalline phase results obtained using quantitative phase analysis by the Rietveld method.

As a consequence of the rapid decomposition of alane at room temperature, samples were synthesised closely, in time, to characterisation unless stated otherwise. However some samples that were synthesised by room temperature milling, before knowledge of the high instability of the alane nanoparticles was known, did not always undergo the same level of temporal scrutiny that later samples received.

4.2.3 Room Temperature Milling

Room temperature milling is reported to produce low yields of alane [67] due to the decomposition of AlH_3 that results from high levels of milling energy. Room temperature ball milling was conducted under a variety of milling conditions in order to understand the impact of these conditions on AlH_3 yields and phase production.

4.2.3.1 *Milling Conditions*

Room temperature milling was initially undertaken using a mixture of 12.7 mm & 7.938 mm balls with a 39:1 ball to powder ratio (B:P) as a function of milling time. A LiCl buffer was used to provide a 2.2:1 volume ratio of $LiCl:AlH_3$ in the final product. XRD data in Figure 4-3 shows that alane was indeed synthesised according to Reaction 4.12, however the milling also resulted in high aluminium yields. The reaction progress is best understood by quantitative Rietveld results given in Table 4-5. It can be seen that the α'-AlH_3 phase is predominantly synthesised which is interesting considering that the α-AlH_3 phase has the most compact crystal structure and as such may be expected to be preferentially synthesised during milling due to high compressive milling forces.

Rietveld results indicate that more than 50% of the alane has decomposed to Al after one hour of milling time. Aluminium content increases as a function of milling time, which is expected given the low thermodynamic stability of alane [131], however the decrease in alane content is insignificant considering the decomposition that occurs after only one hour. The significant decrease in alane content after one hour most likely results from heat energy, not from the milling itself (which only provides slight alane reduction over time), but instead from the exothermic synthesis reaction

(Reaction 4.12). Milling provides the chemical reagents energy but also combines the reagents so that they may react with one another, and because the alane synthesis reaction is moderately exothermic (ΔH = -213 kJ/mol) it provides more than enough energy for AlH_3 to decompose to Al and H_2 due to the low amount of energy required for decomposition (ΔH = +11.4 kJ/mol).

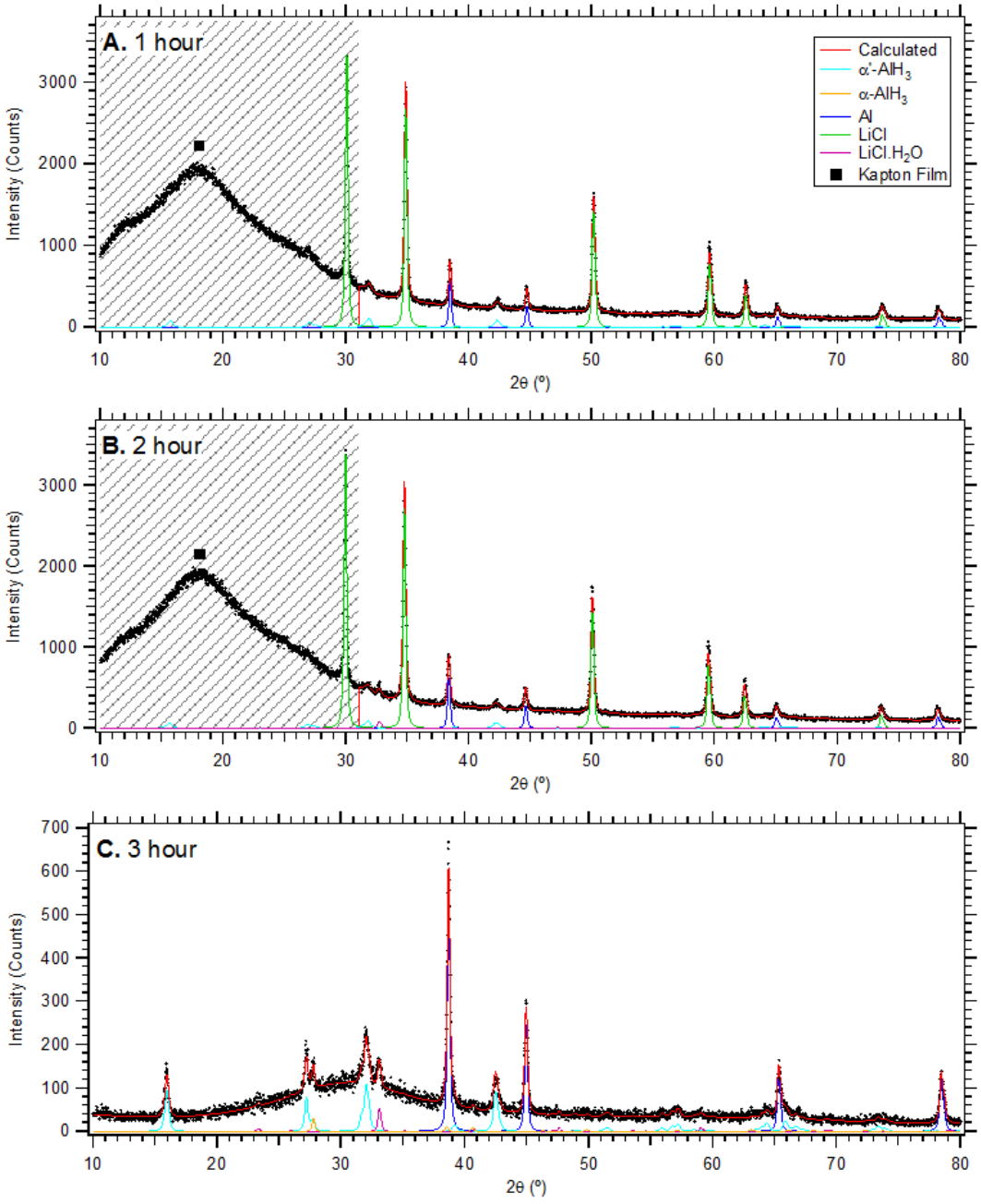

Figure 4-3: X-ray Diffraction (XRD) patterns (D500) from A) AlH3_RT_39.3to1_60min_7.938_12.7, B) AlH3_RT_39.3to1_120min_7.938_12.7, and C) AlH3_RT_39.3to1_180min_7.938_12.7. Patterns were collected before mylar film was available and were collected with either Kapton film or without film in air resulting in a complete reaction of LiCl with the moisture present in the air. Greyed out sections reflect regions not fit using Rietveld due to attenuation from the Kapton film.

It should be noted that the Rietveld fits in Patterns A & B in Figure 4-3 were undertaken at angles greater than 31° 2θ due to attenuation under the amorphous hump from the Kapton film which adversely affects the quantitative phase analysis of diffraction peaks below this angle. The Rietveld results evidence a decrease in the AlH_3 content resulting from longer sample exposure times to high energy milling and consequently an increase in Al content is observed as milling time increases. Although the XRD patterns reveal $LiCl.H_2O$ components in the samples, the overall LiCl content remains constant across the sample time series, indicating reaction completeness. In general, crystallite sizes for all phases decrease over time, except α'-AlH_3 which more than doubles in crystallite size in the 3 hour sample. However this sample was exposed to air, forming large quantities of $LiCl.H_2O$ that may have altered the sample due to moisture in the air. It is not known why AlH_3 crystallites would grow whilst Al crystallites remain a similar size.

Table 4-5: Rietveld fitting results for XRD patterns given in Figure 4-3. * The phase percentages for the 3 hour XRD pattern were calculated using a crystalline content of 24 % based on a fit to the amorphous hump in the data. Mathematical fitting uncertainties are provided (2 standard deviations).

	Phase	Wt. %	Crystallite size (nm)
1 hour	α'-AlH_3	9.7 ± 1.6	16 ± 6
	Al	11.3 ± 0.4	54 ± 6
	LiCl	78.9 ± 1.4	46 ± 6
2 hour	α'-AlH_3	9.0 ± 1.6	13 ± 6
	Al	12.7 ± 0.4	50 ± 6
	LiCl	76.1 ± 1.4	46 ± 6
	$LiCl.H_2O$	2.2 ± 0.6	40 ± 20
3 hour	α'-AlH_3	8.9 ± 0.2	30 ± 4
	α-AlH_3	0.6 ± 0.2	120 ± 180
	Al	13.0 ± 0.2	43 ± 2
	$LiCl.H_2O$	77 ± 16	60 ± 40

It can be seen from the Rietveld results in Table 4-5that more than 50% of the synthesised AlH_3 has decomposed to Al after just one hour of milling. The rapid decomposition is due to the significant energy produced during milling by the large balls. Because of this, room temperature milling was also undertaken using 4 mm balls (13:1 B:P) as a function of milling time with the same 2.2:1 ($LiCl:AlH_3$) final volume ratio. Smaller balls were utilised in a low ball to powder ratio in an attempt to slow the alane synthesis reaction (Reaction 4.12). It was thought that if the reaction proceeded more slowly less aluminium would be generated. A slow reaction

would limit the large quantity of heat rapidly generated by the exothermic synthesis reaction, restricting alane decomposition. XRD data is provided in Figure 4-4 as a function of milling time for "low-energy" alane synthesis.

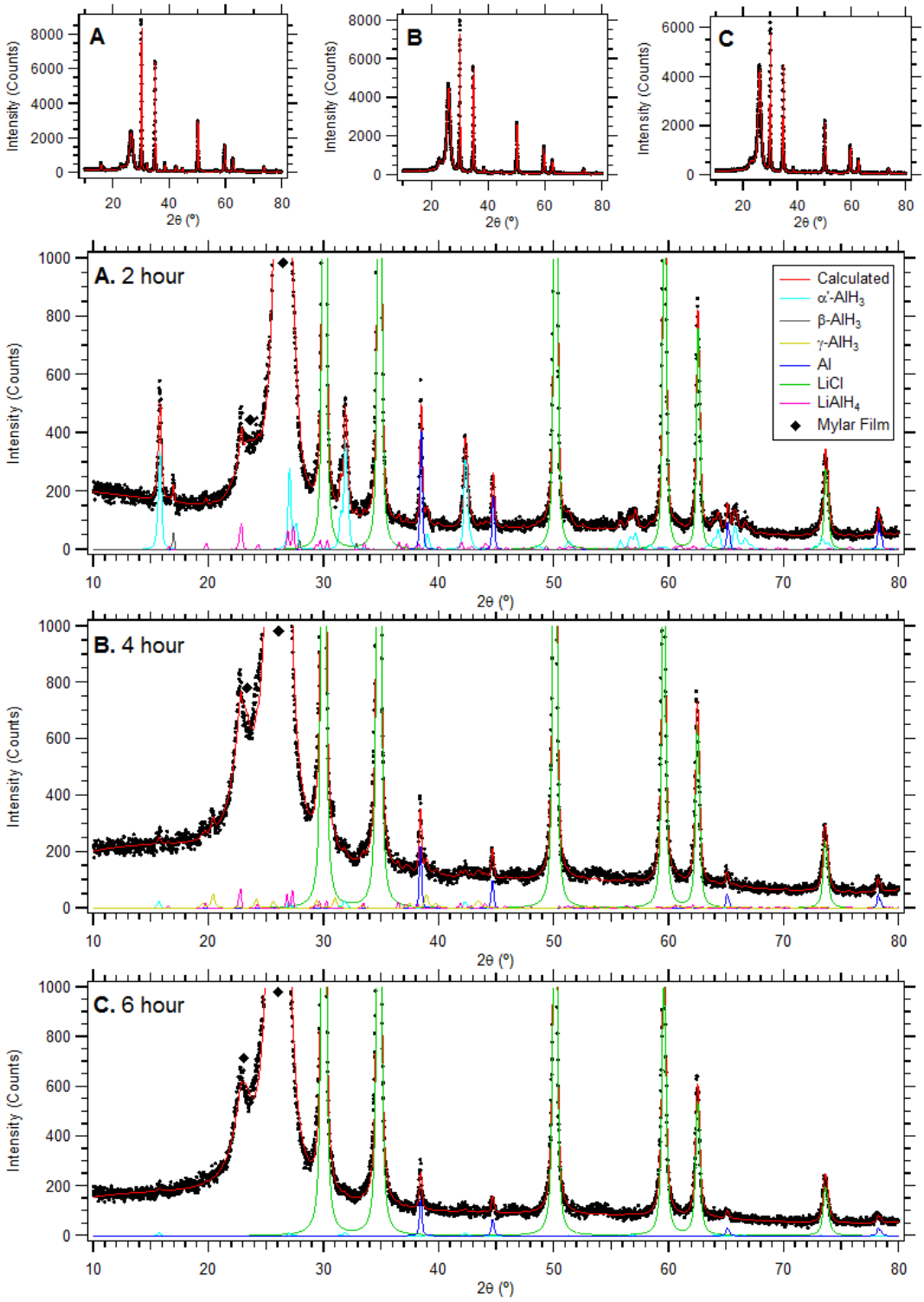

Figure 4-4: X-ray Diffraction (XRD) patterns (D500) from A) AlH3_RT_13.2to1_120min_4, B) AlH3_RT_13.2to1_240min_4, and C) AlH3_RT_13.2to1_360min_4. Full patterns are displayed as insets and scaled patterns are given to properly display minor phases present.

The XRD data is better understood by the quantitative Rietveld analysis provided in Table 4-6. Firstly, it is apparent from the 2 hour XRD data that low energy milling provides high alane content and consequently low aluminium content (3.5:1 AlH_3 to Al). This is in contrast to the "high-energy" room temperature milling XRD results (0.71:1 AlH_3 to Al after 2 hours) given in Table 4-5. However a lower milling energy results in an incomplete chemical reaction that is evidenced by minor traces of $LiAlH_4$ present in the 2 hour and 4 hour milled samples.

Table 4-6: Rietveld fitting results for the XRD patterns given in Figure 4-4. Mathematical fitting uncertainties are provided (2 standard deviations). Some crystallite sizes are not included due to the very low phase wt.% that makes results unreliable.

	Phase	Crystalline wt. %	Crystallite size (nm)
2 hour	α'-AlH_3	12.0 ± 0.2	36.9 ± 3.2
	β-AlH_3	0.7 ± 0.2	-
	Al	3.7 ± 0.2	64.6 ± 8.6
	LiCl	81.7 ± 0.6	407.4 ± 167.2
	$LiAlH_4$	1.9 ± 0.6	-
4 hour	α'-AlH_3	0.7 ± 0.2	-
	γ-AlH_3	2.6 ± 0.4	58.7 ± 33.0
	Al	2.2 ± 0.2	71.5 ± 19.8
	LiCl	92.0 ± 0.8	130.0 ± 21.2
	$LiAlH_4$	2.4 ± 0.8	-
6 hour	α'-AlH_3	0.4 ± 0.2	-
	Al	2.0 ± 0.2	43.2 ± 10.4
	LiCl	97.5 ± 0.2	65.3 ± 6.4

The low-energy XRD data provides unusual phase information as a function of milling time. Crystalline α'-AlH_3 is present in moderate quantities in the sample milled for 2 hours, but the alane content is reduced to almost zero in samples that were milled for longer. Minor traces of both β-AlH_3 and γ-AlH_3 are observed in some XRD patterns, indicating that alane phase transformations occur during milling. Despite the very low crystalline AlH_3 content in the 6 hour milled sample, given by XRD, hydrogen sorption measurements (see Figure 4-20 in Section 4.3) indicate that the sample contains a considerable portion of AlH_3. The 6 hour as-milled sample was incrementally ramped to 150°C over 120 hours and desorbed a quantity of hydrogen that equates to a 8.1 wt.% AlH_3 content in the entire synthesised sample (from a theoretical maximum of 24.6 wt.%). The hydrogen desorption result, in conjunction with the low crystalline Al and AlH_3 content in the sample milled for 6 hours, indicates that there is non-crystalline Al and AlH_3 present. It may also be possible

that the as-synthesised AlH_3 is so nanoscopic that some XRD peaks are hidden under the background noise. To the author's knowledge non-crystalline AlH_3 has not been previously reported in the literature. Theoretical investigations have suggested the possibility of certain crystalline AlH_3 phases existing in real samples that have not been identified experimentally to date [217]. But given that no unidentified crystalline peaks are present in the XRD patterns it is unlikely that these phases exist in the studied samples.

TEM investigations of the alane nanoparticles were performed whilst they were still embedded in salt. Micrographs provided in Figure 4-5 illustrate alane nanoparticles (~ 100 nm) embedded within larger (~ 400 nm) salt clusters. It can be seen that the alane nanoparticles decompose under the electron beam after a short time (3 min), resulting in a decrease in particle size and a change in electron contrast. The TEM investigation showed that the sample primarily consisted of large aggregates of salt containing smaller AlH_3/Al particles.

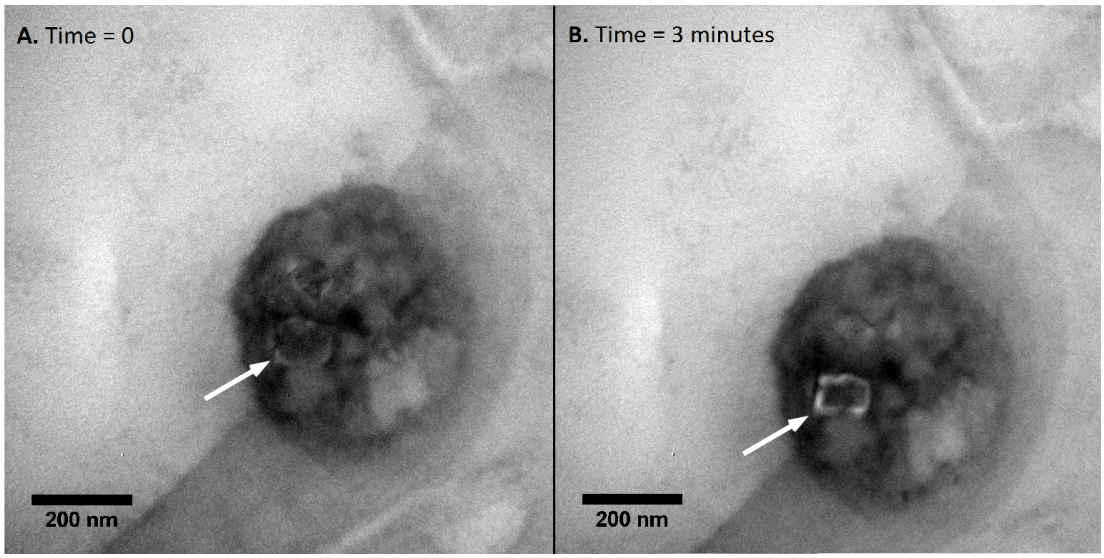

Figure 4-5: Transmission Electron Microscope (TEM) micrographs from AlH3_RT_7.7to1_50min_Step_7.938. Alane nanoparticles (~ 100 nm) embedded in LiCl salt clusters (~ 400 nm) are present. The alane (shown by the white arrow) decomposes over time under the electron beam.

4.2.3.2 *Washing*

Washing was performed three times, twice with a nitromethane/$AlCl_3$ solution and once with pure nitromethane. The samples synthesised at room temperature did not

show any signs of reaction with the solvent (i.e. no gas evolution was noticeable). After the AlH3_RT_39.3to1_60min_7.938_12.7 sample was washed (removing LiCl) two distinct particle morphologies existed. Large geometric-shaped single crystals were found as shown in Figure 4-6 and they were also present in large aggregate structures (see Figure 4-7). The large crystal in Figure 4-6 was identified as a LiCl single crystal using electron diffraction (see inset). Given that the LiCl phase is not detectable using lab-based XRD, its presence only in TEM investigations suggests that it is a minor sample component which is a remnant from the washing process.

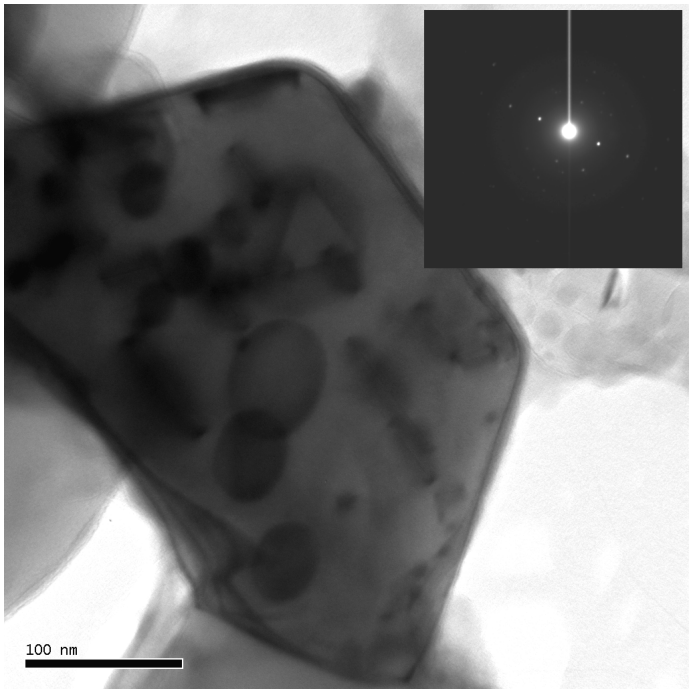

Figure 4-6: Transmission Electron Microscope (TEM) micrographs of a LiCl single crystal present in a washed sample AlH3_RT_39.3to1_60min_7.938_12.7. The contrast of the image has been adjusted for clarity. The inset displays an electron diffraction pattern for the LiCl single crystal.

The washed sample consisted primarily of the smaller crystals shown in Figure 4-8 that were identified to be Al-rich using energy dispersive x-ray spectroscopy (EDS) during TEM investigations. This indicates that these crystals are either AlH_3 or Al (resulting from alane decomposition). The washed AlH_3/Al nanoparticles in Figure 4-8 exist as aggregates and consist of 30 – 50 nm particles that appear similar to TEM micrographs of dehydrided α-AlH_3 particles recently presented in the literature

[222]. Although those shown in Figure 4-8 seem to be clusters of separate particles rather than large particles with internal structure.

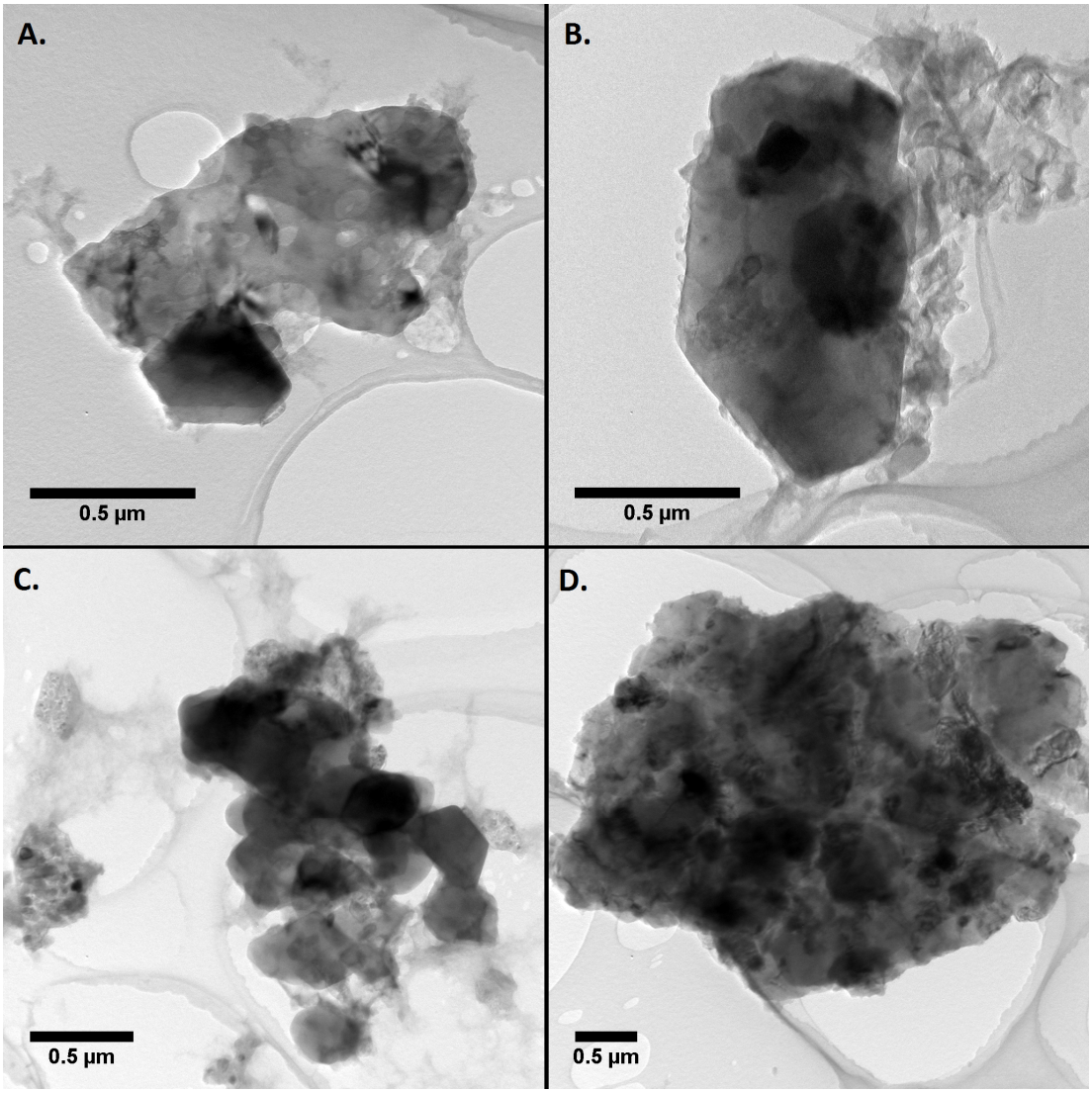

Figure 4-7: Transmission Electron Microscope (TEM) micrographs of a washed sample AlH3_RT_39.3to1_60min_7.938_12.7. A range of images (A – D) are shown to provide an average representation of the sample structure.

During TEM investigations, certain regions of the mechanochemically synthesised alane samples were found to contain some large Al-rich particles (AlH_3 or Al) as shown in Figure 4-9. The large ~1 µm particle contains high quantities of Al in conjunction with low quantities of Cl and O. Therefore the particle is either predominantly AlH_3 or Al and appears to be polycrystalline. EDS data, as provided in Figure 4-10, also verifies the presence of high quantities of Al and low quantities of Cl suggesting that the washing process was close to completion. Hydrogen cannot

be detected using EDS, primarily due to the high x-ray attenuation of the detector window, so AlH_3 and Al can't be differentiated. The fact that large Al/AlH_3 particles have been identified in the sample is an indicator of the low buffer volume ratio used. Smaller, more uniform AlH_3 particles are more likely to be synthesised when using higher reaction buffer volume ratios than those used to date.

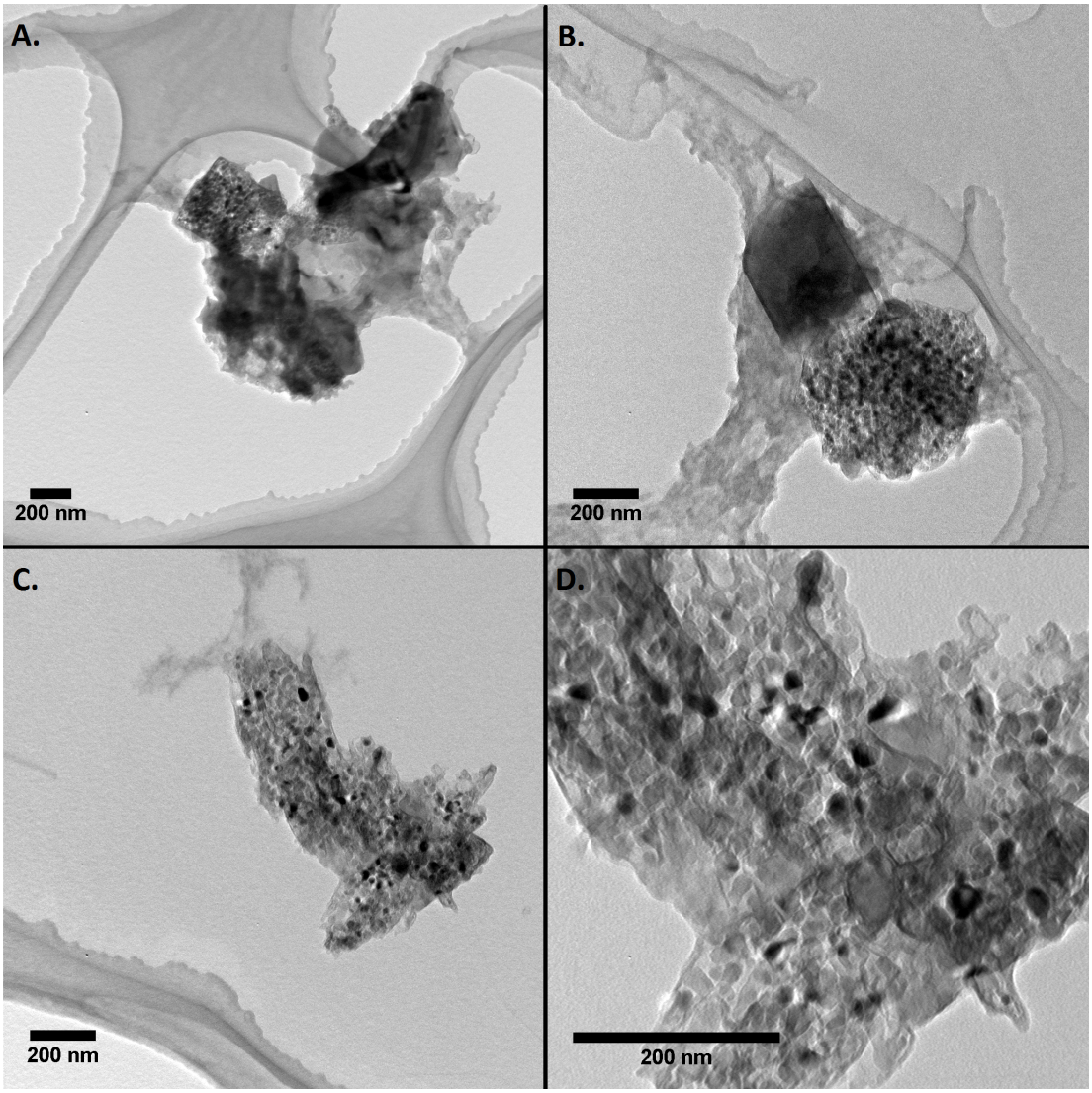

Figure 4-8: Transmission Electron Microscope (TEM) micrographs of a washed sample AlH3_RT_39.3to1_60min_7.938_12.7. A range of images (A – D) are shown to provide an average representation of the sample structure.

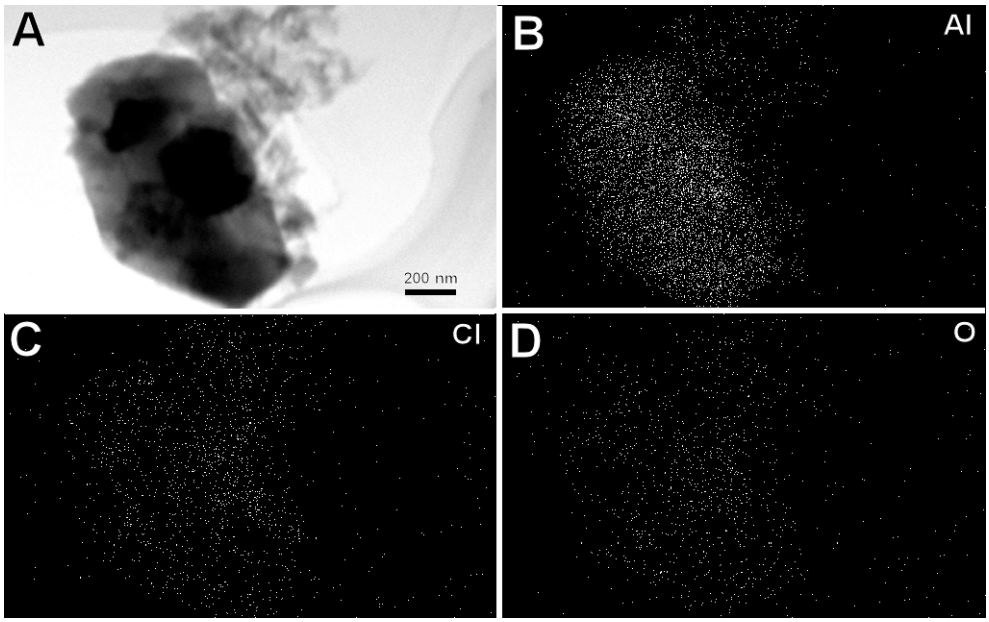

Figure 4-9: Transmission Electron Microscope (TEM) micrographs of a washed sample AlH3_RT_39.3to1_60min_7.938_12.7. EDS maps were collected in scanning TEM mode (STEM) on the particle in Figure 4-7B. A) STEM image with EDS for B) aluminium, C) chlorine, and D) oxygen. White dots indicate x-ray counts from the specified location.

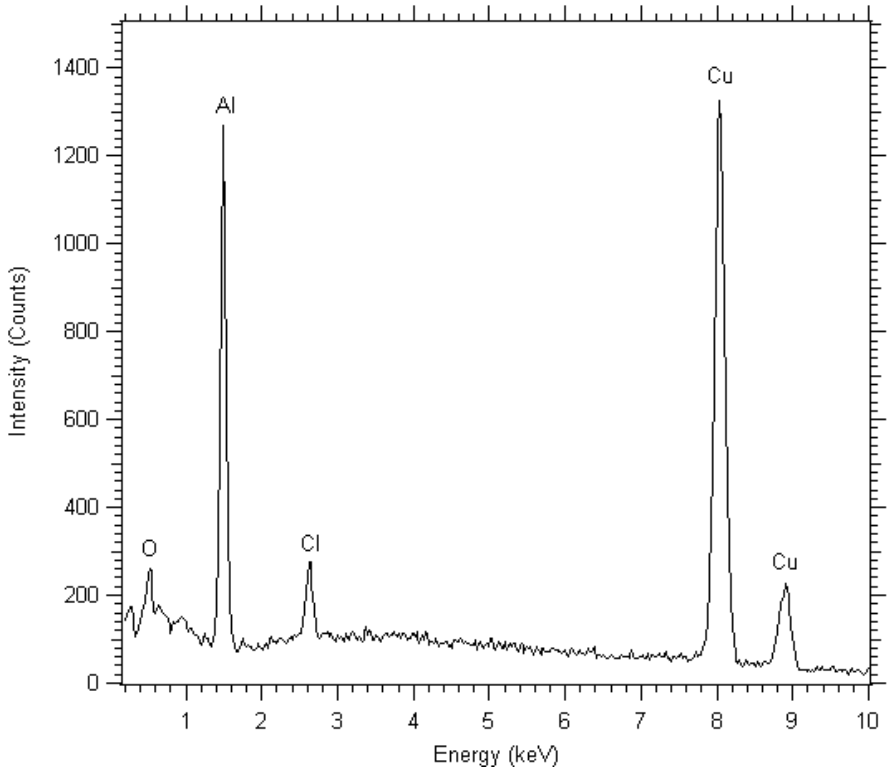

Figure 4-10: Energy dispersive x-ray spectroscopy (EDS) spectra from TEM investigations of washed nanoparticles as given in Figure 4-9 showing a high Al content, minor traces of Cl from residual LiCl, O from aluminium oxide due to sample air-exposure, and TEM grid component Cu.

4.2.4 Cryogenic Milling

Cryogenic (77 K) milling provides high alane yields (low Al content) due to the low milling temperatures, which minimise the decomposition of alane in contrast to room temperature milling [67]. Materials are also more brittle at lower temperatures in general, which can result in smaller crystallite sizes being generated during milling.

4.2.4.1 *Milling Difficulties*

Certain difficulties arose during cryogenic synthesis relating to design issues with the as-supplied Spex milling canisters. Firstly, sealing the as-supplied canisters was impossible due to the poor end-cap design. Secondly, large internal diameters within the 190 cm^3 metal canister combined with the soft metal used in their construction resulted in significant canister wear. Cryomilling did result in well milled samples (see Figure 4-11) but canister wear led to stainless steel contamination within synthesised samples as shown by the EDS results in Figure 4-12.

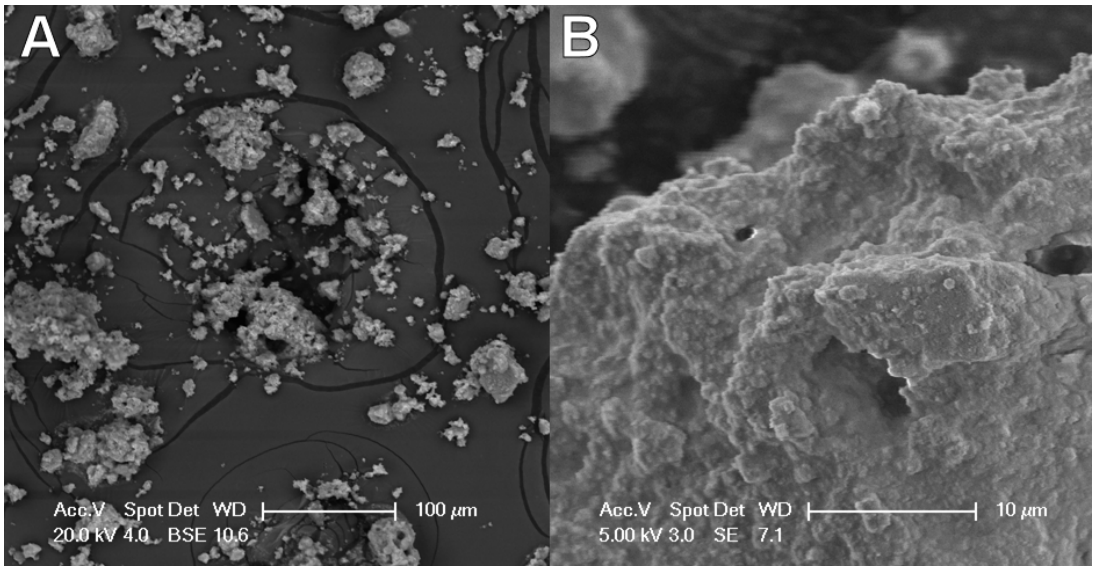

Figure 4-11: Scanning Electron Microscopy (SEM) micrographs from AlH3_Cryo_190cc_180min_0.76vol.

In order to synthesise high quality samples a custom made 14.3 cm^3 canister (obtained from E.MacA. Gray & M.P. Pitt at Griffith University) was utilised in the majority of AlH_3 sample synthesis. The canister was constructed from 440c stainless steel in order to minimise sample contamination and provide a vacuum tight seal with Teflon taped screw fittings which are made from steel and silver.

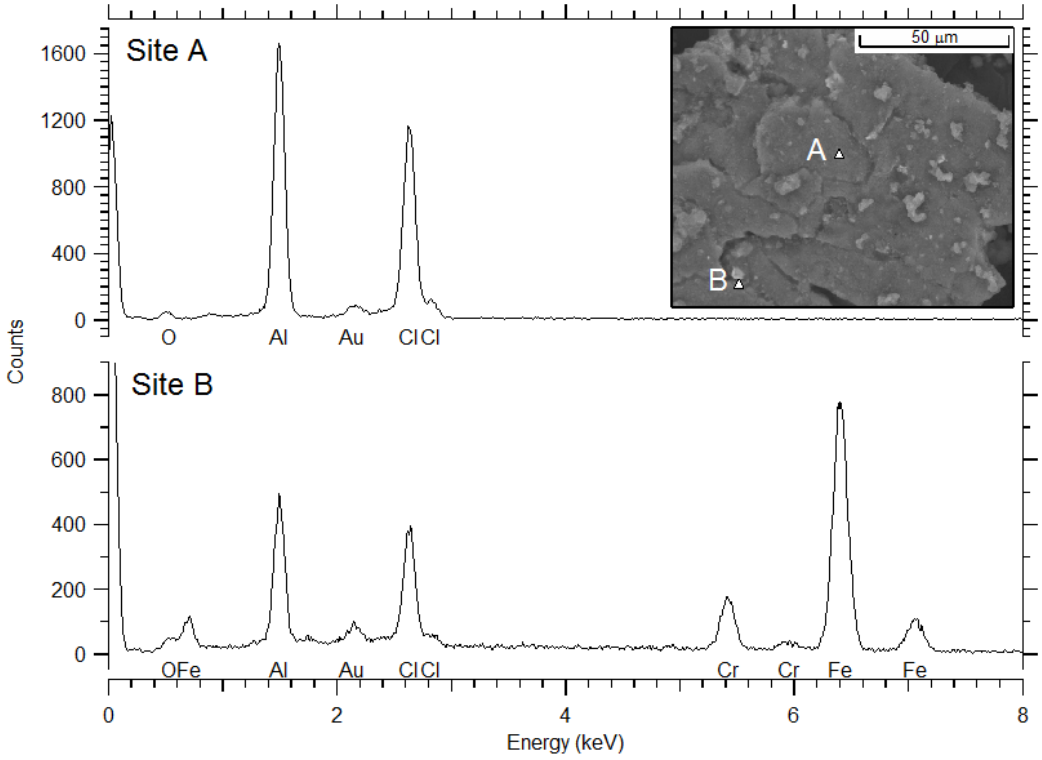

Figure 4-12: Energy dispersive x-ray spectroscopy (EDS) spectra from SEM investigations of AlH3_Cryo_190cc_180min_0.76vol. The inset depicts the sites of interest. The EDS spectra from Site B indicates that there is contamination from the stainless steel milling equipment.

4.2.4.2 *Milling Conditions*

In order to understand progression of the cryogenic synthesis XRD was utilised to analyse samples that were milled for increasing times without the use of a reaction buffer material. XRD data after milling for 1 minute (Figure 4-13) indicates that only starting reagents ($AlCl_3$, $LiAlH_4$, and LiCl) are present. For samples milled for 15 minutes or longer (Figure 4-14) no starting reagents are detected and AlH_3 and LiCl are the only crystalline phases present.

The XRD data in Figure 4-14 indicates that samples milled for 15 and 30 minutes have α'-AlH_3 and α-AlH_3 phases in similar ratios, but in the sample milled for 60 min the α-AlH_3 phase is dominant. Preferential synthesis of α-AlH_3 as milling time increases is likely related to the density of the various alane phases (see Table 4-1). The α-AlH_3 phase has the highest density and its formation should be preferential due to the high compressive forces that occur during milling. Long milling times increase the number of ball-powder impacts that appear to enable AlH_3 phase transformations into α-AlH_3.

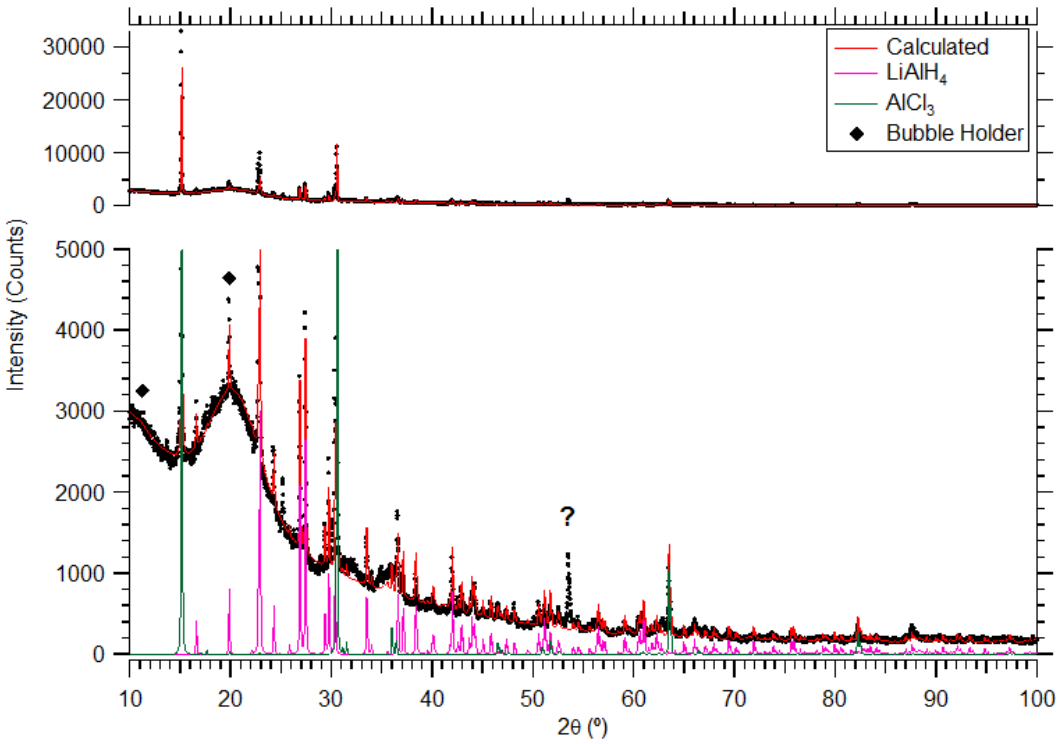

Figure 4-13: X-ray Diffraction (XRD) patterns (D8) from AlH3_Cryo_14.3cc_1min_0.76vol. A scaled plot is shown to clearly display minor diffraction peaks.

Quantitative phase analysis results provided in Table 4-7 indicate that the Al wt.% is 3.0, 5.0, and 11.9 ± 0.6 for the 15, 30, and 60 min samples respectively. Thus longer milling times result in higher Al yields due to the longer times in which AlH_3 is exposed to high energy milling. However, the Al content in cryogenically synthesised samples is much lower than those measured in room temperature synthesised samples, indicating that the low milling temperatures do restrict AlH_3 decomposition and prevent high Al yields.

There is a slight reduction in the AlH_3 and Al crystallite sizes when milling times are increased from 15 min to 30 min. But when milling time is increased to 60 min there is an increase in both the AlH_3 and Al crystallite sizes. Longer milling times increase powder-powder impacts that may allow nanoparticle-nanoparticle impacts to occur when reaction buffer volume ratios are low. Because no additional reaction buffer is used in these samples it is likely that crystallite size growth is due to agglomeration during milling. The LiCl crystallite size is consistently reduced over 15, 30, and 60 min milling times in contrast to AlH_3 and Al. The fact that the LiCl presents no crystallite size growth may be because it has not yet reached a critical crystallite size.

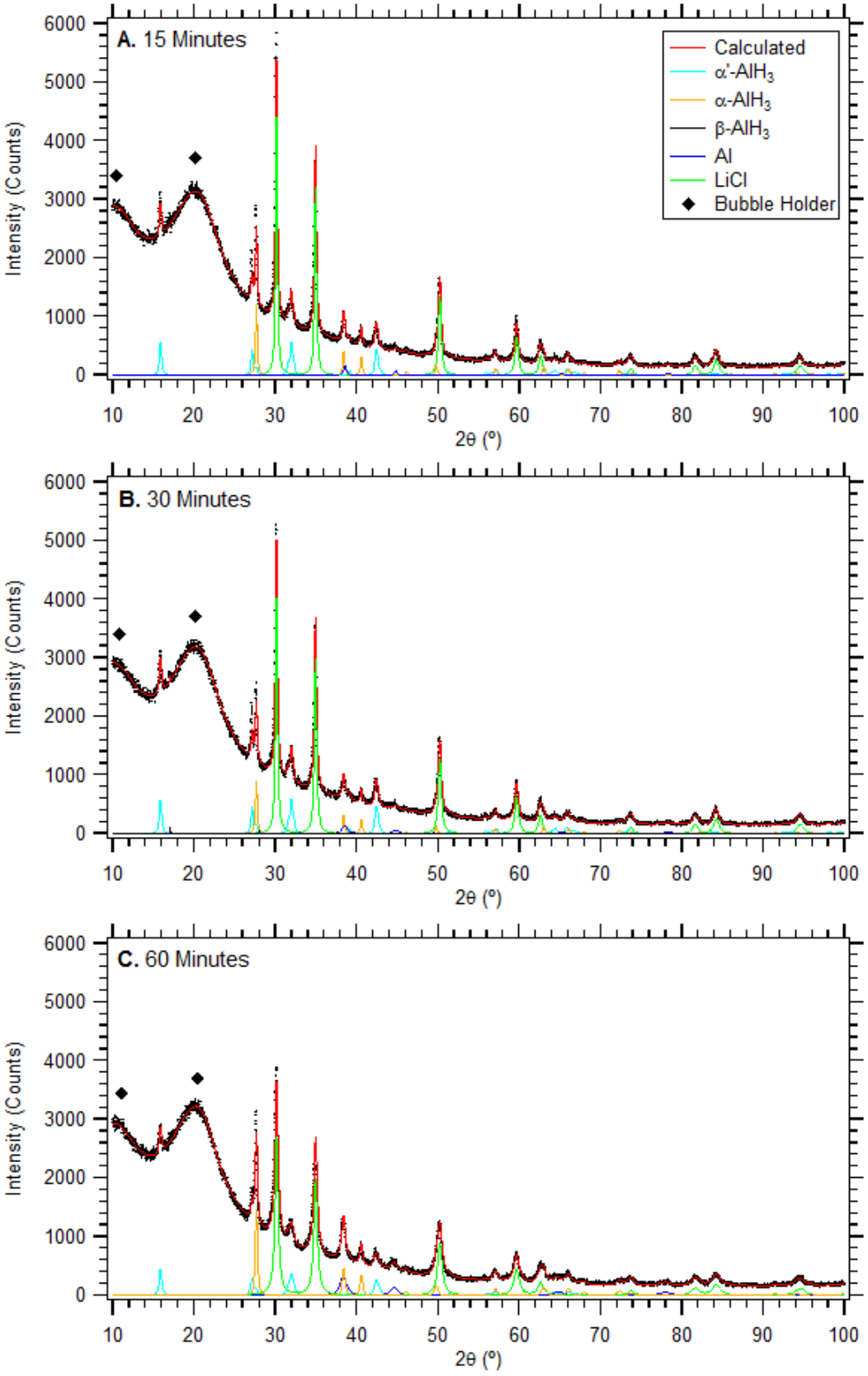

Figure 4-14: X-ray Diffraction (XRD) patterns (D8) from A) AlH3_Cryo_14.3cc_15min_0.76vol, B) AlH3_Cryo_14.3cc_30min_0.76vol, and C) AlH3_Cryo_14.3cc_60min_0.76vol. Rietveld fits to the data are also displayed.

Table 4-7: Rietveld fitting results for XRD patterns given in Figure 4-14. Mathematical fitting uncertainties are provided (2 standard deviations).

	Phase	Wt. %	Crystallite size (nm)
15 min	α'-AlH_3	21.1 ± 0.6	25 ± 2
	α-AlH_3	15.8 ± 0.4	29 ± 2
	Al	3.0 ± 0.4	16 ± 4
	LiCl	60.1 ± 0.6	76 ± 12
30 min	α'-AlH_3	22.0 ± 0.6	23 ± 2
	α-AlH_3	12.4 ± 0.6	26 ± 2
	β-AlH_3	0.5 ± 0.4	-
	Al	4.7 ± 0.6	8.5 ± 2
	LiCl	60.5 ± 0.8	54 ± 6
60 min	α'-AlH_3	15.5 ± 0.6	36 ± 14
	α-AlH_3	19.3 ± 0.6	31 ± 4
	Al	11.4 ± 0.6	11 ± 4
	LiCl	53.9 ± 0.6	24 ± 2

Interestingly, the crystalline phase wt.% results determined from the Rietveld analysis (in Table 4-7) differ from those calculated from expected yields. Reaction completeness should result in 51.4 wt.% LiCl but Rietveld results suggest that crystalline LiCl comprises 60.1, 60.5, and 53.9 wt.% of the sample after 15, 30, and 60 min milling respectively. The disparity in these results suggests that an amorphous phase exists within the synthesised sample. This is due to the fact that the wt.% values from the Rietveld analysis are calculated assuming a 100% crystalline sample content. Because the crystalline LiCl content is larger than the calculated LiCl content a non-LiCl phase (AlH_3 or Al) must be present as an amorphous phase assuming reaction completeness.

In order to promote nanoparticle formation, samples were cryogenically milled for 60 minutes with a moderate quantity of reaction buffer (2:1 LiCl:AlH_3 volume ratio). The quantity of reaction buffer used is a compromise between a high buffer leading to small nanoparticles and a low buffer resulting in better washing yields. XRD results are provided in Figure 4-15 for the as-milled sample, which show a high α-AlH_3 yield with minor α'-AlH_3 and Al phases as well as the LiCl reaction by-product phase. The result is similar to the reaction undertaken cryogenically with no reaction buffer where high α-AlH_3 yields are encountered with some Al decomposition product present.

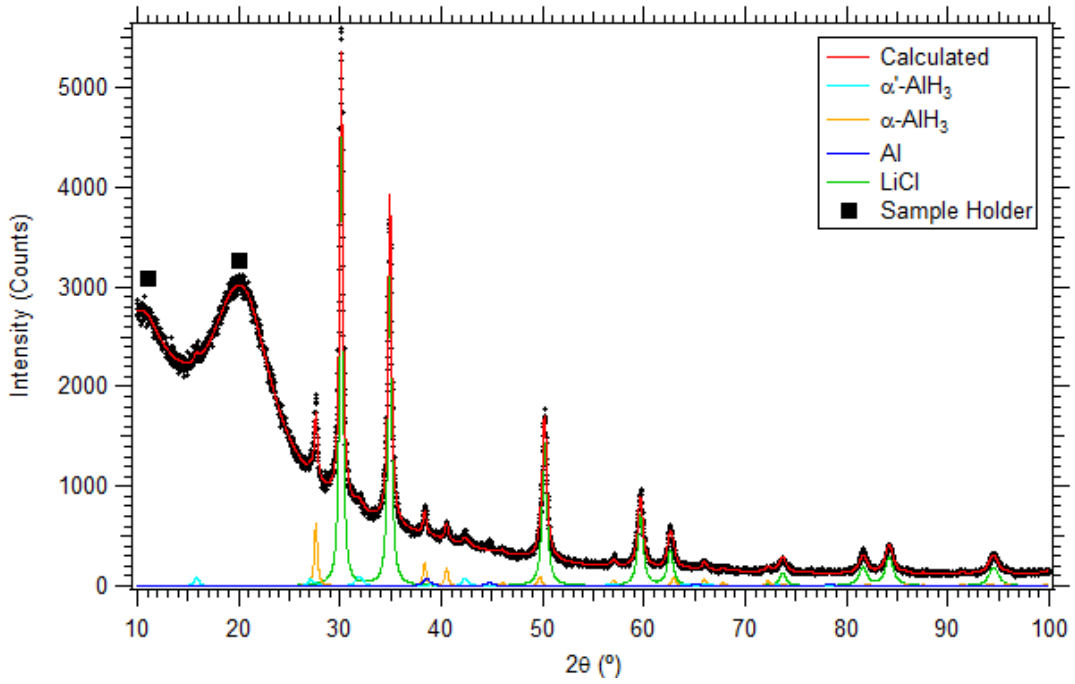

Figure 4-15: X-ray Diffraction (XRD) patterns (D8) from AlH3_Cryo_14.3cc_60min_2vol. Rietveld fits to the data are also displayed.

4.2.4.3 *Washing*

A sample of as-milled powder (AlH3_Cryo_14.3cc_60min_2vol) was washed using nitromethane and $AlCl_3$ to remove the LiCl by-product phase. However noticeable gas evolution was apparent upon addition of the sample to the nitromethane/$AlCl_3$ solution indicating that a reaction between the AlH_3 and the solution occurred. Gas evolution was not noticeable when washing mechanochemically synthesised pure Al nanoparticles (in Section 3.2.2) or room temperature synthesised AlH_3 (in Section 4.2.3.2) indicating that cryogenically synthesised alane is much more reactive. Even though a reaction with the solvent was noted, XRD of the washed sample as shown in Figure 4-16 does not show any unwanted crystalline reaction products. The only crystalline phases present in the washed sample are α'-AlH_3, α-AlH_3, and Al. However, it is possible that an amorphous phase is present that is not detected by XRD.

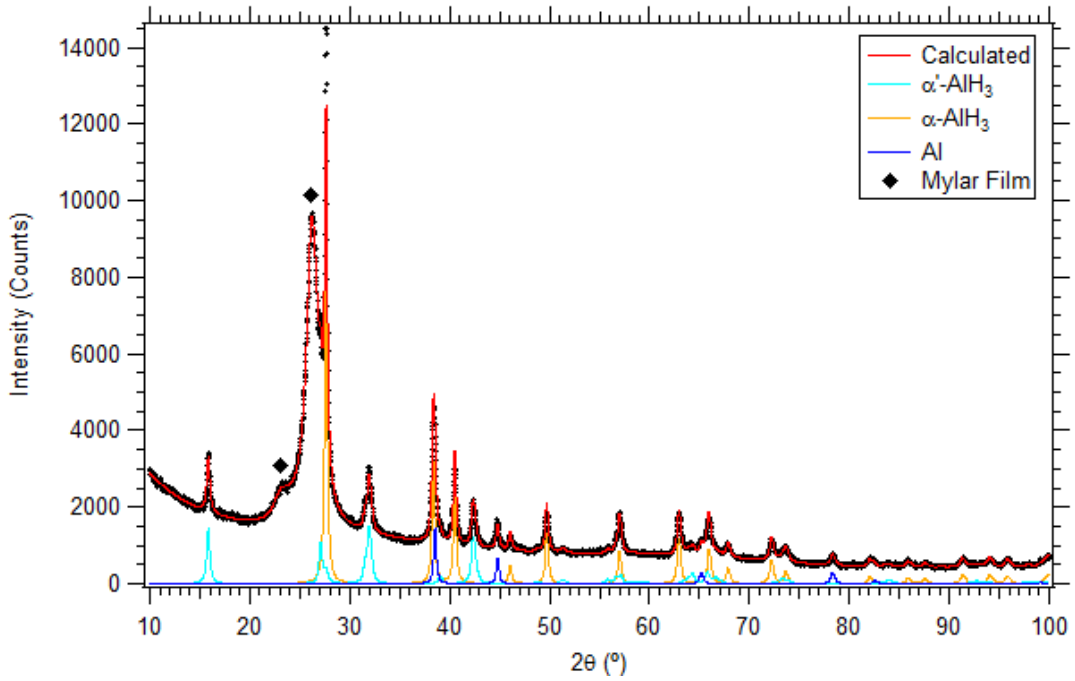

Figure 4-16: X-ray Diffraction (XRD) patterns (D8) for washed AlH3_Cryo_14.3cc_60min_2vol. Rietveld fits to the data are also displayed.

4.3 HYDROGEN SORPTION

Hydrogen desorption experiments were performed on mechanochemically synthesised samples in order to analyse the decomposition kinetics and maximum wt.% H_2 in as-synthesised and washed samples. Hydrogen absorption experiments could not be undertaken due to the lack of success in hydriding Al nanoparticles at pressures up to 2 kbar (see Section 3.3).

4.3.1 Room Temperature Milled

The decomposition plots for two different mechanochemically synthesised samples (AlH3_RT_7.7to1_50min_Step_7.938 & AlH3_RT_7.7to1_60min_7.938) are provided in Figure 4-17. Both samples were milled using the same LiCl:AlH_3 volume ratio, the same ball size, B:P ratio, and similar milling times. However the sample milled for 50 minutes was milled in a stepwise fashion (milled for 2 – 5 minutes and stopped for ~30 minutes incrementally) in an attempt to restrict the amount of heat build-up during milling. Both samples were examined within 1 week of synthesis.

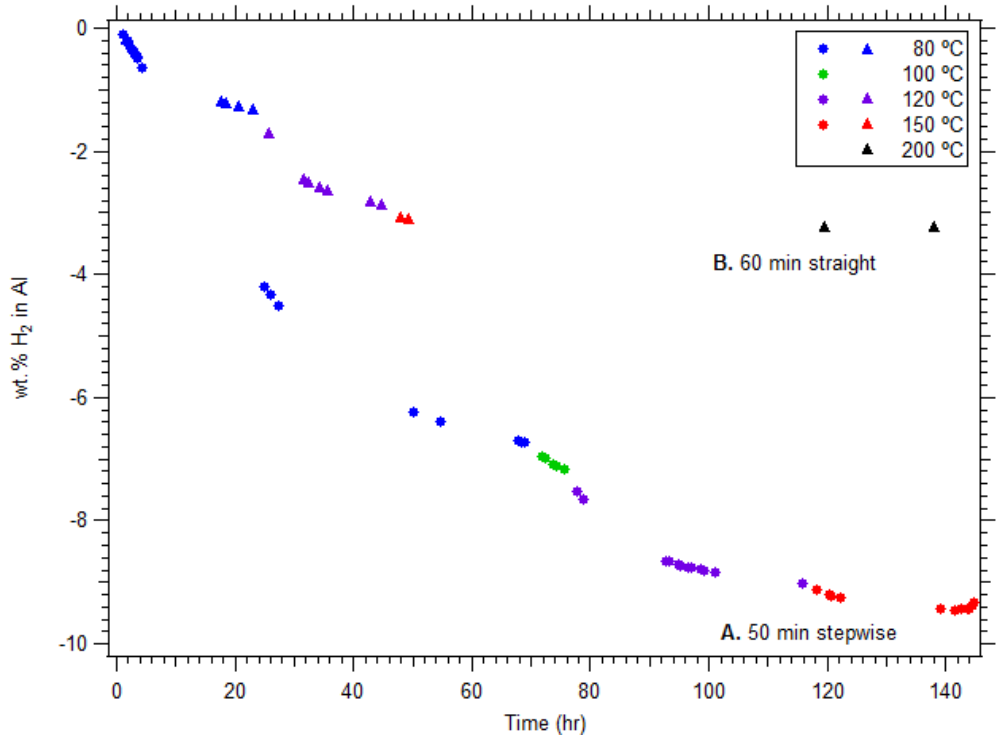

Figure 4-17: Hydrogen desorption data from A) AlH3_RT_7.7to1_50min_Step_7.938 and B) AlH3_RT_7.7to1_60min_7.938. The H_2 wt.% is given as a percentage of the calculated non-salt portion of the samples.

It is apparent that incremental step-wise milling is effective in producing higher AlH_3 yields. The 50 minute sample milled in a stepwise fashion evolves three times as much hydrogen as the 60 minute sample milled straight. Although the samples were not milled for exactly the same time, this small milling time difference is not expected to be a major factor in controlling AlH_3 yields. A significant quantity of heat is evolved during milling from both the mechanical milling process and from the exothermic chemical reaction that forms AlH_3. At 298 K the enthalpy of Reaction 4.12 is ΔH = -213 kJ/mol. This is a significant exothermic reaction that appears to generate enough heat energy during milling to initiate the decomposition of AlH_3 to Al and H_2 according to Reaction 4.4. The alane decomposition reaction is only mildly endothermic (ΔH = +11.4 kJ/mol) suggesting that the decomposition reaction is likely to occur during room temperature milling.

An XRD pattern for the 60 minute sample is provided in Figure 4-18, but unfortunately this data was collected 6 months after sample synthesis. Thus the as-synthesised alane content cannot be determined from the XRD data because of room temperature AlH_3 decomposition which would have occurred between synthesis and XRD data collection. However, the XRD data verifies that no starting reagents are present. XRD could not be collected for the 50 min milled sample because the entire sample was decomposed before air-protective XRD capabilities were available.

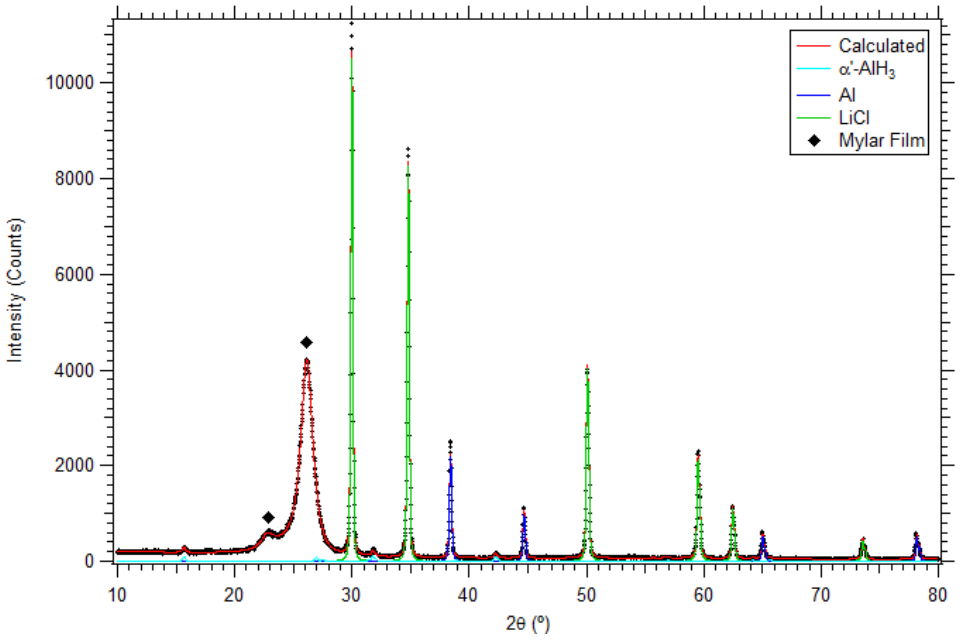

Figure 4-18: X-ray Diffraction (XRD) patterns (D8) for AlH3_RT_7.7to1_60min_7.938. XRD data was collected 6 months after sample synthesis. A Rietveld fit to the data is also displayed.

Given that stepwise room temperature milling generates higher AlH_3 yields it is preferential to synthesise all samples in this fashion. For the sake of practicality (especially during longer milling runs) most room temperature milling was undertaken using continuous milling times. However cryogenic samples were milled at 77 K using stepwise milling.

Hydrogen desorption data is provided in Figure 4-19 for a room temperature synthesised sample (AlH3_RT_39.3to1_60min_7.938_12.7) milled using a high B:P ratio, before and after washing the sample with nitromethane/$AlCl_3$. Firstly, a comparison must be drawn between the desorption data in Figure 4-17B and in Figure 4-19A for samples milled for 1 hr each with different B:P ratios (7.7:1 and 39.3:1 respectively). The comparison draws a curious result. The sample milled with a low B:P evolves a smaller quantity of H_2 (3.2 wt.%) in comparison to the sample milled with a high B:P (4.2 wt.% H_2). The result is unusual because it was expected that higher B:P ratios would result in more heat generation during milling, resulting in higher levels of Al, however the result here proves the opposite.

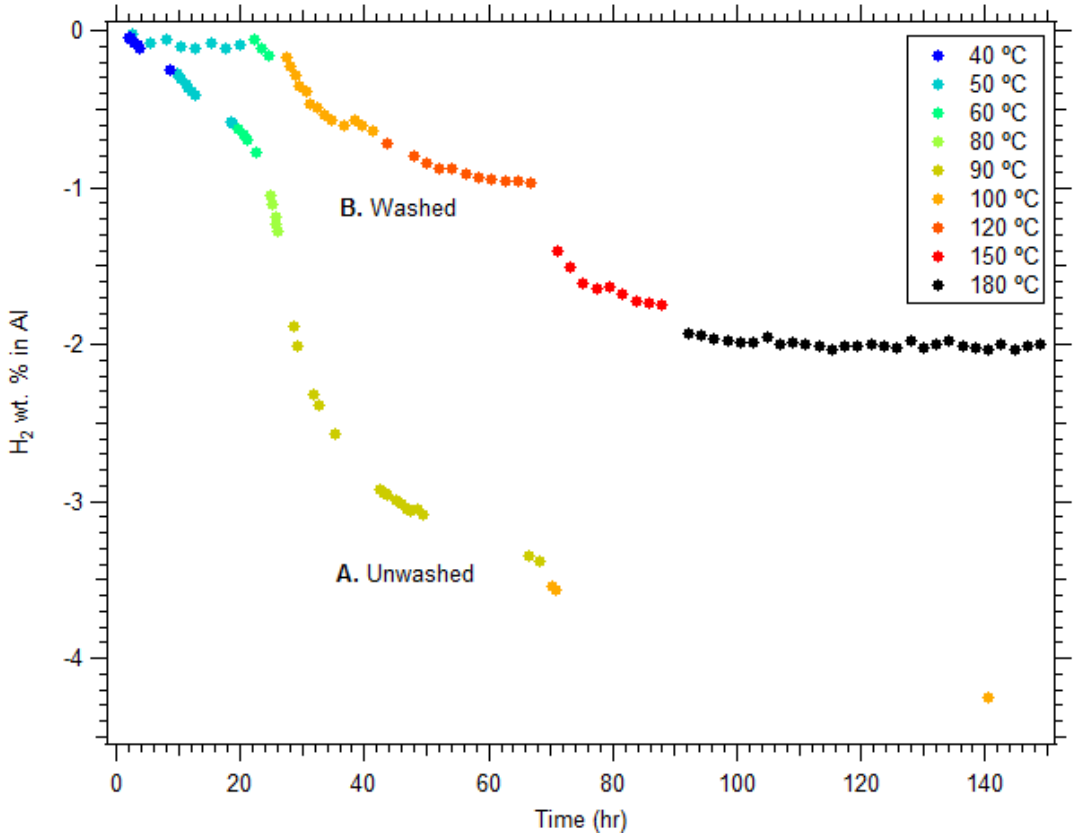

Figure 4-19: Hydrogen desorption data from AlH3_RT_39.3to1_60min_7.938_12.7 for A) as-milled and B) washed samples. The H_2 wt.% is given as a percentage of the calculated non-salt portion of the samples.

It is possible that the maximum H_2 wt.% is higher for the sample milled with a high B:P (Figure 4-17B) than the sample milled with a low B:P (Figure 4-19A) due to an incomplete AlH_3 synthesis reaction for the sample milled with a low B:P (AlH3_RT_7.7to1_60min_7.938). An incomplete reaction would result in $LiAlH_4$ remaining within the sample, which has been shown to decompose at temperatures greater than 100°C. However $LiAlH_4$ milled with $AlCl_3$ and/or $TiCl_3$ additives has been shown to decompose at room temperature [223]. But XRD data provided in Figure 4-18 for the low B:P sample does not display any evidence of starting reagents. In addition, no evidence of $LiAlH_4$ decomposition products (Li_3AlH_6, LiH, or LiAl [224]) were found in the XRD pattern or any other that has been performed before or after sample heating. The reason for the hydrogen capacity difference is still not fully understood, and further work is required to analyse trends in alane decomposition during room temperature milling.

A comparison can also be drawn from the hydrogen desorption data provided in Figure 4-19 between the unwashed and washed samples. The AlH3_RT_39.3to1_60min_7.938_12.7 sample was washed with nitromethane and $AlCl_3$ according to Sections 2.1.5 & 4.2.1. There is an obvious alteration of the kinetics of decomposition as well as a decrease in the maximum H_2 wt.% upon washing. Unfortunately the decomposition of the washed sample (Figure 4-19B) was undertaken 6 months after sample synthesis and washing were performed. As such it was uncertain whether the changes in desorption behaviour were due to the washing procedure or the delayed analysis time. Further analysis of the discrepancy between unwashed and washed samples is given in Section 4.3.2 for cryogenically synthesised samples, where these factors are not an issue.

Hydrogen desorption experiments were also undertaken on the room temperature milled sample (AlH3_RT_13.2to1_360min_4) which displayed almost no AlH_3 phases (0.4 wt.% of the sample) in its corresponding XRD pattern (Figure 4-4C). The hydrogen desorption results are presented in Figure 4-20 for both unwashed and washed (nitromethane/$AlCl_3$) samples. The results indicate that despite XRD displaying only a very minor AlH_3 crystalline phase that in fact 3.3 wt.% H_2 evolves from the non-salt portion of the sample. This suggests that an amorphous phase of AlH_3 may be present as discussed in Section 4.2.3.1.

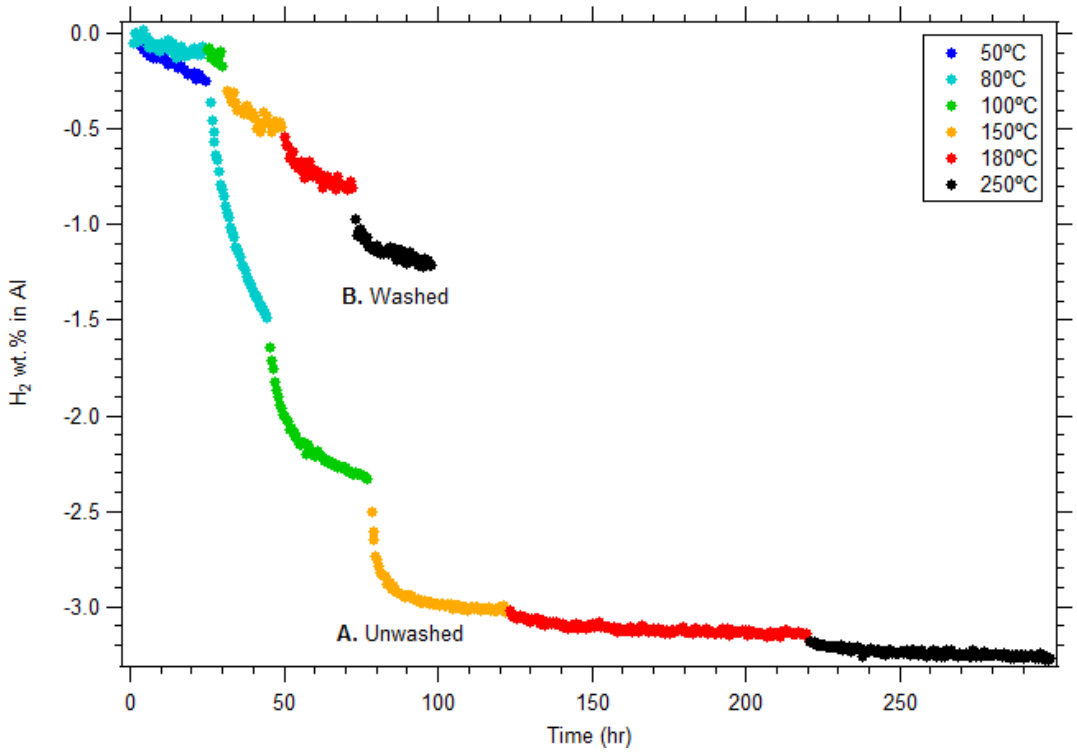

Figure 4-20: Hydrogen desorption data from AlH3_RT_13.2to1_360min_4 for A) as-milled and B) washed samples. The H_2 wt.% is given as a percentage of the calculated non-salt portion of the samples.

The possibility of amorphous alane is also backed up by XRD results in Figure 4-21 for the washed AlH3_RT_13.2to1_360min_4 sample after decomposition is complete. It can be seen that the only crystalline phase present is Al after H_2 desorption. Although the counts are low, no traces of $LiAlH_4$ decomposition products could be identified indicating that the 6 hr milled room temperature sample did contain amorphous AlH_3 before decomposition.

A comparison between the unwashed and washed samples in Figure 4-20 can once again be made. The washed and unwashed samples in this case were decomposed experimentally within 2 weeks of one another, limiting any room temperature decomposition that may affect comparisons. It can be seen that the washed sample is also kinetically restricted and has a reduced H_2 wt.% content (see Section 4.3.2 for further discussion).

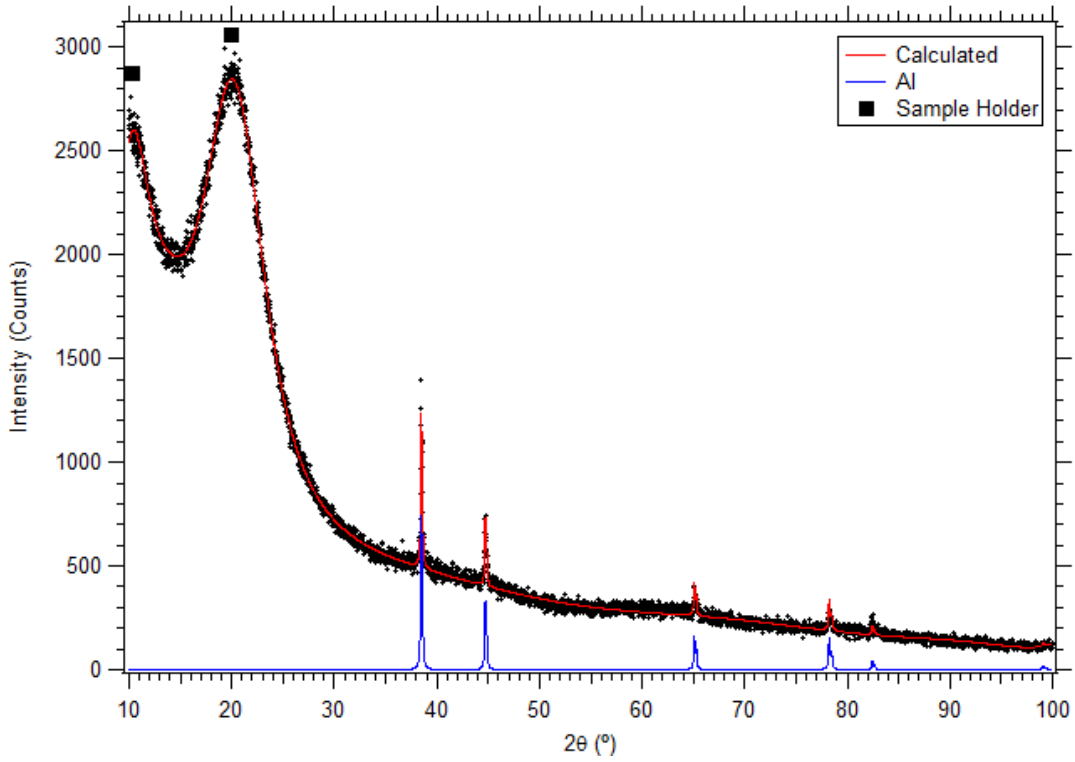

Figure 4-21: X-ray Diffraction (XRD) pattern (D8) from AlH3_RT_13.2to1_360min_4 that was washed and then decomposed as shown in Figure 4-20B. A Rietveld fit to the data is also displayed.

4.3.2 Cryogenically Milled

In this section hydrogen desorption experiments were undertaken within 1 week of sample synthesis and/or washing to ensure room temperature alane decomposition was minimised. Both unwashed (as-milled) and washed samples of cryogenically synthesised alane (AlH3_Cryo_14.3cc_60min_2vol) were loaded into a manometric hydrogen sorption apparatus and initially evacuated at room temperature for 30 minutes. The samples were then raised to 50°C and held at this temperature for 24 hours, followed by 24 hours at 100°C and then 150°C respectively in order to examine the kinetic behaviour and maximum desorbed H_2 wt.% of the samples. Hydrogen desorption data is displayed in Figure 4-22 which depicts the wt.% of H_2 as a function of time in the calculated non-salt portions of the unwashed and washed samples. This relates to the percentage of hydrogen desorbed from the Al/AlH_3 portions of the samples (26.43% and 100% Al/AlH_3 of the unwashed and washed samples respectively).

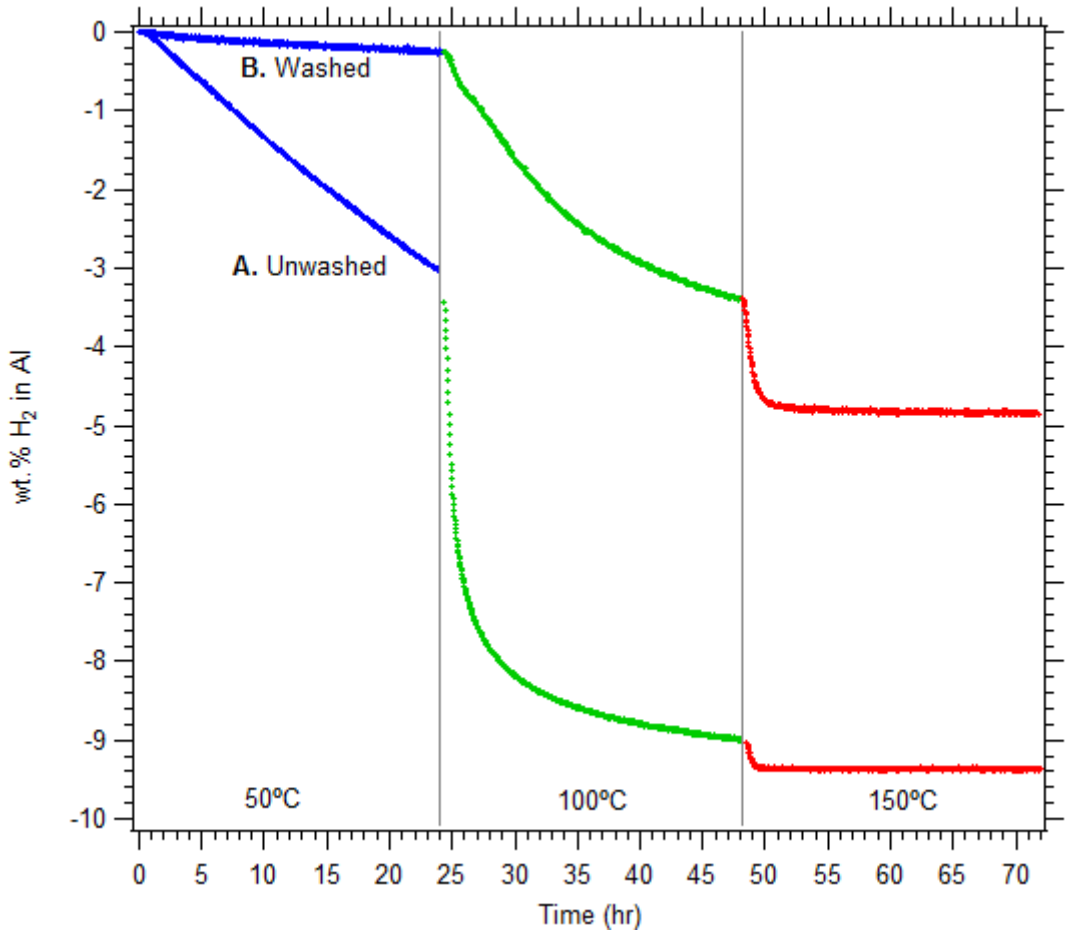

Figure 4-22: Hydrogen desorption data from A) unwashed and B) washed samples of AlH3_Cryo_14.3cc_60min_2vol. The H_2 wt.% is given as a percentage of the calculated non-salt portion of the samples. Data was collected every 2 min for 24 hr periods at each temperature consecutively.

Alane is thermodynamically unstable over a large temperature range and its decomposition is in fact only kinetically limited. Kinetic barriers are crucial in stabilising alane at moderate temperatures given its extreme equilibrium pressures (i.e. 28 kbar at 300°C [4-5]). The unwashed sample desorbs a significant quantity of hydrogen (3 wt.% H_2 from Al) over 24 hours at 50°C. This indicates rapid decomposition at a lower temperature than results reported for bulk, Dow-synthesised alane that provide adequate kinetics in the order of 100°C, although these kinetics can be enhanced by doping [173]. However, similar kinetics to those reported herein have been observed for freshly synthesised alane decomposed at 60°C [185]. Figure 4-22 shows that rapid desorption occurs at 100°C and raising the sample temperature to 150°C results in complete hydrogen desorption. The resultant measured alane content is 25.0 wt.% of the total sample resulting in a calculated as-

milled 1.4 wt.% Al content (73.6 wt.% LiCl). The desorption kinetics will likely be hindered by the fact that the alane particles are embedded within a LiCl salt matrix. Restricted desorption kinetics are beneficial during room temperature storage but LiCl is not fully effective in kinetically stabilising alane decomposition.

The hydrogen desorption results for the washed alane sample are interesting akin to samples examined in Section 4.3.1. Firstly, desorption kinetics are significantly slower, and secondly, the maximum H_2 wt.% is half that of the unwashed sample. Desorption kinetics should be quicker for the washed sample due to the absence of kinetically hindering LiCl salt. However, the slower observed kinetics suggest a limiting factor may be present. Aluminium oxide surface layers can be detrimental to molecular [138] and even atomic [139] hydrogen permeation. Despite XRD showing only AlH_3 and Al in the washed samples, the evolution of gas upon addition of the as-synthesised sample to nitromethane suggests that an unwanted (oxide/hydroxide) phase may have formed. The formation of amorphous aluminium oxide phases rather than crystalline phases has been theoretically shown to be thermodynamically favourable [141]. The theoretical results in the literature have also been reinforced by experimental amorphous oxide formation [142]. Given that no oxide or hydroxide phases were detected with XRD and that the maximum H_2 wt.% is half that of the unwashed sample it seems likely that the washed sample contains a significant amorphous aluminium oxide/hydroxide phase. The extent of oxide contamination would be exacerbated by the small particle size of the synthesised AlH_3 nanoparticles that provides a large surface area in which oxide formation can occur.

XRD was also performed on the desorbed unwashed and washed alane samples (see Figure 4-23). The XRD data verifies that hydrogen desorption was complete for both samples. No crystalline oxide or hydroxide phases are observed in the desorbed sample XRD patterns which were taken after sample heating to 150°C. Quantitative phase analysis results provided in Table 4-8 display the crystalline compositions of both the unwashed and washed alane samples before and after desorption. A comparison between the AlH_3 content derived from hydrogen desorption measurements for the unwashed sample (25.0 wt.%) and the AlH_3 content from XRD results (15.8 wt.%) reveals a disparity between the total amount of alane in the sample and the crystalline content. These results suggest that at least 37% of the

alane present in the unwashed sample is non-crystalline. There is no obvious amorphous hump visible in the XRD data. However, a careful XRD study using an internal standard (a part of future work) should be able to quantify the amorphous portion of the sample using the Rietveld method.

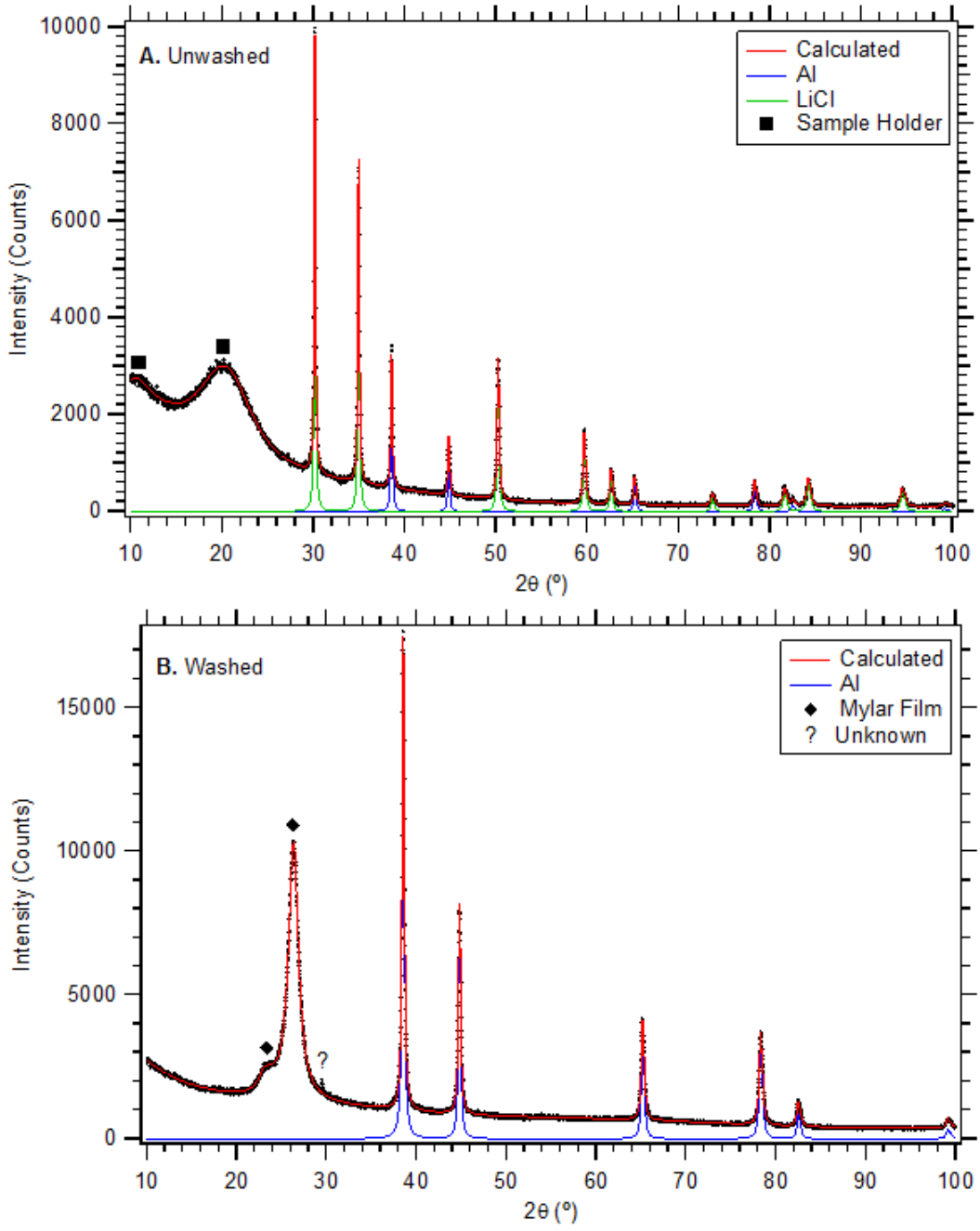

Figure 4-23: X-ray Diffraction (XRD) patterns (D8) for desorbed AlH3_Cryo_14.3cc_60min_2vol A) before and B) after washing with nitromethane & $AlCl_3$. Rietveld fits to the data are also displayed.

Table 4-8: Quantitative crystalline phase results from Rietveld fits to XRD patterns given in Figures 4-15, 4-16, and 4-23 for unwashed and washed alane samples before and after desorption. Wt.%, crystallite sizes, and mathematical fitting uncertainties (2 standard deviations) are provided.

	Phase	Crystalline wt. %	Crystallite size (nm)
Unwashed	α'-AlH_3	5.8 ± 0.8	11.3 ± 3.4
	α-AlH_3	10.0 ± 0.6	20.5 ± 2.0
	Al	2.7 ± 0.6	7.9 ± 2.6
	LiCl	81.5 ± 1.0	40.5 ± 3.6
Unwashed – Desorbed	Al	23.9 ± 0.2	39.0 ± 1.2
	LiCl	76.1 ± 0.2	81.0 ± 6.2
Washed	α'-AlH_3	28.4 ± 0.4	17.7 ± 0.6
	α-AlH_3	62.9 ± 0.4	21.5 ± 0.4
	Al	8.8 ± 0.2	22.3 ± 1.4
Washed – Desorbed	Al	100	26.1 ± 0.2

Based on knowledge of the sample history and crystallite size trends (see Table 4-8), information regarding alane crystallite behaviour upon washing and desorption can be gained. A comparison between unwashed and washed samples reveals an increase in the average crystallite size of AlH_3 and Al upon washing. An average crystallite size increase may occur from two phenomena. Firstly, centrifugation preferentially separates the largest AlH_3/Al particles from solution first, and it is possible that the smallest particles remain in solution increasing the average separated crystallite size. Secondly, it is possible that exothermic amorphous oxide formation during the washing procedure generated heat that promoted crystallite growth in solution. Alternatively physical contact between AlH_3/Al particles upon the removal of the salt matrix may have also resulted in particle agglomeration and crystallite growth.

A comparison between the XRD data for desorbed samples and their precursor materials also reveals alane crystallite behaviour. In the unwashed samples it appears that the 2:1 volume ratio between LiCl and AlH_3 may be insufficient to completely separate the AlH_3 particles. Previous research [76] has required using volume ratios as high as 10:1 to synthesise well separated particles. Consequently, during desorption (heating to 150^{o}C), crystallite size may increase due to both intra-particle crystallite growth and inter-particle agglomeration. In the washed samples, there is very little difference in the crystallite size of the Al upon heating to 150^{o}C. Intra-particle crystallite growth may have already occurred during the washing process and the

amorphous oxide coating generated during this washing may hinder inter-particle growth during heating.

4.4 CONCLUSIONS

Alane nanoparticles were synthesised using both room temperature and cryogenic mechanochemical synthesis. The evolution of alane production was investigated as a function of milling time under a variety of milling conditions. Cryogenic milling was verified to form higher yields of AlH_3 and four different alane phases (α, α', β, γ) were identified in XRD structural investigations. The LiCl reaction by-product phase was removed by washing with a nitromethane/$AlCl_3$ solution, which adversely reacted with the AlH_3 nanoparticles. The hydrogen desorption kinetics were hindered and the maximum H_2 wt.% was halved although no crystalline oxide or hydroxide phases were found using XRD. Unwashed mechanochemically synthesised AlH_3 was found to desorb at room temperature over months and significantly at 50°C in a 24 hr period.

Quantitative Rietveld results coupled with hydrogen desorption measurements suggest the presence of an amorphous AlH_3 phase in mechanochemically synthesised samples, which deserves further study to identify its structural characteristics. If mechanochemically synthesised alane is to be successfully washed from LiCl a less reactive solvent must be discovered that will not alter the alane particle surface. However, alane nanoparticles without a kinetic barrier to hydrogen desorption is extremely unstable at room temperature.

4.5 DIRECTIONS FOR FUTURE WORK

- Synthesise AlH_3 nanoparticles cryogenically with very high ~10:1 LiCl:AlH_3 reaction buffers to promote very small alane nanoparticle production. Ultra small alane particles are likely to decompose more rapidly at all temperatures (including room temperature). However, AlH_3 particles < 10 nm are predicted to undergo thermodynamic changes that may allow hydrogen sorption reversibility at pressures significantly lower than for bulk AlH_3.

- A reaction between the nitromethane/$AlCl_3$ solvent (used for LiCl removal) and the AlH_3 nanoparticles was observed. The reaction caused restricted kinetics and a ~50% reduction in the H_2 content of the sample. Although the stabilisation is likely beneficial during room temperature storage the likelihood of hydrogen reversibility in washed samples is low. As such, an alternate solvent for removal of the reaction by-product phase (i.e. LiCl) must be located which does not adversely react with AlH_3 nanoparticles.

- Room temperature decomposition of AlH_3 nanoparticles dramatically hinders the ability to perform uniform measurements of samples synthesised under different conditions. Samples must be analysed as soon as synthesised otherwise room temperature H_2 desorption will lead to altered sample properties. Given the kinetic restriction caused by washing samples with nitromethane/$AlCl_3$ (possibly forming an amorphous oxide layer) it may be possible to coat the AlH_3 nanoparticle with a more promising material to restrict room temperature H_2 desorption. However preventing desorption may also adversely affect the possibility of re-absorption.

- The absorption of hydrogen in decomposed alane (Al) is an issue that has not been overcome at modest pressures to date. However, in a similar note to aluminium nanoparticle synthesis, doping nanoparticles with other metals such as Ti or Ni may enable hydrogen sorption to proceed under modest pressures especially at low temperatures (i.e. 77 K). Thus, high pressure hydrogen absorption measurements should be undertaken on doped and undoped samples at 77 K at achievable laboratory pressures up to 2 kbar.

- A high wt.% H_2 desorption result was obtained for a sample milled at room temperature using incremental milling times. The step-wise milling appears to restrict thermal energy build up during milling that in turn prevents AlH_3 decomposition during milling. Further investigation into step-wise milling at room temperature may prove beneficial towards increasing alane yields without the need to implement difficult cryogenic milling procedures.

- Results suggest the generation of an amorphous AlH_3 phase upon milling under certain conditions. The analysis and characterisation of this amorphous alane phase is important in order to understand the bonding relationship between hydrogen and aluminium. It is possible that different thermodynamics exist for an amorphous Al-H system that would result in an altered sorption pressure relationship. Amorphous AlH_3 has not been reported in the literature to date, hence the need to analyse its structure, bonding, and thermodynamic properties.

Chapter 5

Magnesium Hydride Nanoparticles

"Scientific principles and laws do not lie on the surface of nature. They are hidden, and must be wrestled from nature by an active and elaborate technique of inquiry" - John Dewey

5.1 BACKGROUND

Magnesium hydride (β-phase) was first synthesised in 1912 from a pyrolysis process, although it was much later (1955) when MgH_2 was first synthesised from its elemental constituents [26]. Over the last 50 years a great amount of research into MgH_2 has been undertaken, primarily due to its high gravimetric hydrogen storage capacity, the abundance of Mg, and it's relatively low cost. Much of the recent work has been focussed on enhancing the kinetics of hydrogen sorption and attempting to reduce the high desorption temperature [225].

5.1.1 Properties

Magnesium hydride (MgH_2) has a high hydrogen gravimetric storage capacity of 7.7 wt.% and a high volumetric storage density of 111 kg H_2 m^{-3}. These properties meet the DOE 2010 targets for a vehicular hydrogen storage material. There are two main factors that prevent pure MgH_2 from becoming a commercial hydrogen storage compound [226]:

1. High desorption temperatures > 300 ºC for pressures > 1 bar
2. Slow kinetics of desorption and absorption

Recently the kinetic issue has been overcome by introducing catalytic oxides during ball milling [227-228] but no alterations to the thermodynamics of pure MgH_2 have been experimentally achieved to date.

Certain studies presented in the literature make claims of lowering the desorption temperature of MgH_2 [229-231] as evidenced by Differential Scanning Calorimetry (DSC). However these studies overlook the fact that the DSC signal contains both a thermal and kinetic component [232] and in many hydride systems (including MgH_2) the onset temperature can be determined by kinetics leading to problems with this method of thermodynamic determination [233].

5.1.1.1 *Phases*

There are three different allotropes of magnesium hydride (MgH_2) that can be formed under various conditions. The three phases refer to different crystal structures

of MgH_2 and do not refer to the "alpha phase" which presents as an Mg crystal structure with dissolved hydrogen occupying interstitial sites. It has also been suggested [26] that dissolved hydrogen may not occupy interstitial sites but instead occupy vacancies within the Mg structure. It should also be noted that there is differing nomenclature used in early literature regarding the MgH_2 phases [234]. The common phase of magnesium hydride (β-MgH_2) has been found to have a rutile-type structure ($P4_2/mnm$) with ionic binding between Mg^{2+} and H^- ions [235]. There are two high pressure phases (γ and δ-MgH_2) [234] where the γ-MgH_2 phase can be formed during milling [236]. The structural details of the different phases are presented in Table 5-1.

Table 5-1: Phase information for magnesium and its hydrides [26]. * at 560°C and 210 bar.

Phase	Composition at.% H	Space Group	Lattice Parameters (Å)		
			a	*b*	*c*
Mg	0	$P6_3/mmc$	0.32093	-	0.52107
"alpha phase"	0 – 9 *	$P6_3/mmc$	0.32093	-	0.52107
β-MgH_2	66.7	$P4_2/mnm$	0.4517	-	0.3020
γ-MgH_2	66.7	Pbcn	0.453	0.544	0.493
δ-MgH_2	66.7	Aba2	0.4470	-	0.4735

The dissolution of hydrogen into magnesium, forming the alpha-phase, is reported to be an endothermic process [26]. The solubility of hydrogen in Mg is very small at atmospheric pressure (up to 6×10^{-2} at.% H at 650°C) [26]. Also, it has been reported by multiple authors [237-238] that there was no evidence of an alpha-phase when collecting hydrogen isotherms up to 427°C at hydrogen pressures up to 50 bar. Although, it is evident from Table 5-1 that the alpha-phase was found in a particular study to be significant (up to 9 at.% H) under high pressure (210 bar) and temperature (560°C) conditions. The presence of an alpha-phase was also indicated by Stampfer *et al.* [239] due to different Mg-H compositions being noted at the low end turnover in equilibrium plateaus as a function of temperature (440 - 560°C). Only one piece of structural information reported in the literature provides a basis for the presence of the alpha phase, and given the conflicting reports on the presence of an alpha-phase its existence warrants further investigation [26]. It is likely that different hydrogen solubility behaviour is a function of the varied sample characteristics in each study where there are variations in particle size, sample processing, or magnesium oxide contamination.

5.1.1.2 *Thermodynamics*

The decomposition of magnesium hydride proceeds via a crystalline phase change as follows:

$$MgH_2 \longrightarrow Mg + H_2 \qquad (5.1)$$

The generally accepted thermodynamic properties for the Mg-H system were provided by Stampfer, Jr. *et al.* in 1960 [239] (see Table 5-2). Stampfer's data is often preferred due to the large number of data points collected over a wide temperature range [26] however it must be noted that the accuracy of this data is very low where listed equilibrium pressure data varies by up to 9% at the same sample temperature. The percentage error in pressure is lower at high temperatures but reported equilibrium pressures still vary by an immense 3 bar at 444°C. The thermodynamic data from a number of sources provided in Table 5-2 illustrates the wide spread in determined decomposition reaction enthalpy (ΔH) and entropy (ΔS) data for MgH_2 measured under similar temperature conditions. The large discrepancies between the determined ΔH and ΔS values are likely a result of the poor MgH_2 desorption kinetics not being adequately accounted for in some studies. If the Mg-H system does not reach a true equilibrium pressure then the resultant thermodynamic values calculated from these pressures will be biased.

Table 5-2: Summary of thermodynamic data for MgH_2 available in the literature.

Source	Enthalpy (ΔH, kJ/mol H_2)	Entropy (ΔS, J/mol H_2/K)
Stampfer 1960 [239] (314 – 576°C)	-74.4 ± 0.3	135.1 ± 1.9
Reilly 1968 [240] (276 – 350°C)	-77.4 ± 4.18	138.3 ± 2.93
Pedersen 1983 [238] (303 – 390°C)	-70.1	126
Friedlmeier 1988 [241] (280 – 370°C)	-74.7	135.3
Klose 1995 [32] (270 – 345°C)	-81.9	146.1
Shao 2004 [242] (350 – 400°C)	-75.0	135.6
Bogdanović 1999 [31] (calculated at 360°C)	-74.9	135.2

Bogdanović *et al.* [31] provide thermodynamic data for MgH_2 obtained from calorimetric means in contrast to the other papers listed in Table 5-2 which obtain

thermodynamic data using equilibrium pressure measurements. Calorimetry allows thermodynamic data to be calculated as a function of temperature. This can be important due to the temperature dependence of the change in enthalpy ΔH and entropy ΔS [243] that are usually assumed to be constant over the temperature range studied with equilibrium pressure measurements.

The presence of a hysteresis effect between the absorption and desorption equilibrium pressures in the MgH_2 system is reported to exist in some studies but reported not to exist in other studies. No absorption/desorption hysteresis effects were evident in the experimental isotherms presented by Belkbir *et al.* [237] or Bogdanović *et al.* [31,244]. Pedersen *et al.* [238] also finds no sign of hysteresis in equilibrium plateau pressures, however notes that some hysteresis exists in low hydrogen concentration regions. However other isotherms presented in the literature display a broad range of different hysteresis effects between absorption and desorption equilibrium pressures (0.1 bar [32], 1 bar [245-246], and 4.4 bar [242], all at ~ 350°C). The hysteresis effect is thought to originate from strain and disorder within the MgH_2 lattice [246]. However, it is very likely that the "hysteresis" reported is due to slow kinetics not being adequately accounted for during thermodynamic measurements. If each data point on a pressure-composition isotherm is collected too quickly then the Mg-H system may not yet be at a true hydrogen pressure equilibrium. This phenomenon results in a pressure difference between the absorption and desorption equilibrium plateaus but is not related to hysteresis. For example, Shao *et al.* [242] present pressure-composition isotherms (PCI's) that appear to be severely affected by kinetics. The PCI curves display large amounts of "hysteresis" that could simply be due to inadequate measurement time. The kinetic plots included therein do not reach equilibrium and it is not clear whether true equilibrium was met. Other PCI features such as shortened equilibrium plateaus at low temperatures also indicate that true equilibrium may not have been met. These features could be due to the slower kinetics at low temperatures and the slower kinetics at extreme hydrogen to metal ratios not being accounted for adequately.

No definitive proof of the differentiation between real hysteresis and kinetic restrictions is given in the literature, such as kinetic curves measured over very long time scales. In fact, many of the sources that report significant hysteresis [242,246] only

present kinetic data collected over short time scales (< 60 minutes) where it is apparent that sorption has not yet completely ceased. Kennelly *et al.* [247] reports that several days were required to reach complete equilibrium for each data point in a Mg-H isotherm. Gerasimov *et al.* [248] provides an analysis of the hysteresis effects reported in the literature for the Mg-H system. They conclude that the hysteresis effect is an apparent phenomenon in the Mg-H system which is due to hindered nucleation at hydrogen pressures close to the equilibrium during absorption. The apparent effect is also reported [248] to be more severe with small Mg crystallite sizes, which may explain the spread of reported hysteresis effects in the literature. Desorption equilibrium pressures reflect the true equilibrium, given kinetics are still adequately accounted for, because desorption is not affected by the hindered nucleation phenomenon.

The fugacity is often assumed to be equal to pressure due to the small deviation from the ideal gas law at low pressures. However, for the equilibrium measurements at 360^{o}C provided in Section 5.3.1 the difference between the measured pressure and the fugacity was of a similar magnitude to the uncertainty in the measured pressure. Consequently all measured pressures were converted to their fugacities using Equation 1.4 in order to provide higher accuracy thermodynamic data. The requirement for using fugacity in determining thermodynamics from a van't Hoff plot is especially important when dealing with higher pressure data. For example, Stampfer, Jr. *et al.* [239] utilizes the Beattie-Bridgeman EOS [249] to account for the compressibility of hydrogen and to calculate the fugacity of hydrogen at given pressure and temperature. Stampfer's pressure data extends up to ~280 bar where the compressibility of hydrogen is vital in determining accurate fugacity values. Reprocessing Stampfer's pressure data reveals that the fugacity values that were calculated using the Beattie-Bridgeman EOS do not match fugacities calculated using more recent EOS models [122,125]. The disparity leads to a change in Stampfer's reported ΔH and ΔS values from 74.4 ± 0.3 kJ/mol H_2 and 135.1 ± 1.9 J/mol H_2/K to 76.2 ± 1.1 kJ/mol H_2 and 137.4 ± 1.4 J/mol H_2/K respectively. The reported uncertainties were calculated using a weighted least squares method (given in Section 5.3.2). Given the large ~2% difference in calculated ΔH and ΔS values by using different EOS models it can be seen that an accurate fugacity is essential in

determining accurate thermodynamics from a van't Hoff plot, especially with high measured pressures.

Reilly & Wiswall [240] also calculate the decomposition thermodynamics of the Mg-H system as shown in Table 5-2. Although they report that the enthalpy and entropy are converted to 25°C, reprocessing their data shows that these thermodynamic properties are in fact not converted and are valid at their temperature range mid-point (313°C). Reprocessing of Reilly's raw pressure data instead using fugacity also results in different enthalpy and entropy values (ΔH = 78.8 kJ/mol H_2 and ΔS = 140.9 J/mol H_2/K) than those originally reported in Table 5-2.

5.1.1.3 *Kinetics*

The kinetics of hydrogen sorption in the Mg system have been described by numerous sources in a contradictory fashion, although the kinetics of hydrogen sorption in pure Mg are generally thought to be very poor [250]. Hydrogen absorption into bulk Mg particles is often described to be limited due to the generation of a MgH_2 layer upon a Mg core [26]. The presence of a MgH_2 layer restricts hydrogen absorption because of the very slow diffusivity of hydrogen through MgH_2 (D = 1.55 $\times 10^{-16}$ m^2/s) [251].

A large range of metal oxides (0.2 mol.%) have been milled with MgH_2 providing an enhancement to the kinetics of both desorption and absorption [252]. Given that the best kinetic results were obtained from transition metal oxides (that can take different valence states) it was concluded that the electronic structure of the catalysts play a crucial part in improving kinetics [252]. Extremely fast kinetics were achieved when a Nb_2O_5 catalyst was used [227,253] where more than 6 wt.% absorption occurred in 60 seconds and 6 wt.% desorption was achieved in 500 seconds at only 250°C. The Nb_2O_5 work supports the claim that oxide catalysts lead to an improvement in the electronic exchange reaction with the hydrogen molecules, hence enhancing kinetics. The use of metal oxide catalysts has provided a solution to the kinetic issues that have hindered the Mg-H system for many years.

The use of MgO as a catalyst to improve the hydrogen sorption properties of Mg has also been studied in detail [254], where kinetic benefits were found to be similar to transition metal oxide catalysts. Creating an oxide-free Mg surface is incredibly

difficult because magnesium reacts 100 times faster with oxygen in comparison to Al [25]. It has been shown [255] that Mg and MgH_2 powders that are handled within a "clean" argon environment are immediately coated with a 3 – 4 nm oxide layer that acts to minimise further oxidation. Although magnesium oxide barriers have been noted to inhibit hydrogen sorption [250] partially reduced oxides have been shown to act as catalytic sites for hydrogen sorption [26,227,253].

Gerasimov *et al.* [248] stated that an apparent hysteresis effect is often observed in sub-micron scale Mg/MgH_2 powders due to hindered nucleation during hydriding at pressures close to equilibrium. However it is noted [248] that the decomposition equilibrium represents the real equilibrium as the desorption process is not limited by poor nucleation. Many researchers do not appear to wait long enough during sorption studies to determine the true equilibrium of the Mg-H system. The problem is exacerbated by the fact that kinetic data is often not presented along with thermodynamic studies of the Mg-H system.

5.1.2 Synthesis

Much of the literature focuses on synthesising Mg and Mg-based alloys by ball milling due to its simplicity and cost effectiveness. Ball milling is primarily used to increase the kinetics of hydrogen sorption on the as-milled product by [225]: creating clean oxide-free surfaces, increasing surface area, forming micro/nanostructures, and creating lattice defects. The Mg is then hydrided under pressure, at temperature, after milling. Other work involves ball milling Mg under a hydrogen atmosphere in order to mechanochemically synthesise MgH_2 during milling [256-257]. Only a relatively small percentage of the literature deals with pure MgH_2 samples, whereas most studies focus on alloys and intermetallic Mg compounds.

There are also several novel techniques that have been used to synthesise bulk-scale magnesium hydride in the literature. For example magnesium hydride whiskers (< 1 μm in diameter) have been synthesised by chemical vapour deposition (CVD) under a 40 bar hydrogen atmosphere [258]. Thin films (200 nm) of Mg have also been synthesised using a sputter coating technique in order to study the effect of crystallisation on hydrogen sorption properties [259].

5.1.2.1 *Nanoscale Systems*

Recent theoretical work [44] suggests that a reduction in Mg particle size below 10 nm can result in thermodynamic instability of magnesium hydride hence altering its 1 bar equilibrium sorption temperature (T_{1bar}) where this destabilization becomes significant for particles below 3 nm in size [44-45,260-261]. As a result of the promising theoretical investigations a number of recent attempts have been made to experimentally synthesize Mg or MgH_2 nanoparticles in this size regime.

Magnesium metal nanocrystallites < 5 nm have been formed within a nanoporous carbon matrix using a melt infiltration technique [262]. The Mg particle size is likely a function of the size of the carbon pores. The presence of Mg with particle sizes less than 10 nm is likely as BET results show a number of pores present with diameters less than 10 nm. XRD does not detect any Mg peaks at 10 wt.% loading which is an indication of either very small or amorphous Mg. More recent work [263] involves first "wetting" the a porous carbon with Ni or Cu before melting Mg into the carbon host in order to improve Mg uptake. No thermodynamic changes were found from hydrogen sorption results from the Mg nanoparticles within the carbon host (inferred to be 13 nm from the carbon pore size distribution). However, the accuracy of the Sieverts apparatus used in this work is not very high and would likely only resolve drastic changes in the thermodynamics of the Mg-H system.

The formation of MgH_2 embedded within a carbon aerogel scaffold has also been undertaken by means of deposition of a dibutylmagnesium precursor [264]. The impregnated material was hydrogenated under ~50 bar at 170°C to form MgH_2 whilst reaction by-products were extracted by filtration and evacuation. The two-phase system displayed very fast hydrogen sorption kinetics attributed to the fact that MgH_2 particles were oxide-free and nanoscopic.

Magnesium metal nanoparticles have also been synthesised using a sonoelectrochemical technique [265]. TEM shows evidence of some 4 nm particles, however XRD reveals that on average the sample consists of particles with crystallite sizes greater than 20 nm. Much larger particles (~ 70 nm) are also shown in SEM micrographs that are not shown to be aggregates of smaller particles.

Recently an electrochemical method has also been used to synthesise a colloid containing 18 wt.% Mg nanoparticles (5 nm) stabilised by tetrabutylammonium bromide (TBA) [266]. After hydriding, the material displayed a hydrogen desorption pressure of 0.3 kPa at just 85°C (40 times higher than bulk MgH_2). However, it appears as though the increased pressure (a result of destabilised thermodynamics) is not due to the MgH_2 particle size as claimed by the authors, but in fact due to a chemical reaction between the Mg and the ammonium salt. Such large changes in the thermodynamics of hydrides have been observed for AlH_3-adduct systems (see Section 4.1.1.8).

Although many techniques have been utilised to synthesise nanoscopic Mg and MgH_2 there have been no experimental measurements that indicate alterations of the thermodynamics in the Mg-H system with particle size. Thus, the synthesis of MgH_2 nanoparticles and thermodynamic measurements were performed in the present work.

5.2 MECHANOCHEMICAL SYNTHESIS

Mechanochemical synthesis was chosen as the MgH_2 synthesis process due to the ability to control particle size by addition of a LiCl reaction buffer. The aim of using LiCl as a reaction buffer is not to produce a new hydrogen storage material comprising MgH_2 and LiCl but to produce separated nanosized particles of MgH_2 for which the thermodynamics can be compared to theoretical predictions. A mechanochemical process was constructed in order to synthesise magnesium hydride nanoparticles as follows:

$$MgCl_2 + 2LiH \longrightarrow MgH_2 + 2LiCl \qquad \begin{aligned} \Delta_r G_{298K} &= -72.8 \text{ kJ/mol} \\ \Delta_r G_{77K} &= -70.5 \text{ kJ/mol} \end{aligned} \qquad (5.2)$$

The reaction between LiH and $MgCl_2$ was undertaken by Ashby & Schwartz in 1971 within a tetrahydrofuran (THF) solvent [267]. The reaction was only found to progress at elevated temperature and not at room temperature. However Reaction 5.2 is thermodynamically viable at room temperature where the Gibbs free energy of reaction (ΔG) is negative. The synthesis reaction unfortunately has a very low Gibbs free energy of reaction which is a measure of the tendency for the reaction to proceed. Consequently, the Gibbs free energy also has an impact on the speed of the reaction. As such room temperature milling times during synthesis were set at 18 hrs, much longer than the milling times for both the Al or AlH_3 mechanochemical synthesis reactions that had much higher ΔG*'s* of reaction.

In order to synthesise MgH_2 particles of different sizes, four samples of MgH_2 were produced using various amounts of LiCl buffer added to the starting reagents. The amount of LiCl added for each sample corresponded to 0 (MgH_2-A), 1.05 (MgH_2-B), 2.62 (MgH_2-C) and 6.82 (MgH_2-D) moles of LiCl added to the left hand side of Reaction 5.2. Samples were synthesised by milling at both room temperature and cryogenically at 77 K as shown in Table 5-3. Samples synthesised at room temperature were preferentially investigated due to the sample reaction completeness. Long milling times are impractical for samples that are cryogenically synthesised and as such Reaction 5.2 does not proceed to completion under short milling times.

Table 5-3: Summary of MgH_2 sample details. B:P and R:P are the ball to powder and rod to powder mass ratios respectively. Equal numbers of different sized balls were used. Volume ratios refer to final reaction products.

Sample Name	Milling Temp. (K)	Time (min)	B:P / R:P	Volume Ratio ($LiCl:MgH_2$)	Ball and Canister Sizes
MgH_2-A	298	1080	90:1	2.21:1	7.938 & 12.7 mm
MgH_2-B	298	1080	90:1	3.37:1	7.938 & 12.7 mm
MgH_2-C	298	1080	90:1	5.10:1	7.938 & 12.7 mm
MgH_2-D	298	1080	90:1	9.79:1	7.938 & 12.7 mm
MgH_2-Purchased	298	1080	90:1	N/A	7.938 & 12.7 mm
MgD_2-A	298	1080	90:1	2.21:1	7.938 & 12.7 mm
MgD_2-B	298	1080	90:1	3.37:1	7.938 & 12.7 mm
MgD_2-C	298	1080	90:1	5.10:1	7.938 & 12.7 mm
MgD_2-D	298	1080	90:1	9.79:1	7.938 & 12.7 mm
MgH_2-A-cryo	77	60	32:1	2.21:1	14.3 cm^3
MgH_2-B-cryo	77	60	32:1	3.37:1	14.3 cm^3
MgH_2-C-cryo	77	60	32:1	5.10:1	14.3 cm^3
MgH_2-D-cryo	77	60	32:1	9.79:1	14.3 cm^3

5.2.1 Room Temperature Milling

The mechanochemical synthesis of MgH_2 was undertaken according to Reaction 5.2 by means of ball milling at room temperature. Table 5-3 outlines the milling conditions used for each of the samples synthesised using different quantities of LiCl buffer. The LiCl by-product phase in mechanochemically synthesised MgH_2 samples is expected to form an agglomeration barrier, minimizing particle growth during thermodynamic investigations when samples are heated up to 360°C. All reagents were ball milled separately for 3 hours at a ball-to-powder ratio of 30:1 prior to use, as reducing the grain size of the starting reagents has been shown to accelerate the kinetics of mechanochemical reactions [76].

Synchrotron XRD data for each of the pre-milled reagents is provided in Figure 5-1 with experimental details provided in Section 2.2.3. The $MgCl_2$ XRD pattern displays a large degree of asymmetric peak broadening, most likely a result of deformation of the crystal structure during milling. The $MgCl_2$ crystal structure contains planes (see Figure 5-1B inset) that can easily shear free during milling, causing irregular crystal structure deformation, resulting in asymmetric peak broadening. Both the LiH and LiCl XRD patterns still display relatively sharp peaks even after milling for 3 hours. The sharp peaks are indicative of large crystallites suggesting that longer milling times could help to further reduce the crystallite size in future work. Large crystallites are present after milling due to the very large initial particle size of the as received starting reagents. As-received LiH had a -30 mesh size

(< 600 μm) and as-received LiCl had a -10 mesh size (< 2000 μm). Large initial particle sizes indicate that much longer milling times are required to grind the reagents effectively.

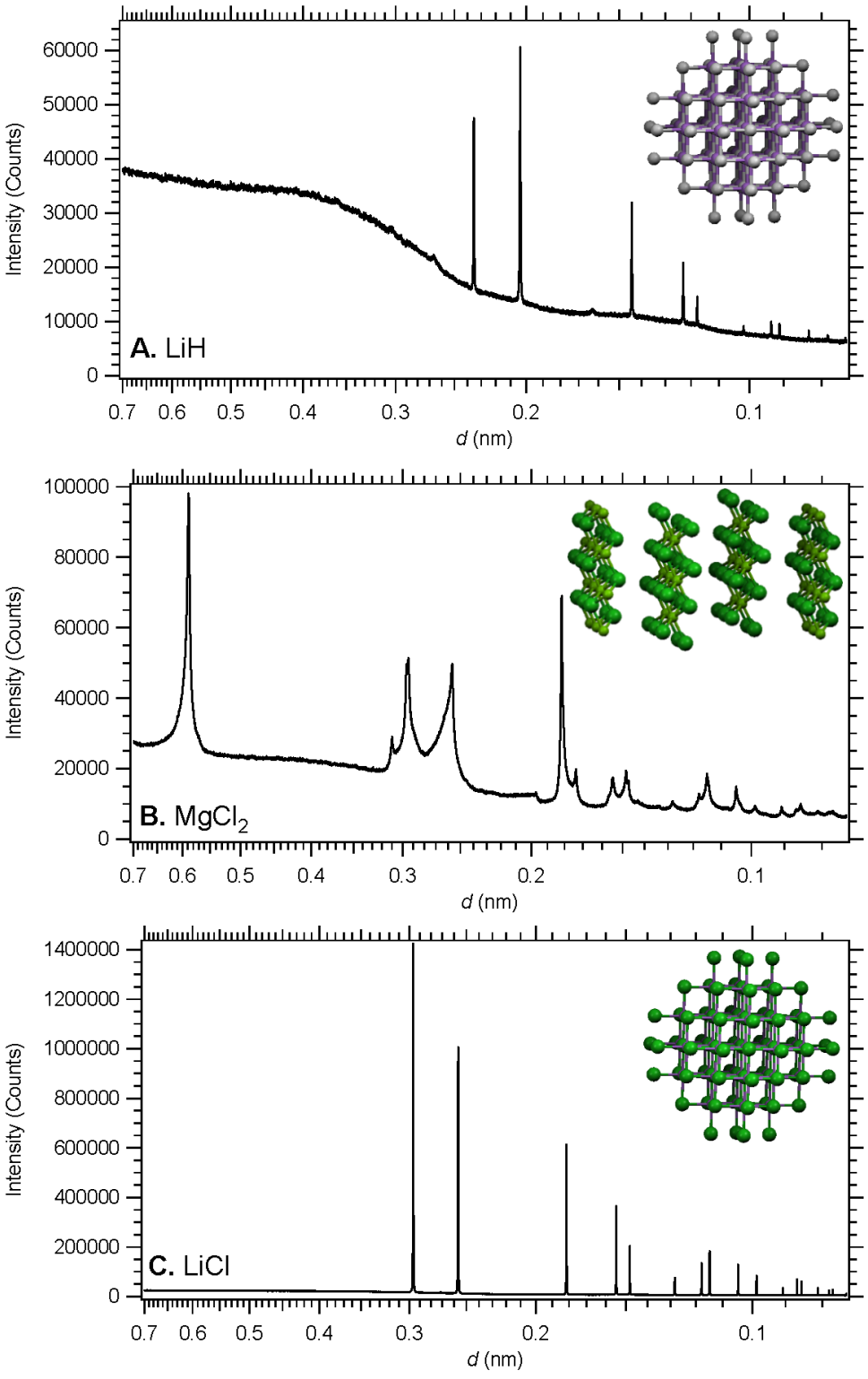

Figure 5-1: X-ray Diffraction (XRD) patterns (Australian Synchrotron) from pre-milled starting reagents A) LiH, B) $MgCl_2$, and C) LiCl. The crystal structures are displayed as insets.

XRD patterns for MgH_2-A, MgH_2-B, MgH_2-C, and MgH_2-D are displayed in Figure 5-2. Synchrotron XRD data was collected because of poor minor phase detection with laboratory based XRD. The MgH_2 phase is dilute in MgH_2-D and was not detected with laboratory XRD. Synchrotron XRD was imperative in allowing for MgH_2 crystallite size determination. The XRD pattern for MgH_2-A reveals only MgH_2 and LiCl (Figure 5-2A). No starting reagents are detectable. As expected, the MgH_2 peak intensities decrease for subsequent samples as the amount of LiCl buffer added to the initial starting reagents increases. The XRD patterns for MgH_2-A, MgH_2-B and MgH_2-C show a minor unknown peak at d = 0.3142 nm which is expected to be a minor reagent impurity phase that was not detected by laboratory based XRD. The unknown peak did not match any phase that consisted of elements within the starting reagents.

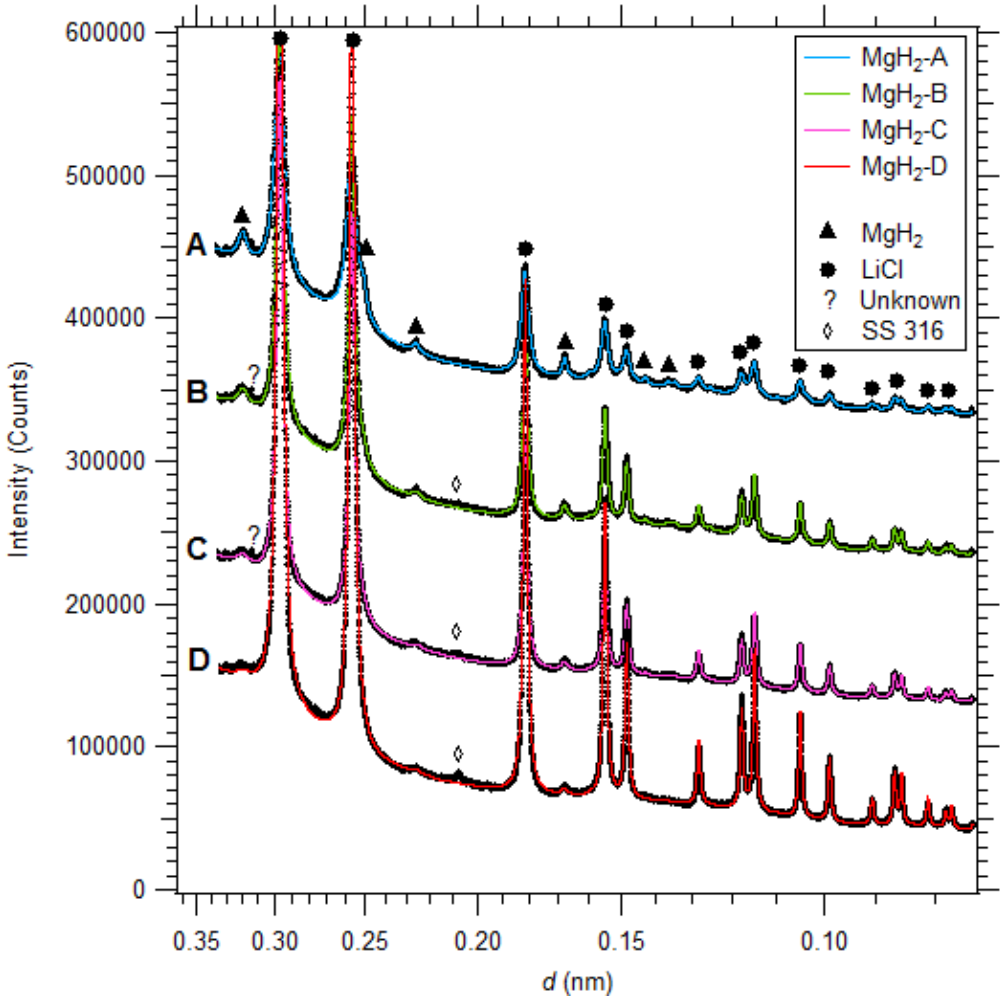

Figure 5-2: X-ray Diffraction (XRD) patterns (Australian Synchrotron) from A) MgH_2-A, B) MgH_2-B, C) MgH_2-C, and D) MgH_2-D. Rietveld fits to the data are displayed.

A peak in Figure 5-2 at d = 0.2075 nm is clearly discernable in MgH_2-D and was attributed to 316 stainless steel, a minor contaminant from the ball milling canister. The presence of stainless steel phases such as Fe will not adversely affect thermodynamic investigations. All of the MgH_2 samples, including the bulk reference (MgH_2-Purchased), were all milled under identical conditions for the same length of time. Therefore similar levels of any contaminants from the ball milling equipment will be present in all samples. No thermodynamic changes have been reported in the literature for the multitude of Mg samples that have undergone ball milling in the past, and hence been introduced to stainless steel impurities. Any kinetic enhancement due to contamination is irrelevant as hydrogen measurements are collected until final equilibrium is reached regardless of the decomposition rate. Furthermore, the possibility of an Mg_2FeH_x intermetallic forming is not supported by XRD results and its presence would not affect MgH_2 thermodynamic investigations due to the low hydrogen equilibrium pressure of Mg_2FeH_6, half that of MgH_2 [268].

The MgH_2 crystallite sizes were determined from Rietveld analysis as shown in Table 5-4. The MgH_2 phase becomes increasingly dilute as a consequence of LiCl buffer addition. The average LiCl crystallite size also grows as a function of LiCl buffer. Samples with high buffer quantities display larger LiCl crystallite sizes as the crystallites from purchased LiCl are larger than those formed in the mechanochemical reaction. A reduction in the MgH_2 crystallite size with increasing buffer is also evident from the Rietveld results. The crystallite size does not change significantly between samples, however this is not a measure of the MgH_2 particle size which cannot be determined from XRD.

Table 5-4: Rietveld fitting results for mechanochemically synthesised MgH_2 XRD patterns given in Figure 5-2. Mathematical fitting uncertainties are provided (2 standard deviations).

	Phase	Wt. %	Crystallite size (nm)
MgH_2-A	MgH_2	10.9 ± 0.2	10.0 ± 0.2
	LiCl	89.1 ± 0.2	12.8 ± 0.2
MgH_2-B	MgH_2	8.3 ± 0.2	7.6 ± 0.2
	LiCl	91.7 ± 0.2	18.8 ± 0.2
MgH_2-C	MgH_2	5.2 ± 0.2	6.7 ± 0.4
	LiCl	94.8 ± 0.2	19.6 ± 0.2
MgH_2-D	MgH_2	1.9 ± 0.2	6.7 ± 0.6
	LiCl	98.1 ± 0.2	22.5 ± 0.2

As a result of the inability to detect minor light element phases, quantitative phase analysis from XRD diffraction may prove unreliable in measuring the extent to which Reaction 5.2 is complete in mechanochemically synthesised samples. Consequently, hydrogen sorption measurements were performed to determine the MgH_2 content in each sample. The samples were placed in a manometric hydrogen sorption apparatus, without exposure to air, and out-gassed at 300°C under vacuum for 24 hours. This temperature is insufficient to remove hydrogen from any unreacted LiH and therefore the subsequent hydrogen absorption can be attributed solely to Mg. In considering the extent to which Reaction 5.2 had gone to completion during ball milling for each sample, the fact that the starting reagent, LiH, had only 95% purity must be considered. From the hydrogen sorption measurements it was found that for MgH_2-A, MgH_2-B, MgH_2-C and MgH_2-D the reaction was 94.5, 84.9, 82.2 and 78.1% complete, respectively (uncertainties are ± 0.5%). The decrease in the extent to which Reaction 5.2 is complete is an expected consequence of the dilution of the starting reagents, LiH and $MgCl_2$ which hinders reagent contact and thus reaction kinetics.

Neutron diffraction (ND) was undertaken in addition to synchrotron XRD in an attempt to provide larger diffraction peaks for the magnesium hydride nanoparticles, allowing for more accurate crystallite size information. Different diffraction peak intensity profiles result from ND in contrast to XRD due to the different interactions that neutrons and x-rays have with matter. This phenomenon can allow light-element phases to be more easily identified with diffraction as in the case of a low concentration magnesium hydride phase. It is unfortunate that hydrogen produces a large incoherent scattering background in neutron diffraction patterns as MgH_2 contains significant quantities of hydrogen. Thus deuterated samples (MgD_2) were prepared replicating the MgH_2 nanoparticle synthesis procedure (see Table 5-3), utilising a LiD (98 at.% D, Sigma Aldrich) starting reagent instead of LiH.

Neutron diffraction patterns were collected for each of the mechanochemically synthesised MgD_2 samples as shown in Figure 5-3 where experimental details are provided in Section 2.2.4. It is evident that the MgD_2 phase produces a more intense diffraction pattern than MgH_2 did in the synchrotron diffraction pattern (Figure 5-2). However the instrument peak broadening in the neutron diffraction patterns

significantly affects the MgD_2 diffraction peaks and in the case of MgD_2-D it effectively smears the peaks into the background. Longer data collection times didn't improve the resolution but only acted to slightly improve the signal to noise ratio.

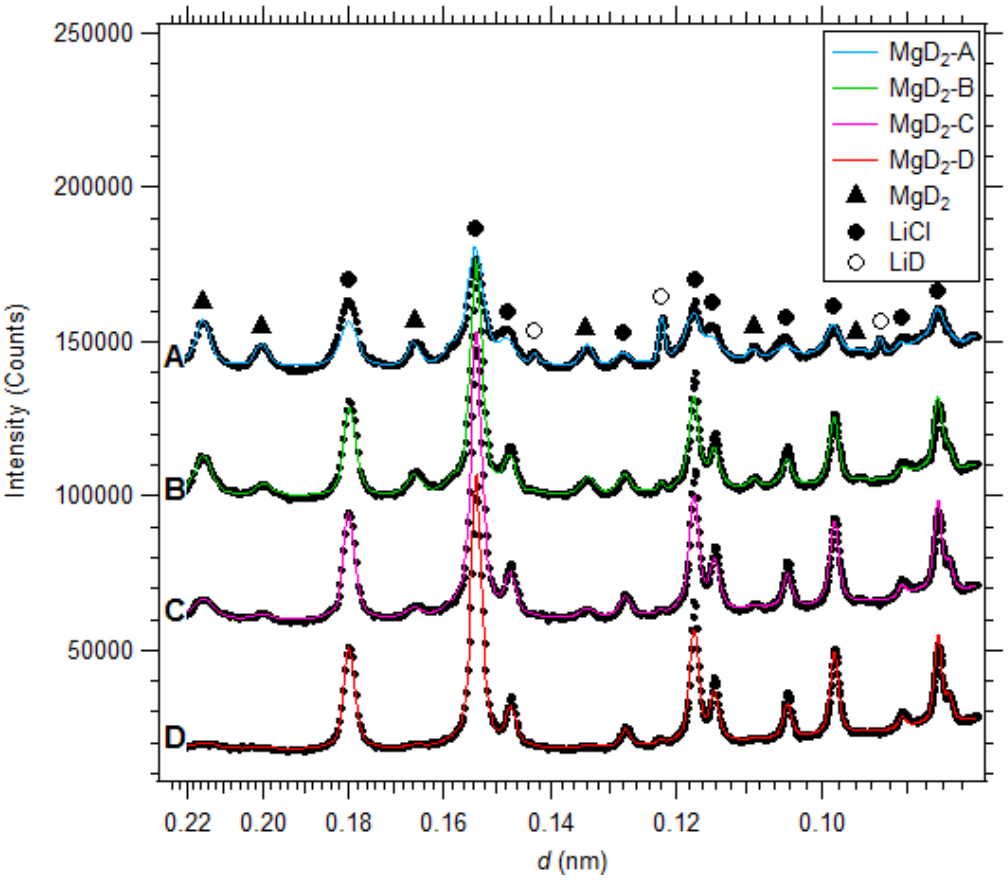

Figure 5-3: Neutron Diffraction (ND) patterns (ANSTO: Wombat) from A) MgD_2-A, B) MgD_2-B, C) MgD_2-C, and D) MgD_2-D. Rietveld fits to the data are displayed.

A Rietveld analysis was performed on the neutron diffraction data as shown by the fits to the data in Figure 5-3 and the quantitative phase information is provided in Table 5-5. The instrument profile used in Rietveld analysis was generated from an alumina standard over a given *d*-spacing data range (see Section 2.2.4). The MgD_2 samples were only modelled over the *d*-spacing data range (given in Figure 5-3) that was modelled by the instrument function. Neutron diffraction patterns for different isotopes can have very different peak intensity profiles. As such, a ratio between ^{6}Li- and ^{7}Li-based LiCl (7.6% ^{6}Li natural abundance) had to be implemented during Rietveld analysis to provide a better fit to the LiCl peak profiles. However it can be seen that the Rietveld fit to the LiCl phase in the MgD_2-A ND pattern is not very good. The reason for this poor LiCl fit is not yet known, however it is not expected to

greatly impact the quality of the MgD_2 refinement. The LiCl peaks in MgD_2-B, MgD_2-C, and MgD_2-D were also modelled using two different LiCl phases with different crystallite sizes as these samples contain both mechanochemically synthesised LiCl (LiCl-synth) and LiCl present as a buffer (LiCl-buffer). In order to constrain the large number of correlated variables regarding the LiCl phases, a fixed ratio between LiCl-synth and LiCl-buffer was implemented that was equal to the theoretically calculated ratio. All other parameters were refined.

It should be noted that although the fits to the ND data in Figure 5-3 look relatively good, a high level of correlation between fitted parameters exists, especially in the case of the LiCl phase. The problem arises due to the low number of peaks that are fitted with functions containing a high number of variables. This issue is much more significant in Rietveld analysis of the ND data than in the XRD data due to the added complication of isotopic diffraction variation, in addition to the extra consideration of dual LiCl phases in MgD_2-B, MgD_2-C, and MgD_2-D. The difficulty in achieving a realistic fit to the data is also exacerbated by the fact that the instrument broadening is so severe, resulting in a dominant cause of peak broadening. Due to these concerns it must be noted that the Rietveld results from XRD (Table 5-4) are more reliable than those determined by ND (Table 5-5). The reliability is also reflected in the mathematical fitting uncertainties provided, which are often an order of magnitude larger for the ND Rietveld results.

Table 5-5: Rietveld fitting results for mechanochemically synthesised MgD_2 ND patterns given in Figure 5-3. Mathematical fitting uncertainties are provided (2 standard deviations).

	Phase	Wt. %	Crystallite size (nm)
MgD_2-A	MgD_2	11.9 ± 1.2	7.3 ± 1.1
	LiCl-synth	84.4 ± 1.3	10.3 ± 3.6
	LiD	3.7 ± 0.4	48.1 ± 35.2
MgD_2-B	MgD_2	10.9 ± 0.9	5.4 ± 0.6
	LiCl-synth	58.1 ± 0.8	6.2 ± 1.2
	LiCl-buffer	30.5 ± 0.6	30.4 ± 14.4
	LiD	0.6 ± 0.2	-
MgD_2-C	MgD_2	6.1 ± 0.9	4.3 ± 0.7
	LiCl-synth	40.6 ± 0.8	7.0 ± 3.6
	LiCl-buffer	53.1 ± 0.9	11.5 ± 1.9
	LiD	0.2 ± 0.2	-
MgD_2-D	MgD_2	2.1 ± 1.0	3.9 ± 2.0
	LiCl-synth	22.0 ± 1.0	-
	LiCl-buffer	75.6 ± 1.3	9.8 ± 0.9
	LiD	0.2 ± 0.2	-

The MgD_2 crystallite sizes determined from ND are consistently in the order of 60-70% of the MgH_2 crystallite sizes determined from XRD. The variation may be due to the difference in forming deuterated magnesium hydride nanoparticles by a mechanochemical synthesis process. It should be reiterated that the MgD_2 crystallite size has no impact on the MgD_2 particle size. Although in MgD_2-D it is expected that the particle size does approach the crystallite size due to the large amount of LiCl buffer used that restricts particle agglomeration during milling. The quantitative MgD_2 wt.% values (from ND) are typically equivalent to the MgH_2 wt.% values (from XRD) within uncertainty, illustrating that the mechanochemical reactions both progress to a similar level of completion. A LiD phase was also found in ND data, an indication of an incomplete mechanochemical reaction. LiD was not found in XRD due to the low level of scattering from such a light element phase using x-rays, however neutrons are much more sensitive to Li and D and as such high intensity LiD peaks are present in the ND pattern.

Transmission electron microscopy (TEM) investigations were undertaken for each of the mechanochemically synthesised samples that were milled with different quantities of LiCl buffer. TEM allows for particle size determination in comparison to crystallite size results from diffraction. MgH_2 particle size is crucial given the theoretical predictions linking particle size to the Mg-H system's thermodynamic properties.

TEM micrographs for MgH_2-A (2.21:1 LiCl:MgH_2 volume ratio) are provided in Figure 5-4. MgH_2-A primarily showed large geometrical particle shapes (typically hexagons) 1 to 2 μm in size. The large geometrical structures, which were initially dark, showed a steadily increasing light band over time around the outer edge on exposure to the electron beam (Figure 5-4A & B). This effect ceased after some minutes. The growth of the light band suggested that these micron sized particles are MgH_2 that underwent hydrogen desorption under the beam. The large hexagonal particles were polycrystalline where each individual crystallite is generally less than 50 nm as shown in Figure 5-4C & D.

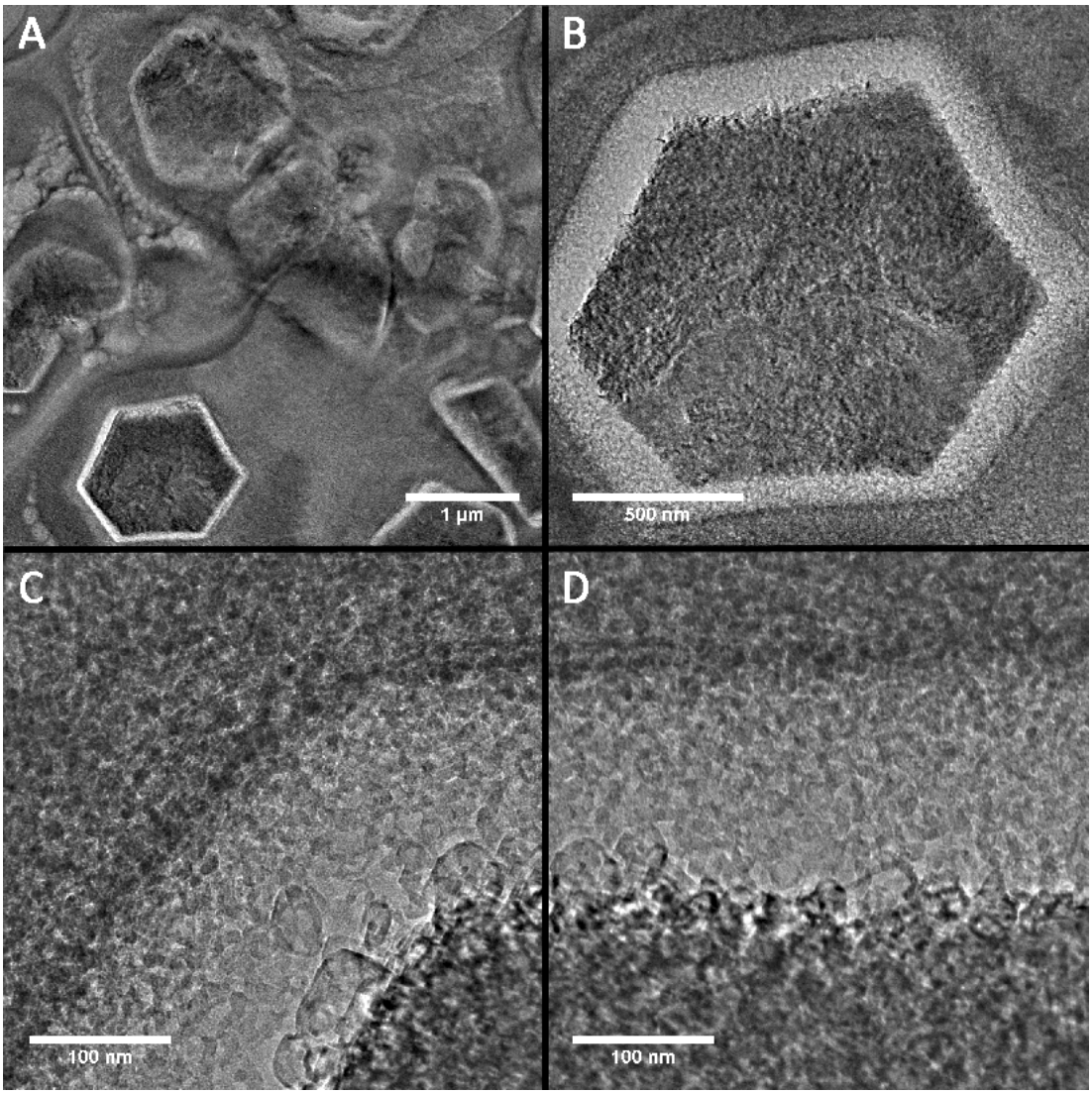

Figure 5-4: Representative Transmission Electron Microscope (TEM) micrographs of MgH_2-A. The sample primarily consisted of A & B) hexagonal particles that were polycrystalline, consisting of C & D) many smaller crystallites.

MgH_2-B showed no large geometrical shapes such as those in MgH_2-A. Typical morphologies (Figure 5-5) consisted of aggregates of irregularly shaped particles 15 - 40 nm in size. Time lapse TEM images showed that some particles within the aggregates changed under the electron beam over the course of several minutes. These particles, however, maintained their morphology. It is likely that the MgH_2 is decomposed under the high energy electron beam causing visible changes in the particle morphology over time.

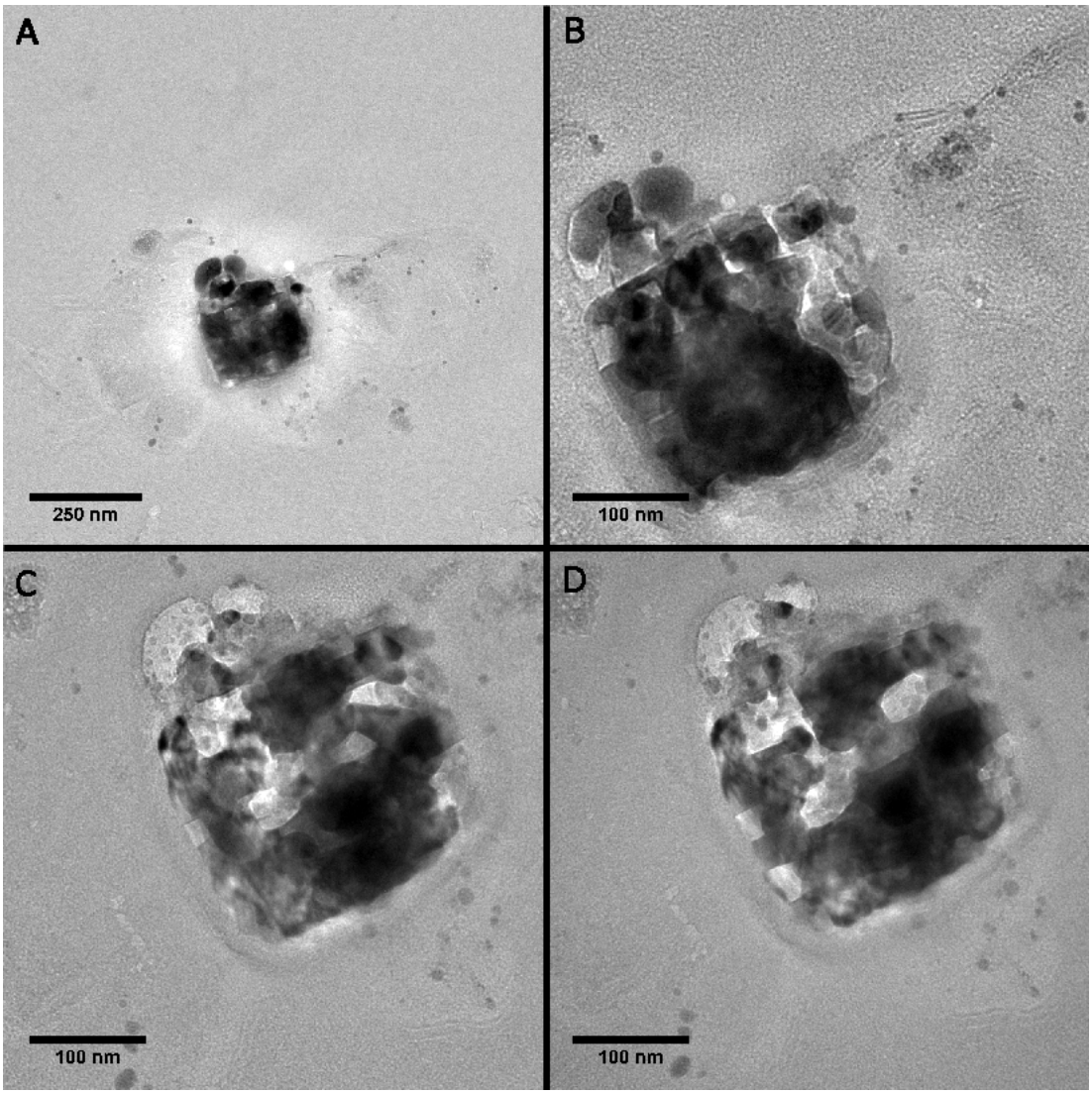

Figure 5-5: Transmission Electron Microscope (TEM) micrographs of MgH_2-B. The images form a time sequence where the sample was exposed to the beam for A) 0 minutes, B) 2 minutes, C) 10 minutes, and D) 12 minutes.

MgH_2-C primarily comprises of a single morphology (Figure 5-6A & B) consisting of well dispersed 12 – 20 nm particles. Given the average MgH_2 crystallite size from XRD is 6.7 nm, it is suggested that each particle in MgH_2-C consists of several crystallite domains. Some particles were found separated from the LiCl matrix (Figure 5-6C) that were the same size as those within the matrix. However when separated from LiCl the MgH_2 is very unstable under the electron beam and decomposes completely in less than 1 minute (Figure 5-6D).

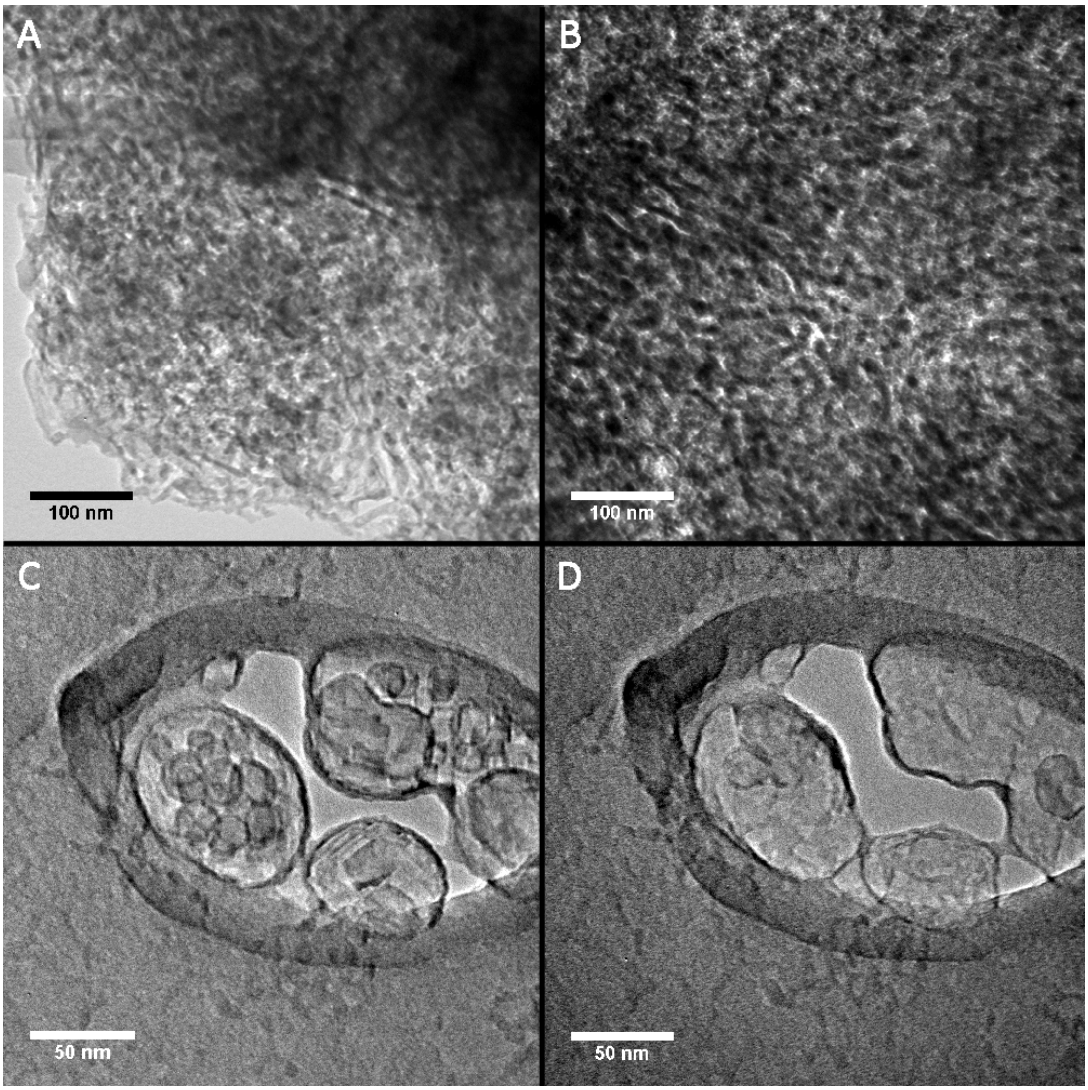

Figure 5-6: Representative Transmission Electron Microscope (TEM) micrographs of MgH_2-C. The sample primarily consists of A) & B) well dispersed MgH_2 particles in a LiCl matrix. However some particles were C) found separated from the matrix that disappeared under the beam D) after 1 minute.

Energy dispersive spectroscopy (EDS) was undertaken in particular regions of MgH_2-C that displayed different electron contrast as shown in Figure 5-7. The EDS data shows that brighter regions investigated using TEM are typically chlorine-rich (from LiCl) and darker regions are typically magnesium-rich (from MgH_2). It should be noted that both hydrogen and lithium are not identified using EDS due to their low number of electrons. Contrast variation can also be related to sample thickness and not just phase variation, however given the thin nature of the regions investigated it is expected that phase contrast is dominant.

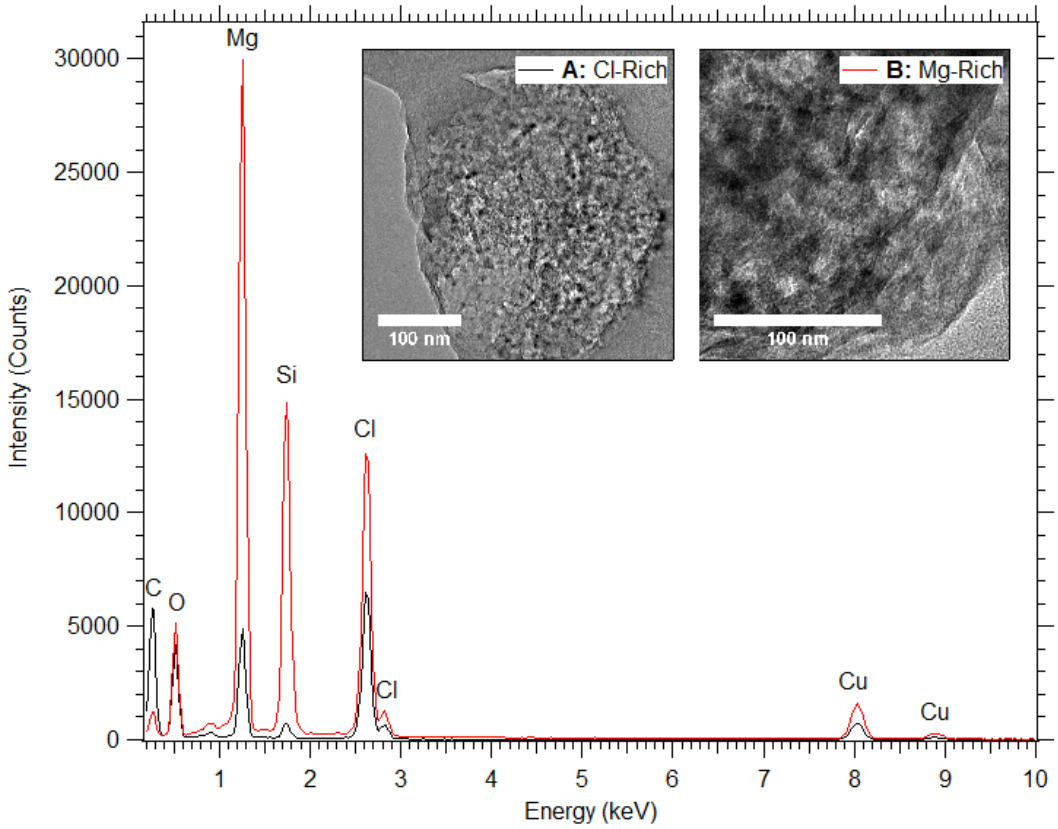

Figure 5-7: Energy dispersive spectroscopy (EDS) patterns from two regions of MgH_2-C. TEM insets are provided displaying the regions of interest.

MgH_2-D is largely homogenous but does show some recognisable particle morphology (Figure 5-8A & B). The white arrows in Figure 5-8 identify MgH_2 particles approximately 7 nm in size. The particles are difficult to discern due to the sample thickness but TEM imaging of thin sample regions resulted in rapid sample decomposition. High magnification TEM identified lattice fringing regions that extended for 2 – 4 nm (Figure 5-8C & D) suggesting very small MgH_2 crystallites were synthesised where lattice fringing was limited to the MgH_2 *hkl* = 020 plane. EDS data collected in regions with high levels of lattice fringing also displayed high levels of magnesium similar to the EDS pattern for MgH_2-C provided in Figure 5-7B. It is interesting that only one crystal plane for MgH_2 could be discerned from TEM. It may be possible that there is MgH_2 crystal growth along a preferred crystallographic axis in the mechanochemically synthesized nanoparticles.

It should be noted that there is a reasonable correlation between the crystallite sizes determined from TEM lattice fringing for sample MgH_2-D with those determined

from XRD even though TEM provides number-weighted crystallite size and XRD provides volume-weighted crystallite size [104]. The correlation between the crystallite size for MgH_2 from XRD (6.7 nm) and the particle size from TEM (~7 nm) is excellent. The result suggests that the MgH_2 particles are primarily single crystals given that the average particle size cannot be smaller than the average crystallite size. Therefore the particle morphology seen during TEM investigations is representative of the average particle structure throughout the sample. This is in contrast to other results for Mg metal nanoparticles in the literature [262] where XRD crystallite size is almost an order of magnitude larger than the reported TEM crystallite size.

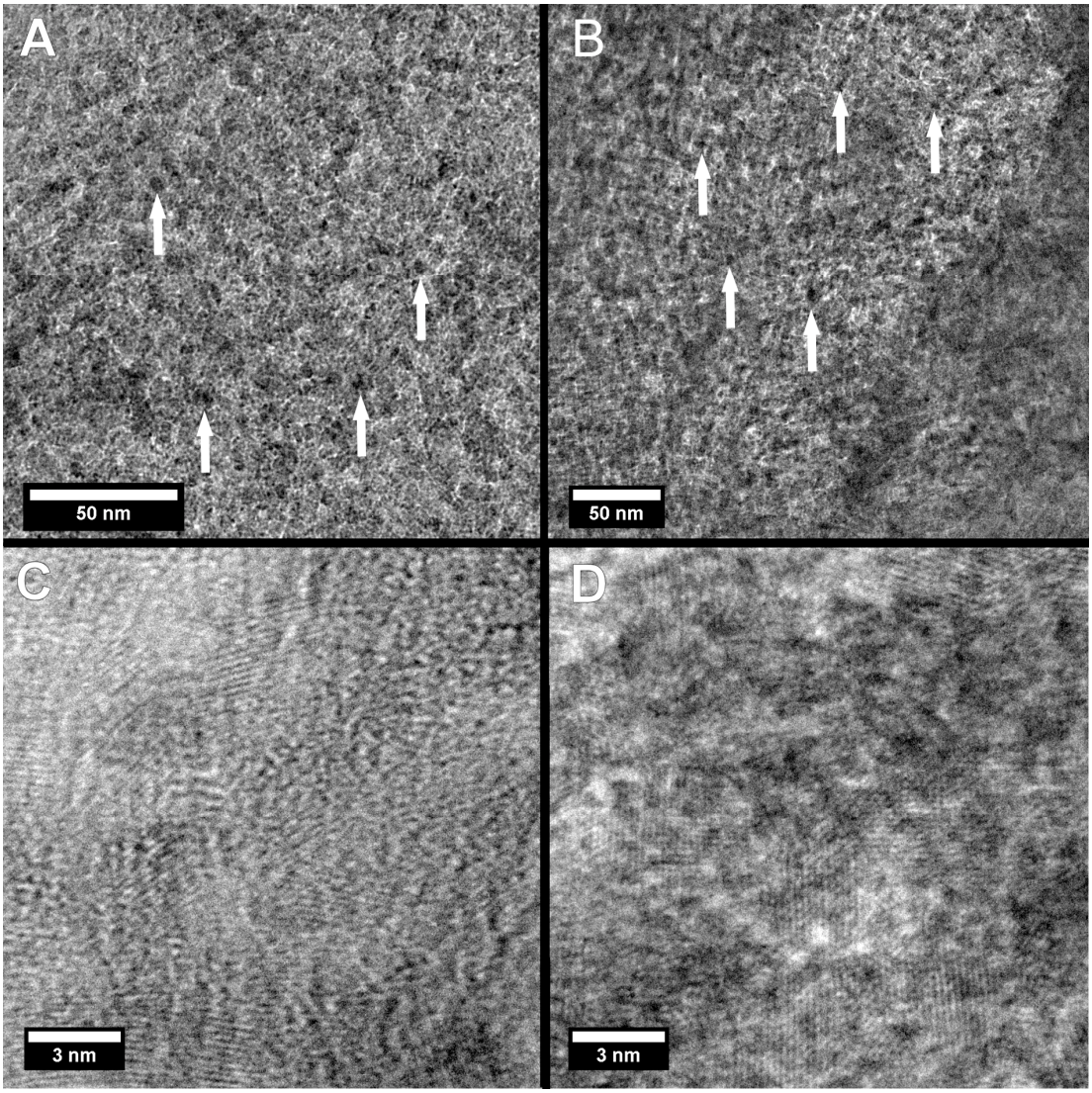

Figure 5-8: Representative Transmission Electron Microscope (TEM) micrographs of MgH_2-D. The sample consists of A) & B) a homogenous morphology with single MgH_2 particles (~7 nm) indicated by the white arrows. C) & D) Lattice fringing from MgH_2 was evident with crystallite domains from 2 – 4 nm.

MgH_2-Purchased (used as a bulk MgH_2 standard) was analysed by XRD before and after ball milling for 18 hours as shown in Figure 5-9. Quantitative phase analysis results are provided in Table 5-6 from the Rietveld fits to the data. Before milling the MgH_2, XRD peaks are quite narrow due to its large crystallite size (152 ± 4 nm), however after milling the peaks are very broad due to the reduction in crystallite size (~ 6 nm). Even though the MgH_2 crystallite size for MgH_2-Purchased was determined to be nanoscopic the particle size in the purchased sample is likely even larger than particles in MgH_2-A (1 – 2 μm), due to particle agglomeration during milling when no buffering agent is present. The quantitative phase analysis results in Table 5-6 show that the wt.% of MgH_2 remains constant after milling. However, upon milling, some of the MgH_2 undergoes a phase transition from the β-phase to the γ-phase. The production of the γ-MgH_2 phase has been found previously after mechanically alloying MgH_2 with other metals [269]. The Rietveld fit to the XRD data for MgH_2-Purchased does not adequately model the peak intensities from the γ-MgH_2 phase. This may be due to preferential cleavage along particular γ-MgH_2 crystal planes during milling. Minor traces of both Mg and MgO are present in the sample due to the purity (≥ 96.5%) of the as-received MgH_2 reagent.

Table 5-6: Rietveld fitting results for the ball milled, purchased MgH_2 XRD pattern given in Figure 5-9. Mathematical fitting uncertainties are provided (2 standard deviations).

	Phase	Wt. %	Crystallite size (nm)
MgH_2 (as received)	β-MgH_2 ($P4_2/mnm$) [234]	93.5 ± 0.4	152 ± 4
	Mg	3.7 ± 0.1	245 ± 92
	MgO	2.8 ± 0.4	3.8 ± 0.8
MgH_2-Purchased	β-MgH_2 ($P4_2/mnm$) [234]	79.2 ± 1.4	6.4 ± 0.2
	γ-MgH_2 (Pbcn) [234]	13.8 ± 1.2	5.5 ± 0.6
	Mg	1.3 ± 0.4	18.3 ± 9.2
	MgO	5.6 ± 1.0	3.4 ± 0.8

Table 5-7 provides an overview of the crystallite and particle size information obtained from XRD and TEM for each of the mechanochemically synthesised MgH_2 samples as well as the milled purchased sample. The average MgH_2 crystallite size does decrease with increasing buffer (MgH_2-A → MgH_2-D) however the change is very minor. It should be also noted that the crystallite size of MgH_2-Purchased is also equivalent to the samples mechanochemically synthesised. However, it is the particle size that is of greatest importance. TEM results demonstrate that a dramatic reduction

in MgH_2 particle size occurs when samples are mechanochemically synthesised with large LiCl buffers. The particle size of MgH_2-D (~7 nm from TEM) is within the range that thermodynamic changes in the Mg-H system are predicted (< 10 nm, see Section 1.4.2).

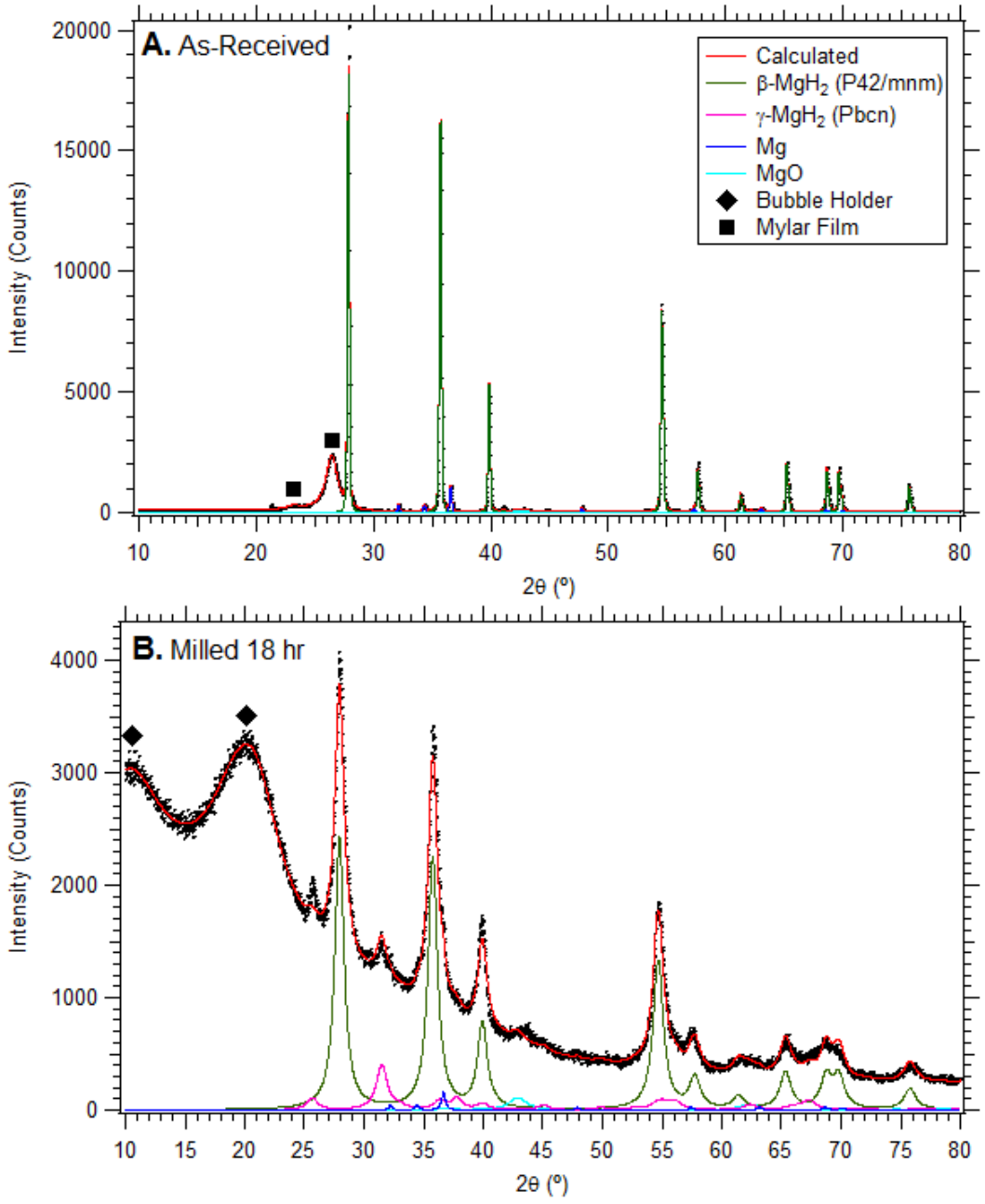

Figure 5-9: X-ray Diffraction (XRD) patterns (D8) for MgH_2-Purchased A) before and B) after ball milling. Rietveld fits to the data are also displayed.

Table 5-7: Summary of MgH_2 particle and crystal size information as determined using TEM and XRD. *only crystallites could be discerned from the homogenous sample. Mathematical fitting uncertainties are provided (2 standard deviations).

	TEM average particle size	XRD average crystallite size
MgH2-A	1 – 2 μm	10.0 ± 0.2 nm
MgH2-B	15 – 40 nm	7.6 ± 0.2 nm
MgH2-C	12 – 20 nm	6.7 ± 0.4 nm
MgH2-D	2 – 7 nm *	6.7 ± 0.6 nm
MgH2-Purchased	N/A	6.4 ± 0.2 nm

5.2.2 Cryogenic Milling

The cryogenic mechanochemical synthesis of MgH_2 was undertaken according to Reaction 5.2 by milling at 77 K. All reagents were cryogenically milled separately for 30 minutes prior to use. Characterisation of the milled reagents was performed using synchrotron XRD as shown in Figure 5-10.

The XRD results for the cryogenically pre-milled reagents are similar to those for reagents milled at room temperature (as displayed in Figure 5-1). The LiH and LiCl reagents display relatively sharp XRD peaks, indicative of large crystallites, for both room temperature and cryogenic milling. The $MgCl_2$ XRD patterns differ between the different milling conditions, where the cryogenically milled $MgCl_2$ presents broader peaks indicating that smaller crystallites have been generated. In fact, the cryogenically milled $MgCl_2$ XRD pattern displays extremely broad peaks indicating that there is a significant amount of structural deformation in the crystal structure.

XRD results for each of the samples cryogenically milled with different quantities of LiCl buffer (given by Table 5-3) are presented in Figure 5-11.

The XRD results indicate that the starting reagent phases ($MgCl_2$ & LiH) are still present in the as-milled samples, although dilution with LiCl does hinder identification of these phases in high buffer samples. It is evident that cryogenically milling for 1 hour does not allow adequate time for Reaction 5.2 to progress. Cryogenic milling requires at least 5 litres of liquid nitrogen to be added to the mill every half hour, leading to impracticality in any cryogenic milling runs that approach the milling times undertaken during room temperature milling. Given the labour intensive nature of cryogenically milling for very long periods of time, room

temperature milling was identified as the most practical mechanochemical synthesis pathway.

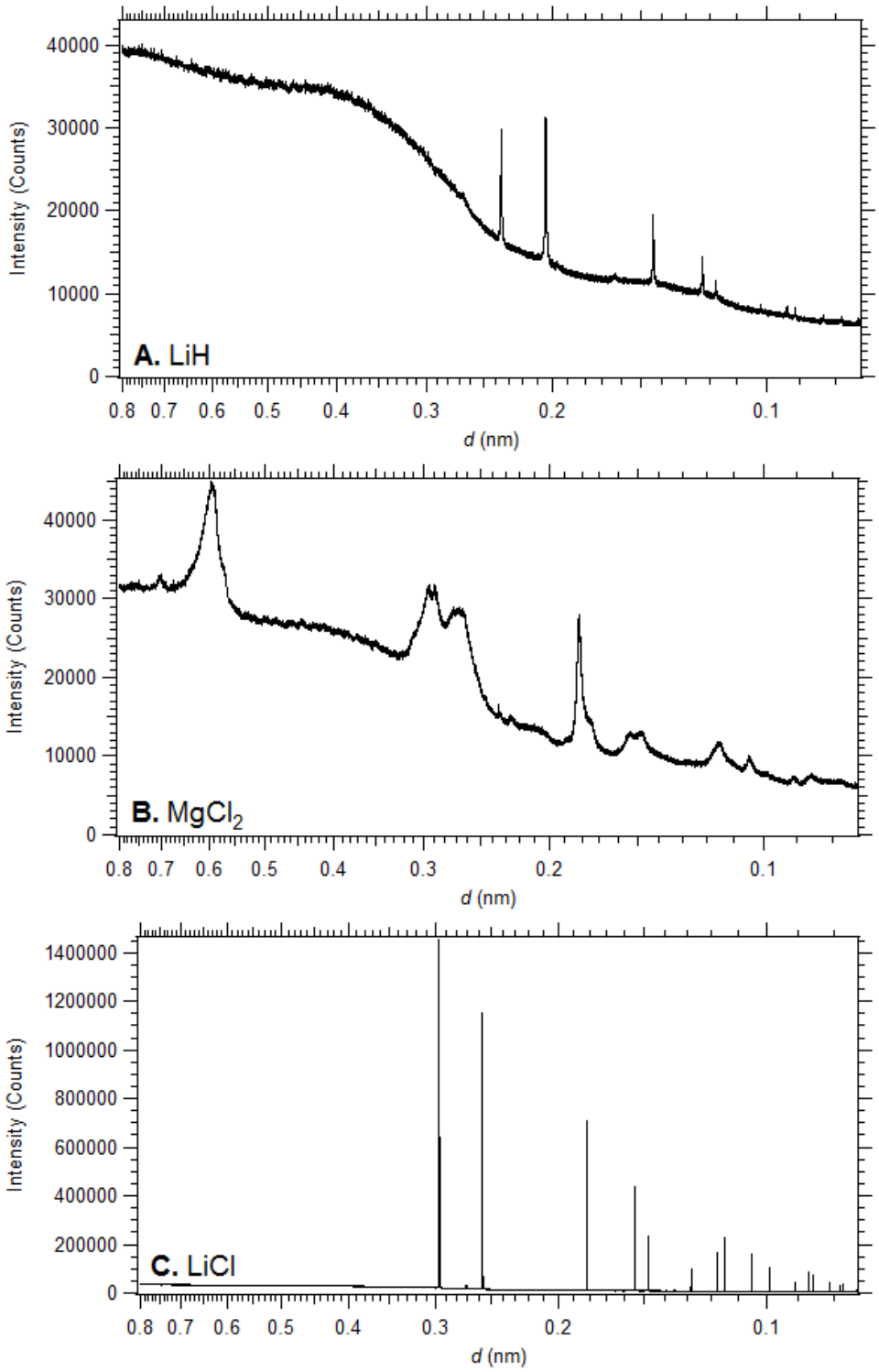

Figure 5-10: X-ray Diffraction (XRD) patterns (Australian Synchrotron) from cryogenically pre-milled starting reagents A) LiH, B) $MgCl_2$, and C) LiCl.

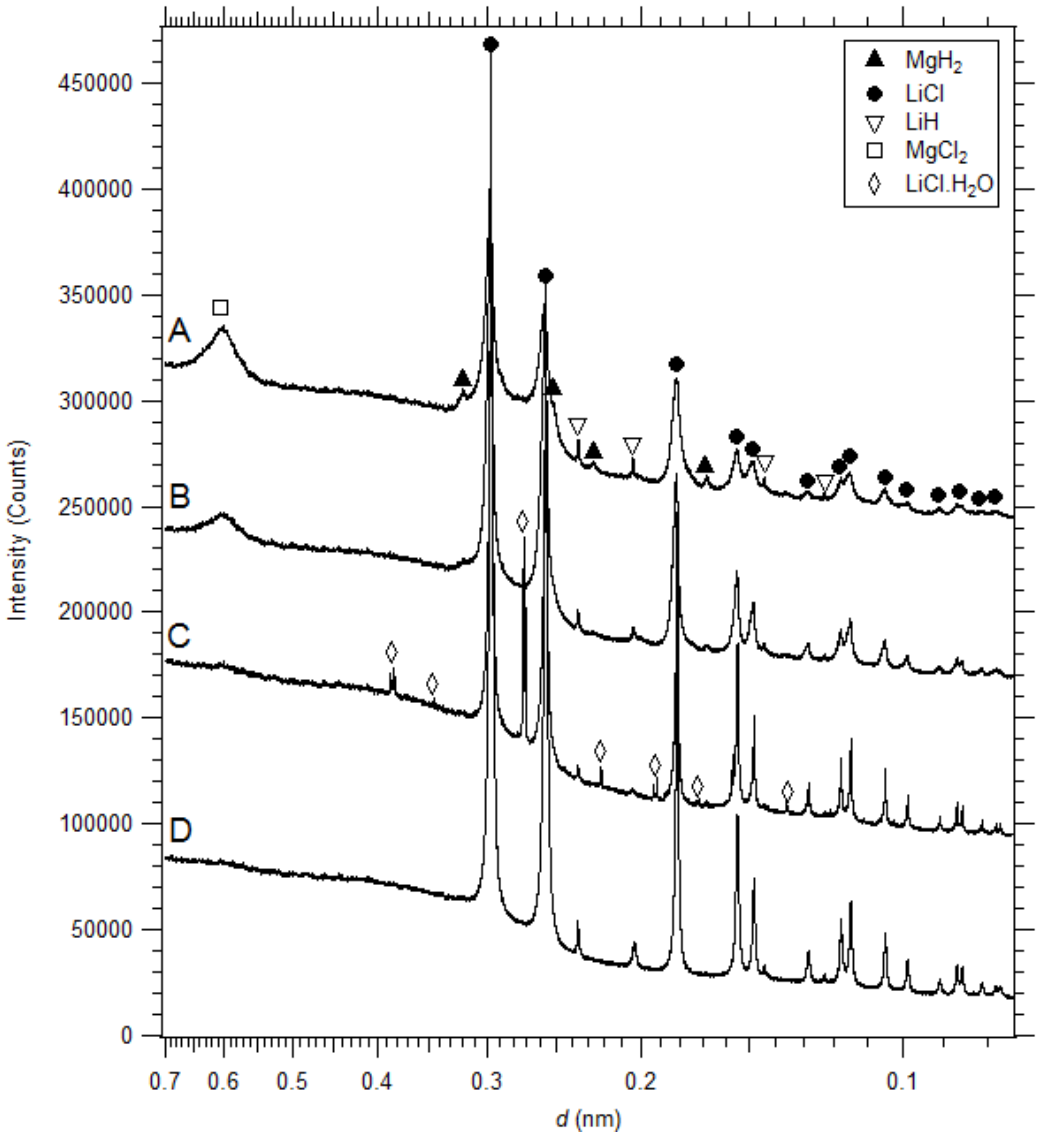

Figure 5-11: X-ray Diffraction (XRD) patterns (Australian Synchrotron) from A) MgH_2-A-cryo, B) MgH_2-B-cryo, C) MgH_2-C-cryo, and D) MgH_2-D-cryo.

5.2.3 Washing

In order to synthesise pure MgH_2 nanoparticles the LiCl salt by-product must be removed. The removal of the salt is generally undertaken by a washing procedure with a solvent that is able to dissolve LiCl and is unreactive towards MgH_2. It is expected that removal of the LiCl buffer would result in significant MgH_2 agglomeration especially when the nanoparticles are heated to decomposition temperatures (~300°C).

Initially the mechanochemically synthesised MgH_2 nanoparticles embedded in LiCl were washed with a nitromethane/$AlCl_3$ solution, as was undertaken with Al and AlH_3 (see Sections 3.2.2 & 4.2.3.2). However, significant gas evolution was observed upon addition of the MgH_2/LiCl sample to the nitromethane/$AlCl_3$ solvent. In addition, no MgH_2 was present after the washing process was taken to completion. The lack of a MgH_2 product must be a consequence of either MgH_2 solubility or reactivity in the nitromethane/$AlCl_3$ system. A similar problem arose when a toluene/$AlCl_3$ solvent was used to dissolve LiCl from the mechanochemically synthesised MgH_2/LiCl sample. Although no reaction was observed between the sample and the toluene/$AlCl_3$ solvent, after washing was complete it also appeared as though MgH_2 had dissolved into solution. It may be possible that the MgH_2 nanoparticles remained suspended in solution and would not separate with centrifugation, however they were not visible.

Tetrahydrofuran (THF) was also tested as a solvent in washing LiCl from MgH_2, due to the fact that MgH_2 is reportedly insoluble [270], however it was found to be highly reactive with THF causing bubbling and fizzing when placed into solution. Mg metal has been treated with THF in a study by Au [271]. Although it appears as though the Mg does not adversely react with THF, once the sample is hydrided a destabilised hydride product is evident from a pressure composition isotherm at 400°C. Au's XRD data for the hydrided sample also displays significant broad peaks suggesting a large quantity of MgO may be present in addition to an unknown compound that was tentatively identified as a Mg-THF-H_x complex. These results indicate that MgH_2 does in fact interact with THF, at least at high temperature.

In order to synthesise a washed nanoparticle product, given the difficulties in washing MgH_2, the magnesium hydride was first desorbed under vacuum at 360°C for 48 hrs to form Mg nanoparticles embedded in LiCl. Mg was found to be unreactive towards THF and thus it is able to be washed from its LiCl matrix. Washing was performed 3 times with THF and all the LiCl was removed as shown by the XRD results in Figure 5-12.

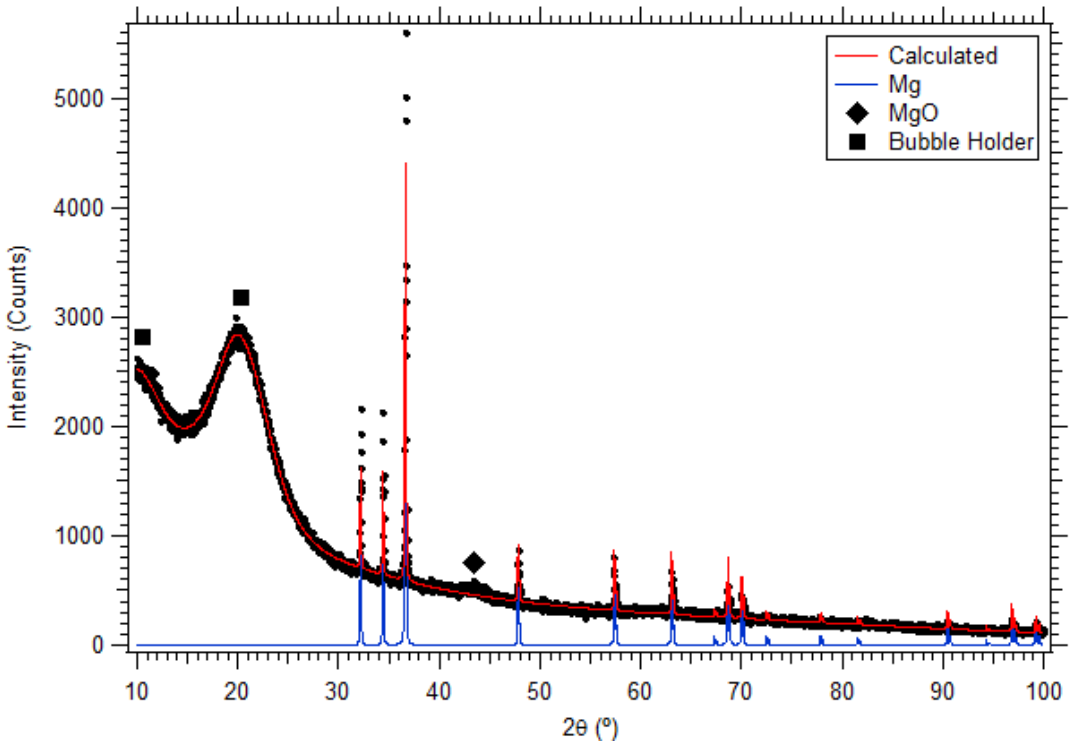

Figure 5-12: X-ray Diffraction (XRD) patterns (D8) for MgH_2-D after 360°C decomposition and LiCl salt removal by means of a THF solvent. A Rietveld fit to the data is displayed.

A Rietveld fit to the XRD data for the washed Mg resulted in a poor fit (see Figure 5-12) due to an unaccounted angular dependence. The washed Mg had to be analysed using a low background holder due to the small quantity of sample. Unfortunately the x-ray footprint on the sample changes as a function of collection angle and thus there is an angular dependent interaction volume that dictates the amount of collected counts. At low angles the x-ray foot print is large resulting in a large number of counts from a large sample interaction volume, but at high angles the x-ray foot print is small resulting in a reduced number of collected counts.

Despite the problem with collected intensity, the washed Mg phase presents extremely sharp peaks indicative of quite large crystallites. The Rietveld analysis adequately models the width of the XRD peaks and provides a Mg crystallite size of 126 ± 8 nm. The significant increase in crystallite size is thought to arise from the washing process itself. The dissolution of LiCl is exothermic and results in considerable sample/solution heating. Heating the Mg whilst it is embedded in LiCl will only result in minor crystallite growth due to the low number of crystallites in each isolated Mg/MgH_2 particle. However once the LiCl is removed Mg-Mg particle

aggregation can occur in solution and the presence of a heat source will allow for agglomeration and crystallite size growth to occur. A small quantity of MgO is also present in the washed XRD pattern that is thought to be due to the presence of lithium oxide in the starting reagents. Lithium oxide will be reduced by $MgCl_2$ resulting in minor quantities of MgO. The washed samples were not analysed further due to their large crystallite and hence particle sizes that are unfavourable for use in the current thermodynamic study.

5.3 HYDROGEN SORPTION

The mechanochemical synthesis of MgH_2 nanoparticles was performed in order to formulate different MgH_2 particles sizes. The particle size of MgH_2 has been theoretically predicted to alter the thermodynamics of the hydrogen decomposition reaction (see Section 1.4.2), hence altering desorption pressures. Hydrogen desorption experiments were undertaken in order to determine hydrogen equilibrium pressures in the Mg-H system. Desorption was undertaken at four different temperatures (300°C, 320°C, 340°C, & 360°C) in order to determine the thermodynamics properties (ΔH & ΔS) for the MgH_2 decomposition reaction given by Reaction 5.1. The experiments were performed in order to determine if there was a relationship between MgH_2 particle size and desorption equilibrium pressure. This relationship would experimentally demonstrate thermodynamic alterations with particle size. The determination of correct thermodynamic properties requires measurements with high levels of accuracy and precision. The custom-built automated Sieverts apparatus utilised allows for small thermodynamic changes to be discerned due to the high precision pressure and temperature data that are collected.

5.3.1 Equilibrium Pressure Measurements

Initially, desorption experiments were performed on the MgH_2-Purchased sample which was first ball milled to improve its kinetics. The purchased sample consisted of small 6.4 nm crystallites but these crystallites are part of much larger particles. MgH_2-Purchased was therefore used as a reference material in order to provide bench-mark equilibrium pressures for bulk MgH_2. A reference material is required because of the lack of consistent thermodynamic data available in the literature for MgH_2 (see Section 5.1.1.2). Due to limitations with extremely slow kinetics full pressure-composition isotherms were not generated. As such, equilibrium pressure data was collected over the hydrogen equilibrium plateau between hydrogen to metal ratios (H/M) of 0.8 to 1.8. Due to the flat nature of the equilibrium plateau in the Mg-H system repeat equilibrium measurements over this range were found to be equivalent within reported uncertainties. For example, at 360°C equilibrium pressures of 8.05 ± 0.02 bar and 8.06 ± 0.03 bar were measured at H/M ratios of 1.28 and 1.78 respectively for MgH_2-C.

Certain issues arise due to the slow kinetics of the Mg-H system near equilibrium, and a number of measures were taken to minimize detrimental effects. The room temperature part of the system typically drifted within 22 ± 1°C during the course of 24 hours. In principle, with fast enough kinetics, this room temperature variation would have no impact on the measured equilibrium pressure as the hydride system would respond to a system pressure change caused by room temperature variation by absorbing or desorbing hydrogen to maintain an equilibrium pressure. In reality, the slow kinetics of the system near equilibrium meant that changes in room temperature resulted in small but discernable changes in system pressure. To account for this change in system pressure with room temperature fluctuations, pressure measurements were collected every 2 minutes over at least 24 hours. The equilibrium pressure was then taken as being the average over the last 6 hours of data collection. The uncertainty in the measured equilibrium pressure was taken as two times the standard deviation (95% confidence interval) of the averaged data over this 6 hour period. In the course of these experiments it was also noted that argon can be adsorbed during the milling process and produce inflated equilibrium pressures during measurements. To alleviate this factor all samples were first out-gassed under vacuum at moderate temperature (> 100°C) to remove this adsorbed argon. Due to problems in the literature relating to inadequate measurement time (see Section 5.1.1.2) care was taken in an effort to provide high quality equilibrium data for MgH_2. This was required in order to provide accurate bulk thermodynamic data and to study the variation in thermodynamics with changes in MgH_2 particle size.

The kinetics of decomposition are quite slow for the mechanochemically synthesised MgH_2 samples. This can be attributed to the fact that the MgH_2 particles are embedded within a LiCl salt by-product matrix. Kinetic hydrogen desorption data is provided in Figures 5-13 to 5-17 that illustrate the majority of decomposition occurs within 2 – 5 hours, however minor but significant changes in pressure are still evident until 24 hours have passed. It is likely that MgH_2 nanoparticles that are not embedded within a LiCl matrix would present much faster hydrogen sorption kinetics. However, removal of the LiCl by-product phase results in significant crystallite and hence particle growth.

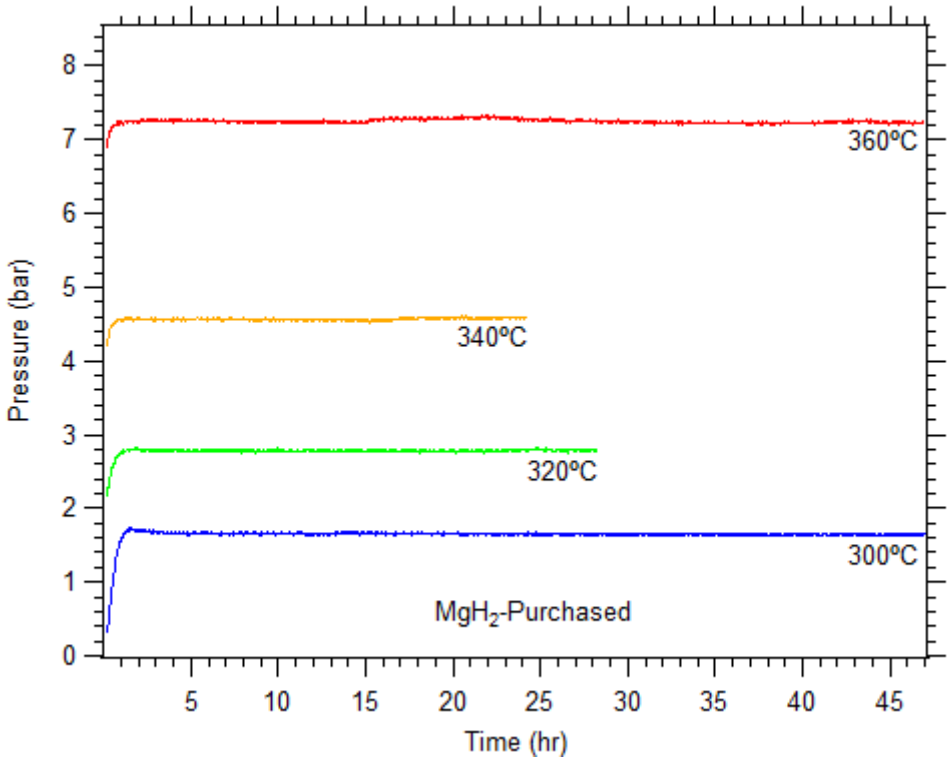

Figure 5-13: Hydrogen desorption kinetics for MgH_2-Purchased displaying the hydrogen equilibrium pressure at 300°C, 320°C, 340°C, and 360°C.

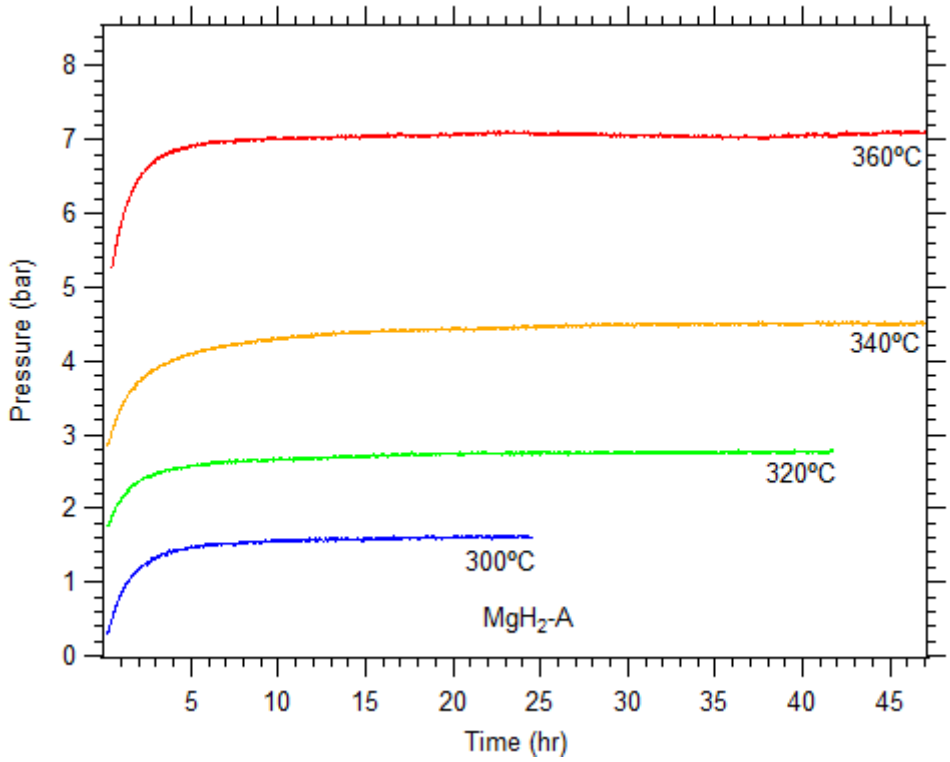

Figure 5-14: Hydrogen desorption kinetics for MgH_2-A displaying the hydrogen equilibrium pressure at 300°C, 320°C, 340°C, and 360°C.

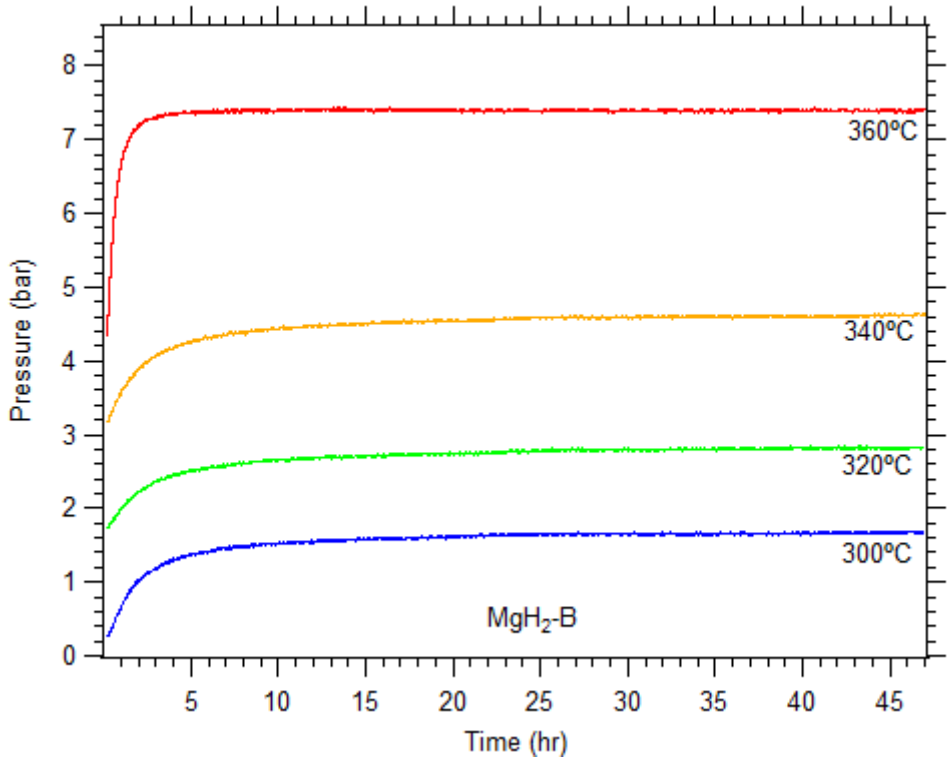

Figure 5-15: Hydrogen desorption kinetics for MgH_2-B displaying the hydrogen equilibrium pressure at 300°C, 320°C, 340°C, and 360°C.

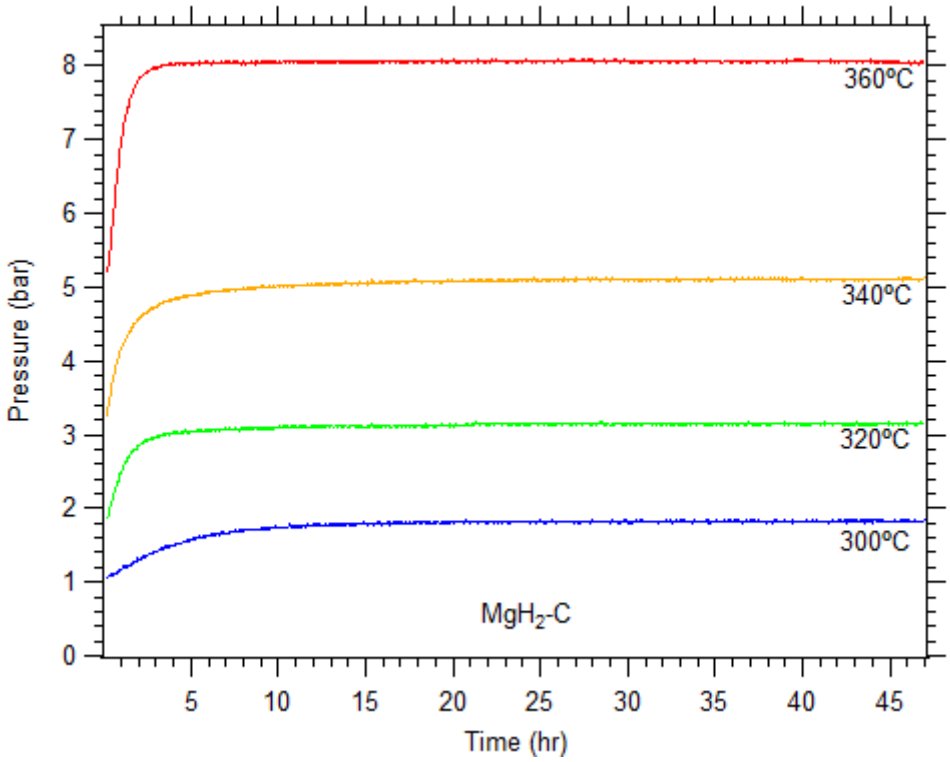

Figure 5-16: Hydrogen desorption kinetics for MgH_2-C displaying the hydrogen equilibrium pressure at 300°C, 320°C, 340°C, and 360°C.

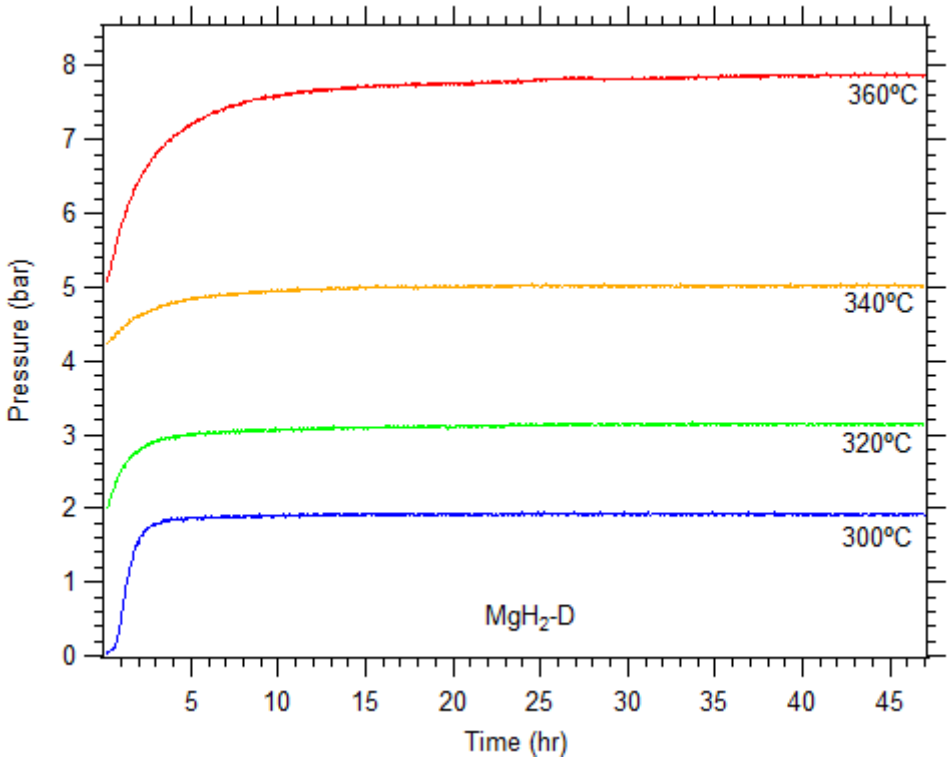

Figure 5-17: Hydrogen desorption kinetics for MgH_2-D displaying the hydrogen equilibrium pressure at 300°C, 320°C, 340°C, and 360°C.

The hydrogen equilibrium pressures are presented in Table 5-8. It is evident that there is a significant change in the hydrogen equilibrium pressure between the samples analysed. The equilibrium pressures for MgH_2-A and MgH_2-B are similar to the pressures obtained for MgH_2-Purchased at all measured temperatures. The similarity in equilibrium pressures is expected for MgH_2-A due to the large MgH_2 particle size (1 – 2 μm) which is effectively bulk. However the similarity between the equilibrium pressures of MgH_2-B and MgH_2-Purchased is interesting as the MgH_2-B particle size from TEM was found to be relatively nanoscopic (15 – 40 nm). The result indicates that MgH_2 particle sizes smaller than this are required to observe measureable thermodynamic changes, as is predicted by theoretical studies. A large increase in the equilibrium pressure is found for both MgH_2-C and MgH_2-D in comparison to MgH_2-Purchased at all measured temperatures. It can be deduced that the change in equilibrium pressure is a result of thermodynamic changes within the Mg/MgH_2 system due to nanoscopic particle size as this is the only variable between mechanochemically synthesised samples.

Table 5-8: Measured desorption equilibrium pressures for mechanochemically synthesised and purchased MgH_2 samples. Uncertainties are calculated with a 95% confidence interval.

	MgH_2-Purchased	MgH_2-A	MgH_2-B	MgH_2-C	MgH_2-D
Pressure at 300°C (bar)	1.636 ± 0.020	1.622 ± 0.018	1.671 ± 0.019	1.824 ± 0.017	1.919 ± 0.018
Pressure at 320°C (bar)	2.789 ± 0.019	2.763 ± 0.019	2.837 ± 0.020	3.146 ± 0.018	3.134 ± 0.020
Pressure at 340°C (bar)	4.581 ± 0.021	4.506 ± 0.022	4.622 ± 0.021	5.086 ± 0.017	5.019 ± 0.019
Pressure at 360°C (bar)	7.196 ± 0.019	7.092 ± 0.027	7.370 ± 0.020	8.053 ± 0.023	7.862 ± 0.044

5.3.2 Thermodynamics

A van't Hoff plot was constructed as shown in Figure 5-18 that illustrates the significant change in measured pressures for MgH_2-C and MgH_2-D that have average particle sizes below 20 nm. The decomposition reaction enthalpy (ΔH) and entropy (ΔS) were calculated by a weighted least squares method (described below) and are provided in Table 5-9. ΔH for MgH_2-Purchased is equivalent to ΔH for MgH_2-A, MgH_2-B, and even MgH_2-C within uncertainty, however a significant reduction in ΔH of 2.84 kJ/mol H_2 is determined for MgH_2-D in contrast to the bulk. The measured change in ΔH for MgH_2-D is similar to theoretical predictions for ~ 4 nm MgH_2 nanoparticles by Kim *et al.* [44].

The average MgH_2 particle size in MgH_2-D cannot be smaller than the average crystallite size (6.7 ± 0.7 nm) as determined by XRD. The small difference between the experimentally measured minimum particle size (6.7 nm) and the theoretically predicted particle size (4 nm) for the given change in ΔH may simply relate to minor inaccuracies in the theoretical model. However it is also likely that some MgH_2 particle size polydispersity exists within MgH_2-D. If significant levels of polydispersity exist, the hydrogen equilibrium pressure will be controlled by certain MgH_2 particle sizes at different H/M ratios. Desorption measurements for each sample began at H/M = 2. It follows that initially the particles with the smallest size will contribute to the equilibrium pressure (above the bulk value) due to their larger change in ΔH and hence higher inherent equilibrium pressure. As the hydrogen in the smallest particles is exhausted the elevated equilibrium pressure will no longer be maintained and the equilibrium pressure will begin to approach the bulk value. The equilibrium pressure was found to be repeatable (within uncertainty) at the different

H/M ratios (0.8 – 1.8) in which measurements were taken. Given the change in ΔH measured for MgH_2-D, it is likely that the equilibrium pressure in this H/M range is controlled by small MgH_2 particles whilst larger particles (with larger crystallite sizes) may dominate equilibrium pressures at lower H/M ratios.

Table 5-9: Calculated thermodynamic properties for mechanochemically synthesised and purchased MgH_2 samples. Uncertainties are calculated with a 95% confidence interval.

	MgH_2-Purchased	MgH_2-A	MgH_2-B	MgH_2-C	MgH_2-D
Decomposition enthalpy (ΔH, kJ/mol H_2)	74.06 ± 0.42	73.92 ± 0.45	74.75 ± 0.42	74.15 ± 0.37	71.22 ± 0.49
Decomposition entropy (ΔS, J/mol H_2/K)	133.4 ± 0.7	133.1 ± 0.7	134.7 ± 0.7	134.5 ± 0.6	129.6 ± 0.8
Calculated 1 bar H_2 equilibrium temperature (T_{1bar}) (K)	555.0 ± 2.2	555.4 ± 2.2	554.9 ± 2.1	551.3 ± 2.1	549.4 ± 2.4

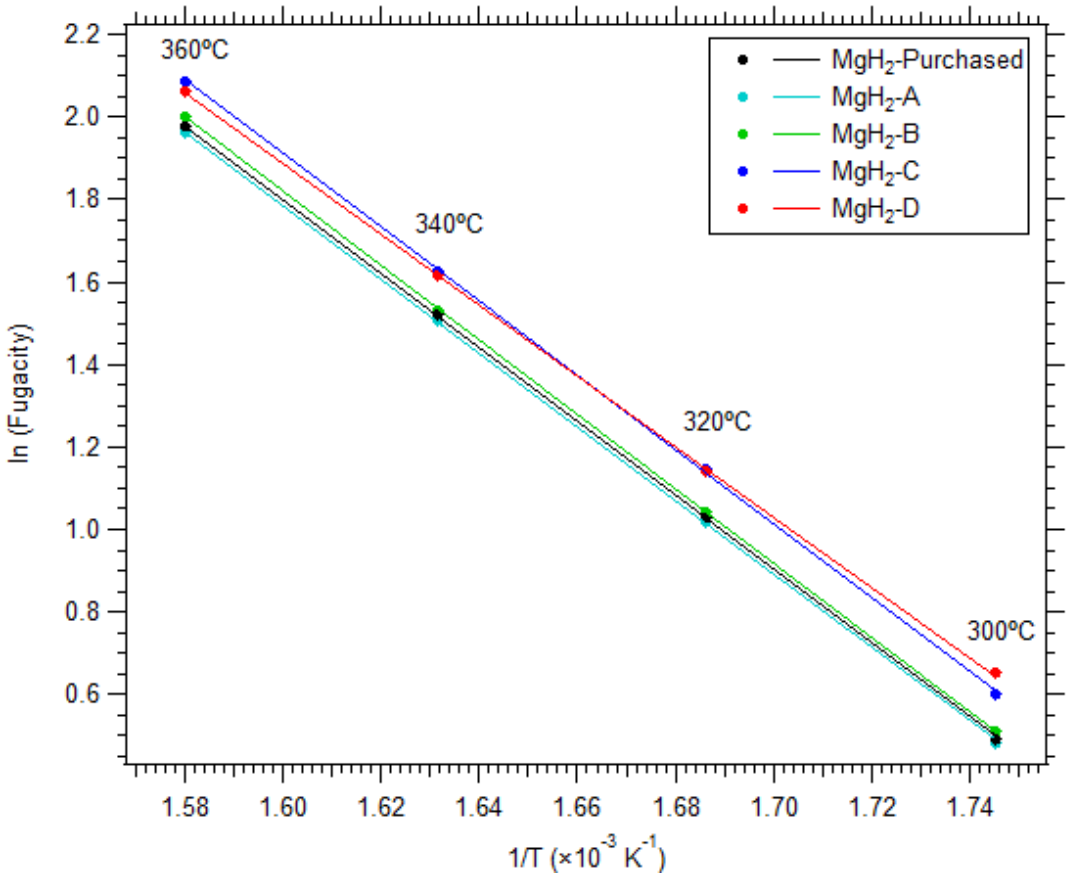

Figure 5-18: van't Hoff plot for the decomposition of MgH_2 in the four mechanochemically synthesized samples as well as the bulk reference (MgH_2-Purchased).

The calculation of uncertainties for the calculated ΔH and ΔS quantities from a van't Hoff plot is often overlooked in the literature leading to uncertainties often not being reported, or being reported incorrectly. Uncertainty analysis is made complicated due to the exponential form of the van't Hoff equation. The major factor in determining uncertainties in ΔH and ΔS is the uncertainties on the measured pressures, which were determined from the standard deviation after averaging 180 pressure data points (6 hours of data). A weighted least squares method was utilised in determining ΔH and ΔS from the van't Hoff plot. The weighted least squares method is suited to small data sets when each data point has a different uncertainty [272]. The method is useful when the uncertainties are known from a large number of observations [272] such as when each data point has been averaged from a larger data set in the case of the pressure data provided in Figures 5-13 to 5-17.

A van't Hoff plot is constructed from measured equilibrium pressure data as shown in Figure 1-9. The gradient ($m = \Delta H/R$), intercept ($c = \Delta S/R$), and their respective uncertainties (σ_m and σ_c) are calculated by [273]:

$$m = \frac{\sum \frac{1}{\sigma_i^2} \sum \frac{x_i y_i}{\sigma_i^2} - \sum \frac{x_i}{\sigma_i^2} \sum \frac{y_i}{\sigma_i^2}}{\alpha} \tag{5.3}$$

$$\sigma_m = \left(\frac{\sum \frac{1}{\sigma_i^2}}{\alpha} \right)^{\frac{1}{2}} \tag{5.4}$$

$$c = \frac{\sum \frac{x_i^2}{\sigma_i^2} \sum \frac{y_i}{\sigma_i^2} - \sum \frac{x_i}{\sigma_i^2} \sum \frac{x_i y_i}{\sigma_i^2}}{\alpha} \tag{5.5}$$

$$\sigma_c = \left(\frac{\sum \frac{x_i^2}{\sigma_i^2}}{\alpha} \right)^{\frac{1}{2}} \tag{5.6}$$

where:

$$\alpha = \sum \frac{1}{\sigma_i^2} \sum \frac{x_i^2}{\sigma_i^2} - \left(\sum \frac{x_i}{\sigma_i^2} \right)^2 \tag{5.7}$$

Given that the van't Hoff equation is expressed in the form of an exponential, the equation must be linearised in order to adequately account for the uncertainties involved in the weighted fit. In this case the y-axis is plotted as $y = \ln f$ where f is fugacity and thus the uncertainty in y (σ_i) can be determined by partial differentiation as follows:

$$\sigma_i = \frac{\delta y}{\delta f} \Delta f = \frac{\Delta f_i}{f_i} \tag{5.8}$$

where Δf_i is the measured uncertainty on fugacity (to one standard deviation) for a particular fugacity data point (f_i). Consequently y_i and x_i values are equivalent to $(\ln f)_i$ and $(1/T)_i$ respectively.

Figure 5-19 provides a visual representation of the calculated ΔH and ΔS quantities for each of the samples analysed. There is an interesting correlation between ΔH and ΔS where a lower decomposition reaction enthalpy in MgH_2-D is matched by a lower reaction entropy, and even subtle changes in enthalpy are closely matched by corresponding changes in entropy. Mg and MgH_2 particles that have nanoscopic sizes contain a large number of atoms that are influenced by the particle surface [274]. The influence of the particle surface affects the Mg and MgH_2 phases to different degrees that results in a reduction in the overall MgH_2 decomposition reaction enthalpy (ΔH). The same phase-preferred destabilization also appears to apply to ΔS (between Mg and MgH_2). In the literature, changes in ΔS are not considered in theoretical investigations and instead constant bulk ΔS quantities have been assumed [45]. Recently Fichtner [46] noted that nothing had been reported to date on whether changes in ΔS with particle size would positively or negatively affect equilibrium pressures. In a bulk system the reaction entropy (ΔS) upon $MgH_2 \rightarrow Mg + H_2$ at 25°C can be expressed as S_{Mg} (32.52 J/mol H_2/K) + S_{H2} (130.00 J/mol H_2/K) - S_{MgH2} (31.08 J/mol H_2/K) = ΔS (131.44 J/mol H_2/K) [29]. S_{H2} is not affected by alterations in the particle structure but it can be seen that a disproportionate change in the entropy of Mg and MgH_2 with particle size would lead to a change in ΔS. A lower ΔS will be

generated if the entropy of an MgH_2 nanoparticle increases by a greater quantity than the entropy for an Mg nanoparticle as particle size is reduced.

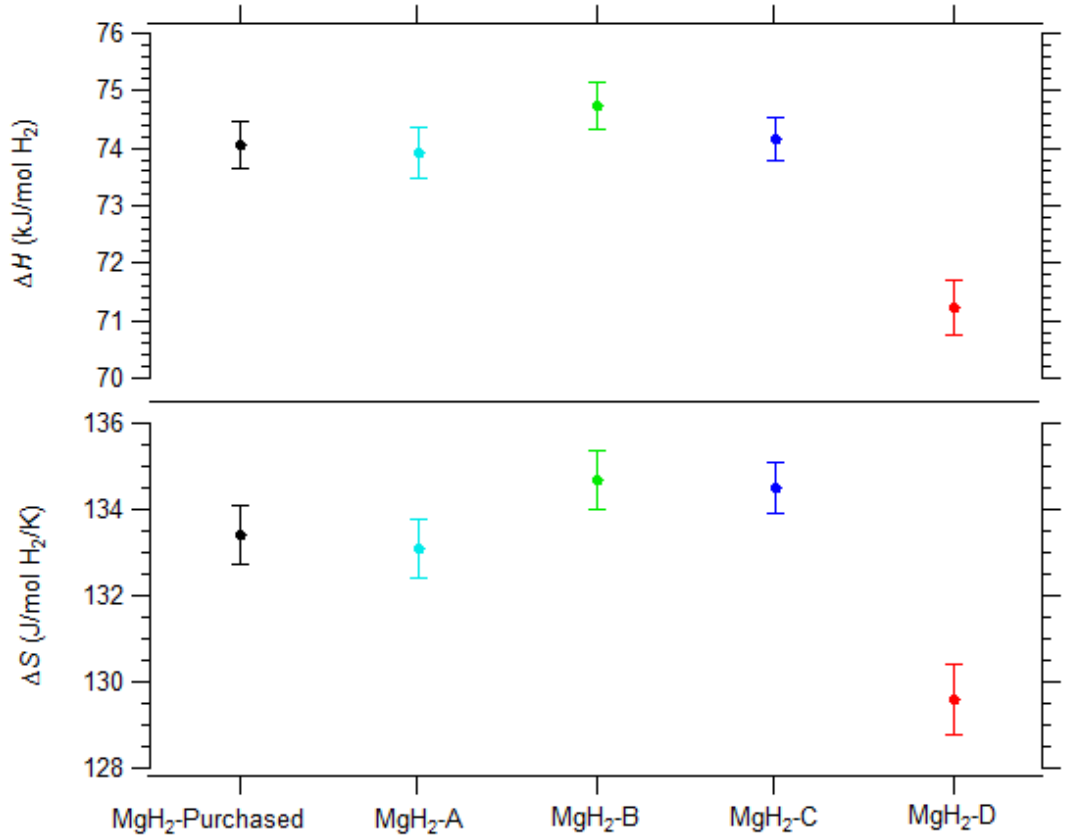

Figure 5-19: Calculated thermodynamic values for MgH_2 decomposition from the van't Hoff plot in Figure 5-18. Uncertainties are calculated with a 95% confidence interval.

The measured thermodynamics for MgH_2-D act to lower the 1 bar hydrogen equilibrium temperature (T_{1bar}) (see Table 5-9) as predicted by theoretical investigations. However, the measured reduction in T_{1bar} is not in line with the magnitude of the changes predicted. T_{1bar} is reduced by ~6°C for MgH_2-D in contrast to the bulk (MgH_2-Purchased). A reduction in T_{1bar} of ~4°C is also found for MgH_2-C even though its enthalpy was found to be close to that of the bulk. The result indicates that entropy also plays a large part in determining changes in T_{1bar}. Given the change in ΔH determined for MgH_2-D (2.84 kJ/mol H_2) a reduction in T_{1bar} is theoretically predicted to be ~15°C [44] when using a constant bulk ΔS. This result is in contrast to the ~6°C calculated due to the change in ΔS relative to the bulk. The fact that a decrease in T_{1bar} is still observed indicates that the change in ΔH due to particle size reduction has a larger impact of the T_{1bar} than the corresponding change in ΔS.

The observed change in ΔS in parallel with the observed change in ΔH can be explained as follows: The enthalpy, or internal energy (if the PV term is neglected), of a solid can be considered to be the summation of the vibrational energy of the atoms comprising the crystal solid [275]. The consequence of this is that as the particle size decreases below a certain threshold there is a deviation in the crystal structure of both Mg and MgH_2 from their bulk structures leading to changes in enthalpy. Because the rate of change of the enthalpy is different between Mg and MgH_2 we see an overall change in ΔH of the reaction $MgH_2 \rightarrow Mg + H_2$. Likewise, the entropy of a solid can be considered to be the vibrational entropy (a measure of the disorder in the system caused by atomic vibrations), a function of the vibrational partition function [275]. The vibrational partition function is dependent on phonon frequencies/phonon density of states. Given that the phonon density of states is also dependent on the crystal structure we see that a change in entropy must also occur when there are changes in the crystal structures of the solids in a given reaction. Such changes in entropy should therefore be included in future theoretical predictions of particle size dependent hydride thermodynamics.

5.4 CONCLUSIONS

The mechanochemical synthesis of MgH_2 has been undertaken with varying LiCl buffer quantities. Increasing the buffer results in MgH_2 crystallite sizes down to 6.7 nm, measured by XRD, whilst TEM investigations show that increasing buffer results in smaller, more highly dispersed MgH_2 nanoparticles. The size of these MgH_2 particles approaches theoretical predictions for thermodynamic changes and the MgH_2 is only physically bound by the LiCl.

Hydrogen equilibrium pressure measurements have been used to determine the decomposition enthalpy and entropy for MgH_2 nanoparticles that were mechanochemically synthesized. A reduction in both the decomposition enthalpy and entropy was found for ~7 nm MgH_2 nanoparticles in relation to bulk MgH_2. The consequence of this thermodynamic destabilization is a drop in the 1 bar hydrogen equilibrium pressure of ~6°C. The temperature drop is not as large as theoretical predictions due to the effect of the decrease in reaction entropy which partially counteracts the decrease in reaction enthalpy. It is not known if the thermodynamics of smaller nanoparticles will be dominated by changes in either the reaction enthalpy or entropy. Further theoretical and experimental studies on MgH_2 nanoparticles will need to be performed with a focus on reaction entropy changes to accurately quantify the thermodynamic destabilization of the Mg-H nanoparticle system in order to determine whether large reductions in the 1 bar hydrogen equilibrium temperature are possible.

5.5 DIRECTIONS FOR FUTURE WORK

- There are a number of techniques that may be used to more accurately determine the MgH_2 particle size in MgH_2-D. Small angle scattering is a technique that can be used to determine particle size but complications arise due to the fact that the MgH_2 particles are embedded within salt. The salt produces a high degree of surface scattering that masks any Guinier regime that may provide information about MgH_2 particle size. Synchrotron SAXS may be able to distinguish the scattering from the MgH_2 and LiCl by tuning the x-ray energy to that of the Mg K-edge (1.3 keV). However SAXS beamlines do not operate at this energy. A more promising solution is to use contrast matching with SANS to match the scattering length density of LiCl (-4.39×10^{8} cm^{-2}) with a mixture of hydrogenated toluene (-1.35×10^{12} cm^{-2}) and deuterated toluene ($+1.73\times10^{12}$ cm^{-2}).

- Smaller MgH_2 nanoparticles may be formed by altering the mechanochemical synthesis conditions. If the LiCl:MgH_2 buffer ratio is increased (> 10:1) then it is expected that further reductions in MgH_2 particle size will be observed. It may also be possible to reduce the MgH_2 particle size further by changing other milling parameters such as the ball to powder ratio or the ball size. However a critical lower limit to MgH_2 particle size does exist due to the inherent limitations of the mechanochemical process. The method is limited because mechanical milling is used to form MgH_2 sites that result from $MgCl_2$-LiH interactions, and these sites will always be a formed at a certain finite scale. Further MgH_2-MgH_2 interactions will also increase this lower MgH_2 particle size limit.

- The mechanochemical synthesis of MgH_2 could be attempted by different synthesis pathways. A variation of the starting reagents will lead to different product phases and different reaction kinetics during ball milling. Alteration of these parameters could lead to smaller MgH_2 particle sizes. For example, the following reaction should proceed faster during milling due to the higher Gibbs free energy:

$$MgCl_2 + 2NaH \longrightarrow MgH_2 + 2NaCl \qquad \Delta_r G_{298K} = -142.6 \text{ kJ/mol} \qquad (5.9)$$

A different by-product phase may also allow for faster hydrogen sorption kinetics due to variations in hydrogen diffusion through the by-product phase.

References

1. Earth Audit, *New Scientist* 2605, 34-41, 2007.
2. Hetherington, L. E., Brown, T. J., Benham, A. J., Bide, T., Lusty, P. A. J., Hards, V. L., Hannis, S. D., and Idoine, N. E., *World Mineral Production 2002-06*, British Geological Survey, 2008.
3. Winter, M., 2008, Abundance in Earth's Crust, WebElements, http://www.webelements.com/periodicity/abundance_crust/, November 4 2008.
4. Baranowski, B. and Tkacz, M., The Equilibrium Between Solid Aluminium Hydride and Gaseous Hydrogen, *Zeitschrift für Physikalische Chemie* 135, 27-38, 1983.
5. Konovalov, S. K. and Bulychev, B. M., The P,T-State Diagram and Solid Phase Synthesis of Aluminium Hydride, *Inorganic Chemistry* 34, 172-175, 1995.
6. Ellinger, F. H., Holley, C. E., Jr., McInteer, B. B., Pavone, D., Potter, R. M., Staritzky, E., and Zachariasen, W. H., Preparation and some properties of magnesium hydride, *Journal of the American Chemical Society* 77, 2647-2648, 1955.
7. Snow, D. G. and Brumlik, C. J., United States of America US 6,589,312 B1, 2003, Nanoparticles for hydrogen storage, transportation, and distribution. July 8.
8. Kerr, R. A., OIL RESOURCES: The Looming Oil Crisis Could Arrive Uncomfortably Soon, *Science* 316 (5823), 351, 2007.
9. Ogden, J. M., Prospects for Building a Hydrogen Energy Infrastructure, *Annual Review of Energy and the Environment* 24 (1), 227-279, 1999.
10. Zhou, L., Progress and problems in hydrogen storage methods, *Renewable and Sustainable Energy Reviews* 9 (4), 395-408, 2005.
11. Schlapbach, L. and Zuttel, A., *Hydrogen Storage*, Risø Energy Report 3, Report No. Risø-R-1469, Risø National Laboratory, 2004.
12. Strahan, D., Hydrogen's long road to nowhere, *New Scientist* 2684, 40-43, 2008.
13. Ritter, J. A., Ebner, A. D., Wang, J., and Zidan, R., Implementing a hydrogen economy, *Materials Today* 6 (9), 18-23, 2003.
14. Sandrock, G. and Bowman, J. R. C., Gas-based hydride applications: recent progress and future needs, *Journal of Alloys and Compounds* 356-357, 794-799, 2003.
15. Chandra, D., Reilly, J. J., and Chellappa, R., Metal Hydrides for Vehicular Applications: The State of the Art, *The Journal of The Minerals, Metals & Materials Society* 58 (2), 26-32, 2006.
16. Zuttel, A., Materials for hydrogen storage, *Materials Today* 6 (9), 24-33, 2003.
17. Fichtner, M., Nanotechnological Aspects in Materials for Hydrogen Storage, *Advanced Engineering Materials* 7 (6), 443-455, 2005.
18. Gasoline-free SUV, Ford Motor Company, http://www.ford.com/innovation/environmentally-friendly/hydrogen/gasoline-free-suv/fuel-cell-explorer-362p, October 16 2008.
19. The BMW Hydrogen 7, BMW, http://www.bmw.com/com/en/insights/technology/efficient_dynamics/phase_2/clean_energy/bmw_hydrogen_7.html, October 16 2008.
20. Tian, H. Y., Buckley, C. E., Mulè, S., Paskevicius, M., and Dhal, B. B., Preparation, microstructure and hydrogen sorption properties of nanoporous carbon aerogels under ambient drying, *Nanotechnology* 19, 475605, 2008.
21. Panella, B., Hirscher, M., and Roth, S., Hydrogen adsorption in different carbon nanostructures, *Carbon* 43 (10), 2209-2214, 2005.
22. Rosi, N. L., Eckert, J., Eddaoudi, M., Vodak, D. T., Kim, J., O'Keeffe, M., and Yaghi, O. M., Hydrogen storage in microporous metal-organic frameworks, *Science* 300 (5622), 1127-1129, 2003.
23. Christmann, K., Some general aspects of hydrogen chemisorption on metal surfaces, *Progress in Surface Science* 48 (1-4), 15-26, 1995.
24. Fukai, Y., *The Metal-Hydrogen System*, Springer-Verlag, Heidelberg, 2005.
25. Schlapbach, L., Surface Properties and Activation, in *Hydrogen in Intermetallic Compounds II*, Schlapbach, L. Springer-Verlag, New York, 1992.
26. Manchester, F. D. and San-Martin, A., H-Mg (Hydrogen-Magnesium), in *Phase Diagrams of Binary Hydrogen Alloys*, Manchester, F. D. ASM International, Ohio, 2000.
27. Spencer, N. D. and Moore, J. H., *Encyclopedia of Chemical Physics and Physical Chemistry*, Institute of Physics, 2001.
28. Atkins, P. and Paula, J. d., *Atkins' Physical Chemistry*, 7th ed., Oxford University Press, New York, 2002.
29. Outukumpu, *HSC Chemistry*, 6.1 ed. Chemistry Software, Houston, 2006.

30. Chambers, C. and Holliday, A. K., *Modern Inorganic Chemistry*, Butterworth & Co, Sussex, 1975.
31. Bogdanović, B., Bohmhammel, K., Christ, B., Reiser, A., Schlichte, K., Vehlen, R., and Wolf, U., Thermodynamic investigation of the magnesium-hydrogen system, *Journal of Alloys and Compounds* 282 (1-2), 84-92, 1999.
32. Klose, W. and Stuke, V., Investigation of the thermodynamic equilibrium in the hydrogen-magnesium-magnesium hydride system, *International Journal of Hydrogen Energy* 20 (4), 309-316, 1995.
33. Marchi, C. S., Somerday, B. P., and Robinson, S. L., Permeability, solubility and diffusivity of hydrogen isotopes in stainless steels at high gas pressures, *International Journal of Hydrogen Energy* 32 (1), 100-116, 2007.
34. Alapati, S. V., Johnson, J. K., and Sholl, D. S., Using first principles calculations to identify new destabilized metal hydride reactions for reversible hydrogen storage, *Physical Chemistry Chemical Physics* 9, 1438-1452, 2007.
35. Alapati, S. V., Thesis: *Density Functional Theory Studies of Destabilized Metal Hydrides for Hydrogen Storage Applications*, Carnegie Mellon University, 2007.
36. Latroche, M., Structural and thermodynamic properties of metallic hydrides used for energy storage, *Journal of Physics and Chemistry of Solids* 65 (2-3), 517-522, 2004.
37. Zhang, Y., Liao, S., Fan, Y., Xu, J., and Wang, F., Chemical reactivities of magnesium nanopowders, *Journal of Nanoparticle Research* 3, 23-26, 2001.
38. Kelsall, R. W., Hamley, I. W., and Geoghegan, M., *Nanoscale Science and Technology*, John Wiley & Sons, Ltd, West Sussex, 2005.
39. Dunlap, R. A., Small, D. A., MacKay, G. R., Brien, J. W. O., and et al., Materials preparation by ball milling, *Canadian Journal of Physics* 78 (3), 211-229, 2000.
40. McCormick, P. G., Tsuzuki, T., Robinson, J. S., and Ding, J., Nanopowders Synthesized by Mechanochemical Processing, *Advanced Materials* 13 (12-13), 1008-1010, 2001.
41. Zdujic, M. V., Kobayashi, K. F., and Shingu, P. H., Structural changes during mechanical alloying of elemental aluminium and molybdenum powders, *Journal of Materials Science* 26, 5502-5508, 1991.
42. Oleszak, D. and Shingu, P. H., Nanocrystalline metals prepared by low energy ball milling, *Journal of Applied Physics* 79 (6), 2975-2980, 1996.
43. Al Sadi, A., Bonetti, E., Mattioli, P., and Valdre, G., Internal friction, thermal and structural analysis of nanocrystalline aluminium, *Journal of Alloys and Compounds* 211-212, 489-493, 1994.
44. Kim, K. C., Dai, B., Johnson, J. K., and Sholl, D. S., Assessing nanoparticle size effects on metal hydride thermodynamics using the Wulff construction, *Nanotechnology* 20, 204001, 2009.
45. Wagemans, R. W. P., van Lenthe, J. H., de Jongh, P. E., van Dillen, A. J., and de Jong, K. P., Hydrogen Storage in Magnesium Clusters: Quantum Chemical Study, *Journal of the American Chemical Society* 127 (47), 16675-16680, 2005.
46. Fichtner, M., Properties of nanoscale metal hydrides, *Nanotechnology* 20, 204009, 2009.
47. Baldé, C. P., Hereijgers, B. P. C., Bitter, J. H., and Jong, K. P. d., Sodium Alanate Nanoparticles - Linking Size to Hydrogen Storage Properties, *Journal of the American Chemical Society* 130, 6761-6765, 2008.
48. Baletto, F. and Ferrando, R., Structural properties of nanoclusters: Energetic, thermodynamic, and kinetic effects, *Reviews of Modern Physics* 77 (1), 371-53, 2005.
49. Burkart, S., Blessing, N., Klipp, B., Muller, J., Gantefor, G., and Seifert, G., Experimental verification of the high stability of $Al_{13}H$: a building block of a new type of cluster material?, *Chemical Physics Letters* 301 (5-6), 546-550, 1999.
50. Cox, D. M., Trevor, D. J., Whetten, R. L., and Kaldor, A., Aluminum clusters: ionization thresholds and reactivity toward deuterium, water, oxygen, methanol, methane, and carbon monoxide, *Journal of Physical Chemistry* 92 (2), 421-429, 1988.
51. Duque, F., Molina, L. M., Lopez, M. J., Mananes, A., and Alonso, J. A., Assembling of hydrogenated aluminum clusters, *European Physics Journal D* 16, 285-288, 2001.
52. Grubisic, A., Li, X., Stokes, S. T., Cordes, J., Gantefor, G. F., Bowen, K. H., Kiran, B., Jena, P., Burgert, R., and Schnockel, H., Closo-alanes (Al_4H_4, Al_nH_{n+2}, $4 \leq n \leq 8$): A New Chapter in Aluminum Hydride Chemistry, *Journal of the American Chemical Society* 129 (18), 5969-5975, 2007.

53. Kawamura, H., Kumar, V., Sun, Q., and Kawazoe, Y., Magic behavior and bonding nature in hydrogenated aluminum clusters, *Physical Review B (Condensed Matter and Materials Physics)* 65 (4), 045406-11, 2002.
54. Kawamura, H., Kumar, V., Sun, Q., and Kawazoe, Y., Cyclic and linear polymeric structures of Al_nH_{3n} (n=3-7) molecules, *Physical Review A (Atomic, Molecular, and Optical Physics)* 67 (6), 063205-8, 2003.
55. Khanna, S. N. and Jena, P., Reactivity of hydrogen with open and closed shell clusters, *Chemical Physics Letters* 218 (4), 383-386, 1994.
56. Rao, B. K., Jena, P., Burkart, S., Gantefor, G., and Seifert, G., AlH_3 and Al_2H_6: Magic Clusters with Unmagical Properties, *Physical Review Letters* 86 (4), 692-695, 2001.
57. Upton, T. H., Structural, electronic, and chemisorption properties of small aluminum clusters, *Physical Review Letters* 56 (20), 2168-2171, 1986.
58. Yarovsky, I. and Goldberg, A., DFT study of hydrogen adsorption on Al_{13} clusters, *Molecular Simulation* 31 (6-7), 475-481, 2005.
59. Rao, B. K., Atomic clusters - a possible source for novel materials, *Materials Science and Engineering A* 304-306, 211-214, 2001.
60. Hu, J., Wu, R., Huang, W., Wang, A., and Xie, C., Ultrafine Zn powders produced by laser-induction complex heating evaporation condensation method, *Laser Technology* 24 (2), 99-101, 2000.
61. Weigle, J. C., Luhrs, C. C., Chen, C. K., Perry, W. L., Mang, J. T., Nemer, M. B., Lopez, G. P., and Phillips, J., Generation of Aluminum Nanoparticles Using an Atmospheric Pressure Plasma Torch, *Journal of Physical Chemistry B* 108 (48), 18601-18607, 2004.
62. Smetana, A. B., Klabunde, K. J., Sorensen, C. M., Ponce, A. A., and Mwale, B., Low-Temperature Metallic Alloying of Copper and Silver Nanoparticles with Gold Nanoparticles through Digestive Ripening, *Journal of Physical Chemistry B* 110 (5), 2155-2158, 2006.
63. Graetz, J. and Reilly, J., Nanoscale Energy Storage Materials Produced by Hydrogen-Driven Metallurgical Reactions, *Advanced Engineering Materials* 7 (7), 597-601, 2005.
64. Tsuzuki, T. and McCormick, P. G., Mechanochemical synthesis of nanoparticles, *Journal of Materials Science* 39 (16 - 17), 5143-5146, 2004.
65. Suryanarayana, C., Mechanical alloying and milling, *Progress in Materials Science* 46 (1-2), 1-184, 2001.
66. McCormick, P. G., Ding, J., Miao, W.-F., and Street, R., Unites States of America US 6,203,768 B1, 2001, Process for the production of ultrafine particles. March 20.
67. Brinks, H. W., Istad-Lem, A., and Hauback, B. C., Mechanochemical Synthesis and Crystal Structure of α'-AlD_3 and α-AlD_3, *Journal of Physical Chemistry B* 110, 25833-25837, 2006.
68. Kojima, Y., Kawai, Y., Haga, T., Matsumoto, M., and Koiwai, A., Direct formation of $LiAlH_4$ by a mechanochemical reaction, *Journal of Alloys and Compounds* 441 (1-2), 189-191, 2007.
69. Fichtner, M., Frommen, C., and Fuhr, O., Synthesis and Properties of Calcium Alanate and Two Solvent Adducts, *Inorganic Chemistry* 44 (10), 3479-3484, 2005.
70. Varin, R. A., Chiu, C., Czujko, T., and Wronski, Z., Mechano-chemical activation synthesis (MCAS) of nanocrystalline magnesium alanate hydride [$Mg(AlH_4)_2$] and its hydrogen desorption properties, *Journal of Alloys and Compounds* 439 (1-2), 302-311, 2007.
71. Dymova, T. N., Mal'tseva, N. N., Konoplev, V. N., Golovanova, A. I., Aleksandrov, D. P., and Sizareva, A. S., Solid-Phase Solvate-Free Formation of Magnesium Hydroaluminates $Mg(AlH_4)_2$ and $MgAlH_5$ upon Mechanochemical Activation or Heating of Magnesium Hydride and Aluminum Chloride Mixtures, *Russian Journal of Coordination Chemistry* 29 (6), 385-389, 2003.
72. Kim, Y., Lee, E.-K., Shim, J.-H., Cho, Y. W., and Yoon, K. B., Mechanochemical synthesis and thermal decomposition of $Mg(AlH_4)_2$, *Journal of Alloys and Compounds* 422 (1-2), 283-287, 2006.
73. Mamatha, M., Bogdanović, B., Felderhoff, M., Pommerin, A., Schmidt, W., Schuth, F., and Weidenthaler, C., Mechanochemical preparation and investigation of properties of magnesium, calcium and lithium-magnesium alanates, *Journal of Alloys and Compounds* 407 (1-2), 78-86, 2006.
74. Ding, J., Tsuzuki, T., McCormick, P. G., and Street, R., Ultrafine Cu particles prepared by mechanochemical process, *Journal of Alloys and Compounds* 234 (2), L1-L3, 1996.
75. Ding, J., Tsuzuki, T., and McCormick, P. G., Microstructural evolution of Ni-NaCl mixtures during mechanochemical reaction and mechanical milling, *Journal of Materials Science* 34 (21), 5293-5298, 1999.

76. Tsuzuki, T., Ding, J., and McCormick, P. G., Mechanochemical synthesis of ultrafine zinc sulfide particles, *Physica B: Condensed Matter* 239 (3-4), 378-387, 1997.
77. Tsuzuki, T. and McCormick, P. G., Synthesis of Cr_2O_3 nanoparticles by mechanochemical processing, *Acta Materialia* 48 (11), 2795-2801, 2000.
78. Ivanov, E., Konstanchuk, I., and Boldyrev, V., Hydriding Properties of Magnesium-Salt Mechanical Alloys, in *Hydrogen Materials Science and Chemistry of Carbon Nanomaterials* Springer, Netherlands, 2005, pp. 489-502.
79. Hsu, H.-W., *Separations by Centrifugal Phenomena*, John Wiley & Sons, Inc., New York, 1981.
80. Lide, D. R., *CRC Handbook of Chemistry and Physics*, 88th ed., CRC Press, Boca Raton, FL, 2008.
81. Stephen, H. and Stephen, T., *Solubilities of Inorganic and Organic Compounds*, Pergamon Press Ltd., Oxford, 1979.
82. Burgess, J., *Metal Ions in Solution*, Ellis Horwood, New York, 1978.
83. Shannon, M. L., European Patent EP0090926, 1983, A soluble magnesium hydride reagent. December 10.
84. Benje, M., United States of America US 6,956,143 B2, 2005, Process for Dissolving Salts in 1,2-Dichloroethane using Ultrasound and a Device for Carrying Out Said Process. October 18.
85. Jansons, V. and Gors, H. C., United States of America 4,721,771, 1988, Preparation of Aromatic Polymers. January 26.
86. Kumar, A., Phalgune, U. D., and Pawar, S. S., Salt solutions in different solvents and their effect on the stereoselectivity of products of Diels-Alder reaction, *Journal of Physical Organic Chemistry* 14 (8), 577-582, 2001.
87. Brown, H. C., Choi, Y. M., and Narasimhan, S., Addition compounds of alkali metal hydrides. 22. Convenient procedures for the preparation of lithium borohydride from sodium borohydride and borane-dimethyl sulfide in simple ether solvents, *Inorganic Chemistry* 21 (10), 3657-3661, 1982.
88. Pruntsev, A. E., Arkhipov, S. M., and Mikheeva, V. I., Solubility in the systems $AlCl_3$-LiCl-ether, $AlCl_3$-LiCl-toluene, and $AlBr_3$-NaBr-toluene at 25°C, *Russian Chemical Bulletin* 21 (12), 2581-2585, 1972.
89. Brown, H. C. and Yoon, N. M., Selective Reductions. X. Reaction of Aluminum Hydride with Selected Organic Compounds Containing Representative Functional Groups. Comparison of the Reducing Characteristics of Lithium Aluminum Hydride and Its Derivatives, *Journal of the American Chemical Society* 88 (7), 1464-1472, 1966.
90. Suzuki, H. and Koyama, Y., United States of America 5,262,137, 1993, Method for Recovering Lithium Chloride. November 16.
91. Davis, S. G., United States of America 4,450,214, 1984, Lithium Halide Additives for Nonaqueous Cell Systems. May 22.
92. Popov, A. I., Alkali metal NMR and vibrational spectroscopic studies on solvates in non-aqueous solvents, *Pure & Applied Chemistry* 41 (3), 275-289, 1975.
93. Briscoe, H. V. A., Eldridge, A. A., Dyson, G. M., and Welch, A. J. E., *Mellor's Comprehensive Treatise on Inorganic and Theoretical Chemistry*, Longman Group Limited, London, 1972.
94. Podorvan, I. M. and Penkalo, I. I., Electrochemical investigation of solutions of titanium tetrachloride and lithium chloride in nitromethane, in *Visnik Kiivs'kogo Universitetu, Seriya Fiziki ta Khimii* from: Ref. Zh., Khim. 1968, Abstr. No. 3B901., 1967, pp. 97-104.
95. Schultze, L. E., Bauer, D. J., and Arington, R. M., United States of America 4,588,565, 1986, Separation of Lithium Chloride from Impurities. May 13.
96. Wilkes, J. S., A short history of ionic liquids—from molten salts to neoteric solvents, *Green Chemistry* 4, 73-80, 2002.
97. Wasserscheid, P. and Keim, W., Ionic Liquids - New "Solutions" for Transition Metal Catalysis, *Angewandte Chemie* 39, 3772-3789, 2000.
98. Cheary, R. W., Coelho, A. A., and Cline, J. P., Fundamental Parameters Line Profile Fitting in Laboratory Diffractometers, *Journal of Research of the National Institute of Standards and Technology* 109 (1), 1-25, 2004.
99. Jenkins, R., X-ray Techniques: Overview, in *Encyclopedia of Analytical Chemistry*, Meyers, R. A. John Wiley & Sons Ltd, Chichester, 2000, pp. 13269-13288.

100. Balzar, D., Voigt-function model in diffraction line-broadening analysis, in *Microstructure Analysis from Diffraction*, Snyder, R. L., Bunge, H. J., and Fiala, J. International Union of Crystallography, 1999.
101. Williams, R., Synthesis of Y_2O_3, Curtin University of Technology, Perth, 2008.
102. Richard, D., Ferrand, M., and Kearley, G. J., Analysis and visualisation of neutron-scattering data, *Journal of Neutron Research* 4 (1), 33 - 39, 1996.
103. Von Dreele, R. B. and Cline, J. P., The Impact of Background Function on High Accuracy Quantitative Rietveld Analysis (QRA): Application to NIST SRMs 676 and 656, *Advances in X-Ray Analysis* 38, 59-68, 1995.
104. Coelho, A. A., *Topas User Manual*, 3.0 ed. Bruker AXS GmbH, Karlsruhe, Germany, 2003.
105. Klug, H. P. and Alexander, L. E., *X-Ray Diffraction Procedures*, John Wiley & Sons, 1974.
106. Schmidt, P. W., Hohr, A., Neumann, H.-B., Kaiser, H., Avnir, D., and Lin, J. S., Small-angle x-ray scattering study of the fractal morphology of porous silicas, *Journal of Chemical Physics* 90 (9), 5016-5023, 1989.
107. Schmidt, P. W., Some Fundamental Concepts and Techniques Useful in Small-Angle Scattering Studies of Disordered Solids, in *Modern Aspects of Small-Angle Scattering*, Brumberger, H. Kluwer Academic Publishers, Netherlands, 1995, pp. 1-56.
108. Guinier, A. and Fournet, G., *Small-Angle Scattering of X-Rays*, John Wiley & Sons, New York, 1955.
109. Spalla, O., Lyonnard, S., and Testard, F., Analysis of the small-angle intensity scattered by a porous and granular medium, *Journal of Applied Crystallography* 36 (2), 338-347, 2003.
110. Lowell, S., Shields, J. E., Thomas, M. A., and Thommes, M., *Characterization of Porous Solids and Powders: Surface Area, Pore Size and Density*, Kluwer Academic Publishers, 2004.
111. Beaucage, G., Small-Angle Scattering from Polymeric Mass Fractals of Arbitrary Mass-Fractal Dimension, *Journal of Applied Crystallography* 29 (2), 134-146, 1996.
112. Zarzycki, J. and Woignier, T., Aerogels: Precursors or End Materials?, in *Aerogels: Proceedings of the First International Symposium*, Fricke, J. Springer-Verlag, Berlin, 1986, pp. 42-48.
113. Beaucage, G., Approximations Leading to a Unified Exponential/Power-Law Approach to Small-Angle Scattering, *Journal of Applied Crystallography* 28 (6), 717-728, 1995.
114. Beaucage, G. and Schaefer, D. W., Structural studies of complex systems using small-angle scattering: a unified Guinier/power-law approach, *Journal of Non-Crystalline Solids* 172-174 (Part 2), 797-805, 1994.
115. Abramowitz, M. and Stegun, I. A., *Handbook of Mathematical Functions*, Dover, New York, 1972.
116. Beaucage, G., Determination of branch fraction and minimum dimension of mass-fractal aggregates, *Physical Review E (Statistical, Nonlinear, and Soft Matter Physics)* 70 (3), 031401-10, 2004.
117. Ilavsky, J. and Jemian, P. R., Irena: tool suite for modeling and analysis of small-angle scattering, *Journal of Applied Crystallography* 42 (2), 2009.
118. Ramos, I. N., Brandao, T. R. S., and Silva, C. L. M., Structural Changes During Air Drying of Fruits and Vegetables, *Food Science and Technology International* 9 (3), 201-206, 2003.
119. Bendersky, L. A. and Gayle, F. W., Electron Diffraction using Transmission Electron Microscopy, *Journal of Research of the National Institute of Standards and Technology* 106, 997-1012, 2001.
120. Checchetto, R., Trettel, G., and Miotello, A., Sievert-type apparatus for the study of hydrogen storage in solids, *Measurement Science and Technology* 15 (1), 127-130, 2004.
121. Broom, D. P., The accuracy of hydrogen sorption measurements on potential storage materials, *International Journal of Hydrogen Energy* 32 (18), 4871-4888, 2007.
122. Hemmes, H., Driessen, A., and Griessen, R., Thermodynamic properties of hydrogen at pressures up to 1 Mbar and temperatures between 100 and 1000 K, *Journal of Physics: Solid State Physics* 19, 3571-3585, 1986.
123. McLennan, K. G. and Gray, E. M., An equation of state for deuterium gas to 1000 bar, *Measurement Science and Technology* 15 (1), 211-215, 2004.
124. McCarty, R. D., Hord, J., and Roder, H. M., Selected Properties of Hydrogen (Engineering Design Data), Monograph 168, National Bureau of Standards, U.S. Government Printing Office, 1981.

125. Lemmon, E. W., McLinden, M. O., and Friend, D. G., Thermophysical Properties of Fluid Systems, in *NIST Standard Reference Database Number 69*, Linstrom, P. J. and Mallard, W. G. National Institute of Standards and Technology, Gaithersburg MD, 20899, 2005.
126. *Alcodens*, 2.0 ed. Katmar Software, Westville, South Africa, 2007.
127. Sheppard, D. A., Thesis: *Hydrogen Storage Studies of Mesoporous and Titanium Based Materials*, Curtin University, 2009.
128. Blach, T. P. and Gray, E. M., Sieverts apparatus and methodology for accurate determination of hydrogen uptake by light-atom hosts, *Journal of Alloys and Compounds* 446-447, 692-697, 2007.
129. Holleman, A. F. and Wiberg, E., *Inorganic Chemistry*, Academic Press, San Diego, 2001.
130. Mondolfo, L. F., *Aluminum Alloys: Structure and Properties*, Butterworth & Co, London, 1976.
131. Sinke, G. C., Walker, L. C., Oetting, F. L., and Stull, D. R., Thermodynamic Properties of Aluminum Hydride, *Journal of Chemical Physics* 47 (8), 2759-2761, 1967.
132. Brousseau, P. and Anderson, C. J., Nanometric Aluminum in Explosives, *Propellants, Explosives, Pyrotechnics* 27 (5), 300-306, 2002.
133. Kwok, Q. S. M., Fouchard, R. C., Turcotte, A.-M., Lightfoot, P. D., Bowes, R., and Jones, D. E. G., Characterization of Aluminum Nanopowder Compositions, *Propellants, Explosives, Pyrotechnics* 27 (4), 229-240, 2002.
134. Rai, A., Park, K., Zhou, L., and Zachariah, M. R., Understanding the mechanism of aluminium nanoparticle oxidation, *Combustion Theory and Modelling* 10 (5), 843 - 859, 2006.
135. Craig, N. C., Charles Martin Hall - The Young Man, His Mentor, and His Metal, *Journal of Chemical Education* 63 (7), 557-559, 1986.
136. Compilation of Air Pollutant Emission Factors, AP-42, Office of Air Quality Planning and Standards, U.S. Environmental Protection Agency, 1995.
137. Serra, E., Calza Bini, A., Cosoli, G., and Pilloni, L., Hydrogen Permeation Measurements on Alumina, *Journal of the American Ceramic Society* 88 (1), 15-18, 2005.
138. Maienschein, J. L., Musket, R. G., McMurphy, F. E., and Brown, D. W., Reduction of tritium permeation through 304L stainless steel using aluminum ion implantation, *Applied Physics Letters* 50 (14), 940-942, 1987.
139. Yamada-Takamura, Y., Koch, F., Maier, H., and Bolt, H., Hydrogen permeation barrier performance characterization of vapor deposited amorphous aluminum oxide films using coloration of tungsten oxide, *Surface and Coatings Technology* 153 (2-3), 114-118, 2002.
140. Rai, A., Lee, D., Park, K., and Zachariah, M. R., Importance of Phase Change of Aluminum in Oxidation of Aluminum Nanoparticles, *Journal of Physical Chemistry B* 108 (39), 14793-14795, 2004.
141. Jeurgens, L. P. H., Sloof, W. G., Tichelaar, F. D., and Mittemeijer, E. J., Thermodynamic stability of amorphous oxide films on metals: Application to aluminum oxide films on aluminum substrates, *Physical Review B* 62 (7), 4707-4719, 2000.
142. Jeurgens, L. P. H., Sloof, W. G., Tichelaar, F. D., and Mittemeijer, E. J., Growth kinetics and mechanisms of aluminum-oxide films formed by thermal oxidation of aluminum, *Journal of Applied Physics* 92 (3), 1649-1656, 2002.
143. Ermoline, A., Schoenitz, M., Dreizin, E., and Yao, N., Production of carbon-coated aluminium nanopowders in pulsed microarc discharge, *Nanotechnology* 13, 638-643, 2002.
144. Kwon, Y.-S., Gromov, A. A., Ilyin, A. P., and Rim, G.-H., Passivation process for superfine aluminum powders obtained by electrical explosion of wires, *Applied Surface Science* 211 (1-4), 57-67, 2003.
145. Glebov, E. M., Yuan, L., Krishtopa, L. G., Usov, O. M., and Krasnoperov, L. N., Coating of Metal Powders with Polymers in Supercritical Carbon Dioxide, *Industrial and Engineering Chemistry Research* 40 (19), 4058-4068, 2001.
146. Kimura, I., Taguchi, Y., Yoshii, H., and Tanaka, M., Encapsulation of aluminum flakes by dispersion polymerization of styrene in a nonaqueous system with reactive surfactants, *Journal of Applied Polymer Science* 81 (3), 675-683, 2001.
147. Mary, B., Dubois, C., Carreau, P. J., and Brousseau, P., Rheological properties of suspensions of polyethylene-coated aluminum nanoparticles, *Rheologica Acta* 45 (5), 561-573, 2006.
148. Cheng, Q., United States of America US 2005/0274226 A1, 2005, Method of Preparing Aluminum Nanorods. December 15.

149. Zhukov, V., Ferstl, A., Winkler, A., and Rendulic, K. D., Adsorption and desorption kinetics for hydrogen on modified aluminum (110) surfaces, *Chemical Physics Letters* 222 (5), 481-485, 1994.
150. Manchester, F. D. and San-Martin, A., Al-H (Aluminum-Hydrogen), in *Phase Diagrams of Binary Hydrogen Alloys*, Manchester, F. D. ASM International, Ohio, 2000.
151. Paskevicius, M. and Buckley, C. E., Analysis of polydisperse bubbles in the aluminium-hydrogen system using a size-dependent contrast, *Journal of Applied Crystallography* 39 (5), 676-682, 2006.
152. Buckley, C. E., Birnbaum, H. K., Lin, J. S., Spooner, S., Bellmann, D., Staron, P., Udovic, T. J., and Hollar, E., Characterization of H defects in the aluminium-hydrogen system using small-angle scattering techniques, *Journal of Applied Crystallography* 34, 119-129, 2001.
153. Young Jr, G. A. and Scully, J. R., The diffusion and trapping of hydrogen in high purity aluminum, *Acta Materialia* 46 (18), 6337-6349, 1998.
154. Li, Y., Song, W., Xie, C., Zeng, D., Wang, A., and Hu, M., Influence of humidity on the thermal behavior of aluminum nanopowders, *Materials Chemistry and Physics* 97 (1), 127-131, 2006.
155. Ramaswamy, A. and Kaste, P., A "Nanovision" of the Physiochemical Phenomena Occurring in Nanoparticles of Aluminum, *Journal of Energetic Materials* 23 (1), 1-25, 2005.
156. Fargeot, D., Mercurio, D., and Dauger, A., Structural characterization of alumina metastable phases in plasma sprayed deposits, *Materials Chemistry and Physics* 24 (3), 299-314, 1990.
157. Ilavsky, J., *Irena*, 2.25 ed. Argonne, Illinois, 2005.
158. Huot, J., Bouaricha, S., Boily, S., Dodelet, J. P., Guay, D., and Schulz, R., Increase of specific surface area of metal hydrides by lixiviation, *Journal of Alloys and Compounds* 266 (1-2), 307-310, 1998.
159. Graetz, J., New approaches to hydrogen storage, *Chemical Society Reviews* 38 (1), 73-82, 2009.
160. Chaudhuri, S. and Muckerman, J. T., First-Principles Study of Ti-Catalyzed Hydrogen Chemisorption on an Al Surface: A Critical First Step for Reversible Hydrogen Storage in NaAlH4, *Journal of Physical Chemistry B* 109 (15), 6952-6957, 2005.
161. Muller, E., Sutter, E., Zahl, P., Ciobanu, C. V., and Sutter, P., Short-range order of low-coverage Ti/Al(111): Implications for hydrogen storage in complex metal hydrides, *Applied Physics Letters* 90 (15), 151917-3, 2007.
162. Predel, B., Crystallographic and Thermodynamic Data of Binary Alloys, Volume 5 - Light Metal Structural Alloys, in *Landolt-Bornstein, Group IV Physical Chemistry - Phase Equilibria*, Madelung, O. Springer-Verlag, New York, 1998.
163. Hashi, K., Ishikawa, K., Suzuki, K., and Aoki, K., Hydrogen absorption and desorption in the binary Ti-Al system, *Journal of Alloys and Compounds* 330-332, 547-550, 2002.
164. Hashi, K., Ishikawa, K., Suzuki, K., and Aoki, K., Emergence of Hydrogen Absorption Ability in Metastable HCP, FCC and Amorphous Ti-AI Alloys Prepared by Mechanical Grinding, *Materials Transactions* 43 (11), 2734-2740, 2002.
165. Semenenko, K. P., Verbetskii, V. N., Zontov, V. S., Ioffe, M. I., and Tsutsuran, S. V., Interaction of Titanium Intermetallic Compounds with Hydrogen, *Russian Journal of Inorganic Chemistry* 27 (6), 766-768, 1982.
166. Masel, R. I., *Principles of Adsorption and Reaction on Solid Surfaces*, Wiley–Interscience, New York, 1996.
167. Pozzo, M., Alfè, D., Amieiro, A., French, S., and Pratt, A., Hydrogen dissociation and diffusion on Ni- and Ti-doped Mg(0001) surfaces, *Journal of Chemical Physics* 128, 094703, 2008.
168. Foley, T. J., Johnson, C. E., and Higa, K. T., Inhibition of Oxide Formation on Aluminum Nanoparticles by Transition Metal Coating, *Chemistry of Materials* 17 (16), 4086-4091, 2005.
169. Shafirovich, E. and Varma, A., Nickel-Coated Aluminum Particles: A Promising Fuel for Mars Missions, in *Strategic Research to Enable NASA's Exploration Missions Conference* NASA, Cleveland, Ohio, 2004, pp. 151-152.
170. Paskevicius, M., Webb, J., Pitt, M. P., Blach, T. P., Hauback, B. C., Gray, E. M., and Buckley, C. E., Mechanochemical synthesis of aluminium nanoparticles and their deuterium sorption properties to 2 kbar, *Journal of Alloys and Compounds* 481, 595-599, 2009.
171. Graetz, J., Chaudhuri, S., Lee, Y., Vogt, T., Muckerman, J. T., and Reilly, J. J., Pressure-induced structural and electronic changes in α-AlH_3, *Physical Review B* 74 (21), 214114, 2006.

172. Graetz, J. and Reilly, J., Thermodynamics of the α, β and γ polymorphs of AlH_3, *Journal of Alloys and Compounds* 424, 262-265, 2006.
173. Sandrock, G., Reilly, J., Graetz, J., Zhou, W. M., Johnson, J., and Wegrzyn, J., Accelerated thermal decomposition of AlH_3 for hydrogen-fueled vehicles, *Applied Physics A: Materials Science & Processing* 80 (4), 687-690, 2005.
174. Petrie, M. A., Bottaro, J. C., Schmitt, R. J., Penwell, P. E., and Bomberger, D. C., United States of America US 6,228,338 B1, 2001, Preperation of Aluminum Hydride Polymorphs, Particularly Stabilized α-AlH_3. May 8.
175. Antonov, V. E., Kolesnikov, A. I., Markushkin, Y. E., Sakharov, M. K., and Udovic, T. J., Phase Equilibria in the Al-H System by Inelastic Neutron Scattering, in *MH2008*, Reykjavík, Iceland, 2008.
176. Baranowski, B., Investigation of some metal-hydrogen systems in the high pressure region, *Journal of the Less Common Metals* 101, 115-129, 1984.
177. Klingler, R., 2005, Lightweight and Robust Hydrogen Storage Materials for Automotive Fuel Cells, http://www.cmt.anl.gov/science-technology/basicsci/alane-hydrogen.shtml, December 15 2005.
178. Appel, M. and Frankel, J. P., Production of Aluminum Hydride by Hydrogen-Ion Bombardment, *Journal of Chemical Physics* 42 (11), 3984-3988, 1965.
179. Rice Jr., M. J., Non-Solvated Aluminum Hydride, AD 106967, Office of Naval Research, 1956.
180. Brower, F. M., Matzek, N. E., Reigler, P. F., Rinn, H. W., Roberts, C. B., Schmidt, D. L., Snover, J. A., and Terada, K., Preparation and properties of aluminum hydride, *Journal of the American Chemical Society* 98, 2450-2453, 1976.
181. Turley, J. W. and Rinn, H. W., The Crystal Structure of Aluminum Hydride, *Inorganic Chemistry* 8, 18-22, 1969.
182. Pranevicius, L., Milcius, D., Pranevicius, L. L., and Thomas, G., Plasma hydrogenation of Al, Mg and MgAl films under high-flux ion irradiation at elevated temperature, *Journal of Alloys and Compounds* 373 (1-2), 9-15, 2004.
183. Siegel, B., The Reaction between Aluminum and Atomic Hydrogen, *Journal of the American Chemical Society* 82, 1535-1537, 1960.
184. Finholt, A. E., Bond Jr., A. C., and Schlesinger, H. I., Lithium Aluminum Hydride, Aluminum Hydride and Lithium Gallium Hydride, and Some of their Applications in Organic and Inorganic Chemistry, *Journal of the American Chemical Society* 69, 1199-1203, 1947.
185. Graetz, J. and Reilly, J. J., Decomposition Kinetics of the AlH_3 Polymorphs, *Journal of Physical Chemistry B* 109 (47), 22181-22185, 2005.
186. Ashby, E. C., Taylor, W. D., and Winkler, D. A., United States of America Patent US 3,829,390, 1974, Aluminum Hydride Product. August 13.
187. Lund, G. K., Hanks, J. M., and Johnston, H. E., United States of America US 2005/0222445 A1, 2005, Method for the Production of Alpha-Alane. October 6.
188. Schmidt, D. L. and Diesen, R. W., United States of America 3,840,654, 1974, Process for Preparing Crystalline, Non-Solvated Aluminum Hydride. October 8.
189. Baranowski, B., Hochheimer, H. D., Strossner, K., and Honle, W., High pressure X-ray investigation of AlH_3 and Al at room temperature, *Journal of the Less Common Metals* 113 (2), 341-347, 1985.
190. Brown, G. M., Schneibel, J. H., Knight, D. A., Ilgner, R. H., Sloop Jr., F. V., and Smithwick III, R. M., *Metal Borohydrides and Aluminum Hydrides*, DOE Hydrogen Program Annual Merit Review, Report No. ST35, Oak Ridge National Laboratory, June 12 2008.
191. Knott, W., European Patent EP0650924, 1995, Process for the preparation of aluminium hydride (AlH_3) by the reaction of magnesium hydride with aluminium halide. May 3.
192. Sartori, S., Istad-Lem, A., Brinks, H. W., and Hauback, B. C., Mechanochemical synthesis of alane, *International Journal of Hydrogen Energy* 34, 6350-6356, 2009.
193. McGrady, S., Canada WO/2006/063456, 2005, Synthesis, Recharging and Processing of Hydrogen Storage Materials Using Supercritical Fluids. December 7.
194. Humphries, T., McGrady, G. S., Ayabe, R., and Jensen, C. M., Toward the Direct Synthesis of Alane: Hydrogenation Studies of Aluminum in Supercritical Fluid Media, in *MH2008*, Reykjavík, Iceland, 2008, Poster Session II, pp. 71.
195. Darr, J. A. and Poliakoff, M., New Directions in Inorganic and Metal-Organic Coordination Chemistry in Supercritical Fluids, *Chemical Reviews* 99, 495-541, 1999.

196. Jensen, C. M. and McGrady, S., *Fundamental Studies of Advanced High-Capacity Reversible Metal Hydrides*, DOE Hydrogen Program Annual Merit Review, Report No. ST38, University of Hawaii, University of New Brunswick, June 12 2008.
197. Zidan, R., Garcia, B., Harter, A., Stowe, A., and Gray, J., *Electrochemical Reversibility of Alane*, DOE Hydrogen Program Annual Merit Review, Report No. STP19, Savannah River National Laboratory, June 13 2008.
198. Graetz, J., Wegrzyn, J., Reilly, J., Johnson, J., Celebi, Y., and Zhou, W. M., *Aluminum Hydride Regeneration*, DOE Hydrogen Program Annual Merit Review, Report No. ST39, Brookhaven National Laboratory, June 12 2008.
199. Herley, P. J., Christofferson, O., and Todd, J. A., Microscopic observations on the thermal decomposition of α-aluminum hydride, *Journal of Solid State Chemistry* 35 (3), 391-401, 1980.
200. Herley, P. J., Christofferson, O., and Irwin, R., Decomposition of alpha-aluminum hydride powder. 1. Thermal decomposition *Journal of Physical Chemistry* 85, 1874-1881, 1981.
201. Herley, P. J. and Christofferson, O., Decomposition of alpha-aluminum hydride powder. 2. Photolytic decomposition *Journal of Physical Chemistry* 85, 1882-1886, 1981.
202. Herley, P. J. and Christofferson, O., Decomposition of alpha-aluminum hydride powder. 3. Simultaneous photolytic-thermal decomposition *Journal of Physical Chemistry* 85, 1887-1892, 1981.
203. Sandrock, G., Reilly, J., Graetz, J., Zhou, W.-M., Johnson, J., and Wegrzyn, J., Alkali metal hydride doping of α-AlH_3 for enhanced H_2 desorption kinetics, *Journal of Alloys and Compounds* 421 (1-2), 185-189, 2006.
204. Wong, C.-P. and Miller, P. J., Vibrational Spectroscopic Studies of Alane, *Journal of Energetic Materials* 23, 169-181, 2005.
205. Brinks, H. W., Brown, C., Jensen, C. M., Graetz, J., Reilly, J. J., and Hauback, B. C., The crystal structure of γ-AlD_3, *Journal of Alloys and Compounds* 441, 364-367, 2007.
206. Brinks, H. W., Langley, W., Jensen, C. M., Graetz, J., Reilly, J. J., and Hauback, B. C., Synthesis and crystal structure of β-AlD_3, *Journal of Alloys and Compounds* 433, 180-183, 2007.
207. Tkacz, M., Palasyuk, T., Graetz, J., and Saxena, S., High-pressure Raman spectroscopy study of alpha and gamma polymorphs of AlH_3, *Journal of Raman Spectroscopy* 39 (7), 922-927, 2008.
208. Wolverton, C., Ozolins, V., and Asta, M., Hydrogen in aluminum: First-principles calculations of structure and thermodynamics, *Physical Review B (Condensed Matter and Materials Physics)* 69 (14), 144109-16, 2004.
209. Ke, X., Kuwabara, A., and Tanaka, I., Cubic and orthorhombic structures of aluminum hydride AlH_3 predicted by a first-principles study, *Physical Review B (Condensed Matter and Materials Physics)* 71 (18), 184107-7, 2005.
210. Ismail, I. M. K. and Hawkins, T., Kinetics of thermal decomposition of aluminium hydride: I-non-isothermal decomposition under vacuum and in inert atmosphere (argon), *Thermochimica Acta* 439 (1-2), 32-43, 2005.
211. Graetz, J., Reilly, J., Sandrock, G., Johnson, J., Zhou, W. M., and Wegrzyn, J., Aluminium Hydride, AlH_3, as a Hydrogen Storage Compound, in *Advanced Materials for Energy Conversion III*, Chandra, D., Petrovic, J. J., Bautista, R., and Imam, A., San Antonio, Texas, 2006, pp. 57-63.
212. Claudy, P., Bonnetot, B., Etienne, J., and Turck, G., Etude de Proprietes Physico-Chimiques de L'Hydrure D'Aluminium, *Journal of Thermal Analysis* 8, 255-262, 1975.
213. DeLuca, L. T., Galfetti, L., Severini, F., Rossettini, L., Meda, L., Marra, G., D'Andrea, B., Weiser, V., Calabro, M., Vorozhtsov, A. B., Glazunov, A. A., and Pavlovets, G. J., Physical and ballistic characterization of AlH_3-based space propellants, *Aerospace Science and Technology* 11 (1), 18-25, 2007.
214. Hatch, J. E., *Aluminum: Properties and Physical Metallurgy*, American Society for Metals, Metals Park, Ohio, 1984.
215. Tarasov, V. P., Muravlev, Y. B., Bakum, S. I., and Novikov, A. V., Kinetics of Formation of Metallic Aluminum upon Thermal and Photolytic Decomposition of Aluminum Trihydride and Trideuteride as Probed by NMR, *Doklady Physical Chemistry* 393 (4-6), 353-356, 2003.
216. Self, J. M. and Matzek, N. E., United States of America 3,844,854, 1974, Stabilization of Light Metal Hydride. October 29.
217. Sun, S., Ke, X., Chen, C., and Tanaka, I., First-principles prediction of low-energy structures for AlH_3, *Physical Review B* 79, 024104, 2009.

218. Grove, H., Sørby, M. H., Brinks, H. W., and Hauback, B. C., In Situ Synchrotron Powder X-ray Diffraction Studies of the Thermal Decomposition of β-and γ-AlD3, *Journal of Physical Chemistry C* 111, 16693-16699, 2007.

219. Maehlen, J. P., Yartys, V. A., Denys, R. V., Fichtner, M., Frommen, C., Bulychev, B. M., Pattison, P., Emerich, H., Filinchuk, Y. E., and Chernyshov, D., Thermal decomposition of AlH_3 studied by in situ synchrotron X-ray diffraction and thermal desorption spectroscopy, *Journal of Alloys and Compounds* 446-447, 280-289, 2007.

220. Sartori, S., Opalka, S. M., Løvvik, O. M., Guzik, M. N., Tang, X., and Hauback, B. C., Experimental studies of α-AlD3 and α'-AlD3 versus first-principles modelling of the alane isomorphs, *Journal of Materials Chemistry* 18, 2361-2370, 2008.

221. Saitoh, H., Machida, A., Katayama, Y., and Aoki, K., Formation and decomposition of AlH_3 in the aluminum-hydrogen system, *Applied Physics Letters* 93, 151918, 2008.

222. Ikeda, K., Muto, S., Tatsumi, K., Menjo, M., Kato, S., Bielmann, M., Züttel, A., Jensen, C. M., and Orimo, S., Dehydriding reaction of AlH_3: in situ microscopic observations combined with thermal and surface analyses, *Nanotechnology* 20, 204004, 2009.

223. Easton, D. S., Schneibel, J. H., and Speakman, S. A., Factors affecting hydrogen release from lithium alanate ($LiAlH_4$), *Journal of Alloys and Compounds* 398 (1-2), 245-248, 2005.

224. Zheng, X., Qu, X., Humail, I. S., Li, P., and Wang, G., Effects of various catalysts and heating rates on hydrogen release from lithium alanate, *International Journal of Hydrogen Energy* 32 (9), 1141-1144, 2007.

225. Sakintuna, B., Lamari-Darkrim, F., and Hirscher, M., Metal hydride materials for solid hydrogen storage: A review, *International Journal of Hydrogen Energy* 32 (9), 1121-1140, 2007.

226. Reule, H., Hirscher, M., Weißhardt, A., and Kronmüller, H., Hydrogen desorption properties of mechanically alloyed MgH_2 composite materials, *Journal of Alloys and Compounds* 305 (1-2), 246-252, 2000.

227. Barkhordarian, G., Klassen, T., and Bormann, R., Effect of Nb_2O_5 content on hydrogen reaction kinetics of Mg, *Journal of Alloys and Compounds* 364 (1-2), 242-246, 2004.

228. Aguey-Zinsou, K. F., Nicolaisen, T., Ares Fernandez, J. R., Klassen, T., and Bormann, R., Effect of nanosized oxides on MgH_2 (de)hydriding kinetics, *Journal of Alloys and Compounds* 434-435, 738-742, 2007.

229. Dobrovolsky, V. D., Ershova, O. G., Solonin, Y. M., Khyzhun, O. Y., and Paul-Boncour, V., Influence of TiB_2 addition upon thermal stability and decomposition temperature of the MgH_2 hydride of a Mg-based mechanical alloy, *Journal of Alloys and Compounds* 465 (1-2), 177-182, 2008.

230. Ershova, O. G., Dobrovolsky, V. D., Solonin, Y. M., Khyzhun, O. Y., and Koval, A. Y., Influence of Ti, Mn, Fe, and Ni addition upon thermal stability and decomposition temperature of the MgH_2 phase of alloys synthesized by reactive mechanical alloying, *Journal of Alloys and Compounds* 464 (1-2), 212-218, 2008.

231. Yu, X. B., Guo, Y. H., Yang, Z. X., Guo, Z. P., Liu, H. K., and Dou, S. X., Synthesis of catalyzed magnesium hydride with low absorption/desorption temperature, *Scripta Materialia* 61 (5), 469-472, 2009.

232. Marsh, K. N., Ott, J. B., Wormald, C. J., Yao, H., Hatta, I., Claudy, P. M., Herwaarden, S. V., A.R.H. Goodwin, K. N. M., and Wakeham, W. A., Calorimetry, in *Experimental Thermodynamics* Elsevier, 2003, pp. 325-385.

233. Rongeat, C., Llamas-Jansa, I., Doppiu, S., Deledda, S., Borgschulte, A., Schultz, L., and Gutfleisch, O., Determination of the Heat of Hydride Formation/Decomposition by High-Pressure Differential Scanning Calorimetry (HP-DSC), *The Journal of Physical Chemistry B* 111 (46), 13301-13306, 2007.

234. Bastide, J.-P., Bonnetot, B., Létoffé, J.-M., and Claudy, P., Polymorphisme de l'hydrure de magnesium sous haute pression, *Materials Research Bulletin* 15 (12), 1779-1787, 1980.

235. Zachariasen, W. H., Holley, C. E., and Stamper, J. F. J., Neutron diffraction study of magnesium deuteride, *Acta Crystallographica* 16 (5), 352-353, 1963.

236. Bououdina, M., Grant, D., and Walker, G., Review on hydrogen absorbing materials--structure, microstructure, and thermodynamic properties, *International Journal of Hydrogen Energy* 31 (2), 177-182, 2006.

237. Belkbir, L., Joly, E., and Gerard, N., Comparative study of the formation-decomposition mechanisms and kinetics in $LaNi_5$ and magnesium reversible hydrides, *International Journal of Hydrogen Energy* 6 (3), 285-294, 1981.

238. Pedersen, A. S., Kjøller, J., Larsen, B., and Vigeholm, B., Magnesium for Hydrogen Storage, *International Journal of Hydrogen Energy* 8 (3), 205-211, 1983.
239. Stampfer, J. F., Holley, C. E., and Suttle, J. F., The Magnesium-Hydrogen System, *Journal of the American Chemical Society* 82 (14), 3504-3508, 1960.
240. Reilly, J. J. and Wiswall, R. H., The Reaction of Hydrogen with Alloys of Magnesium and Nickel and the Formation of Mg_2NiH_4, *Inorganic Chemistry* 7, 2254-2256, 1968.
241. Friedlmeier, G. M. and Bolcich, J. C., Production and Characterization of Mg-10 wt% Ni Alloys for Hydrogen Storage, *International Journal of Hydrogen Energy* 13 (8), 467-474, 1988.
242. Shao, H., Wang, Y., Xu, H., and Li, X., Hydrogen storage properties of magnesium ultrafine particles prepared by hydrogen plasma-metal reaction, *Materials Science and Engineering B* 110, 221-226, 2004.
243. Bohmhammel, K., Wolf, U., Wolf, G., and Königsberger, E., Thermodynamic optimization of the system magnesium-hydrogen, *Thermochimica Acta* 337 (1-2), 195-199, 1999.
244. Bogdanović, B. and Spliethoff, B., The Magnesium Hydride System for Heat Storage and Cooling, *Zeitschrift für physikalische Chemie, Neue Folge* 164, 1497-1508, 1989.
245. Tanguy, B., Soubeyroux, J.-L., Pezat, M., Portier, J., and Hagenmuller, P., Amelioration des conditions de synthese de l'hydrure de magnesium a l'aide d'adjuvants, *Materials Research Bulletin* 11 (11), 1441-1447, 1976.
246. Gupta, R., Agresti, F., Russo, S. L., Maddalena, A., Palade, P., and Principi, G., Structure and hydrogen storage properties of MgH_2 catalysed with La_2O_3, *Journal of Alloys and Compounds* 450 (1-2), 310-313, 2008.
247. Kennelley, J. A., Varwig, J. W., and Myers, H. W., Magnesium-Hydrogen Relationships, *Journal of Physical Chemistry* 64 (5), 703-704, 1960.
248. Gerasimov, K. B., Konstanchuck, I. G., Chizhik, S. A., and Bobet, J. L., "Hysteresis" in interaction of nanocrystalline magnesium with hydrogen, *International Journal of Hydrogen Energy* 34 (4), 1916-1921, 2009.
249. Holley Jr., C. E., Worlton, W. J., and Zeigler, R. K., Compressibility Factors and Fugacity Coefficients Calculated from the Beattie-Bridgeman Equation of State for Hydrogen, Nitrogen, Oxygen, Carbon Dioxide, Ammonia, Methane and Helium, LA-2271, Los Alamos Scientific Laboratory, 1958.
250. Gérard, N. and Ono, S., Hydride Formation and Decomposition Kinetics, in *Hydrogen in Intermetallic Compounds II*, Schlapbach, L. Springer-Verlag, New York, 1992.
251. Stioui, M., Grayevsky, A., Moran, A., Kreitzman, S., Kaplan, N., and Shaltiel, D., Proton magnetic resonance study of diffusion-related properties in magnesium-rich compounds, *Journal of the Less Common Metals* 104 (1), 119-124, 1984.
252. Oelerich, W., Klassen, T., and Bormann, R., Metal oxides as catalysts for improved hydrogen sorption in nanocrystalline Mg-based materials, *Journal of Alloys and Compounds* 315 (1-2), 237-242, 2001.
253. Barkhordarian, G., Klassen, T., and Bormann, R., Fast hydrogen sorption kinetics of nanocrystalline Mg using Nb_2O_5 as catalyst, *Scripta Materialia* 49 (3), 213-217, 2003.
254. Aguey-Zinsou, K. F., Ares Fernandez, J. R., Klassen, T., and Bormann, R., Using MgO to improve the (de)hydriding properties of magnesium, *Materials Research Bulletin* 41 (6), 1118-1126, 2006.
255. Friedrichs, O., Sánchez-López, J. C., López-Cartes, C., Dornheim, M., Klassen, T., Bormann, R., and Fernández, A., Chemical and microstructural study of the oxygen passivation behaviour of nanocrystalline Mg and MgH_2, *Applied Surface Science* 252 (6), 2334-2345, 2006.
256. Huot, J., Akiba, E., and Takada, T., Mechanical alloying of Mg-Ni compounds under hydrogen and inert atmosphere, *Journal of Alloys and Compounds* 231 (1-2), 815-819, 1995.
257. Chen, Y. and Williams, J. S., Formation of metal hydrides by mechanical alloying, *Journal of Alloys and Compounds* 217 (2), 181-184, 1995.
258. Saita, I., Toshima, T., Tanda, S., and Akiyama, T., Hydrogen storage property of MgH_2 synthesized by hydriding chemical vapor deposition, *Journal of Alloys and Compounds* 446-447, 80-83, 2007.
259. Higuchi, K., Kajioka, H., Toiyama, K., Fujii, H., Orimo, S., and Kikuchi, Y., In situ study of hydriding-dehydriding properties in some Pd/Mg thin films with different degree of Mg crystallization, *Journal of Alloys and Compounds* 293-295, 484-489, 1999.

260. Liang, J. J., Theoretical insight on tailoring energetics of Mg hydrogen absorption/desorption through nano-engineering, *Applied Physics A: Materials Science & Processing* 80 (1), 173-178, 2005.
261. Cheung, S., Deng, W. Q., vanDuin, A. C. T., and Goddard, W. A., $ReaxFF_{MgH}$ Reactive Force Field for Magnesium Hydride Systems, *Journal of Physical Chemistry A* 109 (5), 851-859, 2005.
262. de Jongh, P. E., Wagemans, R. W. P., Eggenhuisen, T. M., Dauvillier, B. S., Radstake, P. B., Meeldijk, J. D., Geus, J. W., and de Jong, K. P., The Preparation of Carbon-Supported Magnesium Nanoparticles using Melt Infiltration, *Chemistry of Materials* 19, 6052-6057, 2007.
263. Gross, A. F., Ahn, C. C., Van Atta, S. L., Liu, P., and Vajo, J. J., Fabrication and hydrogen sorption behaviour of nanoparticulate MgH_2 incorporated in a porous carbon host, *Nanotechnology* 20, 204005, 2009.
264. Zhang, S., Gross, A. F., Van Atta, S. L. L., Maribel, Liu, P., Ahn, C. C., Vajo, J. J., and Jensen, C. M., The synthesis and hydrogen storage properties of a MgH_2 incorporated carbon aerogel scaffold, *Nanotechnology* 20, 204027, 2009.
265. Haas, I. and Gedanken, A., Synthesis of metallic magnesium nanoparticles by sonoelectrochemistry, *Chemical Communications*, 1795-1797, 2008.
266. Aguey-Zinsou, K.-F. and Ares-Fernández, J.-R., Synthesis of Colloidal Magnesium: A Near Room Temperature Store for Hydrogen, *Chemistry of Materials* 20, 376-378, 2008.
267. Ashby, E. C. and Schwartz, R. D., Reactions of lithium, sodium, and potassium hydrides with magnesium halides in ether solvents. Convenient and economic route to reactive magnesium hydride, *Inorganic Chemistry* 10 (2), 355-357, 1971.
268. Didisheim, J. J., Zolliker, P., Yvon, K., Fischer, P., Schefer, J., Gubelmann, M., and Williams, A. F., Dimagnesium iron(II) hydride, Mg_2FeH_6, containing octahedral FeH_6^{4-} anions, *Inorganic Chemistry* 23 (13), 1953-1957, 1984.
269. Shang, C. X., Bououdina, M., Song, Y., and Guo, Z. X., Mechanical alloying and electronic simulations of (MgH_2+M) systems (M=Al, Ti, Fe, Ni, Cu and Nb) for hydrogen storage, *International Journal of Hydrogen Energy* 29 (1), 73-80, 2004.
270. Becker, W. E. and Ashby, E. C., Hydrogenolysis of the Grignard Reagent, *The Journal of Organic Chemistry* 29 (4), 954-955, 1964.
271. Au, M., The influence of tetrahydrofuran treatment on hydrogen storage properties of the magnesium, *Journal of Materials Science* 41 (18), 5976-5980, 2006.
272. *NIST/SEMATECH e-Handbook of Statistical Methods*, http://www.itl.nist.gov/div898/handbook/ September 1, 2009.
273. Kirkup, L., *Experimental Methods*, John Wiley & Sons, Singapore, 1994.
274. Sergeev, G. B., *Nanochemistry*, Elsevier, Amsterdam, 2006.
275. Seddon, J. M. and Gale, J. D., *Thermodynamics and Statistical Mechanics*, The Royal Society of Chemistry, London, 2002.

Appendix A

Maple Code: Hydrogen Compressibility

The following Maple (Maplesoft, Ontario, Canada) code was written to numerically solve an equation of state for hydrogen [122-123]. The user inputs the measured pressure (1 bar – 1 Mbar) and temperature (100 K – 1000 K) of the hydrogen gas and the molar volume, compressibility, and the fugacity of hydrogen is the output.

```
#User input for pressure and temperature
p := 100; #PRESSURE (bar)
T := 298.15; #TEMPERATURE (K)
#
#Define constants
R:=83.1451: #Converted from Pascals and cubic metres to bar and
          cubic centimetres
alpha0:=2.9315:
alpha1:=-1.531e-3:
alpha2:=4.154e-6:
a1:=19.599:
a2:=-0.8946:
a3:=-18.608:
a4:=2.6013:
b0:=20.285:
b1:=-7.44171:
b2:=7.318565:
b3:=-3.463717:
b4:=0.87372903:
b5:=-0.12385414:
b6:=9.8570583e-3:
b7:=-4.1153723e-4:
b8:=7.02499e-6:
printf("Constants & Functions Loaded");
#
#Define variables
unassign('a','b','alpha','V');
if p > 1 then assign(a=evalf(exp(a1+a2*ln(p)-exp(a3+a4*ln(p)))))
          else printf("error") end if;
if p > 1 and p < 100 then
          assign(b=evalf(b0*ln(100)^0+b1*ln(100)^1+b2*ln(100)^2+b3*ln
          (100)^3+b4*ln(100)^4+b5*ln(100)^5+b6*ln(100)^6+b7*ln(100)^7
          +b8*ln(100)^8)) elif p > 100 or p = 100 then
          assign(b=evalf(b0*ln(p)^0+b1*ln(p)^1+b2*ln(p)^2+b3*ln(p)^3+
          b4*ln(p)^4+b5*ln(p)^5+b6*ln(p)^6+b7*ln(p)^7+b8*ln(p)^8))
          else printf("error") end if;
if T > 300 then assign(alpha=evalf(alpha0+alpha1*300+alpha2*300^2))
          else assign(alpha=evalf(alpha0+alpha1*T+alpha2*T^2)) end
          if;
Vi:=R*T/p; #IDEAL GAS LAW VOLUME (cm3/mol)
#
# Numerically solve Hemmes equation of state
Xtest:=Vi-Vi/8:
Vm:=fsolve((p+a/(V**alpha))*(V-b)-R*T=0,V,Xtest..infinity); #MOLAR
          VOLUME (cm3/mol)
Z:=Vm/Vi; #COMPRESSIBILITY
Fugacity = p*exp(int(Vm/(83.145*T)-1/p, x = 0 .. p)); #(bar)
```

Appendix B

Maple Code: Fugacity to Pressure

The following Maple (Maplesoft, Ontario, Canada) code was written to determine the pressure of hydrogen at a particular fugacity and temperature. Fugacity is related to pressure by Equation 1.4 which must be numerically solved to determine pressure. A second numerical solution is performed on an equation of state for hydrogen [122-123,125] to determine the molar volume of hydrogen. The user inputs the fugacity and temperature (77 K, 100 K – 1000 K) of the hydrogen gas and the corresponding pressure of hydrogen gas is calculated.

```
#User input for fugacity and temperature
Fugacity := 100; #FUGACITY (bar)
T := 298.15; #TEMPERATURE (K)
#
#Define constants
R:=83.1451: #Converted from Pascals and cubic metres to bar and
          cubic centimetres
alpha0:=2.9315:
alpha1:=-1.531e-3:
alpha2:=4.154e-6:
a1:=19.599:
a2:=-0.8946:
a3:=-18.608:
a4:=2.6013:
b0:=20.285:
b1:=-7.44171:
b2:=7.318565:
b3:=-3.463717:
b4:=0.87372903:
b5:=-0.12385414:
b6:=9.8570583e-3:
b7:=-4.1153723e-4:
b8:=7.02499e-6:
printf("Constants & Functions Loaded");
#
#Define variables for fugacity numerical routine
ptest := fsolve(Fugacity=P*exp((P*15.84)/(83.145*T)),P); #initial
      test pressure
p:=ptest:
FugacityCalc:=-1:
#
#Begin fugacity numerical routine
for g from 1 to 5000 while abs(FugacityCalc-Fugacity) > 0.00001 do
      #resolution can be changed depending on pressure
#
#Define variables for equation of state numerical routine
unassign('a','b','alpha','V');
if p > 1 then assign(a=evalf(exp(a1+a2*ln(p)-exp(a3+a4*ln(p)))))
      else printf("error") end if;
if p > 1 and p < 100 then
      assign(b=evalf(b0*ln(100)^0+b1*ln(100)^1+b2*ln(100)^2+b3*ln(10
      0)^3+b4*ln(100)^4+b5*ln(100)^5+b6*ln(100)^6+b7*ln(100)^7+b8*ln
      (100)^8)) elif p > 100 or p = 100 then
      assign(b=evalf(b0*ln(p)^0+b1*ln(p)^1+b2*ln(p)^2+b3*ln(p)^3+b4*
      ln(p)^4+b5*ln(p)^5+b6*ln(p)^6+b7*ln(p)^7+b8*ln(p)^8)) else
      printf("error") end if;
if T > 300 then assign(alpha=evalf(alpha0+alpha1*300+alpha2*300^2))
```

```
      else assign(alpha=evalf(alpha0+alpha1*T+alpha2*T^2)) end if;
Vi:=R*T/p; #IDEAL GAS LAW VOLUME (cm3/mol)
#
#Begin equation of state numerical routine
Xtest:=Vi-Vi/8:
Vm:=fsolve((p+a/(V**alpha))*(V-b)-R*T=0,V,Xtest..infinity); #HEMMES
      EQUATION OF STATE (cm3/mol)
Z:=Vm/Vi; #COMPRESSIBILITY
if T = 77 and p < 140 then Z:= 1-0.0017359*p+1.4459e-5*p**2-6.8988e-
      8*p**3+5.5334e-9*p**4-1.1555e-10*p**5+1.3545e-12*p**6-9.7473e-
      15*p**7+3.9175e-17*p**8-6.6383e-20*p**9 end if; #Lemmon
if T = 77 and p > 140 and p < 5000 then Z:=
      0.68302+0.0028112*p+9.6708e-7*p**2-2.0147e-9*p**3+1.6679e-
      12*p**4-7.9345e-16*p**5+2.2979e-19*p**6-3.9964e-
      23*p**7+3.8367e-27*p**8-1.5627e-31*p**9 end if; #Lemmon
#
#Back-calculate fugacity
FugacityCalc:=p*exp(int((Z-1)/p,x=0..p));
#
#Step pressure in numerical routine
if FugacityCalc < Fugacity then p:=p*(1+1/g/10) else p:=p*(1-1/g/10)
      end if:
end do:
#
#Output data
Iterations:=g;
realZ:=Z;
CalculatedFugacity:=FugacityCalc;
realp:=p;
```

Appendix C

Labview Code Schematics: Automated Rig

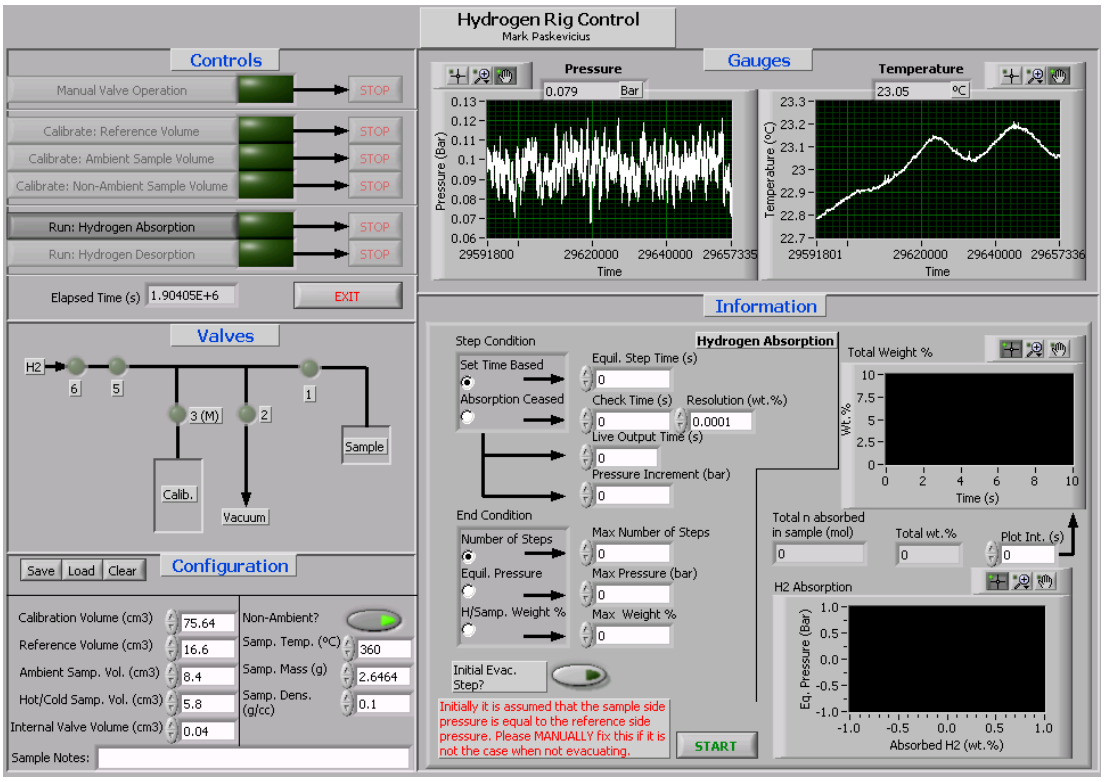

Figure C-1: Automated hydrogen measurement apparatus user interface programmed in Labview. The interface provides live pressure and temperature information, manual control over the pneumatic valves, and the ability to run automated sequences for calibration, absorption and desorption from any sample or instrument configuration.

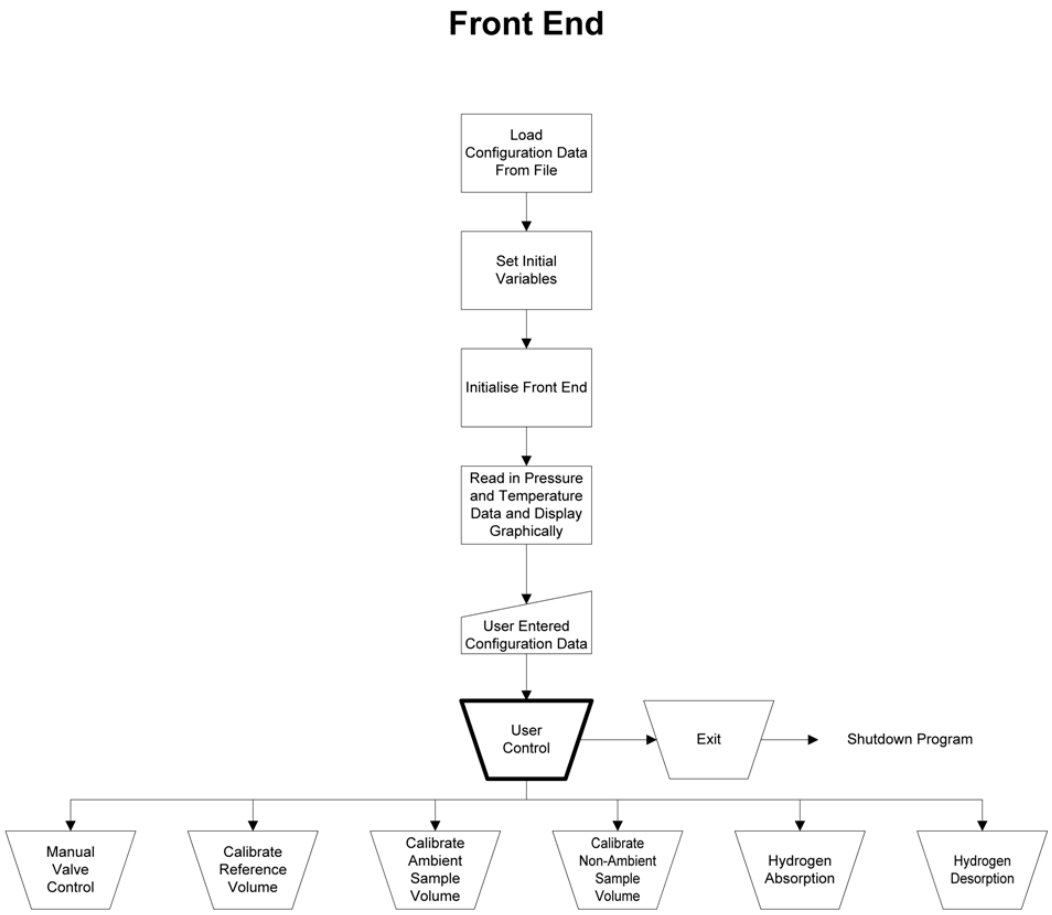

Figure C-2: Basic functionality of front end interface.

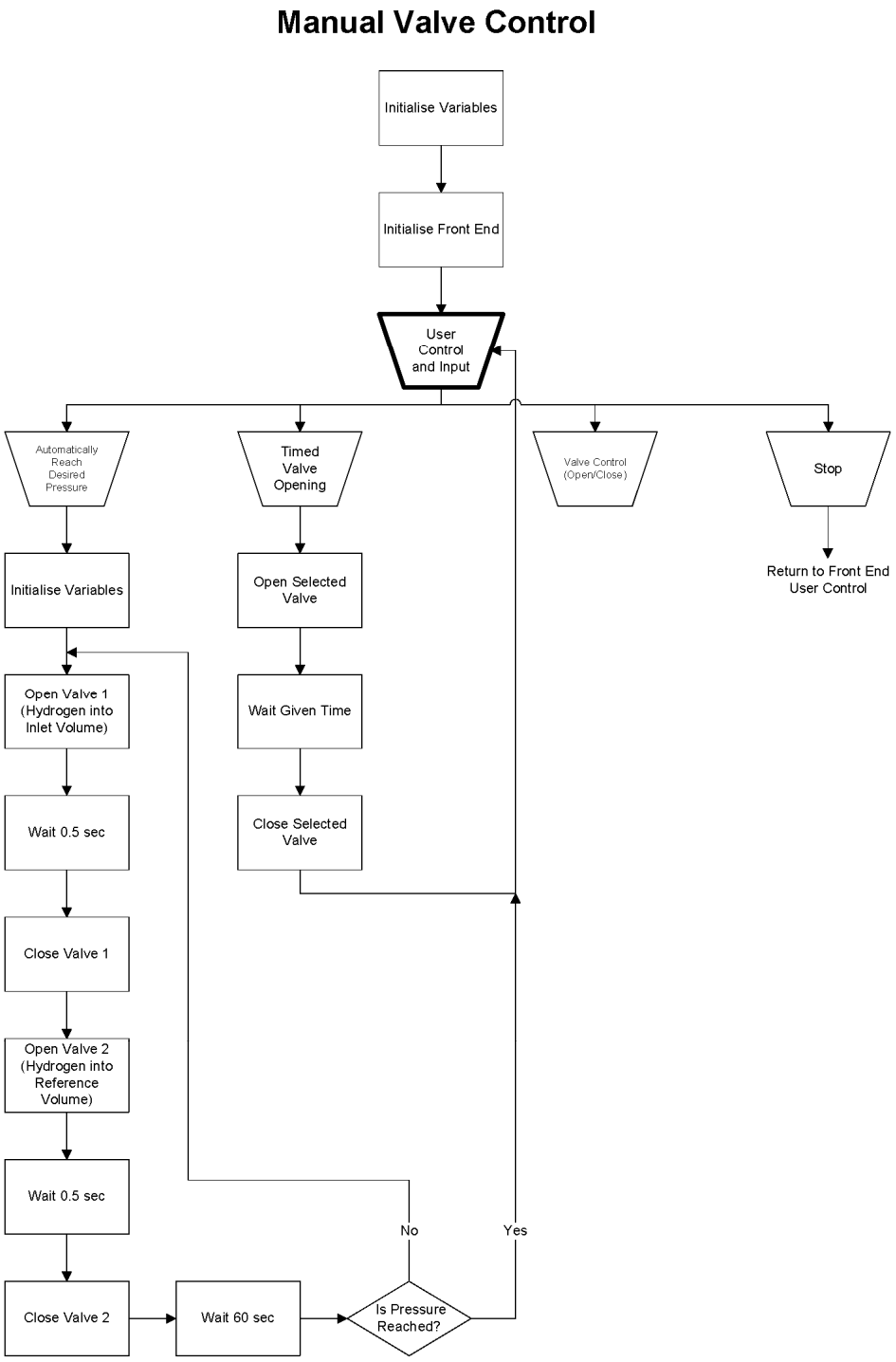

Figure C-3: Manual valve control including automated routines for reaching given pressures and timed opening of valves.

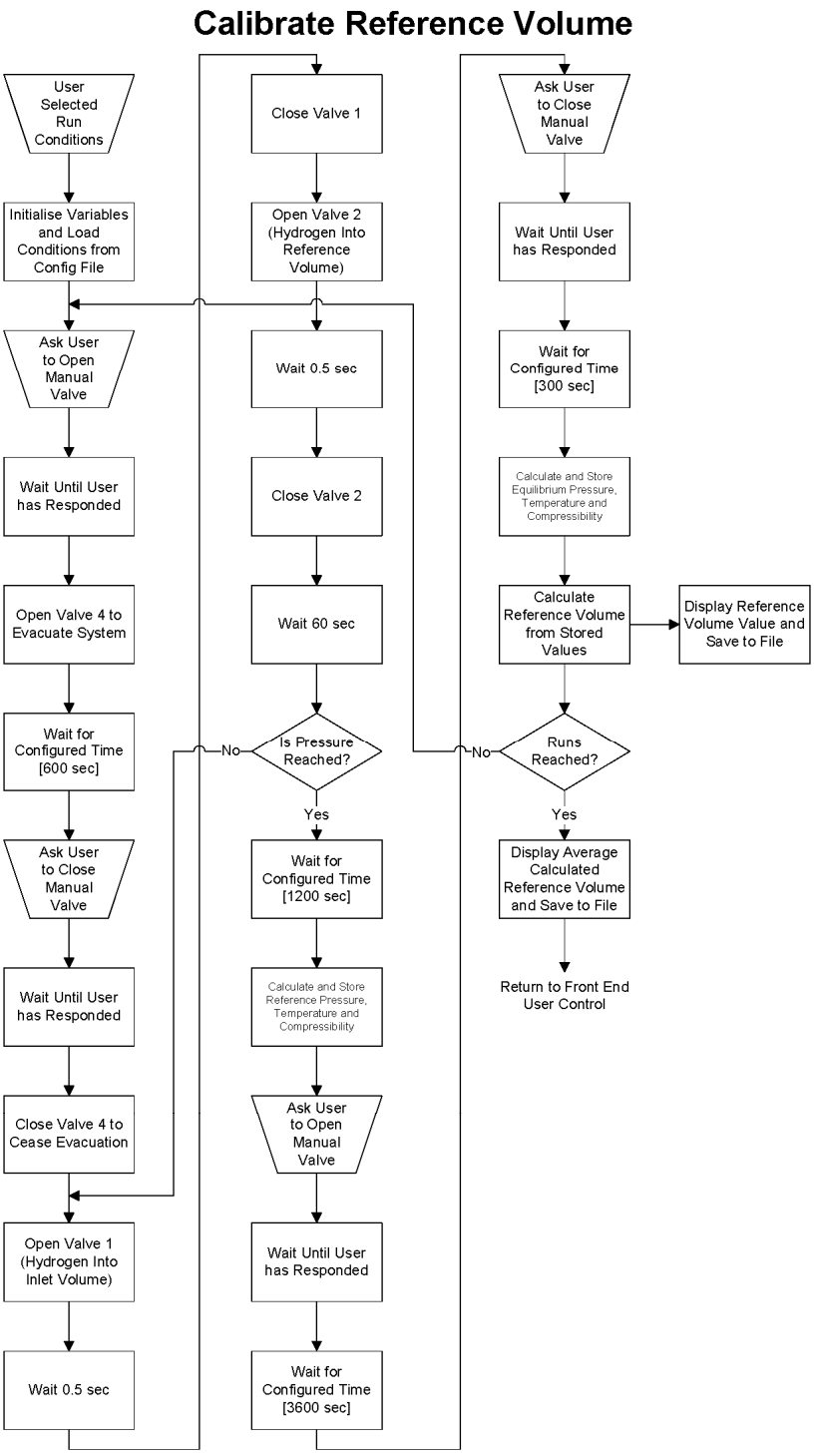

Figure C-4: Routine for reference volume calibration from a known calibration volume.

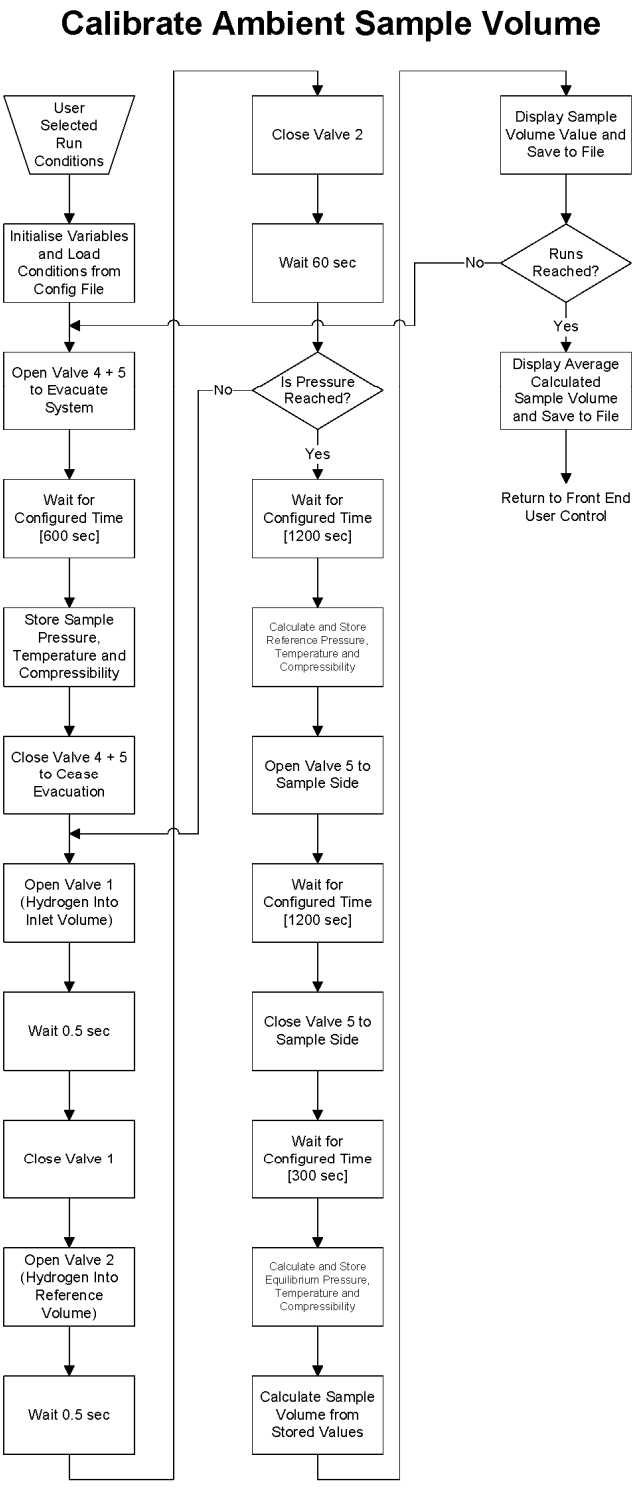

Figure C-5: Routine for sample volume calibration (at ambient temperatures) from a known reference volume.

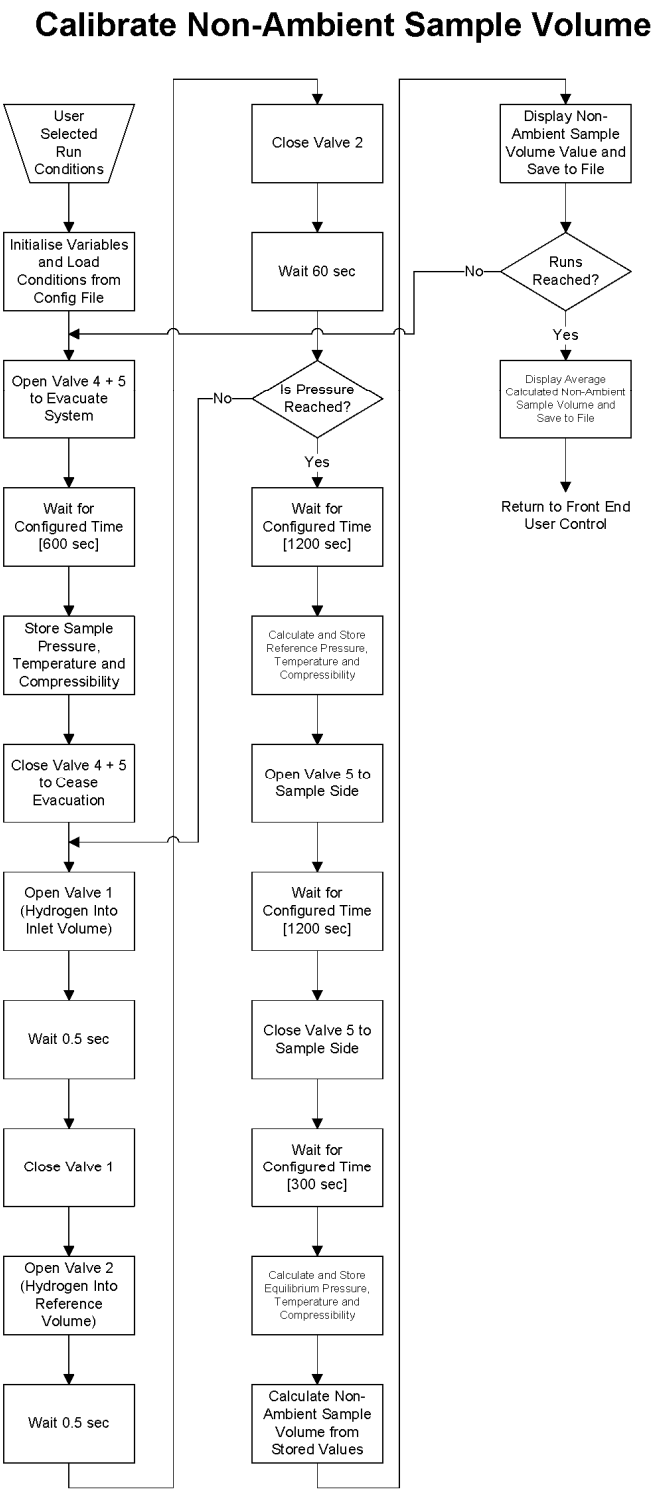

Figure C-6: Routine for sample volume calibration (at non-ambient temperatures) from a known reference volume.

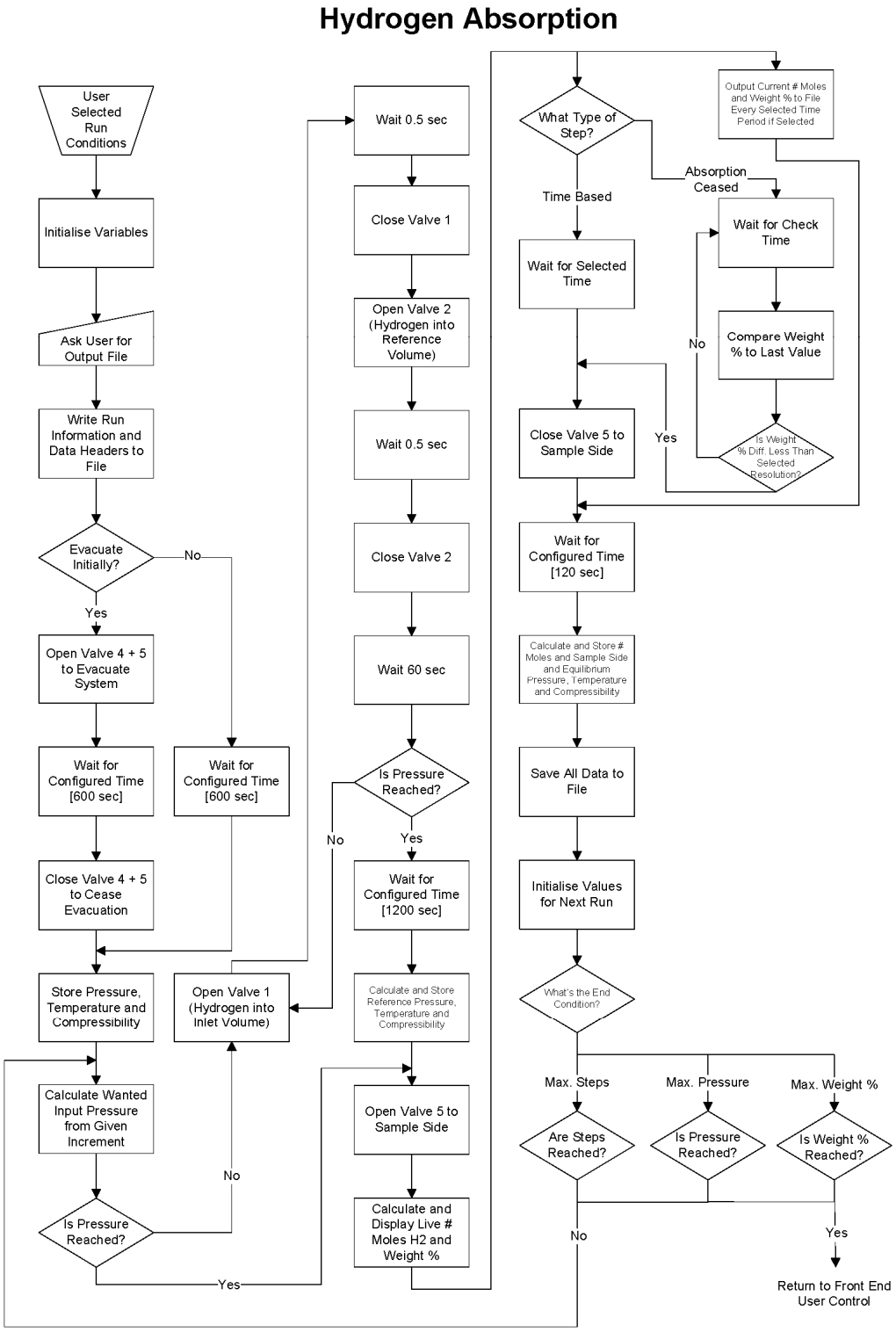

Figure C-7: Routine for hydrogen absorption measurement and data collection.

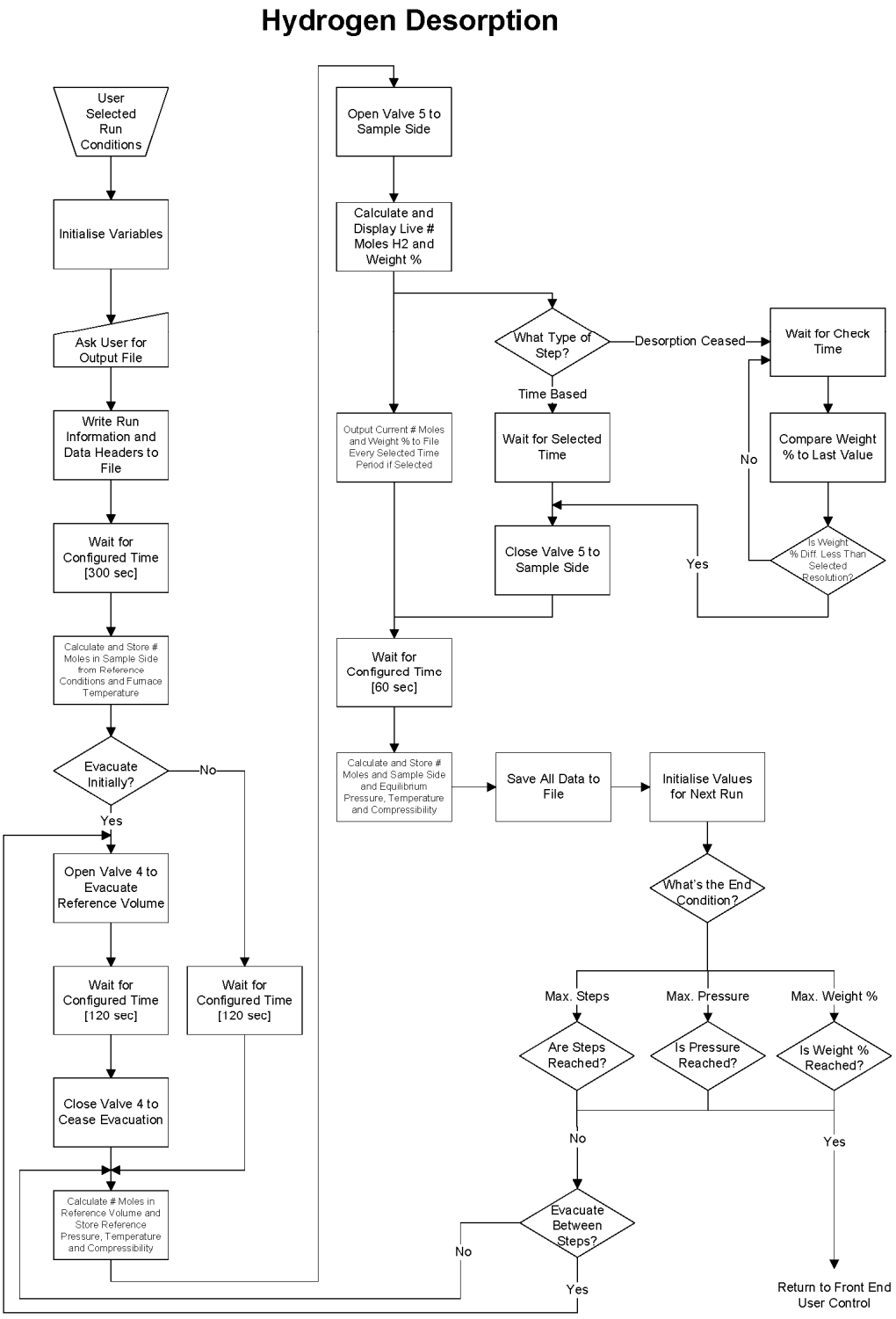

Figure C-8: Routine for hydrogen desorption measurement and data collection.

```
Configuration File

File Loaded When Program Started
Default Settings in []


Max Gauge Pressure (bar) [140]
140
Sorption Ceased Resolution Default (moles H2) [0.01]
0.01
Default Calibration Run Number [5]
5
Temperature Gauge Averaging Samples [100]
100
Pressure Gauge Averaging Samples [500]
500

Ref Cal: Minimum Reference Pressure (bar) [40]
40
Ref Cal: Maximum Reference Pressure (bar) [80]
80
Ref Cal: Reference Pressure Step Size per Run (bar) [5]
5
Ref Cal: Evacuation Time (s) [600]
600
Ref Cal: Reference Wait Time after Input (s) [1200]
1200
Ref Cal: Calibration Volume Equilibrium Wait Time (s) [3600]
3600
Ref Cal: Final Closed Valve Wait Time (s) [300]
300

Amb Samp Cal: Minimum Reference Pressure (bar) [40]
40
Amb Samp Cal: Maximum Reference Pressure (bar) [80]
80
Amb Samp Cal: Reference Pressure Step Size per Run (bar) [5]
5
Amb Samp Cal: Evacuation Time (s) [600]
600
Amb Samp Cal: Reference Wait Time after Input (s) [1200]
1200
Amb Samp Cal: Calibration Volume Equilibrium Wait Time (s) [1200]
1200
Amb Samp Cal: Final Closed Valve Wait Time (s) [300]
300

Non-Amb Samp Cal: Minimum Reference Pressure (bar) [40]
40
Non-Amb Samp Cal: Maximum Reference Pressure (bar) [80]
80
Non-Amb Samp Cal: Reference Pressure Step Size per Run (bar) [5]
5
Non-Amb Samp Cal: Evacuation Time (s) [600]
600
Non-Amb Samp Cal: Reference Wait Time after Input (s) [1200]
1200
Non-Amb Samp Cal: Calibration Volume Equilib Wait Time (s) [1200]
1200
Non-Amb Samp Cal: Final Closed Valve Wait Time (s) [300]
300
```

```
Hyd Abs: Evacuation Time (s) [600]
600
Hyd Abs: Reference Wait Time after Input (s) [1200]
1200
Hyd Abs: Wait Time after Condition Met (s) [120]
120

Hyd Des: Initial Wait Time to find Samp Pres from Ref Pres (s) [300]
300
Hyd Des: Evacuation Time (s) [120]
120
Hyd Des: Wait Time after Condition Met (s) [60]
60
```

Appendix D

Calculation: Bulk Density

The bulk density of a material (ρ_{bulk}) can be calculated as follows if the true atomic density (ρ_{base}) and both the one-dimensional bulk (d_{tot}) and the atomic (d_{sp}) sample thicknesses are known.

The density is generally described as the ratio between mass (m) and volume (V):

$$\rho = \frac{m}{V} \tag{D.1}$$

Let us consider the bulk takes the form of a cubic volume given in Figure D-1 where each side length is equal to d_{tot}. In doing so we assume that the material has an isotropic density, which is the case for the materials in the present study. A subset of the bulk volume is displayed (in Figure D-1) that is equivalent to the atomic volume of the material (no porosity) where each side length is equal to d_{sp}.

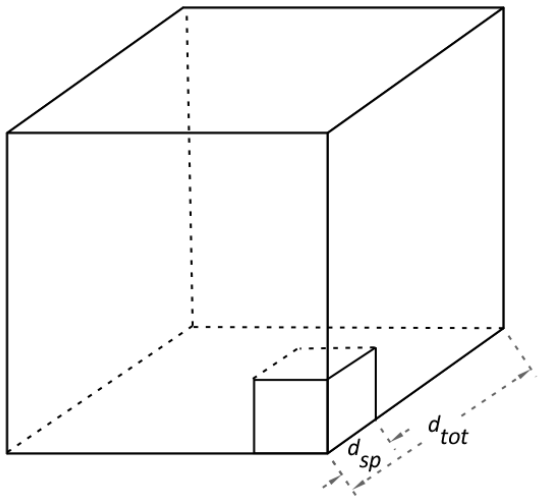

Figure D-1: Schematic of an arbitrary bulk volume and the atomic volume which occupies a percentage based on its anisotropic thickness.

Both the bulk and atomic volume contain the same mass of material by definition. As such the bulk density can be expressed as follows:

$$\begin{aligned} & m = \rho V \\ & \therefore \rho_{bulk} V_{bulk} = \rho_{base} V_{base} \\ & \therefore \rho_{bulk} = \frac{\rho_{base} V_{base}}{V_{bulk}} = \rho_{base} \frac{V_{base}}{V_{bulk}} \end{aligned} \tag{D.2}$$

Therefore, if the atomic density is known along with the bulk and atomic sample thicknesses the following relationship can be formed using an arbitrary volume ratio (given by the cubic schematic in Figure D-1) where:

$$V = d^3$$

$$\therefore \rho_{bulk} = \frac{\rho_{base} d_{sp}{}^3}{d_{tot}{}^3} \tag{D.3}$$

For example, the bulk density (ρ_{bulk}) of aluminium nanoparticles can be calculated given that a sample is packed within a cell of known thickness (d_{tot}). The atomic density is known for aluminium (ρ_{base} = 2.7 g/cm^3) and the thickness of the sample not including porosity (d_{sp}) can be determined from x-ray transmission measurements.

Appendix E

Peer Reviewed Publications

Journal of Alloys and Compounds 481 (2009) 595–599

Contents lists available at ScienceDirect

Journal of Alloys and Compounds

journal homepage: www.elsevier.com/locate/jallcom

Mechanochemical synthesis of aluminium nanoparticles and their deuterium sorption properties to 2 kbar

M. Paskevicius[a], J. Webb[b], M.P. Pitt[b], T.P. Blach[b], B.C. Hauback[c], E.MacA. Gray[b], C.E. Buckley[a,*]

[a] Department of Imaging and Applied Physics, Curtin University of Technology, GPO Box U 1987, Perth, WA, Australia
[b] Nanoscale Science and Technology Centre, Griffith University, Brisbane 4111, Australia
[c] Institute for Energy Technology, P.O. Box 40, Kjeller N-2027, Norway

ARTICLE INFO

Article history:
Received 28 January 2009
Received in revised form 3 March 2009
Accepted 7 March 2009
Available online 19 March 2009

Keywords:
Hydrogen storage materials
Metals
Nanostructures
Mechanochemical synthesis

ABSTRACT

A mechanochemical synthesis process has been used to synthesise aluminium nanoparticles. The aluminium is synthesised via a solid state chemical reaction which is initiated inside a ball mill at room temperature between either lithium (Li) or sodium (Na) metal which act as reducing agents with unreduced aluminium chloride ($AlCl_3$). The reaction product formed consists of aluminium nanoparticles embedded within a by-product salt phase (LiCl or NaCl, respectively). The LiCl is washed with a suitable solvent resulting in aluminium (Al) nanoparticles which are not oxidised and are separated from the by-product phase. Synthesis and washing was confirmed using X-ray diffraction (XRD). Nanoparticles were found to be ~25–100 nm from transmission electron microscopy (TEM) and an average size of 55 nm was determined from small angle X-ray scattering (SAXS) measurements. As synthesised Al/NaCl composites, washed Al nanoparticles, and purchased Al nanoparticles were deuterium (D_2) absorption tested up to 2 kbar at a variety of temperatures, with no absorption detected within system resolution.

1. Introduction

Aluminium nanoparticles are of interest to a variety of fields including pyrotechnic, propellant, and explosive industries. Aluminium powder has been added to a variety of these compositions in order to increase their performance through raising reaction energies, flame temperatures, and increasing blast rates [1,2]. Nanoparticles of aluminium are more favourable because of their high enthalpy of combustion [3] and rapid kinetics [1] which increase these reaction properties even further.

Aluminium can also be used as a hydrogen storage compound in the form of alane (AlH_3). Alane is a promising hydrogen storage compound due to its very high hydrogen storage capacity (10.1 wt.%), low hydrogen desorption temperature, fast desorption kinetics, and the widespread availability of aluminium. The major problem related to using aluminium as a hydrogen storage material is the extreme high pressure and temperature (28 kbar at 300 °C) required for the absorption of gaseous H_2 into bulk aluminium metal [4,5], a consequence of its unstable formation enthalpy of −11.4 kJ/mol [6]. The hydrogen absorption properties of Al nanoparticles are not well known, and the mechanochemical synthesis of Al nanoparticles is promising in order to analyse the behaviour of hydrogen at moderate pressures with unoxidised aluminium nanoparticles. It is expected that the small particle size and clean nanoparticle surface would allow hydrogen to absorb into aluminium under more reasonable hydrogen pressures, compared to the very large ~150 μm Al powder used in [4], which was most likely oxidised. Small nanoparticles are expected to alter both the thermodynamics and kinetics of the aluminium–hydrogen system. Significant thermodynamic changes are theoretically predicted for aluminium nanoparticles smaller than 5 nm in comparison to the bulk [7] however these thermodynamic changes have not yet been experimentally demonstrated and it is not yet known with certainty if these changes extend to larger aluminium nanoparticles.

Mechanochemical synthesis differs from standard ball milling. A standard ball milling process under inert atmosphere results in a moderate reduction of powder particle size and eventually the formation of nanosized grains within micron-sized particles [8]. The mechanochemical method involves the initiation of a solid-state displacement reaction during the ball milling process [8] which can result in nanosized particles (down to ~5 nm in size) embedded within larger by-product phase particles. The chemical reaction can, for example, involve the reduction of a metallic compound such as an oxide, chloride, or sulphide [9] with an appropriate reducing agent. The occurrence of combustion due to the very large reaction enthalpies associated with these reactions is typically tempered by the addition of extra by-product phase, and/or milling parameters.

Mechanical milling is utilised in the mechanochemical synthesis of nanoparticles because it effectively blends the reactants, forming

* Corresponding author. Tel.: +61 8 92663532; fax: +61 8 92662377.
E-mail address: C.Buckley@curtin.edu.au (C.E. Buckley).

0925-8388/$ – see front matter © 2009 Elsevier B.V. All rights reserved.
doi:10.1016/j.jallcom.2009.03.031

nanoscale mixtures and increases the chemical reactivity (and also the reaction kinetics) which leads to a chemical reaction between these reactants enabling the product phase to form [10] by virtue of large reaction enthalpies. The mechanochemical synthesis process has been used in the past [9,11] to synthesise a broad range of metal nanoparticles (e.g. Ag, Cd, Co, Cr, Cu, Er, Fe, Gd, Ni, Pb, Sm, Ta, Ti, V, W, Zn, and Zr) as well as other compounds such as oxides and sulphides. Particle size control can be gained by adjusting factors such as: the volume fraction of the by-product phase formed during milling, milling time, milling collision energy (ball-to-powder mass ratio and ball size), milling temperature, and the use of process control agents [9,10].

This paper is organised as follows: Section 3.1 describes the mechanochemical synthesis reactions used to produce Al nanoparticles. Section 3.2 describes the measurement of the Al particle size by X-ray diffraction (XRD), small angle X-ray scattering (SAXS) and transmission electron microscopy (TEM). Section 3.3 discusses the deuterium absorption properties of synthesised and purchased Al nanoparticles up to 2 kbar.

2. Experimental

All handling of chemicals and sealable milling vials was undertaken in an argon-atmosphere glovebox in order to minimise oxygen (O_2 < 5 ppm) and water (H_2O < 0.1 ppm) contamination. Li (Sigma–Aldrich, ≥99.9%), Na (Sigma–Aldrich, 99%), $AlCl_3$ (Sigma–Aldrich, 99%), NaCl (Chem-Supply, 99%), and LiCl (Sigma–Aldrich, ≥99%) were used as starting reagents. Ball milling was performed with a custom made ball milling canister (650 cm^3 internal volume) attached to a Glen Mills Turbula T2C shaker-mixer. The ball milling canister was made from stainless steel (316) and was sealed with an o-ring on both ends. The milling media used was made from the same material as the canister to minimise sample contamination due to the degradation of both the canister and balls. The milling equipment was made from 316 stainless steel, as this grade of steel provides good corrosion resistance and also resistance to pitting. Aluminium nanoparticles were purchased (American Elements, Los Angeles, USA, 99%) in order to provide a comparison between mechanochemically synthesised and commercially available nano-Al. Dry 10–22 nm Al synthesised by colloidal chemistry was also obtained from Meliorum Technologies. The 10–22 nm particle size was determined in-house by Meliorum using photon correlation spectroscopy.

X-ray diffraction was performed using a Siemens D500 diffractometer (CuK_α wavelength, λ, of 1.5418 Å) with a 2θ range of 10–80° using 0.02° steps with 3 s of count time per step and operating conditions were set at 40 kV and 30 mA. Samples were loaded into XRD sample holders in an argon glovebox and were sealed under a 4 μm mylar film to prevent oxygen/moisture contamination during data collection. Rietveld analysis was performed on the XRD patterns using Topas software (Bruker AXS, Karlsruhe, Germany) in order to provide additional structural information from the washed and unwashed samples. The crystallite sizes were determined from an LVol-IB method (volume averaged column height calculated from the integral breadth) [12] which provides a good measure of the physical crystallite size.

Small angle X-ray scattering patterns were collected with a Bruker NanoSTAR SAXS instrument. Samples were loaded and sealed within glass capillaries in an argon glovebox to prevent oxygen/moisture contamination prior to data collection. Data was recorded at a sample-detector distance of 65.0 cm using a wavelength, λ, of 1.5418 Å (CuK_α) and scattered photons were counted with a 2D multiwire detector for 3 h per sample. The raw data was radially averaged and background subtracted. Resulting intensities, after discarding low-q data points affected by the beam stop, spanned a q-range of 0.114–3.27 nm^{-1} ($q = 4\pi \sin\theta/\lambda$, where 2θ is the scattering angle). Scattering data was converted onto an absolute scale by calibrating against a known standard using the method of Spalla et. al. [13].

Transmission electron microscopy was performed on a JEOL JEM2011 instrument operating at 200 kV and a JEOL 3000F FEGTEM instrument operating at 300 kV. Both microscopes were coupled with an Oxford Instruments energy dispersive X-ray spectrometer (EDS) for elemental analysis. Samples were loaded onto 200 mesh copper grids with holey carbon support films drop-wise via suspension in nitromethane. The TEM grids contain minor traces of silicon resulting from the manufacturing process.

Deuterium absorption experiments were performed in a Sieverts manometric apparatus using the Hemmes equation of state [14] via the method of McLennan and Gray [15] to account for the compressibility of deuterium for room temperature measurements and the equation of state from the NIST Standard Reference Database Number 69 was used for 77 K measurements [16]. Deuterium was utilised instead of hydrogen in order to undertake neutron diffraction measurements if absorption was successful. The use of deuterium instead of hydrogen for absorption measurements is routinely undertaken in the literature and is not expected to have any major impact on absorption results.

3. Results and discussion

3.1. Mechanochemical synthesis of Al nanoparticles

The mechanochemical reactions given by reactions (1) and (2) were both initiated within a ball mill at room temperature and both reactions proceeded to completion through the reduction of $AlCl_3$ with lithium or sodium metal, respectively.

$$AlCl_3 + 3Li \rightarrow Al + 3LiCl \quad (1)$$

$$AlCl_3 + 3Na \rightarrow Al + 3NaCl \quad (2)$$

The reaction products are aluminium metal particles which are embedded within larger salt (LiCl or NaCl) clusters. The addition of a buffer material (i.e. LiCl) with the reactants allows for a medium which promotes nanoparticle formation and restricts the growth of large agglomerates of the desired aluminium phase by tempering combustion. Reactions (1) and (2) were both undertaken to determine their viability. Reaction (1) was initiated by milling with a ball-to-powder ratio (B:P) of 35:1 for 180 min using a LiCl buffer (25% mass of milled sample). Reaction (2) was initiated with a B:P of 55:1 for 280 min using a NaCl buffer (30% mass of milled sample). Both reactions proceeded to completion as verified by XRD shown in Fig. 1. There is a minor peak in the pattern for reaction (1) (containing LiCl) at $2\theta = 32.9°$ which has been attributed to lithium chloride hydrate ($LiCl{\cdot}H_2O$) which is most likely present due to an improper seal with the mylar film during XRD as LiCl is hygroscopic. Aluminium nanoparticles embedded within larger NaCl salt clusters are shown in the TEM micrographs in Fig. 2. Much larger aggregate structures of salt were found via TEM but isolated clusters were imaged for clarity. The aluminium particle size (while still embedded in NaCl) was determined via direct TEM imaging as ~40–50 nm.

The mechanochemically synthesised samples can be washed with a solvent capable of removing the salt by-product phase. Samples synthesised via reaction (1) which have a LiCl by-product (rather than NaCl) were more easily washed because of its preferred solubility in a wider range of solvents. However a large range of solvents (e.g. water, alcohol, acetone) are not suitable for washing salt from the aluminium nanoparticles because of aluminium's high reactivity which may result in the formation of surface layers such as aluminium oxide, hydroxide or oxy-hydroxide [17].

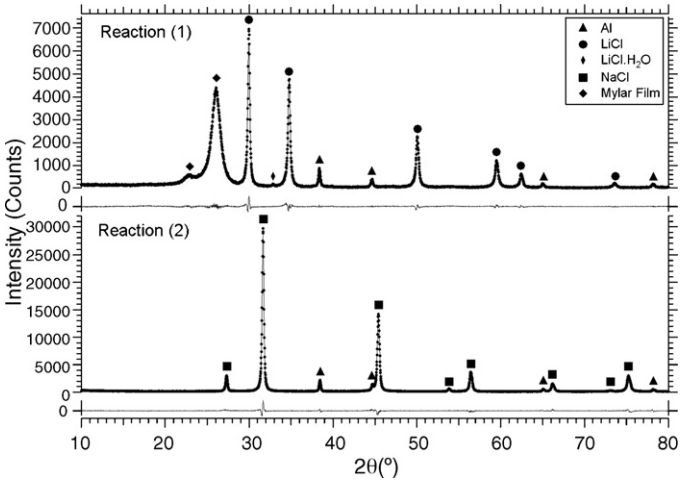

Fig. 1. X-ray diffraction (XRD) patterns for mechanochemically synthesised samples which were initiated via reactions (1) and (2) as given in the text. The patterns were collected after ball milling was complete and show that the reactions ran to completion. The XRD sample for reaction (2) was not sealed under a mylar film as it was air stable. Rietveld fitting results and calculated difference plots are also shown.

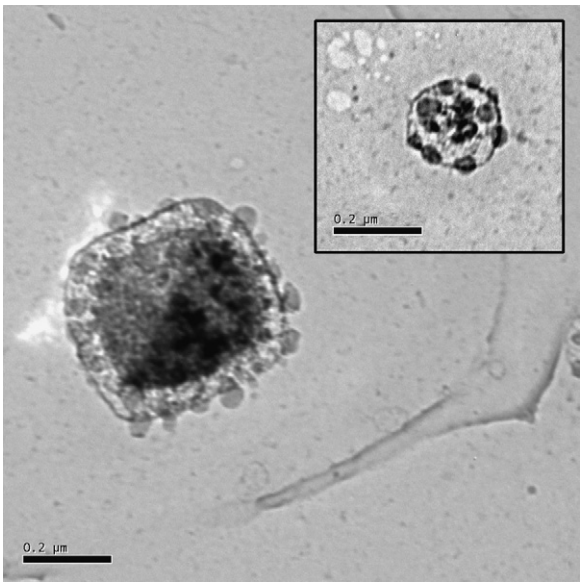

Fig. 2. Transmission electron microscope (TEM) micrographs of aluminium nanoparticles (40–50 nm) embedded within two different (200–500 nm) NaCl salt clusters. Elemental mapping was used to identify the smaller particles as aluminium and the larger matrix as salt. Both scale bars are 200 nm.

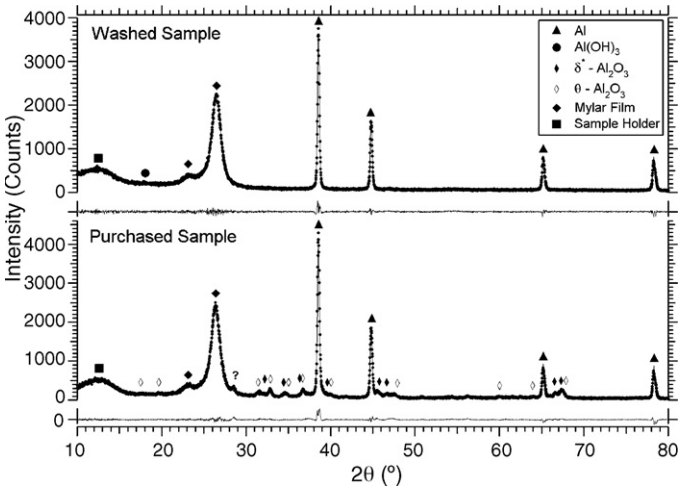

Fig. 3. X-ray diffraction (XRD) pattern for a washed mechanochemically synthesised sample (synthesised via reaction (1)), and for purchased aluminium nanoparticles (American Elements). The XRD pattern for the washed sample shows that the lithium chloride salt is completely removed after washing and only aluminium nanoparticles remain. The purchased aluminium nanoparticles show high quantities of aluminium oxide and there is also one unknown peak. Rietveld fitting results and calculated difference plots are also shown.

Nitromethane (Sigma–Aldrich, 96%) was used as the LiCl solvent because it was found to be relatively inert towards the aluminium nanoparticles, and had a low viscosity which made particle separation possible. However, in order to promote LiCl solubility in nitromethane, aluminium chloride was added in a 3:1 ratio of $AlCl_3$:LiCl because the presence of certain other salts in solution have been found to promote the solubility of LiCl in nitromethane [18]. A centrifuge was used to separate the solvent (containing the dissolved LiCl by-product phase) from the aluminium nanoparticle product before the saline solution was decanted. Washing was performed three times, twice with a nitromethane/$AlCl_3$ solution and once with pure nitromethane. The final aluminium product was put under vacuum at room temperature to remove residual traces of solvent to obtain pure aluminium nanoparticles.

XRD data is displayed in Fig. 3 for the Al/LiCl composite sample after washing with the nitromethane/$AlCl_3$ solution. After washing it is clear that all of the LiCl has been completely removed and that only Al remains. There is a very minor peak in the washed mechanochemically synthesised sample pattern at 17.95° which has been attributed to trace aluminium hydroxide $Al(OH)_3$ during Rietveld analysis, although the peak position is offset by 0.3° in 2θ which suggests that this may not be a positive match (which is made difficult due to the very low peak intensity). It is also possible that the peak at 17.95° is due to an amorphous hump present at ~18° from minor amounts of soft paraffin used to seal the mylar film during XRD analysis. There are no aluminium oxide (Al_2O_3) peaks present in the washed XRD pattern which suggests that there was no significant reaction between the solvent and the aluminium nanoparticles. The aluminium nanoparticles are therefore very pure and any oxide content is either amorphous or below the XRD resolution limit suggesting the nanoparticles possess relatively oxide-free clean surfaces. A low aluminium oxide content is beneficial for hydrogen storage where aluminium oxide surface layers can be detrimental to molecular [19] and even atomic [20] hydrogen permeation. Low oxide content is also beneficial for the pyrotechnic, propellant, and explosive industries where aluminium nanoparticles with thinner oxide layers are associated with higher reactivities [2]. An XRD pattern is also shown in Fig. 3 for the commercially available sample (American Elements) which shows a significant aluminium oxide content. Two Al_2O_3 phases were identified as δ^* [21] and θ because these phases provide the best match to the collected data as shown by the Rietveld fit in Fig. 3. However a single peak in the purchased sample pattern at 28.5° could not be indexed to any known aluminium oxide, hydroxide, or oxy-hydroxide phase and is an unknown sample component.

3.2. Measurement of Al particle size by XRD, TEM, and SAXS

All XRD patterns (in Figs. 1 and 3) were analysed using the Rietveld method. The results from the Rietveld analysis are shown in Table 1. The crystallite sizes from XRD and particle sizes from TEM cannot be directly compared because the XRD crystallite size is a volume weighted mean whereas the TEM particle size is a number weighted mean. However, the aluminium crystallite size from XRD is of the same order of magnitude as the particle size from TEM measurements which suggests that each nanoparticle consists of few individual crystallites. During Rietveld analysis it was assumed that the peak at $2\theta = 17.95°$ in the XRD pattern for the washed sample was $Al(OH)_3$ to determine its wt.% contribution to the washed sample assuming that this minor peak is indeed aluminium hydroxide and not soft paraffin. Assuming aluminium hydroxide, this phase was found to have a relatively low mass content with large uncertainties due to the very low intensity of the peak.

Table 1
Results of Rietveld analysis on XRD data. Mathematical uncertainties from the fitting process are also displayed.

	Phase	Wt.%	Crystallite size (nm)
Reaction (1) R_{wp} = 8.8%	Al	8.6 ± 0.1	38 ± 2
	LiCl	90.8 ± 0.1	110 ± 10
	$LiCl{\cdot}H_2O$	0.6 ± 0.1	70 ± 30
Reaction (2) R_{wp} = 6.6%	Al	6.0 ± 0.1	70 ± 2
	NaCl	94.0 ± 0.1	130 ± 5
Washed sample R_{wp} = 8.3%	Al	98.2 ± 0.6	56.5 ± 0.7
	$Al(OH)_3$	1.8 ± 0.6	30 ± 30
Purchased sample R_{wp} = 11.7%	Al	52.3 ± 0.6	46.5 ± 0.7
	δ^*-Al_2O_3	29.4 ± 0.6	11.5 ± 0.6
	θ-Al_2O_3	18.2 ± 0.7	17 ± 1.3

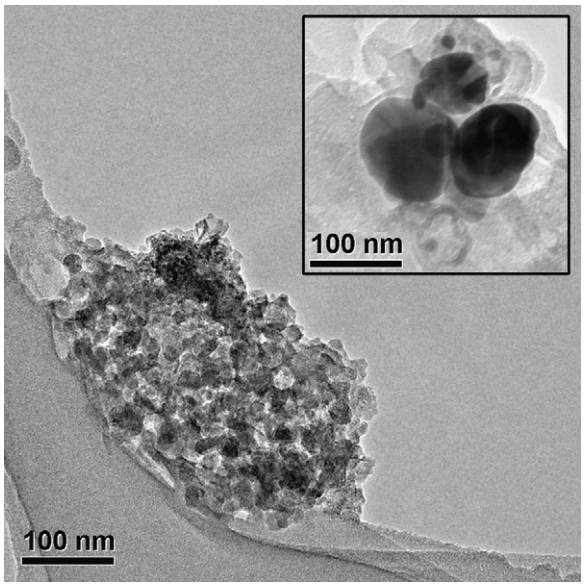

Fig. 4. Transmission electron microscope (TEM) micrographs of aluminium nanoparticles which have been washed with nitromethane to remove the LiCl salt by-product. An aggregate of ~25–40 nm aluminium particles is shown and larger ~100 nm aluminium particles are shown in the insert. Both scale bars are 100 nm.

The washed aluminium nanoparticles were also analysed via TEM to provide more information about the size and distribution of the pure nanoparticles. The TEM micrographs in Fig. 4 show a range of aluminium particles from ~25 to ~100 nm in size which exist in aggregate structures. The particles were identified as aluminium via energy dispersive spectroscopy (EDS) as shown in Fig. 5. TEM investigations revealed polydispersity of the aluminium particles which is most likely due to their formation during the mechanical milling procedure under varied conditions. Crystallite growth was also evidenced in the XRD results provided in Table 1 which show a 50% increase in the average aluminium crystallite size after washing. The salt buffer prevents Al particle growth by physical separation of the nanoparticles, but after the salt is removed via

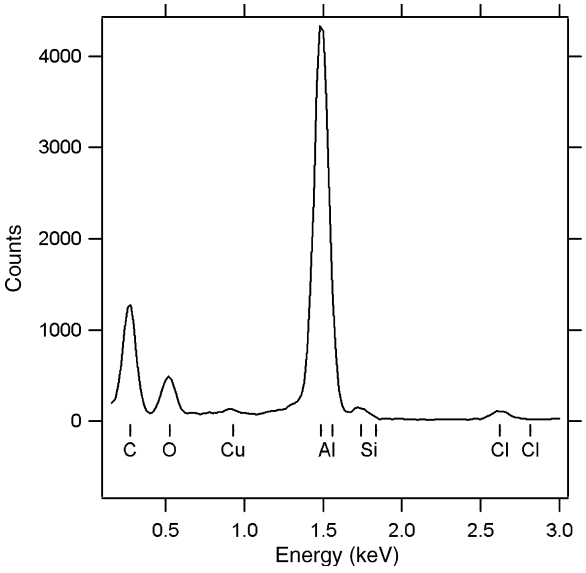

Fig. 5. A typical energy dispersive X-ray spectroscopy (EDS) spectra from TEM investigations of washed nanoparticles showing a high Al content, minor traces of Cl from residual LiCl, O from aluminium oxide due to sample air-exposure, and TEM grid components Cu, C, and Si.

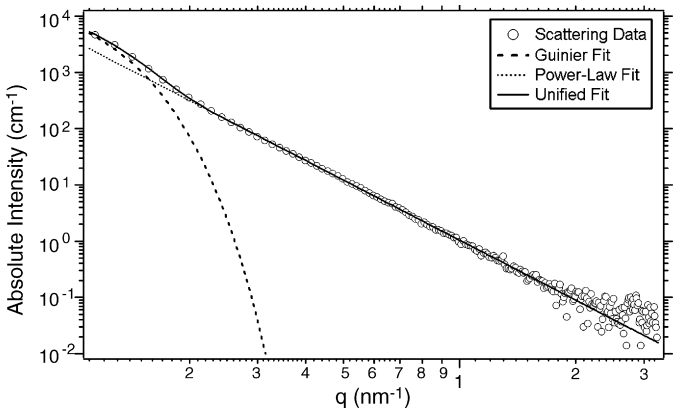

Fig. 6. Small angle X-ray scattering (SAXS) data from washed (LiCl removed) aluminium nanoparticles which are shown in TEM micrographs in Fig. 4. The result of a unified fit to the data is also displayed.

washing nanoparticles come into contact and particle agglomeration can occur.

SAXS data was collected for the washed nanoparticles as shown in Fig. 6 in order to provide more statistically significant structural information. A power law relationship between scattered intensity and the scattering vector q dominates the data set and there is a hump in the data set at low-q which has been attributed to a Guinier region generated by the average aluminium nanoparticle size. The data was modelled using the unified equation [22] with the Irena package [23] for Igor Pro (Wavemetrics, Oregon, USA). A unified fit was applied to the data resulting in a Guinier region at low-q with a radius of gyration R_g = 21.2 nm and a power law region with a slope of −3.55. It is reasonable to assume that the particles are roughly spherical from TEM investigations so that the radius of gyration can be related to the aluminium particle size via $R_g = \sqrt{3/5}r$ where r is the particle radius, resulting in an overall average particle size (diameter) of 55 nm which is in agreement with the average particle size via TEM investigations. The slope of the power law region (−3.55) at high-q is indicative of rough particle surfaces [24] which is expected from a sample which is synthesised via ball milling. Rough particle surfaces are also evidenced via TEM in Fig. 4. SAXS data was also collected for aluminium nanoparticles embedded in salt but the data only contained surface scattering information (a single power law over measured q-space) most likely due to the abundance of surface scattering from salt particles which masked the Guinier regime resulting from the size of the aluminium nanoparticles.

3.3. Deuterium absorption into Al nanoparticles

Deuterium absorption measurements were attempted on three different samples: Al nanoparticles embedded in NaCl, Al nanoparticles (washed from LiCl), and purchased Al nanoparticles (Meliorum). An overview of the absorption conditions is provided in Table 2. Al in NaCl underwent pressures of 1560 bar at room temperature and at 473 K with no measurable deuterium absorption. Al (washed) underwent pressures of 1917 bar at room temperature, 1958 bar at 423 K and up to 1875 bar at 77 K with no measurable deuterium absorption. Similarly, no deuterium absorption could be detected on the as purchased 10–22 nm (Meliorum) Al nanoparticles up to 1900 bar at room temperature. Although these pressures are still considered low compared to the 28 kbar and 573 K conditions required for hydrogen absorption into bulk aluminium [4,5], we can comment on several important features regarding successful potential hydrogen absorption into Al nanoparticles. Conditions of 28 kbar at 573 K in [4] were required to successfully absorb hydro-

Table 2
Overview of deuterium absorption conditions for the three samples tested as described in the text. No measurable absorption was observed for any samples at the conditions indicated.

Sample	Average particle size (nm)	Deuterium absorption conditions	
		Pressure (bar)	Temperature (K)
Al in NaCl	40–50	1560	298
		1560	473
Al (washed)	55	1875	77
		1917	298
		1958	423
Al (purchased)	10–22	1900	298

gen into very large ~150 μm Al powder particles, which were very likely significantly contaminated with oxygen due to handling in atmosphere. Al surfaces are poor at dissociating molecular hydrogen [25,26], and although oxidised AlH_3 powder has successfully prevented H release over a period of decades due to H impermeable surface layers of Al_2O_3 [27], the benefit of possessing small amounts of oxide at the AlH_3 surface remain unknown, and it is not clear if Al_2O_3 is better at dissociating molecular H_2 than pure Al surfaces. As our attempts to hydride Al nanoparticles below 2 kbar were unsuccessful, it is clear that no significant change in the thermodynamic properties compared to the bulk occurs, even at the 10 nm scale, assuming that other factors are favourable for hydrogen absorption at the temperatures studied. Both the absorption kinetics and hydrogen dissociation ability will be hindered at low temperatures, especially 77 K, which could mean that low temperature hydrogen absorption into pure aluminium is extremely slow and near undetectable under normal conditions. Recent theoretical investigations indicate that hydrogen absorption into bulk aluminium may be thermodynamically favourable at low temperatures where very low equilibrium pressures are predicted (7 kbar at 300 K [28] and 50 bar at 77 K [29]). It should be noted that the predicted 50 bar equilibrium pressure in [29] assumes that ΔH and ΔS are temperature independent which is a dubious assumption over a temperature range of 77–1000 K. If we assume that the predicted pressure of 50 bar is correct and compare it to the experimental hydrogen absorption attempt herein (1875 bar at 77 K) then an extreme kinetic barrier must be present given the significant overpressure produced experimentally.

As such, the only remaining option to hydride Al nanoparticles >10 nm in the 2 kbar pressure range, is to modify the Al surface to promote molecular H_2 dissociation. The recent addition of small amounts of transition metals such as Ti to $NaAlH_4$, has resulted in the formation of $Al_{1-x}Ti_x$ surface embedded phases which are efficient at dissociating molecular H_2 [30] which is also reflected by theoretical results [26]. A similar approach can be adopted for pure Al, and the investigation of transition metal enhanced Al nano particles may prove beneficial in the study of hydrogen absorption in the 2 kbar range. It is clear from theoretical predictions that hydrogen absorption would be most thermodynamically favourable at low temperatures and if the kinetic barriers can be overcome using catalysts then absorption at 77 K may be possible at modest pressures.

4. Conclusion

Pure Al nanoparticles have been synthesised via a mechanochemical method. XRD results indicate that the LiCl salt by-product from synthesis can be completely removed via washing with a nitromethane/$AlCl_3$ solution. TEM and SAXS results show that the nanoparticles are on average ~55 nm with particle polydispersity and a rough surface structure. XRD results also show that there is little or no oxide contamination which is beneficial for Al nanoparticle use in the propellant, pyrotechnic and explosives industries. Deuterium absorption measurements were unsuccessful at moderate pressures which indicates that pressures greater than 2 kbar are required to introduce hydrogen into pure Al nanoparticles greater than 10 nm in size at temperatures ranging from 77 to 473 K.

Acknowledgements

M. Paskevicius would like to thank the Australian government for the granting of Australian Post Graduate Awards with Stipend (APAWS), and the Australian Institute of Nuclear Science and Engineering (AINSE) for the granting of a postgraduate research award (PGRA). C.E. Buckley acknowledges the financial support of the Australian Research Council through REIF grant R00107962 2001, which enabled the SAXS studies to be undertaken. The authors acknowledge the facilities, scientific and technical assistance of the Australian Microscopy & Microanalysis Research Facility at the Centre for Microscopy, Characterisation & Analysis, The University of Western Australia, a facility funded by The University, State and Commonwealth Governments.

References

[1] P. Brousseau, C.J. Anderson, Prop. Explos., Pyrotech. 27 (2002) 300–306.
[2] Q.S.M. Kwok, R.C. Fouchard, A.-M. Turcotte, P.D. Lightfoot, R. Bowes, D.E.G. Jones, Prop. Explos., Pyrotech. 27 (2002) 229–240.
[3] A. Rai, K. Park, L. Zhou, M.R. Zachariah, Combust. Theory Model. 10 (2006) 843–859.
[4] B. Baranowski, M.Z. Tkacz, Phys. Chem. 135 (1983) 27–38.
[5] S.K. Konovalov, B.M. Bulychev, Inorg. Chem. 34 (1995) 172–175.
[6] G.C. Sinke, L.C. Walker, F.L. Oetting, D.R. Stull, J. Chem. Phys. 47 (1967) 2759–2761.
[7] J.K. Johnson, D.S. Sholl, 2008 US DOE Annual Merit Review Proceedings, http://www.hydrogen.energy.gov/pdfs/review08/st_33_johnson.pdf.
[8] J. Ding, T. Tsuzuki, P.G. McCormick, R. Street, J. Alloys Compd. 234 (1996) L1–L3.
[9] C. Suryanarayana, Prog. Mater. Sci. 46 (2001) 1–184.
[10] P.G. McCormick, J. Ding, W.-F. Miao, R. Street, *US Patent* 6,203,768, 20 March 2001.
[11] T. Tsuzuki, P.G. McCormick, J. Mater. Sci. 39 (2004) 5143–5146.
[12] A.A. Coelho, Topas User Manual, Bruker AXS GmbH, Karlsruhe, Germany, 2003.
[13] O. Spalla, S. Lyonnard, F. Testard, J. Appl. Crystallogr. 36 (2003) 338–347.
[14] H. Hemmes, A. Driessen, R. Griessen, J. Phys. C: Solid State Phys. 19 (1986) 3571–3585.
[15] K.G. McLennan, E. MacA. Gray, Meas. Sci. Technol. 15 (2004) 211–215.
[16] E.W. Lemmon, M.O. McLinden, D.G. Friend, in: P.J. Linstrom, W.G. Mallard (Eds.), NIST Standard Reference Database Number 69, National Institute of Standards and Technology, Gaithersburg, MD, 2005, p. 20899.
[17] A. Ramaswamy, P. Kaste, J. Energetic Mat. 23 (2005) 1–25.
[18] H.V.A. Briscoe, A.A. Eldridge, G.M. Dyson, A.J.E. Welch (Eds.), Mellor's Comprehensive Treatise on Inorganic and Theoretical Chemistry, Longman Group Limited, London, 1972.
[19] J.L. Maienschein, R.G. Musket, F.E. McMurphy, D.W. Brown, Appl. Phys. Lett. 50 (1987) 940–942.
[20] Y. Yamada-Takamura, F. Koch, H. Maier, H. Bolt, Surf. Coat. Technol. 153 (2002) 114–118.
[21] D. Fargeot, D. Mercurio, A. Dauger, Mater. Chem. Phys. 24 (1990) 299–314.
[22] G. Beaucage, D.W. Schaefer, J. Non-Cryst. Solids 172–174 (1994) 797–805.
[23] J. Ilavsky, P.R. Jemian, J. Appl. Crystallogr. 42 (2009) 347–353.
[24] P.W. Schmidt, in: H. Brumberger (Ed.), Modern Aspects of Small-Angle Scattering, Kluwer Academic Publishers, Netherlands, 1995, pp. 1–56.
[25] R.I. Masel, Principles of Adsorption and Reaction on Solid Surfaces, Wiley–Interscience, New York, 1996.
[26] S. Chaudhuri, J.T. Muckerman, J. Phys. Chem. B 109 (2005) 6952–6957.
[27] G. Sandrock, J. Reilly, J. Graetz, W.M. Zhou, J. Johnson, Wegrzyn, J. Appl. Phys. A: Mat. Sci. Proc. 80 (2005) 687–690.
[28] J. Graetz, S. Chaudhuri, Y. Lee, T. Vogt, J.T. Muckerman, J.J. Reilly, Phys. Rev. B 74 (2006) 1–7 (214114).
[29] J. Graetz, Chem. Soc. Rev. 38 (2009) 73–82.
[30] J.M.B. von Colbe, W. Schmidt, M. Felderhoff, B. Bogdanović, F. Schüth, Angew. Chem. 45 (2006) 3663–3665.

Journal of Alloys and Compounds 487 (2009) 370–376

Contents lists available at ScienceDirect

Journal of Alloys and Compounds

journal homepage: www.elsevier.com/locate/jallcom

Characterisation of mechanochemically synthesised alane (AlH_3) nanoparticles

M. Paskevicius, D.A. Sheppard, C.E. Buckley*

Department of Imaging and Applied Physics, Curtin University of Technology, GPO Box U 1987, Perth, WA, Australia

ARTICLE INFO

Article history:
Received 15 May 2009
Received in revised form 23 July 2009
Accepted 23 July 2009
Available online 30 July 2009

Keywords:
Amorphous materials
Hydrogen storage materials
Nanostructures
Mechanochemical synthesis
X-ray diffraction

ABSTRACT

A mechanochemical synthesis process has been used to synthesise alane (AlH_3) nanoparticles. The alane is synthesised via a chemical reaction between lithium alanate ($LiAlH_4$) and aluminium chloride ($AlCl_3$) at room temperature within a ball mill and at 77 K within a cryogenic mill. The reaction product formed consists of alane nanoparticles embedded within a lithium chloride (LiCl) by-product phase. The LiCl is washed with a solvent resulting in alane nanoparticles which are separated from the by-product phase but are kinetically stabilised by an amorphous particle surface layer. The synthesis of a particular alane structural phase is largely dependent on the milling conditions and two major phases (α, α') as well as two minor phases (β, γ) have been identified. Ball milling at room temperature can also provide enough energy to allow alane to release hydrogen gas and form aluminium metal nanoparticles. A comparison between XRD and hydrogen desorption results suggest a non-crystalline AlH_3 phase is present in the synthesised samples.

1. Introduction

Alane is a metal hydride with a high 10.1 wt.% gravimetric hydrogen capacity. It was first synthesised in a pure form in 1947 [1], but despite its usefulness in a number of industries it has not become widely available primarily due to difficulties in large-scale wet chemical synthesis [2]. Alane has potential applications in the fields of hydrogen storage, chemical catalysis, explosives, propellants and pyrotechnics. As such a number of recent studies have focussed on investigating AlH_3 structural and hydrogen sorption properties. Three of the AlH_3 crystal structures were only recently solved [3–5] even though they had been known to exist for over 30 years [6]. A number of studies have also been undertaken to investigate the kinetics of decomposition of AlH_3 [7,8] including the effect of dopants and/or particle size on the kinetics [9,10].

Traditionally bulk quantities of alane were primarily synthesised via a wet chemical process [6], however the formation of AlH_3 from its elements has also been undertaken under high hydrogen pressure (~2.5 GPa) [11,12]. In the last few years certain novel experimental techniques have been used to synthesise AlH_3 including electrochemical charging [13], supercritical fluid hydrogenation [14], and a range of AlH_3 adducts have been formed which were found to be reversible under much milder hydrogen pressures [15]. The wet chemical process used for alane production involves the synthesis of an alane-ether complex within a solvent (usually diethyl ether) as follows [7]:

$$AlCl_3 + 3LiAlH_4 + n[(C_2H_5)_2O] \rightarrow 4AlH_3 \cdot 1.2[(C_2H_5)_2O] + 3LiCl \quad (1)$$

The wet chemical synthesis of AlH_3 is very sensitive to both temperature and time [7] and as such large-scale production and structural phase selection via this method is very difficult. There are seven structural phases (α, α', β, γ, δ, ε, ζ) which have been synthesised from the wet chemical method under various temperature, pressure and reaction conditions during the ether removal [6]. A mechanochemical synthesis method for alane has been performed previously in the literature [3] which involves the mechanical initiation of the following reaction:

$$AlCl_3 + 3LiAlH_4 \rightarrow 4AlH_3 + 3LiCl \quad \begin{matrix}\Delta_r G_{298\,K} = -191\ kJ/mol \\ \Delta_r G_{77\,K} = -158\ kJ/mol\end{matrix} \quad (2)$$

The reaction progresses both at room temperature and at 77 K due to the relatively high change in Gibbs free energies. Brinks et al. [3] surmised that room temperature synthesis was inefficient in synthesising AlH_3 due to the low alane yields and high Al content. Aluminium forms due to the high milling energy at room temperature which allows for AlH_3 to decompose to Al and H_2. As a result, cryogenic milling is the preferred synthesis method in synthesising AlH_3 because low temperatures maintain lower milling temperatures, restricting AlH_3 decomposition. In the present work, room temperature milling was attempted under a variety of milling conditions (ball size, ball to powder ratio, and time) to explore its usefulness in the synthesis of a variety of alane structural phases and in minimising the aluminium content. Cryomilling at 77 K was also undertaken in order to provide a comparison of synthesis techniques, and a washing

* Corresponding author. Tel.: +61 8 92663532; fax: +61 8 92662377.
E-mail address: C.Buckley@curtin.edu.au (C.E. Buckley).

0925-8388/$ – see front matter © 2009 Elsevier B.V. All rights reserved.
doi:10.1016/j.jallcom.2009.07.124

procedure was utilised to remove the salt by-product from the AlH_3 nanoparticles.

Mechanochemical synthesis differs from standard ball milling. A standard ball milling process results in a reduction in the particle size of a sample and eventually the formation of nanosized grains within micron-sized particles [16]. However the mechanochemical method involves the initiation of a solid-state displacement reaction during the ball milling process [16] which can result in nanosized particles (down to 4 nm in size [17]) embedded within larger by-product phase particles. Mechanical milling is utilised in the mechanochemical synthesis of nanoparticles because it effectively blends the reactants, forming nanoscale mixtures and increases the chemical reactivity (and also the reaction kinetics) leading to a chemical reaction between these reactants enabling the product phase to form [18]. The mechanochemical synthesis process has been used in the past [19,20] to synthesise a broad range of metal nanoparticles as well as other compounds such as oxides and sulphides.

Particle size control can be gained by adjusting such factors as: the volume fraction of the by-product phase formed during milling, milling time, milling collision energy (ball-to-powder mass ratio and ball size) [18], milling temperature, and the use of process control agents [20]. The addition of a buffer material (i.e. LiCl) was utilised in the present work in order to promote nanoparticle formation and restricts the growth of large agglomerates of the desired product phase. The removal of the salt by-product phase was also undertaken and changes regarding AlH_3 decomposition behaviour in washed samples were investigated.

2. Experimental

All handling of chemicals and sealable milling vials was undertaken in an argon-atmosphere glovebox in order to minimise oxygen (O_2 < 5 ppm) and water (H_2O < 3 ppm) contamination. All samples were analysed as close to synthesis as possible in order to prevent sample degradation, during storage, from affecting results. $LiAlH_4$ (Sigma–Aldrich, 95%), $AlCl_3$ (Sigma–Aldrich, 99%), and LiCl (Sigma–Aldrich, ≥99%) were used as starting reagents. Room temperature ball milling was performed with a custom made ball milling canister (650 cm^3 internal volume) attached to a Glen Mills Turbula T2C shaker mixer. The ball milling canister was made from stainless steel (316) and was sealed with an o-ring on both ends. The balls were made from the same material as the canister to minimise sample contamination due to the degradation of both the canister and balls. Cryogenic (77 K) milling was undertaken using a Spex 6850 freezer mill with both a supplied 190 cm^3 milling vial and a custom made [21] 14.3 cm^3 milling vial, using 145.5 g and 32 g milling rods, respectively. Samples were milled with a LiCl buffer which was added to the initial reagents prior to milling to deter agglomeration and promote nanoparticle production. Milling parameters (such as ball size and milling time) were altered to explore the variety of reaction products.

The selection of an appropriate solvent is a crucial part of the synthesis process as the solvent must firstly be able to dissolve large quantities of the by-product phase (LiCl), it must be relatively unreactive to the alane nanoparticles, and it must also have a low viscosity so that it may be separated from the nanoparticles once it has dissolved the by-product phase. Solvent choice is made very difficult because alane is a powerful reducing agent and as such is very reactive with a range of solvents including a variety from the following groups: alcohols, phenols, amines, thiols, aldehydes, ketones, quinones, carboxylic acids, esters and lactones, epoxides, amides and nitriles, and some nitrogen and sulfur compounds [22]. Alane also dissolves in certain solvents which dissolve LiCl such as tetrahydrofuran (THF). However it has been found [22] that some nitro compounds and some sulfur compounds are relatively inert to alane. As such, nitromethane (Sigma–Aldrich, 96%) was used as the LiCl solvent. However in order to promote LiCl solubility in nitromethane, aluminium chloride was added in a 3:1 ratio of $AlCl_3$:LiCl because the presence of certain other salts in solution have been found to promote the LiCl solubility in nitromethane [23].

Centrifugation was used to separate the solvent (containing the dissolved LiCl by-product phase) from the alane nanoparticle product, and the saline solution was decanted. Washing was performed three times, twice with a nitromethane/$AlCl_3$ mix and once with pure nitromethane. Room temperature milled AlH_3 samples did not present any visible signs of reaction with the solvent however noticeable gas evolution was present on addition of the cryogenically milled samples to the nitromethane/$AlCl_3$ solution. The gas evolution indicates an adverse reaction between the solvent and cryogenically milled sample. This is an indication that either the cryogenically milled alane is more reactive, or that a reaction between nitromethane and the $LiAlH_4$ starting reagent was observed due to the reaction of the cryogenically milled sample not reaching completion. It should be noted that $LiAlH_4$ is violently reactive with nitromethane and significant quantities of heat and fumes are generated upon contact with one another, even in dilute concentrations. Given the mild reaction between the solvent and the cryogenically milled sample it is unlikely that $LiAlH_4$ is present. As such a different solvent should be utilised in further studies in order to synthesise pure unreacted AlH_3 nanoparticles. Despite the observed reaction in cryogenically milled samples, the as-synthesised and washed alane samples were characterised to determine their hydrogen desorption kinetics and structural properties. The final washed alane product was put under vacuum for a few hours at room temperature to remove any final traces of solvent to obtain salt-free alane nanoparticles.

X-ray diffraction (XRD) was performed using a Siemens D500 diffractometer (CuK_α radiation) with a 2θ range of 10–80° using 0.02° steps with 3 s of count time per step with operating conditions of 40 kV and 30 mA. XRD was also undertaken on a Bruker D8 Advance diffractometer (CuK_α radiation) with a 2θ range of 10–100° using 0.02° steps with 0.8 s of count time per step with operating conditions of 40 kV and 40 mA. Samples were loaded into XRD sample holders in an argon glovebox and either sealed under a 4 μm mylar film or sealed within a poly(methylmethacrylate) (PMMA) air-tight holder to prevent oxygen/moisture contamination during data collection. The protective holders generate large amorphous humps in the data sets which were removed from the included figures for clarity via peak fitting in Topas (Bruker AXS, Karlsruhe, Germany). The background subtraction resulted in certain angular regions with increased noise content. Rietveld analysis was performed on the XRD patterns using Topas in order to provide additional structural information from the crystalline phases in the washed and unwashed samples. The crystallite sizes were determined from an LVol-IB method (volume averaged column height calculated from the integral breadth) [24] which provides a good measure of the volume-weighted average crystallite size.

Transmission electron microscopy (TEM) was conducted on a JEOL JEM2011 instrument operating at 200 kV which was coupled with an Oxford Instruments energy dispersive X-ray spectrometer (EDS) for elemental analysis. Samples were loaded onto 200 mesh copper grids with holey carbon support films drop-wise via suspension in either nitromethane or toluene. The TEM grids contain minor traces of silicon resulting from the manufacturing process. Samples must be exposed to air before being loaded into the TEM column; however air-exposure time was kept as short as possible.

Hydrogen sorption experiments were performed in a manometric apparatus using the Hemmes equation of state [25] and the method of McLennan and Gray [26] to account for the compressibility of hydrogen. The digital pressure gauge (Rosemount 3051S) had a precision of 14 mbar and accuracy of 6 mbar, whilst room temperature measurements were recorded using a 4-wire platinum resistance temperature detector (RTD). Non-ambient sample temperatures were generated using a sealed tube furnace which was externally calibrated to ±1 °C.

3. Results and discussion

Aluminium hydride (AlH_3) has been reported to be stable in air for decades at room temperature due to its heavy oxide coating [9], however freshly mechanochemically synthesised alane is unstable due to its clean oxide-free surface, which does not significantly kinetically restrict decomposition. Alane is prone to decomposition as a result of its thermodynamic properties because ΔG of formation is positive at-temperatures greater than approximately −200 °C (when extrapolated from experimental data [27]). Theoretical calculations [28] suggest that ΔG of formation is positive (for the AlH_3 phases investigated) at all temperatures, and as such decomposition may occur spontaneously. Mechanochemically synthesised samples exhibit relatively rapid decomposition at room temperature (significantly over months) when stored under an argon atmosphere. The decomposition is evidenced by XRD data provided in Fig. 1, which displays a significant reduction in the AlH_3 content over 1 month, matched by an increase in the Al content of the sample when stored at ∼25 °C.

Quantitative phase analysis (QPA) results (see Table 1) outline the decomposition of the mechanochemically synthesised alane sample over time. After 1 month the alane content has been reduced to 73% of its as-synthesised content, increasing the aluminium content significantly. LiCl content does not change over time, although some $LiCl{\cdot}H_2O$ is present in the aged sample due to an improper seal with the mylar film during data collection. The α′-AlH_3 phase decreased by 20.3% whereas the α-AlH_3 phase decreased by 31.9% over 1 month.

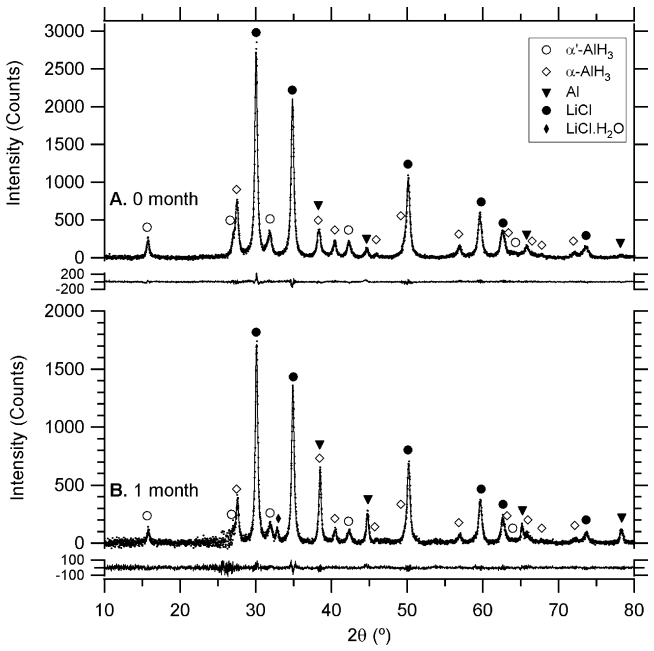

Fig. 1. X-ray diffraction (XRD) patterns from mechanochemically synthesised alane undertaken cryogenically (77 K) with no buffer, which is shown to decompose significantly over time. The patterns are background subtracted for clarity. Rietveld fits to the data are also displayed (solid line) along with difference plots.

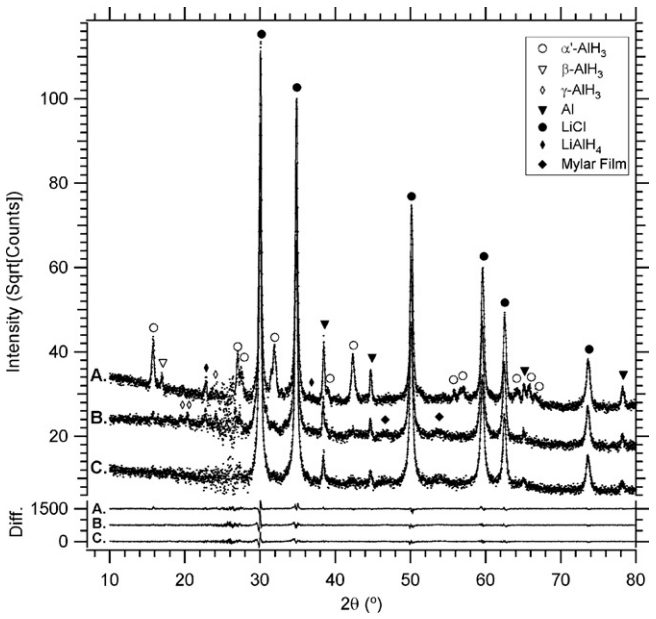

Fig. 2. X-ray diffraction patterns from mechanochemically synthesised alane undertaken at room temperature with a 2.2:1 LiCl:AlH_3 volume ratio for (A) 2 h, (B) 4 h, and (C) 6 h. The patterns are mylar subtracted, offset and the square root of intensity is displayed for clarity, however a high-noise region exists due to the subtraction of a large mylar hump. Rietveld fits to the data are also displayed (solid line) along with difference plots.

The disproportionate decomposition indicates that α-AlH_3 decomposes more readily at room temperature, provided that α-AlH_3 does not undergo a phase transition to α′-AlH_3 during this time. The result is curious because α-AlH_3 is reported to be the most stable alane phase [9] as both β- and γ-AlH_3 were shown to transition to α-AlH_3 before decomposition evidenced by calorimetry [29] and in-situ XRD [30,31]. The calorimetry results discount the possibility of an α-AlH_3 → α′-AlH_3 phase transition as no thermodynamic transitions were found during α-AlH_3 decomposition [29]. In fact, experimental and theoretical results [32] demonstrate that the opposite reaction can occur where α′-AlH_3 → α-AlH_3 if conditions are both kinetically and thermodynamically favourable. Therefore the disproportionate decomposition instead suggests a more rapid α-AlH_3 decomposition at room temperature in comparison to α′-AlH_3. In the literature α-AlH_3 is the phase which is synthesised reversibly via the reaction of hydrogen gas with aluminium at extreme pressures [12,33]. The preferred formation may be due to α-AlH_3 having the most compact crystal structure, but the XRD results herein indicate that α′-AlH_3 is more stable over time at room temperature. In addition theoretical results also show [34] that α′-AlH_3 is more stable than α-AlH_3 in regards to the thermodynamics of decomposition. It is not known if the α′-AlH_3 stability (seen at room temperature herein) is a function of either kinetic or thermodynamic factors. The stability over time does not seem to be related to crystallite size as the average crystallite size of α-AlH_3 was found via Rietveld to be 15.0 ± 0.5 nm and 19 ± 1 nm for the 0 month and 1 month samples respectively whilst the average crystallite size was 17.0 ± 0.6 nm and 17 ± 1 nm for α′-AlH_3 in the 0 month and 1 month samples, respectively. The crystallite sizes are comparable between both phases however it is possible that particle size differences between the phases could lead to different decomposition rates. It is also possible that any phase transformations to or from amorphous phases could bias these crystalline phase results obtained using QPA by the Rietveld method.

Table 1
Crystalline QPA results from Rietveld fits to XRD data given in Fig. 1. Mathematical fitting uncertainties of one standard deviation are provided.

	Phase	Crystalline (wt.%)	Crystallite size (nm)
0 Month	α′-AlH_3	14.8 ± 0.2	16.1 ± 0.6
	α-AlH_3	19.1 ± 0.3	15.0 ± 0.4
	Al	3.6 ± 0.1	18.0 ± 1.2
	LiCl	62.5 ± 0.3	27.5 ± 1.0
1 Month	α′-AlH_3	11.8 ± 0.3	15.6 ± 1.0
	α-AlH_3	13.0 ± 0.3	23.8 ± 1.2
	Al	13.4 ± 0.2	30.0 ± 0.9
	LiCl	59.4 ± 0.4	25.4 ± 1.0
	LiCl·H_2O	2.3 ± 0.2	18.8 ± 10.2

3.1. Room temperature synthesis

Room temperature mechanochemical synthesis is reported to produce low alane yields [3] due to the decomposition of AlH_3 to Al and H_2 resulting from the energy provided during milling. Room temperature ball milling was undertaken under a variety of milling conditions in order to understand the impact of these conditions on AlH_3 yields and phase production. Initially room temperature milling was undertaken using a mixture of 12.7 mm and 7.938 mm balls with a 39:1 ball to powder ratio (B:P) and a LiCl buffer was used to provide a 2.2:1 volume ratio of LiCl:AlH_3 in the final product. However it was determined via XRD that more than 50% of the synthesised AlH_3 had decomposed to Al during just 1 h of milling. The rapid decomposition is a result of the significant energy provided during milling from the large balls. As a result room temperature milling was undertaken using 4 mm balls in a smaller 13:1 B:P ratio in order to lower the milling energy and reduce the decomposition of the as-synthesised AlH_3. XRD was undertaken after milling for 2, 4, and 6 h as provided in Fig. 2.

QPA results (see Table 2) outline the crystalline sample composition as a function of milling time. Crystalline α′-AlH_3 is present in moderate quantities in the sample milled for 2 h (Fig. 2A), however the alane content is reduced almost to zero in samples which were milled for longer (Fig. 2B and C). Minor trace phases of both β-AlH_3 and γ-AlH_3 are noted in some XRD patterns (Fig. 2A and B),

Table 2
Crystalline QPA results from Rietveld fits for the 2 h, 4 h, and 6 h room temperature milled sample XRD patterns given in Fig. 2. Mathematical fitting uncertainties of one standard deviation are provided. Some crystallite sizes are not included due to the very low phase wt.% which makes results unreliable.

	Phase	Crystalline (wt.%)	Crystallite size (nm)
2 h	α′-AlH_3	12.0 ± 0.1	36.9 ± 1.6
	β-AlH_3	0.7 ± 0.1	–
	Al	3.7 ± 0.1	64.6 ± 4.3
	LiCl	81.7 ± 0.3	407.4 ± 83.6
	$LiAlH_4$	1.9 ± 0.3	–
4 h	α′-AlH_3	0.7 ± 0.1	–
	γ-AlH_3	2.6 ± 0.2	58.7 ± 16.5
	Al	2.2 ± 0.1	71.5 ± 9.9
	LiCl	92.0 ± 0.4	130.0 ± 10.6
	$LiAlH_4$	2.4 ± 0.4	–
6 h	α′-AlH_3	0.4 ± 0.1	–
	Al	2.0 ± 0.1	43.2 ± 5.2
	LiCl	97.5 ± 0.1	65.3 ± 3.2

which indicate that alane phase transformations are occurring during milling. Despite the very low crystalline AlH_3 content in the 6 h milled sample, given by XRD (Fig. 2C), hydrogen sorption measurements indicate that the sample contains a considerable portion of AlH_3. The 6 h as-milled sample was incrementally ramped to 150 °C over 120 h and desorbed a quantity of hydrogen that equates to a 8.1 wt.% AlH_3 content in the entire synthesised sample (from a theoretical maximum of 24.6 wt.%). This desorption result in conjunction with the decline in crystalline Al and AlH_3 content with increasing milling time indicates that there is non-crystalline Al and AlH_3 present in the sample after milling at room temperature with small 4 mm balls. It may also be possible that the as-synthesised AlH_3 is so nanoscopic that some XRD peaks are hidden under the background noise. To the authors' knowledge non-crystalline AlH_3 has not been previously reported in the literature. Theoretical investigations have suggested the possibility of crystalline AlH_3 phases existing in real samples which have not been identified experimentally to date [28]. However, given that no unidentified crystalline peaks are present in the XRD patterns it is unlikely that these phases exist in the samples herein.

TEM investigations of the room temperature synthesised alane nanoparticles were performed whilst they were still embedded in salt and after they had been washed with nitromethane and $AlCl_3$ (to remove the LiCl by-product phase). The micrograph provided in Fig. 3A illustrates alane nanoparticles (~100 nm) embedded within larger (~400 nm) salt clusters. It can be seen in Fig. 3B that the alane nanoparticles decompose under the electron beam after a short time (2 min) resulting in a decrease in particle size. After samples were washed (removing LiCl) two distinct particle morphologies existed: Large geometric-shaped single crystals as shown in Fig. 3C and clusters of small irregularly shaped crystals as shown in Fig. 3D. The large crystal in Fig. 3C was identified as a LiCl single crystal via electron diffraction. Given that the LiCl phase is not detectable using lab-based XRD, its presence only in TEM investigations suggests that it is a minor sample component that is a remnant from

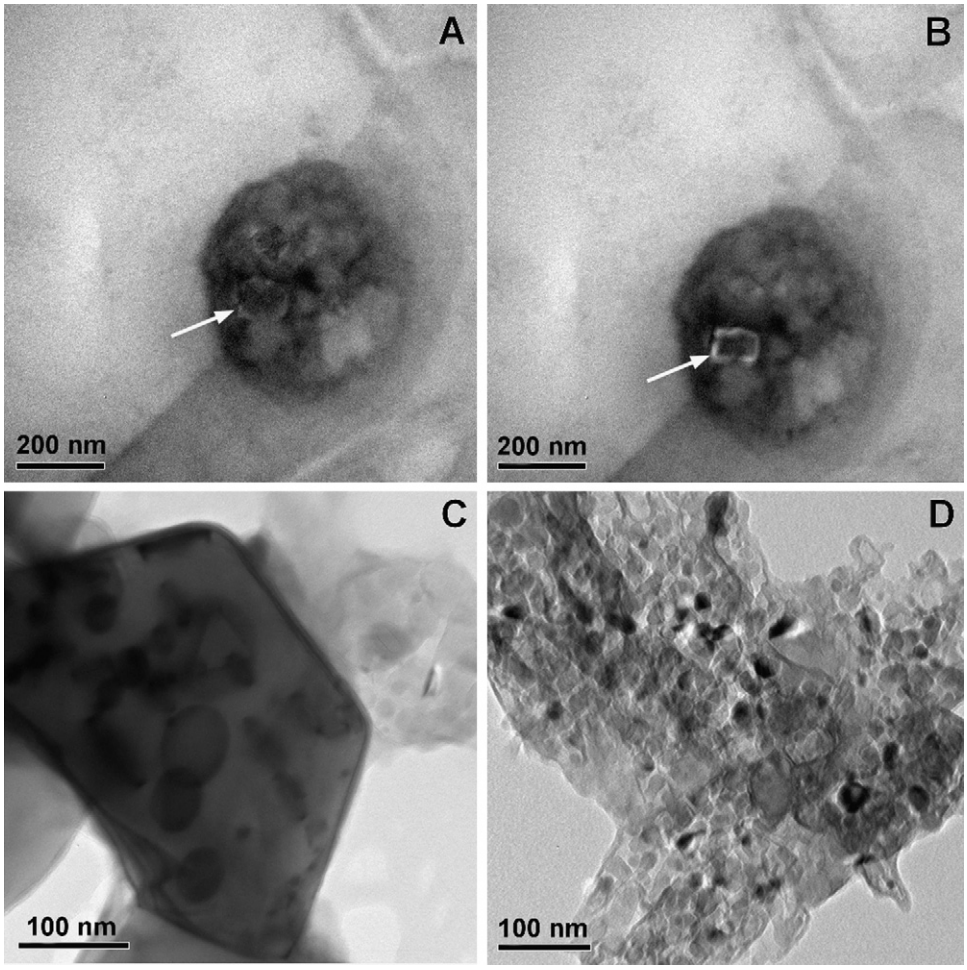

Fig. 3. TEM micrographs of as-milled samples which display (A) AlH_3 nanoparticles embedded in a larger LiCl salt cluster initially and (B) after 2 min under the beam. Washed samples show (C) low quantities of LiCl crystals and predominantly (D) small 30–50 nm Al/AlH_3 particles in aggregate clusters. White arrows depict the AlH_3 particle which decreased in size over time.

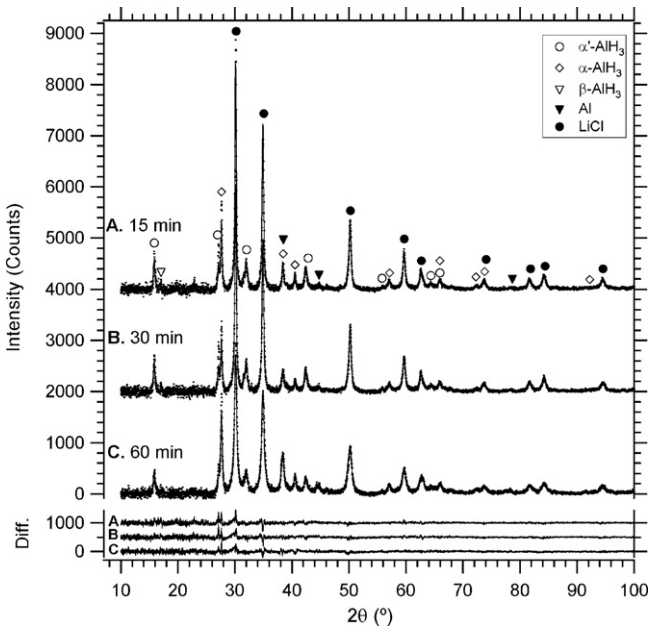

Fig. 4. X-ray diffraction (XRD) patterns from mechanochemically synthesised alane undertaken cryogenically with a 0.76:1 LiCl:AlH_3 final volume ratio, which were milled for (A) 15 min, (B) 30 min and (C) 60 min. Patterns have been background subtracted and offset for clarity. Rietveld fits to the data are also displayed (solid line) along with difference plots.

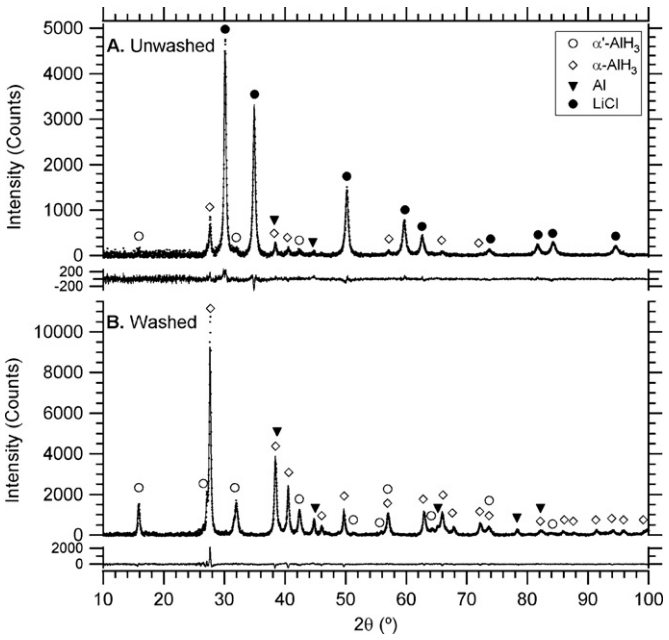

Fig. 5. X-ray diffraction (XRD) patterns for cryogenically synthesised alane milled for 1 h with a 2:1 LiCl:AlH_3 volume ratio (A) before and (B) after washing with nitromethane and $AlCl_3$. Patterns have been background subtracted for clarity. Rietveld fits to the data are also displayed (solid line) along with difference plots.

the washing process. The washed sample primarily consisted of the smaller crystals shown in Fig. 3D, which were identified as Al-rich via energy dispersive X-ray spectroscopy (EDS) during TEM investigations, indicating that these crystals are either AlH_3 or Al (resulting from alane decomposition). The washed AlH_3/Al nanoparticles in Fig. 3D are aggregated together but consist of 30–50 nm particles which appear similar to TEM micrographs of dehydrided α-AlH_3 particles recently presented in the literature [35], although those herein seem to be clusters of separate particles rather than large particles with internal structure.

3.2. Cryogenic synthesis

Cryogenic (77 K) milling provides high alane yields (low Al content) due to the low milling temperatures, which minimises the decomposition of alane in contrast to room temperature milling [3]. XRD was utilised to analyse samples that were cryogenically milled for increasing times without the use of a reaction buffer material as shown in Fig. 4. XRD data after milling for 1 min (not included here) indicates only starting reagents ($AlCl_3$, $LiAlH_4$, and LiCl) are present. For samples milled for 15 min or longer no starting reagents are detected and AlH_3 and LiCl are the only crystalline phases present. The XRD data shows that samples milled for 15 min and 30 min have both α′-AlH_3 and α-AlH_3 phases in similar ratios, however for the sample milled for 60 min the α-AlH_3 phase is dominant. QPA results indicate that the Al wt.% is 3.0, 5.0, and 11.9 ± 0.3 for the 15 min, 30 min, and 60 min samples, respectively. Thus longer milling times result in higher Al yields due to the longer times in which AlH_3 is exposed to high energy milling. However the Al content in cryogenically synthesised samples is much lower than those measured in room temperature synthesised samples, indicating that the low milling temperatures do restrict AlH_3 decomposition and prevent high Al yields.

In order to promote nanoparticle formation, samples were cryogenically milled for 60 min with a large quantity of reaction buffer (2:1 LiCl:AlH_3 volume ratio). XRD results are provided in Fig. 5A for the as-milled sample, which show a high α-AlH_3 yield with minor α′-AlH_3 and Al phases as well as the LiCl reaction by-product phase. The result is similar to the reaction undertaken cryogenically with no reaction buffer where high α-AlH_3 yields are encountered with some Al decomposition product present. A sample of as-milled powder was washed using nitromethane and $AlCl_3$ to remove the LiCl by-product phase. However noticeable gas evolution was apparent upon addition of the sample to the nitromethane/$AlCl_3$ solution during washing indicating that a reaction between the AlH_3 and the solution occurred. Gas evolution was not noticeable when washing mechanochemically synthesised pure Al nanoparticles [36] indicating that cryogenically synthesised alane is much more reactive than Al even though gas evolution from alane would be more noticeable due to its internal hydrogen supply. Even though a reaction with the solvent was noted, XRD of the washed sample as shown in Fig. 5B does not show any unwanted crystalline reaction products. The only crystalline phases present in the washed sample are α′-AlH_3, α-AlH_3, and Al.

Hydrogen desorption experiments were undertaken within 1 week of sample synthesis and/or washing to ensure room temperature alane decomposition was minimised. Both unwashed (as-milled) and washed samples of cryogenically synthesised alane (2:1 LiCl:AlH_3 volume ratio) were loaded into a manometric hydrogen sorption apparatus and initially evacuated at room temperature for 30 min. The samples were then raised to 50 °C and held at this temperature for 24 h, followed by 24 h at 100 °C and then 150 °C respectively in order to examine the kinetic behaviour and maximum desorbed wt.% of the samples. Hydrogen desorption data is displayed in Fig. 6 which depicts the wt.% of H_2 as a function of time in the calculated non-salt portions of the unwashed and washed samples. This relates to the percentage of hydrogen desorbed from the Al/AlH_3 portions of the samples (26.43% and 100% of the unwashed and washed samples, respectively).

Alane is thermodynamically unstable over a large temperature range and its decomposition is in fact only kinetically limited. Kinetic barriers are crucial in stabilising alane at moderate temperatures given its extreme equilibrium pressures (i.e. 28 kbar at 300 °C [11,12]). The unwashed sample desorbs a significant quantity of hydrogen (3 wt.% H_2 from Al) over 24 h at 50 °C. This indicates

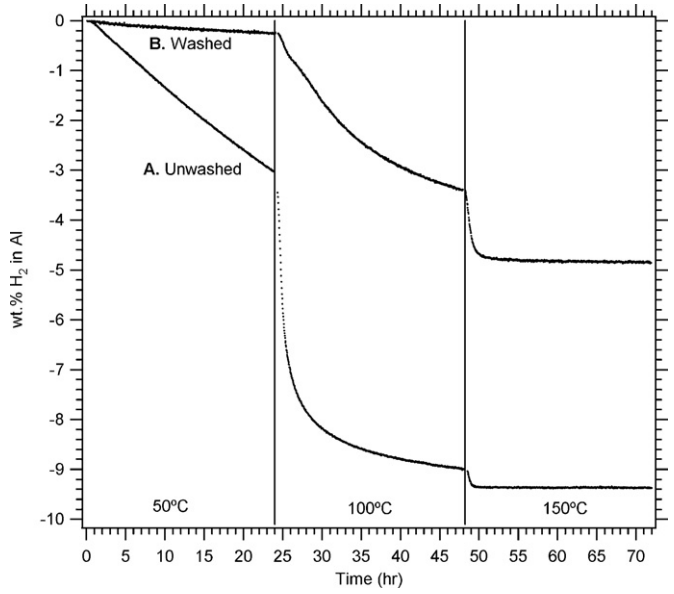

Fig. 6. Hydrogen desorption data from (A) unwashed and (B) washed samples cryogenically milled for 1 h with a 2:1 LiCl:AlH_3 volume ratio. The H_2 wt.% is given as a percentage of the calculated non-salt portion of the samples. Data was collected every 2 min for 24 h periods at each temperature consecutively.

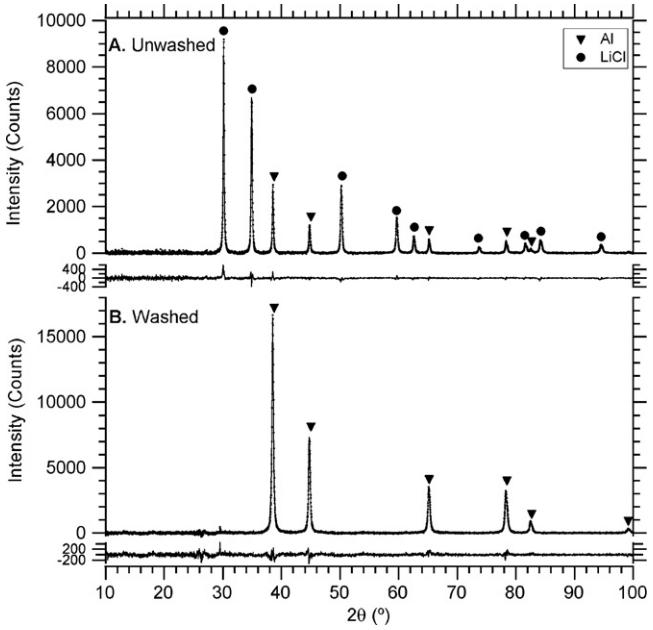

Fig. 7. X-ray diffraction (XRD) patterns for desorbed cryogenically synthesised alane milled for 60 min with a 2:1 LiCl:AlH_3 volume ratio (A) before and (B) after washing with nitromethane and $AlCl_3$. Patterns have been background subtracted for clarity. Rietveld fits to the data are also displayed (solid line) along with difference plots.

rapid decomposition at a lower temperature than results reported for bulk, Dow-synthesised alane which provide adequate kinetics often in the order of 100 °C, although these kinetics can be enhanced by doping [9]. However similar kinetics to those reported herein have been observed for freshly synthesised alane decomposed at 60 °C [7]. Fig. 6 shows that rapid desorption occurs at 100 °C and raising the sample temperature to 150 °C results in complete hydrogen desorption. The resultant measured alane content is 25.0 wt.% in the total sample with only a calculated as-milled 1.4 wt.% Al content (73.6% LiCl). The desorption kinetics will likely be hindered by the fact that the alane particles are embedded within a LiCl salt matrix. Restricted desorption kinetics are beneficial during room temperature storage but LiCl is not fully effective in kinetically stabilising alane decomposition.

The hydrogen desorption results for the washed alane sample are interesting. Firstly desorption kinetics are significantly slower, and secondly the maximum H_2 wt.% is half that of the unwashed sample. Desorption kinetics should be quicker for the washed sample due to the absence of kinetically hindering LiCl salt. However, the slower observed kinetics suggest a limiting factor may be present. Aluminium oxide surface layers can be detrimental to molecular [37] and even atomic [38] hydrogen permeation. Despite XRD showing only AlH_3 and Al in the washed samples, the evolution of gas upon addition of the as-synthesised sample to nitromethane suggests that an unwanted (oxide/hydroxide) phase may have formed. The formation of amorphous aluminium oxide phases rather than crystalline phases have been theoretically shown to be thermodynamically favourable [39]. The theoretical results in the literature have also been reinforced by experimental amorphous oxide formation [40]. Given that no oxide or hydroxide phases were detected with XRD and that the maximum H_2 wt.% is half that of the unwashed sample it seems likely that the washed sample contains a significant amorphous aluminium oxide/hydroxide phase. The extent of oxide contamination would be exacerbated by the small particle size of the synthesised AlH_3 nanoparticles that provides a large surface area in which oxide formation can occur.

XRD was also performed on the desorbed unwashed and washed alane samples (see Fig. 7). The XRD data verifies that hydrogen desorption was complete for both samples. No crystalline oxide or hydroxide phases are observed in the desorbed sample XRD patterns which were taken after sample heating to 150 °C. QPA results provided in Table 3 display the crystalline compositions of both the unwashed and washed alane samples before and after desorption. A comparison between the AlH_3 content derived from hydrogen desorption measurements for the unwashed sample (25.0 wt.%) and the AlH_3 content from XRD results (15.8 wt.%) reveals a disparity between the total amount of alane in the sample and the crystalline content. These results suggest that at least 37% of the alane present in the unwashed sample is non-crystalline.

Based on knowledge of the sample history and crystallite size trends (see Table 3), information regarding alane crystallite behaviour upon washing and desorption can be gained. A comparison between unwashed and washed samples reveals an increase in the average crystallite size of AlH_3 and Al upon washing. An average crystallite size increase may occur from two phenomena. Firstly, centrifugation preferentially separates the largest AlH_3/Al particles from solution first, and it is possible that the smallest particles remained in solution increasing the average separated crystallite size. Secondly, it is possible that exothermic amorphous oxide formation during the washing procedure generated heat that

Table 3
Crystalline QPA results from Rietveld fits for XRD patterns given in Figs. 5 and 7 for unwashed and washed alane samples before and after desorption. Wt.%, crystallite sizes, and mathematical fitting uncertainties of one standard deviation are provided.

	Phase	Crystalline (wt.%)	Crystallite size (nm)
Unwashed	α'-AlH_3	5.8 ± 0.4	11.3 ± 1.7
	α-AlH_3	10.0 ± 0.3	20.5 ± 1.0
	Al	2.7 ± 0.3	7.9 ± 1.3
	LiCl	81.5 ± 0.5	40.5 ± 1.8
Unwashed–desorbed	Al	23.9 ± 0.1	39.0 ± 0.6
	LiCl	76.1 ± 0.1	81.0 ± 3.1
Washed	α'-AlH_3	28.4 ± 0.2	17.7 ± 0.3
	α-AlH_3	62.9 ± 0.2	21.5 ± 0.2
	Al	8.8 ± 0.1	22.3 ± 0.7
Washed–desorbed	Al	100	26.1 ± 0.1

promoted crystallite growth in solution. Alternatively physical contact between AlH_3/Al particles upon the removal of the salt matrix may have also resulted in particle agglomeration and crystallite growth.

A comparison between the XRD data for desorbed samples and their precursor materials also reveals alane crystallite behaviour. In the unwashed samples it appears that the 2:1 volume ratio between LiCl and AlH_3 may be insufficient to completely separate the AlH_3 particles. Previous research [41] has required using volume ratios as high as 10:1 to result in well separated particles. Consequently, during desorption (heating to 150 °C), crystallite size may increase due to both intra-particle crystallite growth and inter-particle agglomeration. In the washed samples, there is very little difference in the crystallite size of the Al upon heating to 150 °C. Intra-particle crystallite growth may have already occurred during the washing process and the amorphous oxide coating generated during this washing may hinder inter-particle growth during heating.

4. Conclusions

Alane nanoparticles have been synthesised via both room temperature and cryogenic mechanochemical synthesis. The evolution of alane production was investigated as a function of milling time under a variety of milling conditions. Cryogenic milling was verified to form higher yields of AlH_3 and four different crystalline alane phases (α, α', β, γ) were identified via XRD structural investigations. The LiCl reaction by-product phase was removed via washing with a nitromethane/$AlCl_3$ solution, which adversely reacted with the AlH_3 nanoparticles. The hydrogen desorption kinetics for the washed sample were hindered and the maximum H_2 wt.% was halved, although no crystalline oxide or hydroxide phases were found via XRD. Unwashed mechanochemically synthesised AlH_3 was found to desorb at room temperature over months and significantly at 50 °C in a 24 h period. QPA results coupled with hydrogen desorption measurements suggest the presence of an amorphous AlH_3 phase in mechanochemically synthesised samples, which deserves further study to identify its structural characteristics. If mechanochemically synthesised alane is to be successfully washed from LiCl a less reactive solvent must be discovered which will not alter the alane particle surface. However, alane without a kinetic barrier to hydrogen desorption is extremely unstable at room temperature.

Acknowledgements

M. Paskevicius would like to thank the Australian government for the granting of Australian Post Graduate Awards with Stipend (APAWS), and the Australian Institute of Nuclear Science and Engineering (AINSE) for the granting of a postgraduate research award (PGRA). The authors would also like to thank R.D. Hart at Curtin University for his assistance during TEM investigations.

References

[1] A.E. Finholt, A.C. Bond Jr., H.I. Schlesinger, J. Am. Chem. Soc. 69 (1947) 1199–1203.
[2] M.A. Petrie, J.C. Bottaro, R.J. Schmitt, P.E. Penwell, D.C. Bomberger, US Patent 6,228,338 B1, 8 May, 2001.
[3] H.W. Brinks, A. Istad-Lem, B.C. Hauback, J. Phys. Chem. B 110 (2006) 25833–25837.
[4] H.W. Brinks, W. Langley, C.M. Jensen, J. Graetz, J.J. Reilly, B.C. Hauback, J. Alloys Compd. 433 (2007) 180–183.
[5] H.W. Brinks, C. Brown, C.M. Jensen, J. Graetz, J.J. Reilly, B.C. Hauback, J. Alloys Compd. 441 (2007) 364–367.
[6] F.M. Brower, N.E. Matzek, P.F. Reigler, H.W. Rinn, C.B. Roberts, D.L. Schmidt, J.A. Snover, K. Terada, J. Am. Chem. Soc. 98 (1976) 2450–2453.
[7] J. Graetz, J.J. Reilly, J. Phys. Chem. B 109 (2005) 22181–22185.
[8] J. Graetz, J.J. Reilly, J.G. Kulleck, R.C. Bowman, J. Alloys Compd. 446–447 (2007) 271–275.
[9] G. Sandrock, J. Reilly, J. Graetz, W.-M. Zhou, J. Johnson, J. Wegrzyn, Appl. Phys. A 80 (2005) 687–690.
[10] G. Sandrock, J. Reilly, J. Graetz, W.-M. Zhou, J. Johnson, J. Wegrzyn, J. Alloys Compd. 421 (2006) 185–189.
[11] B. Baranowski, M. Tkacz, Z. Phys. Chem. 135 (1983) 27–38.
[12] S.K. Konovalov, B.M. Bulychev, Inorg. Chem. 34 (1995) 172–175.
[13] R. Zidan, B.L. Garcia-Diaz, C.S. Fewox, A.C. Stowe, J.R. Gray, A.G. Harter, Chem. Comm. (2009) 3717–3719.
[14] G.S. McGrady, US Patent US 2008/0241056 A1, 2 October, 2008.
[15] J. Graetz, Chem. Soc. Rev. 38 (2009) 73–82.
[16] J. Ding, T. Tsuzuki, P.G. McCormick, R. Street, J. Alloys Compd. 234 (1996) L1–L3.
[17] P.G. McCormick, T. Tsuzuki, J.S. Robinson, J. Ding, Adv. Mater. 13 (2001) 1008–1010.
[18] P.G. McCormick, J. Ding, W.-F. Miao, R. Street, US Patent 6,203,768 B1, 20 March, 2001.
[19] T. Tsuzuki, P.G. McCormick, J. Mater. Sci. 39 (2004) 5143–5146.
[20] C. Suryanarayana, Prog. Mater. Sci. 46 (2001) 1–184.
[21] Personal communication: E.MacA. Gray, M.P. Pitt., Griffith University, Australia.
[22] H.C. Brown, N.M. Yoon, J. Am. Chem. Soc. 88 (1966) 1464–1472.
[23] H.V.A. Briscoe, A.A. Eldridge, G.M. Dyson, A.J.E. Welch (Eds.), Mellor's Comprehensive Treatise on Inorganic and Theoretical Chemistry, Longman Group Limited, London, 1972.
[24] A.A. Coelho, Topas User Manual, Bruker AXS GmbH, Karlsruhe, Germany, 2003.
[25] H. Hemmes, A. Driessen, R. Griessen, J. Phys. C: Solid State Phys. 19 (1986) 3571–3585.
[26] K.G. McLennan, E. MacA. Gray, Meas. Sci. Technol. 15 (2004) 211–215.
[27] Outukumpu, HSC Chemistry 6.1, Chemistry Software, Houston, 2006.
[28] S. Sun, X. Ke, C. Chen, I. Tanaka, Phys. Rev. B 79 (2009) 024104.
[29] J. Graetz, J. Reilly, J. Alloys Compd. 424 (2006) 262–265.
[30] H. Grove, M.H. Sørby, H.W. Brinks, B.C. Hauback, J. Phys. Chem. C 111 (2007) 16693–16699.
[31] J.P. Maehlen, V.A. Yartys, R.V. Denys, M. Fichtner, Ch. Frommen, B.M. Bulychev, P. Pattison, H. Emerich, Y.E. Filinchuk, D. Chernyshov, J. Alloys Compd. 446–447 (2007) 280–289.
[32] S. Sartori, S.M. Opalka, O.M. Løvvik, M.N. Guzik, X. Tang, B.C. Hauback, J. Mater. Chem. 18 (2008) 2361–2370.
[33] H. Saitoh, A. Machida, Y. Katayama, K. Aoki, Appl. Phys. Lett. 93 (2008) 151918.
[34] X. Ke, A. Kuwabara, I. Tanaka, Phys. Rev. B 71 (2005) 184107.
[35] K. Ikeda, S. Muto, K. Tatsumi, M. Menjo, S. Kato, M. Bielmann, A. Züttel, C.M. Jensen, S. Orimo, Nanotechnology 20 (2009) 204004.
[36] M. Paskevicius, J. Webb, M.P. Pitt, T.P. Blach, B.C. Hauback, E.MacA. Gray, C.E. Buckley, J. Alloys Compd. 481 (2009) 595–599.
[37] J.L. Maienschein, R.G. Musket, F.E. McMurphy, D.W. Brown, Appl. Phys. Lett. 50 (1987) 940–942.
[38] Y. Yamada-Takamura, F. Koch, H. Maier, H. Bolt, Surf. Coat. Technol. 153 (2002) 114–118.
[39] L.P.H. Jeurgens, W.G. Sloof, F.D. Tichelaar, E.J. Mittemeijer, Phys. Rev. B 62 (2000) 4707–4719.
[40] L.P.H. Jeurgens, W.G. Sloof, F.D. Tichelaar, E.J. Mittemeijer, J. Appl. Phys. 92 (2002) 1649–1656.
[41] T. Tsuzuki, J. Ding, P.G. McCormick, Physica B 239 (1997) 378–387.

Journal of Alloys and Compounds 492 (2010) L72–L74

Contents lists available at ScienceDirect

Journal of Alloys and Compounds

journal homepage: www.elsevier.com/locate/jallcom

Letter

The Mechanochemical synthesis of magnesium hydride nanoparticles

Drew A. Sheppard [a,*], Mark Paskevicius [a], Craig E. Buckley [a,b]

[a] Department of Imaging and Applied Physics at Curtin University of Technology, GPO Box U 1987, Perth 6845, Australia
[b] CSIRO National Hydrogen Materials Alliance, CSIRO Energy Centre, 10 Murray Dwyer Circuit, Steel River Estate, NSW 2304, Australia

ARTICLE INFO

Article history:
Received 23 July 2009
Received in revised form
27 November 2009
Accepted 3 December 2009
Available online 11 December 2009

Keywords:
Hydrogen storage materials
Nanostructures
Mechanochemical synthesis
X-ray diffraction
Magnesium hydride

ABSTRACT

A mechanochemical method was used to synthesise magnesium hydride nanoparticles with an average crystallite size of 6.7 nm. The use of a reaction buffer was employed as a means of particle size control by restricting agglomeration. Increasing the amount of reaction buffer resulted in a decrease in crystallite size, as determined via X-ray diffraction, and a decrease in particle size, evidenced by transmission electron microscopy.

1. Introduction

Hydrogen is an ideal energy carrier and contains more chemical energy per weight than any hydrocarbon. It can be used in a fuel cell to produce water as the only emission. However, the effective storage of hydrogen still remains a barrier to the implementation of a hydrogen economy. Magnesium has been widely studied due to its ability to absorb 7.7 wt.% of hydrogen but its use is impeded by a high thermal stability and poor sorption kinetics. The kinetic issue has largely been overcome by using ball milling to introduce catalytic metal oxides [1–5] or metal halides [6,7]. Recently, theoretical work has suggested that reducing the MgH_2 particle size below 10 nm [8] should alter the thermodynamics of MgH_2 with the effect becoming appreciable below 3 nm [8–11]. Traditional ball milling can reduce MgH_2 crystallite sizes to ~7 nm [5] but these consist of crystallite domains within much larger particles. Subsequent heating to 300 °C to release hydrogen also results in substantial crystallite growth [5,12]. Recent efforts to produce nanometre-sized magnesium include magnesium melt infiltration into porous carbon [13] and sonoelectrochemical deposition from magnesium salt solutions [14].

Mechanochemical synthesis is a technique that employs solid–state displacement reactions during ball milling [15]. This method has been used recently to synthesize AlH_3 [16] and $Mg(AlH_4)_2$ [17]. However, these authors did not use particle size control methods, such as varying: the amount of buffering agent; the milling time; the milling collision energy and; the milling temperature, that have been used to produce separated, nanosized particles of oxides [18], mixed metal oxides [19], metals [20,21], hydrides [22] and sulphides [23]. Employing the particle size control methods can produce particles as small as 4 nm [24] embedded in larger by-product phase particles. Herein, for the first time, we present the results of the synthesis of MgH_2 nanoparticles using the mechanochemical method. In addition, the variation in the microstructure of the synthesised MgH_2 was examined as a function of the quantity of LiCl used as a reaction buffer. The aim of using LiCl as a reaction buffer is not to produce a new hydrogen storage material comprising MgH_2 and LiCl but to produce separated nanosized particles of MgH_2 for which the thermodynamics can be compared to theoretical predictions. The synthesis of MgH_2 was achieved by utilising the following chemical reaction:

$$2LiH + MgCl_2 \rightarrow MgH_2 + 2LiCl \quad (1)$$

The reaction between LiH and $MgCl_2$ was first undertaken by Ashby & Schwartz in 1971 within a tetrahydrofuran (THF) solvent [25]. The reaction was only found to progress under refluxing conditions and not at room temperature. However, even in the absence of a solvent, Eq. (1) is thermodynamically favourable at room temperature with a Gibbs free energy of −73 kJ/mol [26].

2. Experimental

All handling of chemicals and sealable milling vials was undertaken in an argon-atmosphere glovebox in order to minimise oxygen (O_2 < 1 ppm) and water (H_2O < 1 ppm) contamination. LiH (Sigma–Aldrich, 95%), $MgCl_2$ (Sigma, ≥98%) and

* Corresponding author. Tel.: +61 8 92664955; fax: +61 8 92662377.
E-mail address: drew.sheppard@gmail.com (D.A. Sheppard).

0925-8388/$ – see front matter © 2009 Elsevier B.V. All rights reserved.
doi:10.1016/j.jallcom.2009.12.006

LiCl (Sigma–Aldrich, ≥99.9%) were used as starting reagents without further purification. Ball milling (using equal numbers of 12.7 mm and 7.9 mm 316 stainless steel balls) was performed using a custom made 316 stainless steel ball milling canister (650 cm^3 internal volume) attached to a Glen Mills Turbula T2C shaker mixer operating at 160 rpm. All reagents were ball milled separately for 3 h at a ball-to-powder (BTP) ratio of 30:1 prior to use, as reducing the grain size of the starting reagents has been shown to accelerate the kinetics of mechanochemical reactions [23]. Four samples of MgH_2 were produced (BTP = 90:1) using various amounts of LiCl buffer added to the starting reagents. The amount of LiCl added for each sample corresponded to 0 (sample MgH_2-A), 1.05 (sample MgH_2-B), 2.62 (sample MgH_2-C) and 6.82 (sample MgH_2-D) moles of LiCl added to the left hand side of Eq. (1).

X-ray diffraction patterns (XRD) were collected from samples sealed in 0.5 mm special glass capillaries (Charles Supper Company) at the Australian Synchrotron using a wavelength of 0.10001 nm (12.3985 keV) for 900 s each. The 2θ range spanned 5–85° with a step size of 0.004°. Rietveld analysis of the XRD patterns was performed using the software package Topas (Bruker AXS, Karlsruhe, Germany) using a fundamental parameters approach [27]. The XRD background was modelled using a 7-point polynomial and broad peak fitting was used to model the scattering from the capillary. The crystallite sizes were determined from an LVol-IB method (volume averaged column height calculated from the integral breadth) which provides a good measure of the volume-weighted mean crystallite size [27]. Transmission electron microscopy (TEM) was conducted on a JEOL JEM2011 instrument operating at 200 kV at Curtin University of Technology and a JEOL 3000F FEGTEM instrument operating at 300 kV at the Centre for Microscopy, Characterisation and Analysis (CMCA) at the University of Western Australia. Hydrogen absorption was performed at 300 °C on a Sieverts apparatus using a Rosemount 3051S digital pressure gauge with an accuracy and precision of 0.014 bar. Absorption measurements resulted in pressure drops of greater than 4 bar in a system volume of ~25 cm^3 with samples comprising between 0.12 and 0.24 g of Mg content.

3. Results and discussion

Figure 1 displays the XRD patterns for MgH_2-A, MgH_2-B, MgH_2-C and MgH_2-D. After 18 h of milling XRD of MgH_2-A reveals only MgH_2 and LiCl (Figure 1A). No starting reagents are detectable. As expected, the MgH_2 peak intensities decrease for subsequent samples as the amount of LiCl added to the initial starting reagents increases. The XRD patterns for MgH_2-A, MgH_2-B and MgH_2-C (Figure 1A–C) show a minor unknown peak at $d = 0.3142$ nm, not detected by laboratory based XRD, that did not match any phase that consisted of elements within the starting reagents. A peak at $d = 0.2075$ nm clearly discernable in MgH_2-D is attributed to 316 stainless steel, a minor contaminant from the ball milling canister (also not detected in laboratory based XRD). From Rietveld refinement the MgH_2 crystallite sizes for MgH_2-A, MgH_2-B, MgH_2-C and MgH_2-D were determined to be 10.1 ± 0.3 nm, 7.6 ± 0.3 nm, 6.7 ± 0.4 nm and 6.7 ± 0.7 nm respectively, where uncertainties are quoted as 95% confidence intervals.

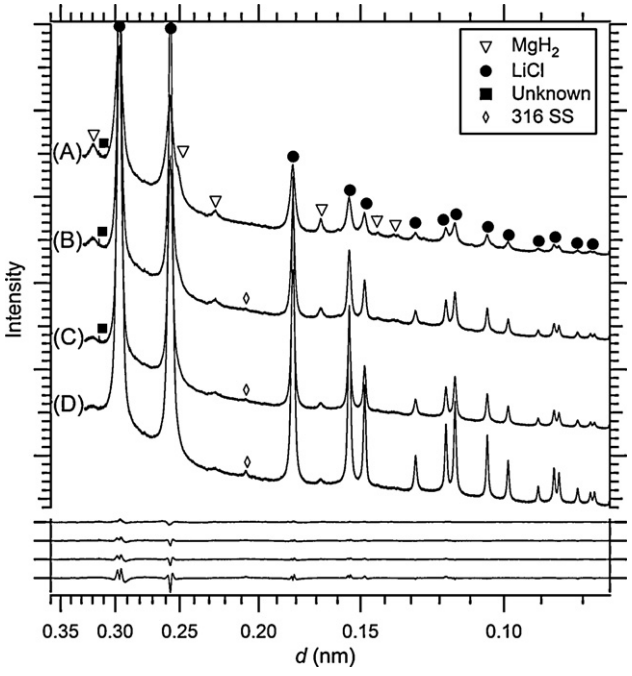

Fig. 1. Synchrotron X-ray diffraction data on sample (A) MgH_2-A, (B) MgH_2-B, (C) MgH_2-C and (D) MgH_2-D. 316 SS refers to stainless steel type 316. Difference plots for the Rietveld fits to the experimental data are shown at the bottom.

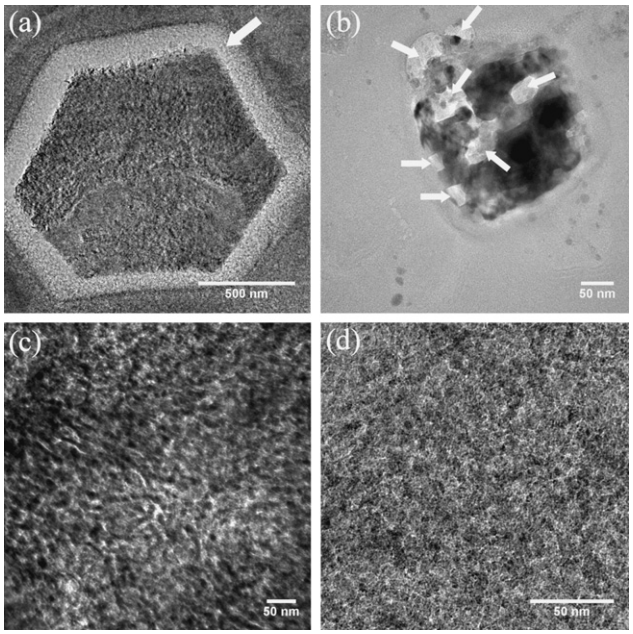

Fig. 2. Representative transmission electron microscopy images of (A) MgH_2-A, (B) MgH_2-B, (C) MgH_2-C and (D) MgH_2-D. White arrows indicating regions that underwent decomposition during exposure to the electron beam.

Though synchrotron XRD was able to distinguish MgH_2 in the sample MgH2-D, it was not detected by laboratory based XRD. As a result of the inability to detect minor light element phases, quantitative phase analysis from XRD diffraction may prove unreliable in measuring the extent to which the reaction in Eq. (1) is complete. Consequently, hydrogen sorption measurements were performed to determine the MgH_2 content in each sample. The samples were placed in a Sieverts hydrogen sorption apparatus, without exposure to air, and out-gassed at 300 °C for 24 h. This temperature is insufficient to remove hydrogen from any unreacted LiH and therefore the subsequent hydrogen absorption can be attributed solely to Mg. In considering the extent to which the reaction in Eq. (1) had gone to completion during ball milling for each sample, the fact that the starting reagent, LiH, had only 95% purity must be considered. From the hydrogen sorption measurements it was found that for MgH_2-A, MgH_2-B, MgH_2-C and MgH_2-D the reactions were 94.5, 84.9, 82.2 and 78.1% complete, respectively (uncertainties are ±0.5%). The decrease in the extent to which Eq. (1) is complete is an expected consequence of the dilution of the starting reagents, LiH and $MgCl_2$, which hinders reagent contact and thus reaction kinetics.

Representative transmission electron microscopy (TEM) images for each sample are displayed in Figure 2. MgH_2-A (Figure 2A) primarily showed large geometrical shapes (typically hexagons) 1–2 μm in size. The large geometrical structures, which were initially dark, showed a steadily increasing light band over time (indicated by an arrow in Figure 2A) around the outer edge on exposure to the electron beam. This effect ceased after some minutes. The growth of the light band suggested that these micron sized particles are MgH_2 that underwent hydrogen desorption under the beam. MgH_2-B showed no large geometrical shapes such as those in MgH_2-A. Typical morphologies (Figure 2B) consisted of aggregates of irregularly shaped particles 15–40 nm in size. Time-lapse TEM images showed that some particles within the aggregates (indi-

cated by arrows in Figure 2B) desorbed under the electron beam over the course of several minutes. These particles, however, maintained their morphology. MgH_2-C (Figure 2C) is comprised of only a single morphology consisting of well-dispersed 12–20 nm particles. Given the average MgH_2 crystallite from XRD is 6.7 nm, it is suggested that each particle in MgH_2-C consists of several crystallite domains. MgH_2-D (Figure 2D) is largely homogenous and does not show any readily recognisable particle morphology. TEM of this site with increased magnification identified lattice-fringing regions that extended for 2–4 nm. The lattice-fringing regions were limited to the MgH_2 $hkl = 0\,2\,0$ plane suggesting very small MgH_2 crystallites were synthesised. Whether these crystallites were part of larger grains or individually dispersed was difficult to determine. However it should be noted that the crystallite sizes, as seen by lattice fringing, in sample MgH_2-D are comparable to that determined via XRD. This is in contrast to other recent efforts in producing nanometre scale magnesium [14] in which the crystallite size, as determined via TEM, is almost an order of magnitude smaller than that determined via XRD. Such a difference may be attributed to the fact that TEM samples therein may not be representative of the average sample structure in comparison to XRD.

An electrochemical method has also recently been used to synthesise a colloid containing 18 mass% 5 nm Mg nanoparticles [28] stabilised by tetrabutylammonium bromide (TBA). After hydriding, the material displayed a hydrogen desorption pressure of 0.3 kPa at just 85 °C. The desorption pressure at this temperature is significantly higher than that predicted by theoretical calculations for even 1 nm MgH_2 particles [8]. It is in our opinion that such a measured desorption pressure is not a result of the particle size, as claimed by the authors, but by a chemical interaction between the Mg and the ammonium salt causing a destabilisation of the hydride phase. Such large changes in the thermodynamics of hydrides have previously been observed for AlH_3-adduct systems [29]. The absence of a TBA melting event in differential thermal analysis [28], which usually occurs at ~100 °C, further suggests that a chemical interaction between the Mg surface and TBA is responsible for the altered thermodynamics observed for the hydrogen desorption over TBA stabilised Mg nanoparticles. In contrast, the MgH_2 nanoparticles produced via the mechanochemical process are only physically bound by the LiCl by-product and their thermodynamic properties should be directly comparable to theoretical predictions of changes in MgH_2 thermodynamic properties with particle size.

4. Conclusions

In the present work the mechanochemical synthesis of MgH_2 has been undertaken with varying LiCl buffer amounts. Increasing buffer results in MgH_2 crystallite sizes down to 6.7 nm, measured via XRD, whilst TEM investigations show that increasing buffer results in smaller, more highly dispersed MgH_2 nanoparticles. The size of these MgH_2 particles approaches theoretical predictions for thermodynamic changes and the MgH_2 is only physically bound by the LiCl. Removal of the LiCl salt by-product phase has thus far proved difficult due to either the high reactivity or the solubility of MgH_2 in solvents which will dissolve LiCl. Preliminary hydrogen sorption measurements also indicate that an increase in the hydrogen equilibrium pressure occurs for samples with higher LiCl buffers (and hence smaller particle sizes). The removal of the by-product phase and thermodynamic measurements are the subject of a forthcoming publication.

Acknowledgements

This work was carried out with the support of the CSIRO Energy Transformed Flagship National Hydrogen Materials Alliance (NHMA), Australia and an Australian Research Council discovery grant DP0877155. The authors acknowledge the facilities, scientific and technical assistance of the Australian Synchrotron and the Australian Microscopy & Microanalysis Research Facility at the Centre for Microscopy, Characterisation & Analysis, the University of Western Australia, a facility funded by The University, State and Commonwealth Governments. M. Paskevicius would also like to thank the Australian government for the granting of Australian Post Graduate Awards with Stipend (APAWS), and the Australian Institute of Nuclear Science and Engineering (AINSE) for the granting of a postgraduate research award (PGRA).

References

[1] M. Polanski, J. Bystrzycki, J. Alloys Compd. 486 (2009) 697–701.
[2] N. Hanada, E. Hirotoshi, T. Ichikawa, E. Akiba, H. Fujii, J. Alloys Compd. 450 (2008) 395–399.
[3] M. Porcu, A.K. Petford, J.M. Sykes, J. Alloys Compd. 453 (2008) 341–346.
[4] G. Barkordarian, T. Klassen, R. Bormann, J. Alloys Compd. 364 (2004) 242–246.
[5] K.F. Aguey-Zinsou, J.R. Ares-Fernandez, T. Klassen, R. Bormann, Mater. Res. Bull. 41 (2006) 1118–1126.
[6] Y. Luo, P. Wang, L.–P. Ma, H.–M. Cheng, J. Alloys Compd. 453 (2008) 138–142.
[7] V.V. Bhat, A. Rougier, L. Aymand, X. Darok, G. Nazri, J.M. Tarascon, J. Power Sources 159 (2006) 107–110.
[8] K.C. Kim, B. Dai, K.J. Johnson, D.S. Sholl, Nanotechnol. 20 (2009) 204001.
[9] J.J. Liang, Appl. Phys. A 80 (2005) 173–178.
[10] R.W.P. Wagemans, J.H. van Lenthe, P.E. de Jongh, A.J. van Dillen, K.P. de Jong, J. Am. Chem. Soc. 127 (2005) 16675–16680.
[11] S. Cheung, W.Q. Deng, A.C.T. van Duin, W.A. Goddard, J. Phys. Chem. A 109 (2005) 851–859.
[12] J. Huot, J.F. Pelletier, L.B. Lurio, M. Sutton, R. Schulz, J. Alloys Compd. 348 (2003) 319–324.
[13] P.E. de Jongh, R.W.P. Wagemans, T.M. Eggenhuisen, B.S. Dauvillier, P.B. Radstake, J.D. Meeldijk, J.W. Geus, K.P. de Jong, Chem. Mater. 19 (2007) 6052–6057.
[14] I. Haas, A. Gedanken, Chem. Comm. (2008) 1795–1797.
[15] J. Ding, W.F. Miao, P.G. McCormick, R. Street, Appl. Phys. Lett. 67 (1995) 3804–3806.
[16] H.W. Brinks, A. Istad-Lem, B.C. Hauback, J. Phys. Chem. B 110 (2006) 25833–25837.
[17] R.A. Varin, C. Chiu, T. Czujko, Z. Wronski, J. Alloys Compd. 439 (2007) 302–311.
[18] J. Ding, T. Tsuzuki, P.G. McCormick, Nanostruct. Mater. 8 (1997) 75–81.
[19] A. Dodd, A. McKinley, T. Tsuzuki, M. Saunders, J. Eur. Ceram. Soc. 29 (2009) 139–144.
[20] C. Suryanarayana, Prog. Mater. Sci. 46 (2001) 1–184.
[21] M. Paskevicius, J. Webb, M.P. Pitt, T.P. Blach, B.C. Hauback, E.MacA. Gray, C.E. Buckley, J. Alloys Compd. 481 (2009) 595–599.
[22] M. Paskevicius, D.A. Sheppard, C.E. Buckley, J. Alloys Compd. 487 (2009) 370–376.
[23] T. Tsuzuki, J. Ding, P.G. McCormick, Physica B 239 (1997) 378–387.
[24] P.G. McCormick, T. Tsuzuki, J.S. Robinson, J. Ding, Adv. Mater. 13 (2001) 1008–1010.
[25] E.C. Ashby, R.D. Schwartz, Inorg. Chem. 10 (1971) 355–357.
[26] Outukumpu, HSC Chemistry, Chemistry Software: Houston, 2006.
[27] A.A. Coelho, Topas User Manual, Bruker AXS GmbH, Karlsruhe, Germany, 2003.
[28] K.F. Aguey-Zinsou, J.R. Ares-Fernandez, Chem. Mater. 20 (2008) 376–378.
[29] J. Graetz, Chem. Soc. Rev. 38 (2009) 73–82.